Southern Hemisphere Regional Precipitation and Climate Variability: Extremes, Trends, and Predictability

Caroline C. Ummenhofer

Climate Change Research Centre, School of Mathematics and Statistics,

The University of New South Wales, Sydney, Australia

April 2008

PhD Thesis

A thesis submitted in fulfillment of the requirements for the degree of Doctor of Philosophy

Originality Statement

'I hereby declare that this submission is my own work and to the best of my knowledge it contains no materials previously published or written by another person, or substantial proportions of material which have been accepted for the award of any other degree or diploma at UNSW or any other educational institution, except where due acknowledgement is made in the thesis. Any contribution made to the research by others, with whom I have worked at UNSW or elsewhere, is explicitly acknowledged in the thesis. I also declare that the intellectual content of this thesis is the product of my own work, except to the extent that assistance from others in the project's design and conception or in style, presentation and linguistic expression is acknowledged.'

Signed .....

Date .....

I have discovered the secret that after climbing a great hill,
one only finds that there are many more hills to climb.

– Nelson Mandela

Abstract

This PhD thesis investigates the relative importance of oceanic and atmospheric influences on extremes, long-term trends, and seasonal to interannual variability of precipitation for different regions in the Southern Hemisphere in observations, reanalysis data, and output from general circulation models (GCM).

Examination of interannual rainfall extremes over southwest Western Australia (SWWA) reveals a characteristic dipole pattern of Indian Ocean sea surface temperature anomalies (SSTA). This coincides with a large-scale reorganization of the wind field over the tropical/subtropical Indian Ocean changing SSTA, via anomalous Ekman transport in the tropical Indian Ocean and via anomalous air-sea heat fluxes in the subtropics, and altering moisture advection onto SWWA. The potential impact of these Indian Ocean SSTA in driving modulations of mid-latitude precipitation across southern and western regions of Australia is assessed in atmospheric GCM simulations. The SSTA give rise to changes in the thermal properties of the atmosphere, meridional thickness gradient, subtropical jet, thermal wind, and baroclinicity over southern regions of Australia, thus modulating precipitation. In addition, links between anomalous wet conditions over East Africa and these characteristic Indian Ocean SSTA are explored during the "short rain" season in October–November.

Interannual extremes in New Zealand rainfall and their modulation by modes of Southern Hemisphere climate variability, namely the Southern Annular Mode (SAM) and El Niño-Southern Oscillation (ENSO), are investigated. Late twentieth Century trends in New Zealand precipitation are examined for the period 1979–2006 to quantify the relative impact of recent changes in the large-scale atmospheric circulation related to the SAM and ENSO. Increasingly drier conditions over much of New Zealand can be partially explained by the SAM and ENSO.

Cool season rainfall variability in southeastern Australia is investigated via a classification and characterization of the predominant types of synoptic systems occurring in the region, focusing on frontal and cutoff low systems. Two definitions of the autumn break developed for northwestern Victoria are employed to produce a synoptic climatology of the break phenomenon. Trends in characteristics of the autumn break indicate that the most recent drought in southeastern Australia is comparable in severity with the two major droughts in the twentieth Century.

Acknowledgments

This thesis would not have been possible without the considerable help of many people. First and foremost I would like to thank my supervisor Matthew England for his unstinting and unwavering support throughout the past four years.

I am much indebted to Alex Sen Gupta for his help throughout the PhD for all sorts of technical, computer-, and model-related problems, plus all others: he has always been there to give support. Extensive joint work has made the PhD a much more interesting, enlightening, and fun experience. I have also enjoyed collaborating with Agus Santoso. I am grateful to all members of CEDL/CCRC who made the time during my PhD here a memorable and very joyful one. Lunch and coffee breaks with Maxwell Gonzalez, Andrea Taschetto, and Jessica Trevena helped to keep me sane during the final stages.

I have immensely enjoyed my collaborative work with Peter McIntosh, Mike Pook, and James Risbey at CSIRO Marine and Atmospheric Research (CMAR) in Hobart. The visits were invariably very stimulating, motivating - and lots of fun. I always came back with many more new ideas, certainly enough to fill two more PhDs. For very insightful advice and discussions, I am also grateful to Gary Meyers at CMAR (now UTAS). During my frequent visits to CMAR, I was always made most welcome and I thank all my friends and staff there.

For financial assistance, I thank the University of New South Wales, the School of Mathematics and Statistics, and ARCNESS. Logistical and computer support by the staff of the School of Mathematics and Statistics and the Australian Partnership for Advanced Computing National Facility is gratefully acknowledged.

Last, but certainly not least, I am extremely grateful to my family for their unconditional support and encouragement throughout all my endeavors. My thanks also go to Björn Brodherr for his support.

Contents

List of Figures

List of Tables

Supporting Publications

England, M. H., C. C. Ummenhofer, and A. Santoso, 2006: Interannual rainfall extremes over Southwest Western Australia linked to Indian Ocean climate variability. *Journal of Climate*, **19**, 1948–1969.

England, M. H., C. C. Ummenhofer, and A. Santoso, 2006: Indian Ocean variability linked to interannual rainfall extremes over southwest Western Australia. *CLIVAR Exchanges*, **11**, 28.

Ummenhofer, C. C., and M. H. England, 2007: Interannual extremes in New Zealand precipitation linked to modes of Southern Hemisphere climate variability, *Journal of Climate*, **20**, 5418–5440.

Ummenhofer, C. C., A. Sen Gupta, and M. H. England, 2007: Causes of late twentieth Century trends in New Zealand precipitation, *Journal of Climate*, revised.

Ummenhofer, C. C., A. Sen Gupta, M. J. Pook, and M. H. England, 2007: Anomalous rainfall over southwest Western Australia forced by Indian Ocean sea surface temperatures. *Journal of Climate*, in press.

Ummenhofer, C. C., A. Sen Gupta, M. J. Pook, and M. H. England, 2007: Seasonal rainfall anomalies over Western Australia forced by Indian Ocean SST - Scope for improved forecasting. *CLIVAR Exchanges*, **12**, 30–32.

Ummenhofer, C. C., A. Sen Gupta, M. H. England, and C. J. C. Reason, 2007: Contributions of Indian Ocean sea surface temperatures to enhanced East African rainfall. *Journal of Climate*, submitted.

Pook, M., S. Lisson, J. Risbey, C. Ummenhofer, P. McIntosh, and M. Rebbeck, 2007: The autumn break for cropping in Southeast Australia: Trends, synoptic influences and impacts on yield, *International Journal of Climatology*, under revision.

Risbey, J. S., M. J. Pook, P. C. McIntosh, C. C. Ummenhofer, and G. Meyers, 2007: Variability of synoptic features associated with cool season rainfall in southeastern Australia, *International Journal of Climatology*, submitted.

Preface

This thesis incorporates several manuscripts written for publication in scientific journals, which are presented as a series of separate chapters. These manuscripts have reached various stages in the review process, which is detailed on the title page of each chapter. In addition, co-authors involved in the separate pieces of work are indicated clearly for each manuscript, as is their affiliation.

Chapter 1 provides a broad overview of the topic of research of the presented PhD thesis. Each subsequent chapter then encompasses a complete scientific manuscript, including abstract, introduction, material and methods, results, and discussion/ conclusions. At the end of each chapter the main results and conclusions of that particular study are summarized, so that the final Chapter 9 is limited to concluding remarks with future work outlined.

For each of the remaining chapters/manuscripts, my exact contributions are outlined below:

Chapter 2: England, M. H., C. C. Ummenhofer, and A. Santoso, 2006: Interannual rainfall extremes over Southwest Western Australia linked to Indian Ocean climate variability. *Journal of Climate*, **19**, 1948–1969.
All the figures and accompanying text in the observational sections are based on my own work. The model results in Section 2.5 and 2.6 were completed by Agus Santoso. Overall compilation for publication was done by Matthew England.

Chapter 3: Ummenhofer, C. C., A. Sen Gupta, M. J. Pook, and M. H. England, 2007: Anomalous rainfall over southwest Western Australia forced by Indian Ocean sea surface temperatures. *Journal of Climate*, revised (accepted).
This chapter is entirely based on my work, with the co-authors involved in interpretation of the results and text edits.

Chapter 4: Ummenhofer, C. C., A. Sen Gupta, M. H. England, and C. J. C. Reason, 2007: Contributions of Indian Ocean sea surface temperatures to enhanced

East African rainfall. *Journal of Climate*, to be submitted.
This chapter is entirely based on my work, with the co-authors involved in interpretation of the results and text edits.

Chapter 5: Ummenhofer, C. C., and M. H. England, 2007: Interannual extremes in New Zealand precipitation linked to modes of Southern Hemisphere climate variability, *Journal of Climate*, **20**, 5418–5440.
All the work for this chapter is my own, with interpretation of the results, text and editing contributed by Matthew England.

Chapter 6: Ummenhofer, C. C., A. Sen Gupta, and M. H. England, 2007: Causes of late twentieth Century trends in New Zealand precipitation, *Journal of Climate*, revised.
In this chapter, the analysis technique in Section 6.4.1 is developed by Alex Sen Gupta. All figures and text are based on my own work. The co-authors' contributions involve interpretation of the results and editing.

Chapter 7: Pook, M., S. Lisson, J. Risbey, C. C. Ummenhofer, P. McIntosh, and M. Rebbeck, 2007: The autumn break for cropping in Southeast Australia: Trends, synoptic influences and impacts on yield, *International Journal of Climatology*, submitted.
My own contributions are limited to Fig. 7.3 and the accompanying text in Section 7.4. All other analyses and text were led by Mike Pook.

Chapter 8: Risbey, J. S., M. J. Pook, P. C. McIntosh, C. C. Ummenhofer, and G. Meyers, 2007: Variability of synoptic features associated with cool season rainfall in southeastern Australia, *International Journal of Climatology*, submitted.
Figs. 8.17 and 8.21 are based on my work, along with the text describing their results in Section 8.6. All other analyses and text were led by James Risbey.

Chapter 1

Introduction

1.1. Motivation

The recent report by the Intergovernmental Panel on Climate Change (IPCC) describes the evidence for global warming as "unequivocal", and anthropogenic greenhouse gases as very likely cause for the observed temperature rise (IPCC, 2007). With a wide range of changes in the climate system already observed and many more projected for the future, impacts will be experienced all over the world. This has far-reaching implications for individuals and societies in general. A thorough understanding of "natural" unforced variability in the climate system is therefore essential, against which future climate change can be assessed. This is especially important for changes to the hydrological cycle. The livelihoods of millions of people are threatened by insecure access to drinking water. Water resources are already highly strained in many places due to an uneven water distribution in both time and space (Oki and Kanae, 2006), and future changes to the distribution of freshwater resources remain poorly understood.

Changes in the large-scale atmospheric circulation in the extratropics of the Southern Hemisphere over recent decades have been widely documented (e.g., Thompson and Solomon, 2002; Fyfe, 2003; Gillett and Thompson, 2003; Marshall *et al.*, 2004; Renwick, 2004). Foremost there has been a positive trend in the leading mode of Southern Hemisphere climate variability, the Southern Annular Mode (SAM; Thompson and Wallace, 2000; Thompson *et al.*, 2000), projected to continue over the 21st Century (e.g., Fyfe *et al.*, 1999; Kushner *et al.*, 2001; Arblaster and Meehl, 2006). It is therefore of interest to investigate the effect of this leading mode of variability on regional precipitation variability and trends over the Southern Hemisphere. This is one of the goals of the present study.

Recent findings suggest that the oceans in the extratropics can influence the overlying atmosphere beyond the marine boundary layer, and thus modulate the

large-scale atmospheric circulation (Kushnir *et al.*, 2002, and references therein). In this study, regional precipitation variability in three regions with different climatic signatures is explored with the aim of understanding the atmospheric mechanisms at play. In addition, I will assess the role of tropical and extratropical Indian Ocean sea surface temperature (SST) in modulating these regional variations. A better understanding of the factors involved in influencing regional rainfall variability could aid in improving seasonal forecasting.

1.2. Characteristics of Southern Hemisphere climate

1.2.1. Mean state

The major driver of the atmospheric circulation is the differential solar heating in the tropical and polar regions, i.e. a net heat gain in the tropics and a net heat loss at high latitudes. The meridional gradient in solar heating is clearly seen in the distribution of SST averaged over the period 1979–2001 (Fig. 1.1a, b). The difference in heating between the low and high latitudes is balanced by the poleward transport of energy in the oceans and the atmosphere. The exact distribution of the general atmospheric circulation is influenced by the Earth's rotation, and the need to globally conserve mass, angular momentum, moisture, and total energy (Karoly *et al.*, 1998). Compared to the Northern Hemisphere, the greater proportion of surface area covered by the ocean in the Southern Hemisphere results in a lower amplitude of the seasonal cycle. In addition, the band of circumpolar ocean uninterrupted by land masses in the Southern Hemisphere allows very strong zonal flow to develop. Thus, the atmospheric circulation, and coincidentally the storm tracks and the passage of weather systems in the Southern Hemisphere, is more zonally symmetric than its northern counterpart (Karoly *et al.*, 1998). This can be clearly seen in the sea level pressure (SLP) distribution shown as a long-term average for the period 1979–2001 in Fig. 1.1c, d. Clearly discernible is the belt of high pressure regions in the subtropics centered at 30°S, strengthened during austral winter. The circumpolar low pressure trough south of 60°S also intensifies during austral winter, enhancing the meridional pressure gradient during this season. The pattern of surface winds is dominated by the strong circumpolar zonal westerlies centered at 50°S (Fig. 1.1e, f). The seasonal strengthening of the subtropical jet is seen during austral winter over the southern Indian Ocean, with increased westerly airflow over southern regions of Australia (Fig. 1.1f). Also apparent is the seasonal reversal of the surface wind field over the equatorial Indian Ocean, with northeasterly trade winds north of the equator during austral summer changing to westerly flow during austral winter. This is indicative of the monsoon circulation over the tropical Indian

Ocean.

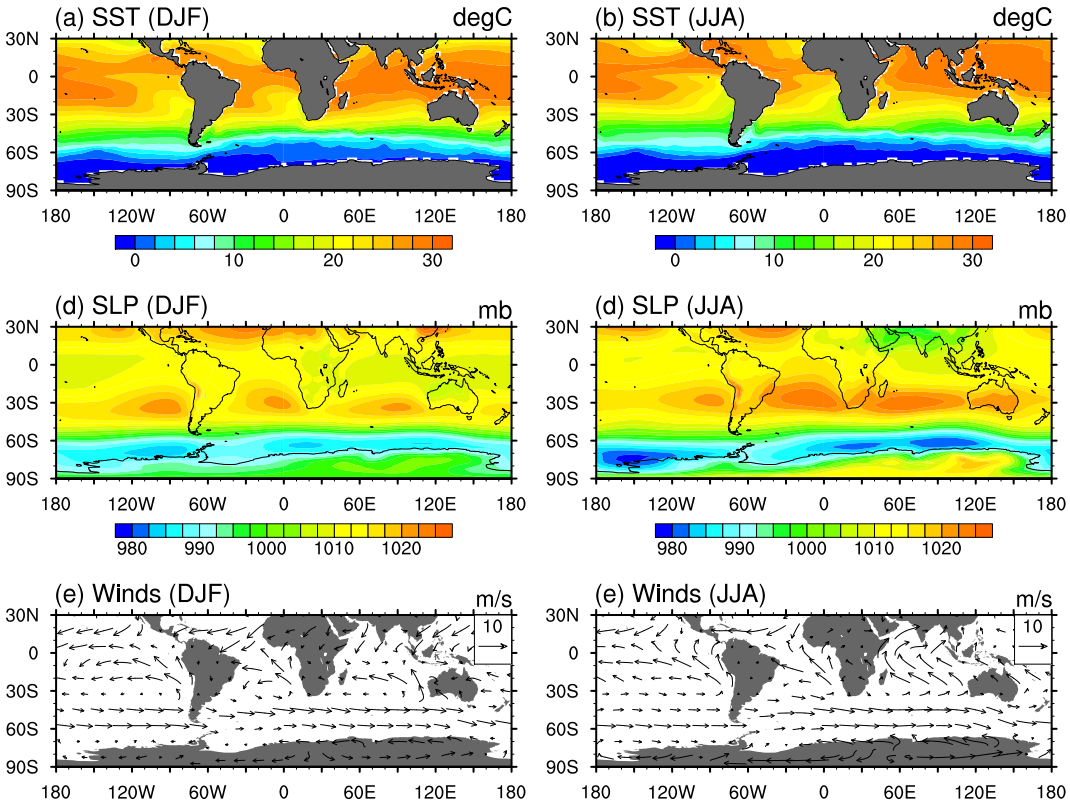

Figure 1.1. Mean fields of (a, b) SST (in °C), (c, d) SLP (in mb), and (e, f) surface winds (in m s^{-1}) south of 30°N for the DJF (left) and JJA (right) seasons, averaged over the period 1979–2001 (data is based on European Centre for Mid-Range Weather Forecasting 40-year Re-analysis; for a detailed description see Section 3.3 and Uppala *et al.*, 2005).

1.2.2. Modes of variability

Globally, the El Niño-Southern Oscillation (ENSO) represents the leading mode of climate variability with far-reaching environmental and socio-economic impacts all over the world (McPhaden *et al.*, 2006). Several studies review the present understanding of this strongly coupled ocean-atmosphere phenomenon (e.g., Wang and Picaut, 2004; McPhaden *et al.*, 2006, and references therein). During an ENSO event, positive ocean-atmosphere feedback, the so-called Bjerknes feedback after Bjerknes (1969), leads to increasingly warm SST anomalies in the eastern and central equatorial Pacific Ocean (Wang and Picaut, 2004). This is caused by a weakening of the equatorial trade winds due to increases (decreases) in pressure in the western (eastern) Pacific, a resultant deepening of the thermocline and reduced upwelling in the eastern Pacific, with the atmospheric and oceanic anomalies reinforcing each other. The propagation of these anomalies as equatorial waves together with the

Bjerknes feedback determines the intensity and duration of a particular El Niño event (McPhaden *et al.*, 2006). The exact nature of the mechanism leading to the onset of an El Niño event is still under debate: either a stable mode triggered by stochastic forcing or a naturally oscillating mode that is self-sustained (Wang and Picaut, 2004). Long persistence and increased predictability of the surface ocean properties during an El Niño event are due to the upwelling linking slow internal ocean dynamics – such as Rossby and Kelvin waves modulating the thermocline – with SST (Meyers *et al.*, 2007).

In the Indian Ocean, the complementary coupled ocean-atmosphere phenomenon to the Pacific's ENSO is the Indian Ocean Dipole (IOD), also called the Indian Ocean zonal mode. Webster *et al.* (1999) describe the IOD as a phenomenon primarily due to internal Indian Ocean dynamics, largely independent of external influences, with a characteristic signal in SST, sea surface height, surface winds, and precipitation across the Indian Ocean region. During positive IOD events, anomalously cold (warm) SST occur off Sumatra in the eastern Indian Ocean (in the equatorial western Indian Ocean), with coincident easterly wind anomalies across the tropics. This pattern of SST only accounts for about 12% of the interannual variability in the Indian Ocean (Saji *et al.*, 1999). This basin-scale pattern of anomalous surface and subsurface ocean temperature peaks during the September–October season (Meyers *et al.*, 2007). Li *et al.* (2003) suggest the phase-locking is due to a seasonally dependent thermodynamic air-sea feedback off Sumatra. In the equatorial Indian Ocean, the deep thermocline and strong negative cloud-SST feedback provide the conditions for a damped oscillator mechanism that determines this thermodynamically coupled atmosphere-ocean mode (Li *et al.*, 2003). Yamagata *et al.* (2004) further summarize the present understanding of the dynamics of the IOD.

The IOD's dependence/independence of ENSO is still very much a topic of research and debate (Meyers *et al.*, 2007). For the period 1876–1999, Meyers *et al.* (2007) classify each year as a positive/negative ENSO/IOD year. During the initial formation phase, the eastern pole of the IOD is especially sensitive to ENSO's influence on the background state of the equatorial Indian Ocean climate, such as the depth of the thermocline and the strength of the upwelling-favorable surface winds (Feng and Meyers, 2003; Wijffels and Meyers, 2004; Meyers *et al.*, 2007; Nagura and Konda, 2007). Meehl *et al.* (2003) examine coupled ocean-atmosphere processes between the tropical Pacific and Indian Oceans linked to the tropospheric biennial oscillation (TBO). Coupled ocean-atmosphere dynamics between the two basins and cross-equatorial heat transport lead to variations in Indian Ocean heat content, which are linked to variability in the large-scale Asian-Australian monsoon system (Loschnigg *et al.*, 2003; Meehl *et al.*, 2003). As the large-scale zonal Walker

circulation forms an integral part of the TBO, Meehl *et al.* (2003) propose that both ENSO and IOD events represent large-amplitude excursions of the TBO. With such a basin-wide reorganization in the ocean-atmosphere system, a suite of studies find the IOD to modulate precipitation around the Indian Ocean region (e.g., Birkett *et al.*, 1999; Clark *et al.*, 2003a; Latif *et al.*, 1999; Ashok *et al.*, 2001, 2003a; Black *et al.*, 2003; Meyers *et al.*, 2007). A goal of this study is to assess the impact of Indian Ocean variability on precipitation around the basin.

The SAM, also called the Antarctic Oscillation, is the leading mode of atmospheric variability in the Southern Hemisphere extratropics, characterized by variations in the strength of the circumpolar vortex (Thompson and Solomon, 2002). The SAM explains around 47% of the natural variability of zonal-mean geopotential height for 1000–50 hPa south of 20°S (Thompson and Wallace, 2000). The SAM represents a zonally symmetric feature with redistribution of mass between the polar latitudes south of 60°S and the mid-latitudes centered around 45°S, and results in modulations of opposite sign in the easterly and westerly wind field centered at 35°S and 60°S, respectively. Modulating the strength and position of the westerlies, the SAM has been implicated in influencing regional climate variability across the Southern Hemisphere mid-latitudes (e.g., Reason and Roualt, 2005; Cai and Cowan, 2006; Gillett *et al.*, 2006; Hendon *et al.*, 2007; Meneghini *et al.*, 2007).

1.2.3. Atmospheric circulation trends

Over the past few decades, trends in various climate variables have been recorded over much of the Southern Hemisphere. The oceans play an important role in modulating the atmospheric circulation, as shown for various coupled ocean-atmosphere modes in Section 1.2.2. Trends in surface ocean properties can thus have important implications for the large-scale atmospheric circulation. For the surface oceans, an overall warming of SST is observed throughout the year around Australia and in the subtropical gyre in the South Pacific Ocean (Fig. 1.2a, b). Levitus *et al.* (2000) describe a net warming of the upper 300 m across all the ocean basins over the last few decades. In contrast, SST in the latitude band 50°–60°S exhibit increasingly colder temperatures, especially during austral summer. Gille (2002) reports a slight cooling of the northern regions of the Southern Ocean, while mid-depth ocean temperatures further south have risen considerably since the 1950s, which Fyfe (2006) links to human influences. Interpretation of these trends, which are not uniform spatially or temporally, are hindered by the sparse data coverage, with few long-term high-quality records over the mid- to high-latitude oceans in the Southern Hemisphere. Alory *et al.* (2007) investigate recent observed Indian Ocean temperature trends and find warming in the subtropics down to 800 m for the latitude band

40–50°S, which they associate with a southward shift in the subtropical gyre and an upward-trending SAM. In the tropics, increased vertical stratification and shoaling of the thermocline leads to subsurface cooling, likely due to a weakening of the Pacific trade winds, with the signal transmitted through the Indonesian Throughflow (Alory *et al.*, 2007).

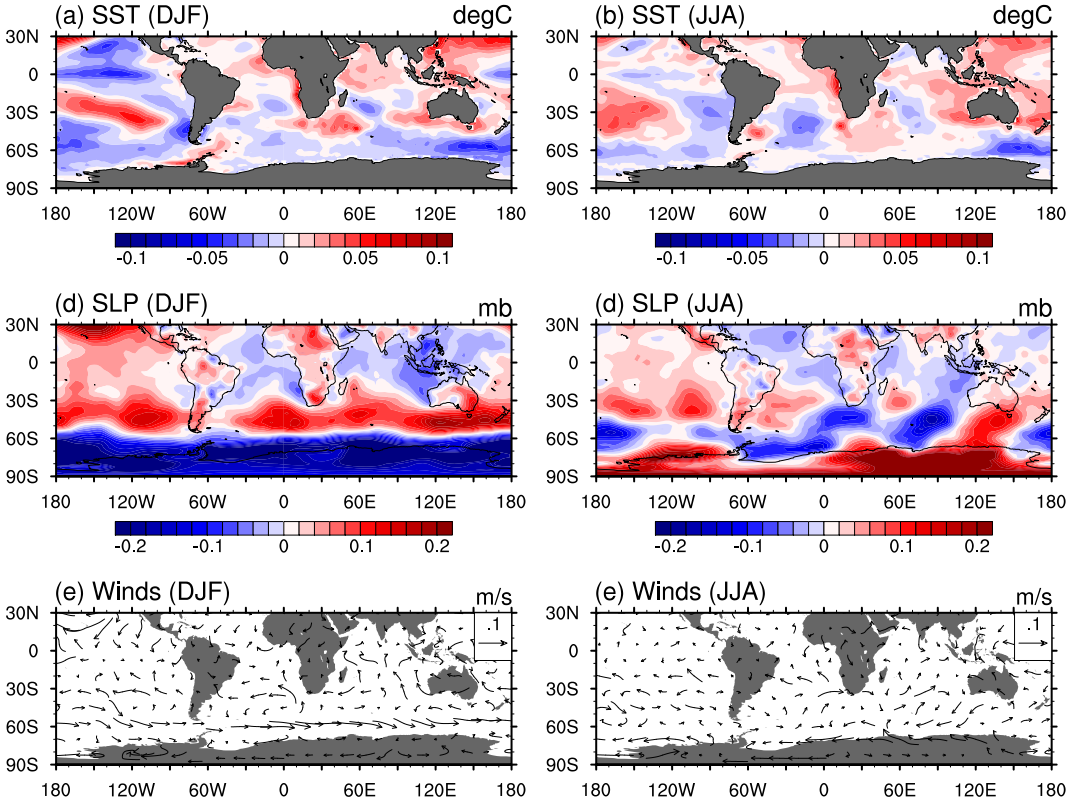

Figure 1.2. Linear trends in mean fields of (a, b) SST (in °C season^{-1}), (c, d) SLP (in mb season^{-1}), and (e, f) surface winds (in m s^{-1} season^{-1}) south of 30°N for the DJF (left) and JJA (right) seasons, averaged over the period 1979–2001 (data is based on European Centre for Mid-Range Weather Forecasting 40-year Re-analysis; for a detailed description see Section 3.3 and Uppala *et al.*, 2005).

A strengthening of the meridional gradient of both geopotential height and SLP during the austral summer (shown for SLP in Fig. 1.2c) has been widely documented (Hines *et al.*, 2000; Thompson *et al.*, 2000; Marshall, 2002, 2003; Renwick, 2004). The increase in mid-latitude SLP is centered at 45°S, while SLP has decreased south of 60°S. Trends in JJA SLP are smaller in magnitude and much less consistent in their spatial structure. In climate model simulations, Gillett *et al.* (2003, 2005) show DJF trends in the high latitude SLP to be consistent with anthropogenic forcing. Coincident with the DJF SLP trends, an intensification and southward shift of the zonal winds in the mid-latitude westerlies is observed (Fig. 1.2e, f). The negative trends in SST underlying the strengthened westerlies (Fig. 1.2a) can be understood

as an increased northward Ekman transport of cold water equatorward (Hall and Visbeck, 2002), along with a net increase in ocean-atmosphere heat loss (Sen Gupta and England, 2006).

These circumpolar changes can largely be understood as a shift towards the high-index phase of the SAM (Kushner *et al.*, 2001; Thompson and Solomon, 2002; Marshall, 2003; Marshall *et al.*, 2004) and have been related to anthropogenic greenhouse warming (Marshall *et al.*, 2004), stratospheric ozone depletion (Thompson and Solomon, 2002; Gillett and Thompson, 2003), and a combination of both (Arblaster and Meehl, 2006). Transient climate model simulations project these trends to continue over the 21st Century (e.g., Fyfe *et al.*, 1999; Kushner *et al.*, 2001; Yin, 2005; Arblaster and Meehl, 2006).

In the Southern Hemisphere tropics and subtropics, recent changes to the Hadley circulation have been recorded. Kobayashi and Maeda (2006) describe a strengthening of the southern cell in September and October. In contrast across a suite of simulations for the IPCC Assessment Report Four (AR4), Lu *et al.* (2007) find a consistent weakening and poleward expansion of the Hadley cell, and hence an expansion of the subtropical dry zone, projected for the 21st Century. With the upward branch of the Hadley cell formed by the Intertropical Convergence Zone (ITCZ), changes in the Hadley circulation are likely accompanied by shifts in the ITCZ.

The zonal tropical circulation, known as the Walker circulation, is closely linked to ENSO over the Pacific. An increased dominance of El Niño over recent decades seems to coincide with a weakening of the Walker circulation (Power and Smith, 2007). This becomes manifest in the weakest equatorial surface wind stress, the highest tropical Pacific SST and Darwin mean SLP observed on record. In general circulation model (GCM) simulations, Vecchi *et al.* (2006) show that weakened equatorial surface winds alter the thermal structure and circulation of the Pacific atmosphere and will result in a further weakening of the Walker circulation by about 10% over the 21st Century. This is consistent with theoretical predictions for a warming world and agrees with observations of SLP trends since the mid-19th Century (Vecchi and Soden, 2007).

1.2.4. Global precipitation trends

With these varied observed and projected changes in the general atmospheric circulation, impacts on the hydrological cycle and shifts in the precipitation distribution can be expected. Trends in precipitation for the period 1979–2006 form, very broadly speaking, latitudinal bands of consistent sign (Fig. 1.3). For these bands, the magnitude of the trend may change spatially and temporally across different

seasons. Broad consistent features across all ocean basins include a decrease (increase) in precipitation for the latitude band 40°–55°S (around 60°S). A drying trend over the Indian Ocean north of 30°S is seen, with the exception of the September–November season, which records increased precipitation over the western tropical Indian Ocean and adjacent equatorial East Africa (Fig. 1.3d). In a multimodel ensemble of global warming simulations, Neelin *et al.* (2006) describe decreases (increases) in tropical precipitation along (within) the margins of the convection zones. For the period 1925–1999, Zhang *et al.* (2007) assess the effect of anthropogenic forcing on observed land precipitation trends. They find that increased precipitation in the subtropics and tropics of the Southern Hemisphere can be largely attributed to human influence. Similarly, Meehl *et al.* (2005) suggest that positive SST anomalies in a warming world produce enhanced precipitation intensity across the tropical land masses due to increased levels of water vapor. In contrast in the mid-latitudes, a rise in precipitation intensity is associated with changes in the atmospheric circulation and with more water vapor being transported to areas of moisture convergence (Meehl *et al.*, 2005). For the 21st Century, the IPCC AR4 models show a robust response with increased horizontal moisture transport, a spatially and temporally more pronounced evaporation minus precipitation pattern, and reduced extratropical sensible heat transport (Held and Soden, 2006). Chou *et al.* (2007) use a similar approach and find that global warming enhances the seasonal precipitation range, with wet (dry) seasons becoming wetter (drier).

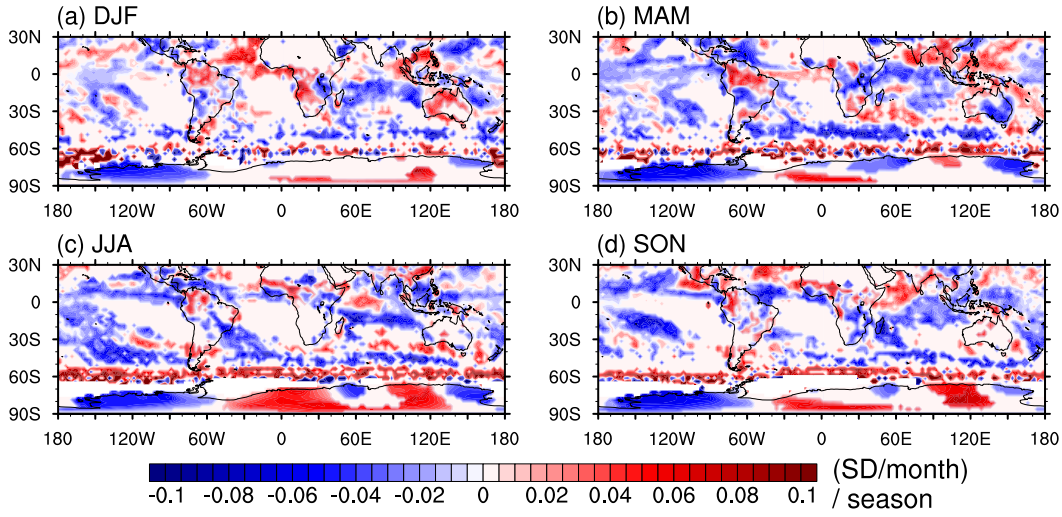

Figure 1.3. Seasonal precipitation trends (significant at the 90% confidence level) south of 30°N for the seasons (a) DJF, (b) MAM, (c) JJA, and (d) SON, averaged over the period 1979–2006 (values are shown as standard deviations month^{-1} season^{-1}; data is based on Climate Prediction Center Merged Analysis of Precipitation; for a detaild description see Section 2.3 and Xie and Arkin, 1996).

As the hydrological cycle intensifies in a warming world, Oki and Kanae (2006) propose that climate change may increase the rate of renewal of available renewable freshwater resources and thus potentially alleviate water stress. However, they find that increased likelihood of extreme events, i.e. more intense and intermittent precipitation leading to floods and droughts, shifts in the spatial and temporal distribution, and degradation of water resources are likely to counteract benefits from an enhanced hydrological cycle. From satellite observations and climate models, an increase in the total amount of water due to global warming can be expected in the atmosphere of about 7% K^{-1} (Wentz *et al.*, 2007). Wentz *et al.* (2007) show that in satellite observations this translates to a comparable rise in precipitation, while climate models indicate a slower rate of 1–3% K^{-1}. This finding of a significant under-estimation of the well-established notion of intensification of the hydrological cycle under global warming could have important implications for projections of future precipitation changes.

1.3. Australian precipitation variability and trends

As a large component of this PhD thesis focuses on Australian precipitation, a general introduction to the continent's variability and trends in regard to precipitation is given here. For the other two regions explored in more detail, namely East Africa and New Zealand, the background on precipitation variability and trends is given in Section 4.3 for East Africa and in Sections 5.2 and 6.2 for New Zealand, respectively.

Australia is characterized by arid to semi-arid climate, being the driest of all the continents (except Antarctica), and with highly variable rainfall, both temporally and spatially. Precipitation is generally limited to the coastal regions, with dryness increasing inland with distance from the coast. Spanning more than 30° of latitude between the tropical north of the country, via the subtropics to the temperate regions of Tasmania, the country experiences a wide range of precipitation regimes. Drosdowsky (1993a) provides a detailed analysis of seasonal rainfall patterns across Australia. The tropical north of the country is dominated by summer rainfall associated with the monsoon circulation (Fig. 1.4a; Gentilli, 1972; Sturman and Tapper, 1996). The northeast and east of the country also receive most of their annual precipitation during this season. The southeast of Australia (SEA) is characterized by wet winters generally (Fig. 1.4c; Gentilli, 1972). Uniform precipitation throughout the year is experienced on the east coast of Australia and in the eastern half of Tasmania, while the west of Tasmania sees predominantly wet winters (Fig. 1.4). Southwest Western Australia (SWWA) is dominated by a Mediterranean climate

with mostly winter rainfall (Fig. 1.4c; Wright, 1974). Generally, little rain occurs over the interior of the continent.

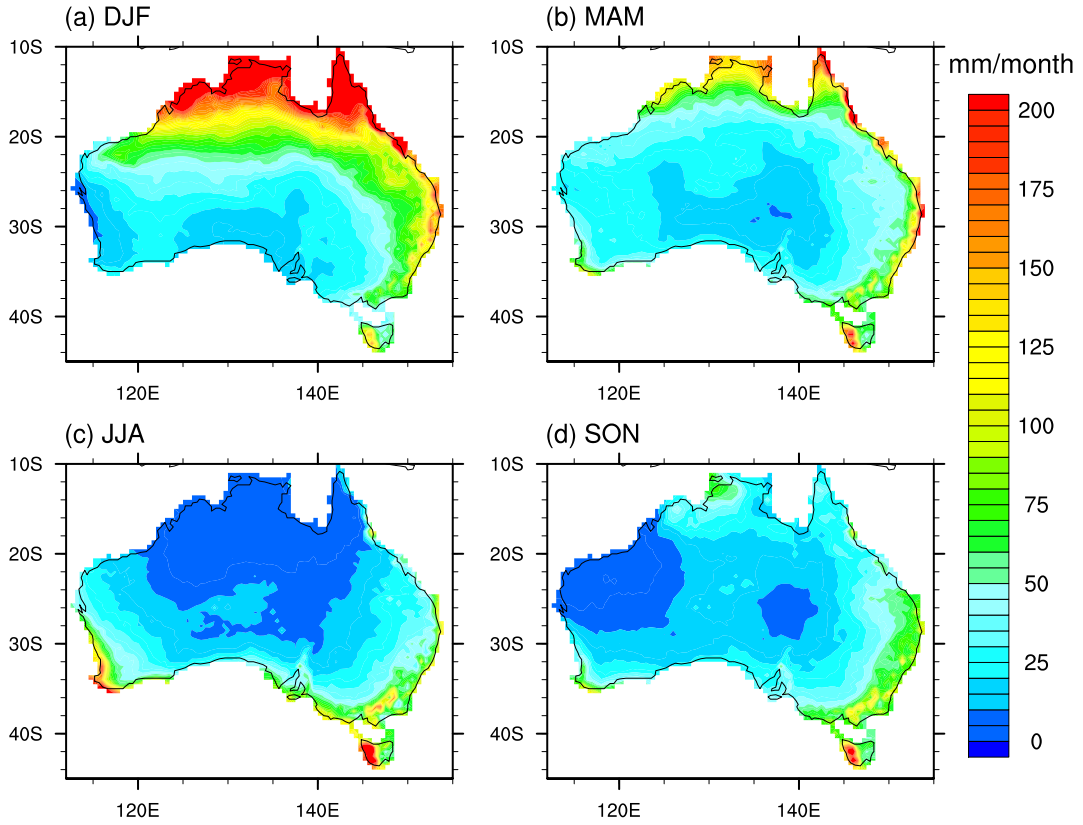

Figure 1.4. Monthly mean precipitation for Australia averaged for the seasons (a) DJF, (b) MAM, (c) JJA, and (d) SON over the period 1960–2004 (values are shown in mm month^{-1}). The data is based on the gridded SILO data produced by the Australian Bureau of Meteorology (Jeffrey *et al.*, 2001).

Variability in Australian precipitation differs widely between regions and seasons (Fig. 1.5). During austral summer (and less so for autumn), rainfall variability is low for the tropical monsoon-dominated north of the country and the east coast, while the interior's rainfall is more variable (Fig. 1.5a, b). The regions dominated by winter rainfall, namely SWWA and SEA, show lower variability during winter and spring (Fig. 1.5c, d). In contrast, the north experiences variations in excess of 200% during winter, as does northwest Western Australia (NWWA) during spring. The arid interior of the continent also records the highest variability with 70–200% throughout the year.

The high seasonal to interannual variability in Australian precipitation is due to a variety of factors impacting on the country's rainfall. These include influences by the surrounding oceans, namely from the Indian Ocean (e.g., Nicholls, 1989; Frederiksen and Balgovind, 1994; Smith *et al.*, 2000; Ashok *et al.*, 2003a; England

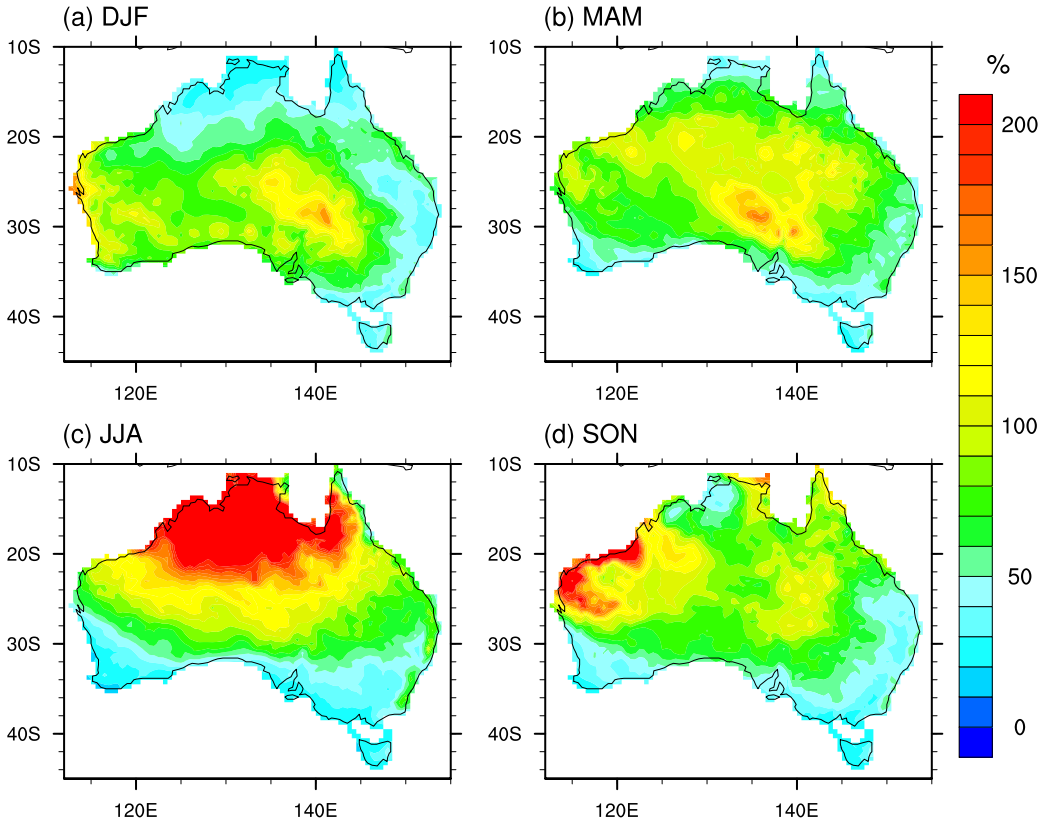

Figure 1.5. Coefficient of variation of precipitation for Australia averaged for the seasons (a) DJF, (b) MAM, (c) JJA, and (d) SON over the period 1960–2004 (values are shown as %).

et al., 2006; Meyers *et al.*, 2007), the Pacific Ocean via ENSO (e.g., Chiew *et al.*, 1998; Murphy and Ribbe, 2004), variations in the atmospheric circulation related to the monsoon (e.g., McBride, 1987; Suppiah, 1992), strength and position of the subtropical ridge, extratropical influences in the south (e.g., Cai and Cowan, 2006; Hendon *et al.*, 2007; Meneghini *et al.*, 2007), amongst others. The influence of ENSO on Australian precipitation has been widely investigated (e.g., Chiew *et al.*, 1998; Power *et al.*, 1998, 1999; Cai *et al.*, 2001; Suppiah, 2004; Meyers *et al.*, 2007; Power and Smith, 2007). Highest negative correlations between Australian rainfall and ENSO are observed over the north and east of the country. However, the impact of ENSO on Australian precipitation varies on decadal timescales (Nicholls *et al.*, 1996; Power *et al.*, 1999; Cai *et al.*, 2001; Arblaster *et al.*, 2002; Suppiah, 2004). In addition, Frederiksen *et al.* (1999) find decadal variations in Australian rainfall linked to northwest cloud bands modulated by periods of a strengthened/weakened subtropical jetstream in observations and GCM simulations. Arblaster *et al.* (2002) show that variations in ENSO, shifts in the position of the Pacific Walker circulation, and western Pacific SST all contribute to decadal variability in Australian rainfall.

Considering the various recent changes in the Southern Hemisphere atmospheric circulation described above, it is not surprising that Australian climate has been affected as well. Nicholls (2006, 2007) provides a thorough review of the present understanding of recent climate change over Australia, and its detection and attribution. Precipitation over Australia has sustained considerable trends over the past few decades, varying widely between seasons (Fig. 1.6). During austral summer and autumn, increases of up to 2 mm month^{-1} season^{-1} have been recorded in the northern and central regions of Australia (Fig. 1.6a, b). Rotstayn *et al.* (2007) associate observed increases in cloudiness and precipitation across northwestern regions of the country since the 1950s with Asian aerosols. They demonstrate that changes in the meridional temperature and pressure gradient across the Indian Ocean region result in increased monsoonal flow over northern Australia.

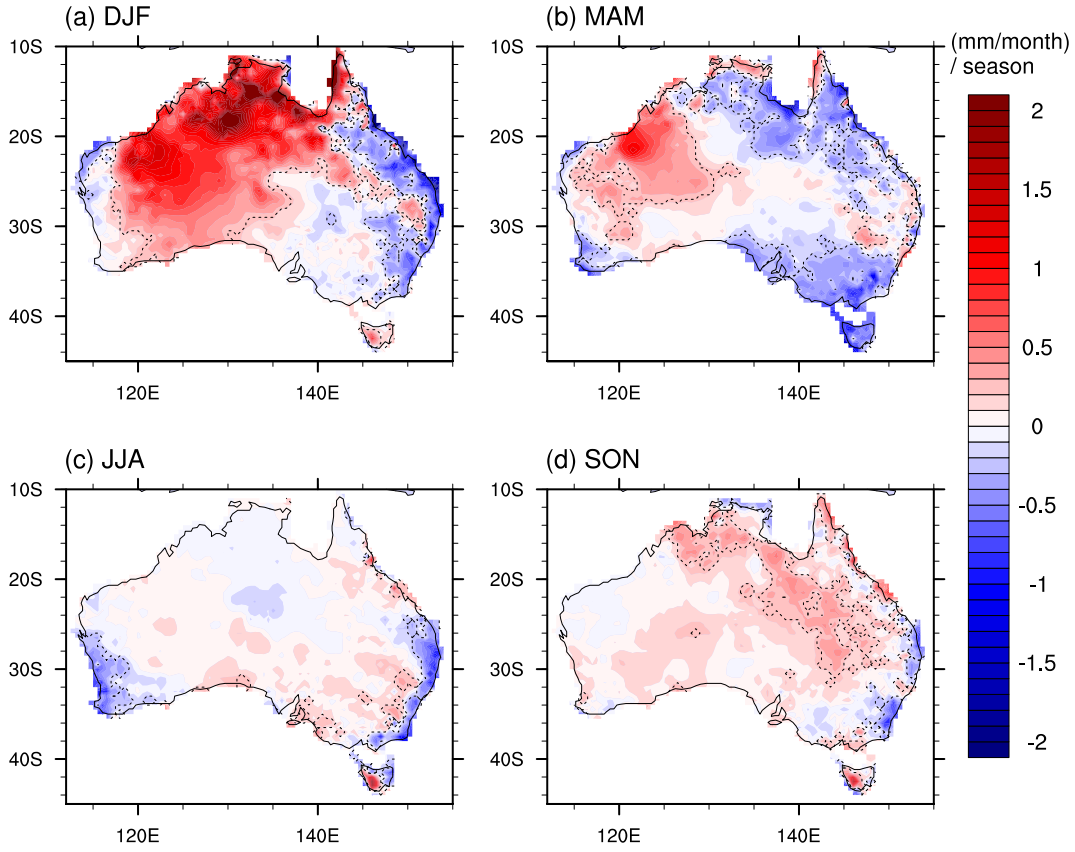

Figure 1.6. Monthly precipitation trends (significant at the 90% confidence level) for Australia for the seasons (a) DJF, (b) MAM, (c) JJA, and (d) SON, averaged over the period 1960–2004 (values are shown in mm month^{-1} season^{-1}).

In contrast, increasingly drier conditions dominate over the northeast of the country, especially pronounced during austral summer and autumn (Fig. 1.6a, b). Chase *et al.* (2003) describe reductions in the global monsoon circulations since the 1950s

that could potentially explain the reductions. The east coast of Australia has also experienced widespread drying for much of the year (Fig. 1.6), with the reasons for this still being debated (Sohn, 2007). More recently, this drying trend is especially pronounced over the Murray-Darling Basin, with decreases in rainfall translating into an even greater reduction in inflows into the river system of only 40% of the long-term mean for 2001–2005 (Murphy and Timbal, 2008). For SEA, negative precipitation trends of more than 1.5 mm month^{-1} season^{-1} for the period 1960–2004 are especially prominent during autumn (Fig. 1.6b). Murphy and Timbal (2008) suggest that large-scale changes in the SAM and regional trends in the position of the subtropical ridge play a role in the reduced number and impact of rain-bearing systems during autumn for SEA. For the period 1951–2003, McAlpine *et al.* (2007) find a significant decrease in summer precipitation linked to historical land cover changes. When focusing on the post-1979 period, Hendon *et al.* (2007) observe increases in DJF rainfall over SEA that they suggest can be accounted for by positive trends in the SAM towards its high-index phase. Decreases in autumn precipitation also occur for much of Tasmania, while the island's west coast has experienced increasingly wetter conditions during other seasons (Fig. 1.6).

Decreasing trends in SWWA rainfall are most pronounced during austral winter (and less so for autumn; Fig. 1.6b, c). A widely investigated step-change in SWWA winter precipitation in the 1970s has been linked to changes in large-scale mean sea level pressure (Allan and Haylock, 1993; IOCI, 2001), shifts in synoptic systems (Hope *et al.*, 2006), the SAM (Li *et al.*, 2005b; Cai and Cowan, 2006; Hendon *et al.*, 2007; Li, 2007), land cover changes (Pitman *et al.*, 2004; Timbal and Arblaster, 2006), anthropogenic forcing (Cai and Cowan, 2006; Timbal *et al.*, 2006), and natural multidecadal variability (Cai *et al.*, 2005b) with a combination of several factors likely playing a role.

The various long-term trends in precipitation towards overall drier conditions have significant implications for Australian society and ecosystems (Sohn, 2007). Climate model simulations under enhanced greenhouse forcing project further reductions in rainfall over much of the country (e.g., Timbal, 2004; Hope, 2006; Meehl *et al.*, 2007). For an arid to semi-arid country such as Australia, this will put further stress on already strained water resources. This thesis aims to develop a better understanding of the processes modulating precipitation variability and trends across the region.

Chapter 2

Interannual Rainfall Extremes over Southwest Western Australia Linked to Indian Ocean Climate Variability

Matthew H. England, Caroline C. Ummenhofer, and Agus Santoso

Centre for Environmental Modelling and Prediction, School of Mathematics, University of New South Wales, Sydney, Australia

Manuscript for: Journal of Climate
Status: published in 2006, Vol. 19, pp. 1948–1969

2.1. Abstract

Interannual rainfall extremes over southwest Western Australia (SWWA) are examined using observations, reanalysis data, and a long-term integration of a coupled climate system model without forcings from changes in atmospheric composition. We reveal a characteristic dipole pattern of Indian Ocean sea surface temperature (SST) anomalies during extreme rainfall years, remarkably consistent between the reanalysis fields and the coupled climate model but different from most previous definitions of SST dipoles in the region. In particular, the dipole exhibits peak amplitudes in the eastern Indian Ocean adjacent to the west coast of Australia. During dry years, anomalously cool waters appear in the tropical/subtropical eastern Indian Ocean, adjacent to a region of unusually warm water in the subtropics off SWWA. This dipole of anomalous SST seesaws in sign between dry and wet years, and appears to occur in phase with a large-scale reorganization of winds over the tropical/subtropical Indian Ocean. The wind field alters SST via anomalous Ekman transport in the tropical Indian Ocean and via anomalous air-sea heat fluxes in the subtropics. The winds also change the large-scale advection of moisture onto the SWWA coast. At the basin scale, the anomalous wind field can be interpreted as an acceleration (deceleration) of the Indian Ocean climatological mean anticyclone during dry (wet) years. In addition, dry (wet) years see a strengthening (weakening) and coinciding southward (northward) shift of the subpolar westerlies, which results in a similar southward (northward) shift of the rain-bearing fronts associated with the subpolar front. A link is also noted between extreme rainfall years and the Indian Ocean Dipole (IOD). Namely, in some years the IOD acts to reinforce the eastern tropical pole of SST described above, and to strengthen wind anomalies along the northern flank of the Indian Ocean anticyclone. In this manner, both tropical and extratropical processes in the Indian Ocean generate SST and wind anomalies off SWWA, which lead to moisture transport and rainfall extremes in the region. An analysis of the seasonal evolution of the climate extremes reveals a progressive amplification of anomalies in SST and atmospheric circulation toward a wintertime maximum, coinciding with the season of highest SWWA rainfall. The anomalies in SST can appear as early as the summertime months, however, which may have important implications for predictability of SWWA rainfall extremes.

2.2. Introduction

The Australian continent experiences high interannual climate variability, particularly in precipitation rates (Power *et al.*, 1998; Drosdowsky, 1993a). Rainfall over southwest Western Australia (hereafter termed SWWA) shows unique characteristics in temporal variability (Smith *et al.*, 2000) and evidence of an overall decline during winter over the past century (Allan and Haylock, 1993; Ansell *et al.*, 2000b). On shorter timescales, interannual variability of SWWA rainfall remains poorly understood, as traditional predictors for Australian climate, such as the Southern Oscillation Index, appear to resolve little of the region's variability (Smith *et al.*, 2000). Several studies have revealed a connection between Indian Ocean sea surface temperature (SST) and Australian rainfall (e.g., Nicholls, 1989; Frederiksen and Balgovind, 1994; Reason *et al.*, 1998; Li and Mu, 2001; Qian *et al.*, 2002). However, these previous studies relate to the large-scale mean Australian or Western Australian rainfall. The focus of our study is on the more localized region of SWWA and more specifically the interannual rainfall variability over the southwestern tip of Western Australia (region shown in Fig. 2.1a). Of particular interest is how the SWWA interannual rainfall variability might be controlled by the adjacent Indian Ocean.

After initial work by Wright (1974) on links between seasonal SWWA rainfall and the general atmospheric circulation, relatively few studies have focused on the natural year-to-year variability of rainfall over the region. Ansell *et al.* (2000b) used empirical orthogonal functions of monthly data to show that SWWA winter rainfall is significantly correlated with winter SST over the subtropical Indian Ocean over the period 1907–1994. However, they found that the links between rainfall and SST are less significant than those for mean sea level pressure (MSLP) and rainfall. Similarly, Smith *et al.* (2000) investigated observations and reanalyses for the period 1950–1994 and found a relationship between SWWA rainfall and SST in the tropical southeast and mid-latitude Indian Ocean. Again, these were found to be less robust than those seen using MSLP. Allan and Haylock (1993) use gridded station data for the period 1911–1989 to show that SWWA winter rainfall anomalies may be associated with fluctuations in mid-latitude frontal systems, resulting from modulation in the semi-permanent long-wave (anticyclone) trough south of Australia. This modulation is caused by interactions between Indian Ocean SST anomalies and the overlying atmosphere. Allan and Haylock (1993) and Smith *et al.* (2000), among other studies, also focus on a long-term winter rainfall decline over SWWA over the past 40 years. The cause of this multidecadal shift in SWWA rainfall remains a topic of debate. For example, the Indian Ocean Climate Initiative (IOCI, 2002) at-

tribute the decrease in winter rainfall in the mid-1970s to an increase in air pressure at 30°–50°S, which forces large-scale atmospheric circulation changes in the region. The IOCI (2002) suggest that these changes may have been forced by increasing atmospheric greenhouse gases. Further evidence of a greenhouse fingerprint in SWWA rainfall decline has recently been provided in the climate change simulations of Cai *et al.* (2003a), who show that increasing CO_2 can force a century-scale decline in winter rainfall. In contrast, Pitman *et al.* (2004) suggest that the rainfall decline and coinciding temperature increase is mostly due to large-scale changes in SWWA land cover over the past fifty years. They use a model to demonstrate that cleared vegetation patterns result in an increased moisture divergence over SWWA and a corresponding enhanced moisture convergence inland. In the present study, however, we focus on the shorter timescale interannual variability, and extend previous studies by evaluating over 30 years of observations and reanalysis data, as well as interannual SWWA rainfall variability in a multi-century coupled climate model.

The tropical Indian Ocean is characterized by a seasonal reversal of the zonal monsoon winds and a resulting seasonal tilt of the thermocline. A positive air-sea thermal feedback between an anomalous atmospheric anticyclone and a cold SST anomaly can result in Indian Ocean dipole (IOD) events in certain years (Saji *et al.*, 1999; Li *et al.*, 2003; Yamagata *et al.*, 2003; Saji *et al.*, 2005). These appear as a pattern of internal Indian Ocean variability with negative SST anomalies off Indonesia and anomalously high SST in the western Indian Ocean, accompanied by changes in zonal wind strength over the equator (Saji *et al.*, 1999). A positive air-sea feedback is set up, reinforcing the anomalous state, until the seasonal reversal of the wind field across the equatorial Indian Ocean counteracts it, leading to a rapid decline of the IOD event. The close relationship between zonal winds and SST indicates strong air-sea coupling over the tropical Indian Ocean (e.g. Rao *et al.*, 2002; Ashok *et al.*, 2003b; Li *et al.*, 2003; Iizuka *et al.*, 2000). Recently, IOD events have been associated with low Australian rainfall due to anomalous anticyclonic circulation over the eastern Indian Ocean and Australia, resulting in anomalous subsidence over the Australian continent (Ashok *et al.*, 2003a; Saji and Yamagata, 2003a). Of the rainfall extremes normally associated with Indian Ocean SST variability, especially in the form of the IOD, most studies concentrate on its effect on Indian (Ashok *et al.*, 2001; Li *et al.*, 2003; Ashok *et al.*, 2004b), Indonesian (Saji *et al.*, 1999) and African (Reason, 1999; Saji *et al.*, 1999; Black, 2003) precipitation. One exception is the study by Ashok *et al.* (2003a), who focus on a link between the IOD and Australian winter rainfall using 20 years of observations and results from an atmospheric general circulation model (GCM). Here, we extend this by analyzing interannual rainfall variability over SWWA, and expand the analyses to a longer

observational record and a multi-century coupled climate model.

In contrast to the above studies whose focus is on the Indian Ocean, White (2000) found evidence that Australian precipitation covaries with Southern Ocean SST. He suggested that the tropospheric moisture flux convergence (divergence) varies such that anomalously moist (dry) marine air is advected onto Australia in phase with warm (cool) SST anomalies to the south, which are linked to the eastward propagation of the Antarctic Circumpolar Wave (ACW). The White (2000) study is, however, based on overall Australian and Western Australian rainfall, so it is of interest to reassess these proposed linkages in the context of the limited domain of SWWA.

The rest of this paper is organized as follows. The observational data and methodologies used in our study are described in Section 2.3. In Section 2.4 we examine observations and reanalysis data with a view to identifying anomalies in climate parameters associated with extreme rainfall events in SWWA. In Section 2.5 we reassess the connection between Indian Ocean climate and SWWA rainfall in a 1000-year integration of a coupled climate model. In Section 2.6 we briefly consider the seasonal evolution of the SWWA climate anomalies in both the model and observations. Finally, in Section 2.7, we discuss and summarize our findings.

2.3. Observational data and data analysis

This study concentrates on southwest Western Australia in a region bound by 30°–35°S, 115°–120°E. To justify the localized region of analysis, Fig. 2.1a shows the net annual rainfall rate over the Australian mainland and Tasmania. Apparent in the west is a localized region of high rainfall – up to 900 mm yr^{-1} – falling within our study domain. This high rainfall region is not only unusual in the context of extratropical Western Australia; it is also relatively unique over the Southern Hemisphere. For example, at comparable latitudes both southwestern Africa and the subtropical western region of South America are characterized by somewhat lower regional rainfall rates ($\sim$300 mm yr^{-1}), in spite of much more pronounced orographic features than SWWA. A likely reason for the unusually high net rainfall over SWWA is the anomalously warm SST over much of the tropical and subtropical eastern Indian Ocean (Gentilli, 1991). The warm waters in the eastern Indian Ocean are due in part to the Indonesian throughflow from the western Pacific, as well as the resultant poleward flowing Leeuwin Current, the world's only subtropical poleward flowing eastern boundary current.

Observed annual rainfall for SWWA within our region of interest is shown in Fig. 2.1b during the period 1970–2003, with a power spectral density (PSD) analysis

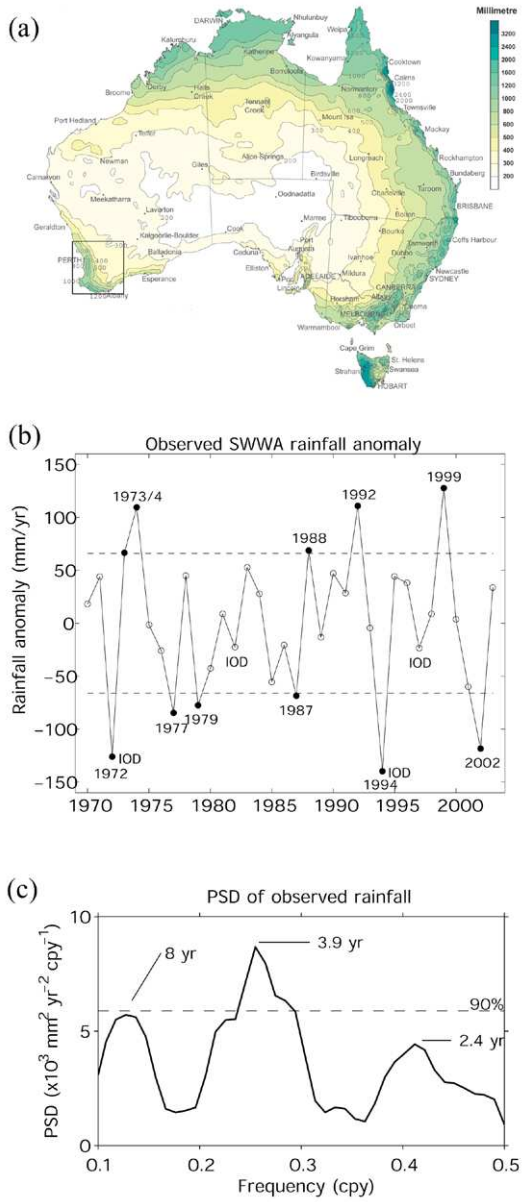

Figure 2.1. (a) Annual precipitation (mm yr^{-1}) over Australia from the Australian Bureau of Meteorology (BoM) gridded rainfall climatology, with the study area in southwest Western Australia indicated (115°–120°E, 30°–35°S). (b) Detrended time-series (solid line) of the observed annual rainfall anomaly (mm yr^{-1}) for SWWA for 1970–2003; dashed lines indicate ± one standard deviation (66 mm yr^{-1}) and years with rainfall exceeding this are marked as extremes (filled circles). Years identified by Saji *et al.* (1999) as Indian Ocean Dipole (IOD) years for the period 1970-1999 are also indicated (1972, 1982, 1994, and 1997). (c) Power spectral density (PSD) of observed SWWA precipitation using the Thomson multi-taper method (Mann and Lees, 1996). The dashed horizontal line represents the estimated white noise spectrum at 90% confidence level.

of this time-series shown in Fig. 2.1c. Observations are taken from the gridded Australian Bureau of Meteorology (BoM) rainfall data sets, averaged over 30°–35°S and 115°–120°E. The time-series in Fig. 1b is detrended and the long-term mean of 520 mm yr^{-1} is removed. The trend in rainfall removed during 1970–2003 is in fact virtually negligible, at only -0.0264 mm yr^{-1} per annum. This equates to less than 1 mm yr^{-1} net decline in annual rainfall over the study region during the 34-year record, indicating that our analysis period largely post-dates the documented 20th Century decline in SWWA rainfall (e.g., see analyses in IOCI, 2002). The PSD analysis shows peak variability at periods of ∼2.4, 3.9 and 8 years (Fig. 2.1c). The standard deviation of the detrended rainfall time-series is 66 mm yr^{-1}; this value is used to define anomalously wet and dry years, as indicated in Fig. 2.1b. In particular, wet (dry) years correspond to those years with rainfall one standard deviation above (below) the long-term mean. In absolute terms, this means wet years receive > 586 mm yr^{-1} and dry years < 454 mm yr^{-1} rainfall, respectively. It is important to note that while highest rainfall over SWWA occurs during austral winter, the extreme years defined above do not correspond exclusively to dry and wet winters. For example, some of the dry years do not correspond to winters of particularly low rainfall, and in some cases high summer rainfall rates push the year average into a wet-year anomaly. With the focus of this paper on year-to-year and not seasonal variations, and with annual rainfall extremes not defined exclusively by wintertime rainfall rates, it is appropriate to form composite statistics based on net annual mean conditions. In Section 2.6 we briefly examine the nature and evolution of sub-annual rainfall anomalies over SWWA.

As direct observations are sparse over the extratropical oceans, including the South Indian and Southern Oceans, we employ reanalysis data to investigate large-scale atmospheric properties during dry/wet years over SWWA. Only the period since 1970 is considered, as prior to this time open-ocean data coverage is extremely sparse. The reanalysis data used is that of the National Center for Environmental Prediction (NCEP) and National Center for Atmospheric Research (NCAR) reanalysis project (Kalnay *et al.*, 1996). It is presently the most extensive reanalysis record available. The NCEP/NCAR reanalyses use a global spectral model with a horizontal resolution of T62 (∼2° latitude by ∼2° longitude) and 28 unequally spaced vertical sigma-levels in the atmosphere (Kalnay *et al.*, 1996). The model includes parameterizations of all major physical processes. A variety of in situ and satellite measurements are assimilated and subjected to quality control before incorporation into the model. For this study, the following NCEP/NCAR reanalysis variables will be discussed: air temperature, sea level pressure (SLP), wind vectors, moisture advection, and outgoing longwave-radiation. For oceanic properties we use the Na-

tional Oceanic and Atmospheric Administration (NOAA) extended reconstructed sea surface temperature (SST) data set with a resolution of ∼2° latitude by ∼2° longitude. The NOAA climatology employs the most recently available Comprehensive Ocean-Atmosphere Data Set (COADS) SST data and improved statistical methods allowing for stable reconstruction using sparse data.

To investigate teleconnections to rainfall variability over larger scales we use the Climate Prediction Center (CPC) Merged Analysis of Precipitation (CMAP; Xie and Arkin, 1996) climatology. The CMAP data set is used instead of the NCEP/NCAR reanalysis rainfall, as potential deficiencies on regional scales were revealed in the latter by Janowiak *et al.* (1998) for parts of the Indian Ocean and over Indonesia[1]. The CMAP data set consists of monthly averaged precipitation on a ∼2.5° latitude by ∼2.5° longitude grid for the period 1979–2003. It combines several data sets of varying origin and characteristics, including gauge-based analyses from the Global Precipitation Climatology Centre, predictions by the operational forecast model of the European Centre for Medium-Range Weather Forecasts, and three types of satellite estimates. As a further assessment of our findings obtained using the various climatological data sets, we will also examine SWWA rainfall variability within a multi-century integration of a coupled climate model (described in Section 2.5).

To form composites of anomalous fields for a variety of parameters during dry and wet years, anomalies were calculated as the deviation of the composite annual mean from the long-term annual mean. By analyzing composite properties, prominent features of selected years are enhanced, while noise present in individual events is mostly removed. Dry SWWA years comprise 1972, 1977, 1979, 1987, 1994, and 2002, while wet SWWA years are 1973, 1974, 1988, 1992, and 1999 (for further details see Fig. 2.1b). For reference, years identified by Saji *et al.* (1999) as IOD years for the period 1970–1999 are the following: 1972, 1982, 1994, and 1997, as is also indicated in Fig. 2.1b.

2.4. Observed climate during extreme years

2.4.1. Rainfall

Composite analyses of annual surface precipitation rate show distinctly different patterns for dry (Fig. 2.2a) and wet (Fig. 2.2b) years in SWWA. The composite maps in Fig. 2.2 use rainfall rates from the CMAP climatology binned into dry

[1]It is noted that the composite rainfall maps in Fig. 2.2 are nonetheless relatively insensitive to the choice of rainfall climatology; including the CMAP, NCEP/NCAR and Global Precipitation Climatology Project (GPCP) data sets.

and wet years. It should be noted that Fig. 2.2 shows the raw composite rainfall anomalies, which tend to be large where the mean annual precipitation is highest (e.g., over southeast Asia). Whilst rainfall anomalies over SWWA do not appear large, mean precipitation there is relatively low compared to the tropics, so the normalized anomalies at SWWA are significant. Anomalously low (high) rainfall persists over much of southeast Asia and the tropical eastern Indian Ocean during dry (wet) SWWA years (Fig. 2.2). Dry (wet) years in SWWA appear to also coincide with dry (wet) years along Australia's eastern seaboard and wet (dry) years in the tropical western Pacific and western Indian Oceans. Hence, dry and wet conditions in SWWA appear to be part of a large-scale phenomenon affecting the Indian Ocean basin and adjacent regions, in particular southeast Asia, parts of eastern Africa, and eastern Australia.

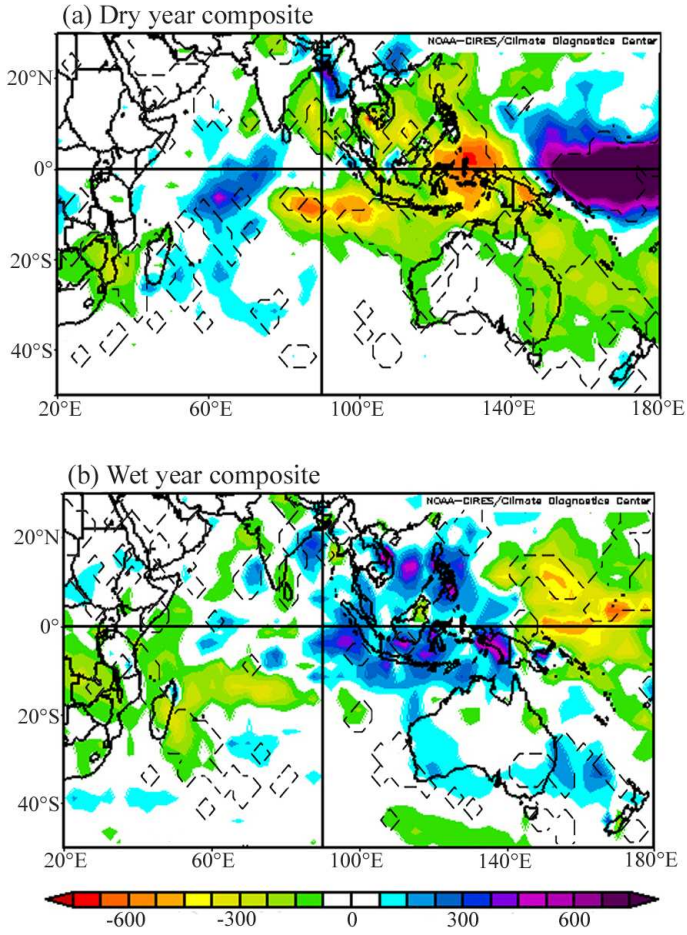

Figure 2.2. Composite of anomalous CMAP surface precipitation rate (mm yr^{-1}) for (a) dry and (b) wet years in SWWA, as compared to the long-term climatological mean. Note that only extreme years from 1979–2003 are used to form the composites, as the CMAP rainfall climatology is only available from 1979. The dashed contours indicate where anomalies exceed the 90% significance level as estimated by a two-tailed t-test.

2.4.2. Sea level pressure

Composite anomalies of SLP fields show that during dry years SLP over the Australian continent is unusually high (up to 1 mb above the long-term mean) with its center over southern Australia (Fig. 2.3a). A band of anomalously low pressure sits further south so that geostrophic wind anomalies drive an intensified westerly wind field at 40°S. The pattern for wet years in SWWA (Fig. 2.3b) is more or less reversed. However, in wet years, the anomalous low SLP across Australia and the eastern Indian Ocean stretches southward to the subpolar region near 60°E. A band of higher than normal SLP appears to the south of Australia, corresponding to weaker geostrophic westerly winds at 100°–140°E. With the wet and dry year composites exhibiting significant SLP anomalies over southern Australia and the Southern Ocean, the SWWA rainfall extremes could be related to the ACW or the Southern Annular Mode (SAM). However, analyses of time lagged SLP maps (figures not shown) reveal little signal of an ACW leading up to wet/dry years, and the SLP anomaly patterns are not circumpolar, so neither of these scenarios appears likely.

2.4.3. Surface winds

The pressure anomalies, in turn, result in changed surface wind fields across wide parts of the Southern Hemisphere, as the winds closely track the pressure fields as expected under geostrophy (composite wind anomalies are shown in Fig. 2.4). This is especially apparent in the subpolar westerlies to the south of the Australian continent, which are strengthened (weakened) by the increased (decreased) meridional SLP gradient during dry (wet) years. A strengthening and coinciding southward shift of the subpolar westerlies to the south of Australia during dry years results in a similar southward shift of the rain-bearing fronts associated with the subpolar front. This situation is reversed during wet years, confirmed by composite plots of moisture advection in the region (figure not shown). Nearer the region of SWWA, Fig. 2.4 shows that the local surface winds are anomalously offshore during dry years, and onshore during wet years. These localized wind changes have the effect of advecting less (more) moist air onto the West Australian coast during dry (wet) years (moisture advection figure not shown).

The composites of surface vector wind anomalies for dry and wet SWWA years also differ distinctly over the Indian Ocean basin. For example, during dry (wet) years there is a strengthening (weakening) of the easterly winds on the northern flank (0°–10°S, 70°–110°E) of the gyre-scale anticlockwise wind system (Fig. 2.4). This agrees with the high (low) SLP anomaly extending from Australia northwards

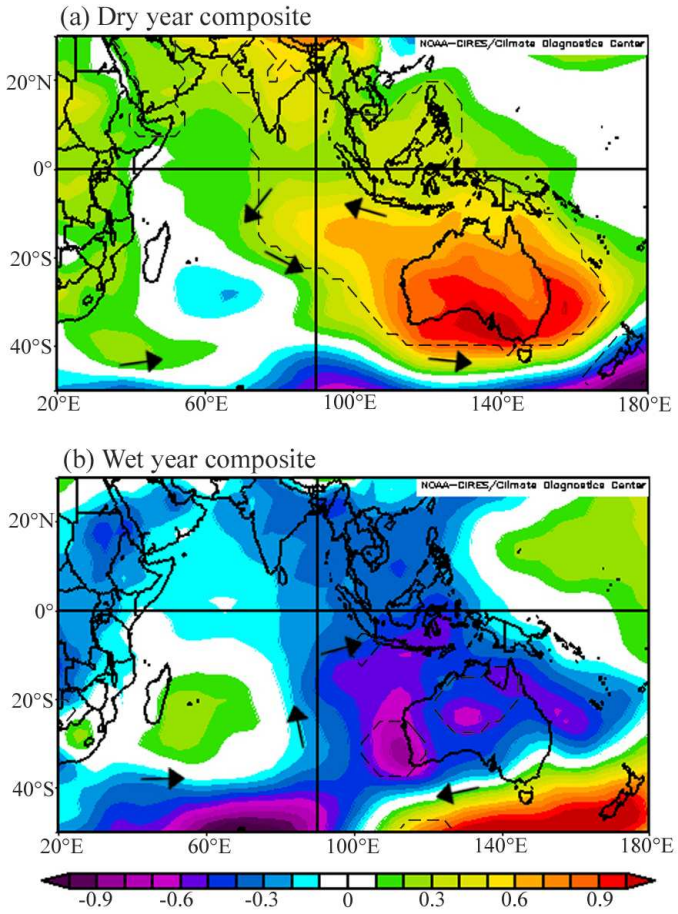

Figure 2.3. NCEP/NCAR reanalysis composite of anomalous SLP (mb) for (a) dry and (b) wet years in SWWA, as compared to the long-term climatological mean. The dashed contours indicate where anomalies exceed the 90% significance level as estimated by a two-tailed t-test.

across southeast Asia. This extension of the SLP anomaly creates a divergence (convergence) in near-surface flow across Indonesia, resulting in subsidence (convection) of upper-atmospheric air masses, which leads to reduced (increased) local precipitation. Accordingly, decreased (increased) cloud formation is observed in the anomalous patterns of outgoing longwave radiation (OLR; figure not shown) across southeast Asia and SWWA (increased OLR for clearer skies, decreased OLR for greater cloud coverage). These mechanisms explain the pattern of anomalous rainfall (Fig. 2.2) seen across southeast Asia during dry and wet years in SWWA. Additionally, there is a broad band of anomalous meridional winds at 80°–110°E and 15°–30°S during extreme SWWA rainfall years; characterized by unusually strong southward (northward) components during dry (wet) years. We will see below that these north-south wind anomalies contribute to local changes in atmospheric and oceanic temperatures. In summary, annual rainfall extremes over SWWA coincide

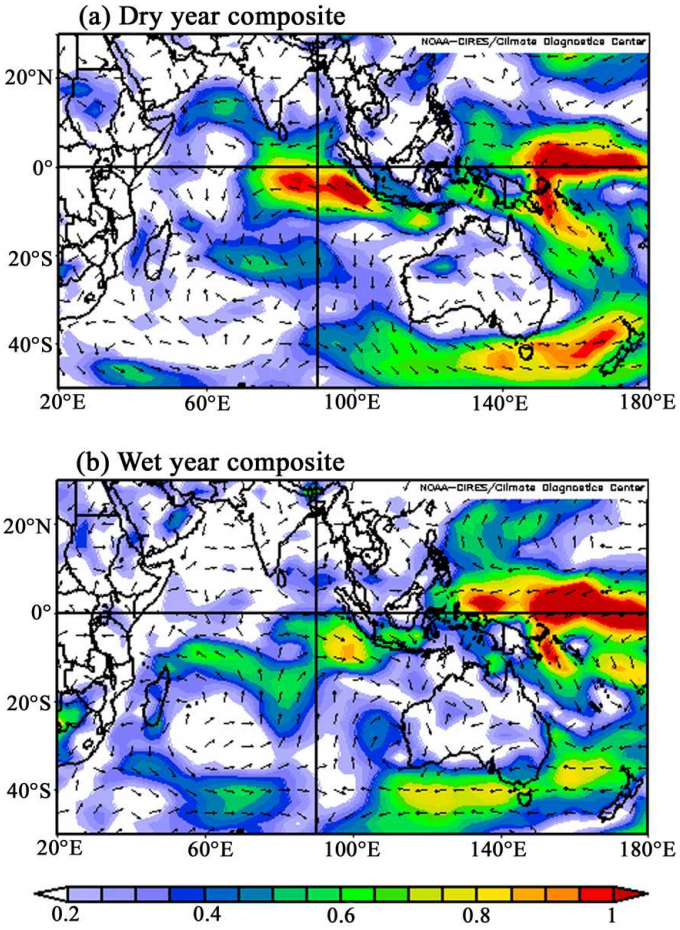

Figure 2.4. NCEP/NCAR reanalysis composite of anomalous annual surface wind vector direction and speed (m s^{-1}) for (a) dry and (b) wet years in SWWA, as compared to the long-term climatological mean. Vectors indicate direction only, with color shading denoting speed in m s^{-1}. Wind anomalies in excess of 0.5 m s^{-1} are significant at the 90% significance level as estimated by a two-tailed *t*-test.

with anomalies on both the tropical and extratropical flanks of the gyre-scale anticlockwise Indian Ocean wind system, with additional mid-basin meridional wind anomalies occurring near ∼100°E.

2.4.4. Sea surface and air temperature

Anomalous SST composite maps for extreme SWWA rainfall years are shown in Figure 2.5. In the eastern Indian Ocean a prominent dipole in SST exists off Western Australia during years of extreme rainfall; one pole (P1) is centered over the Northwest Shelf extending northwestwards to Sumatra, the other pole (P2) sits over the open ocean to the southwest centered at ∼30°S, 100°E. A third local extreme (P3) in SST is also apparent in the southwest Indian Ocean to the southeast of southern Africa.

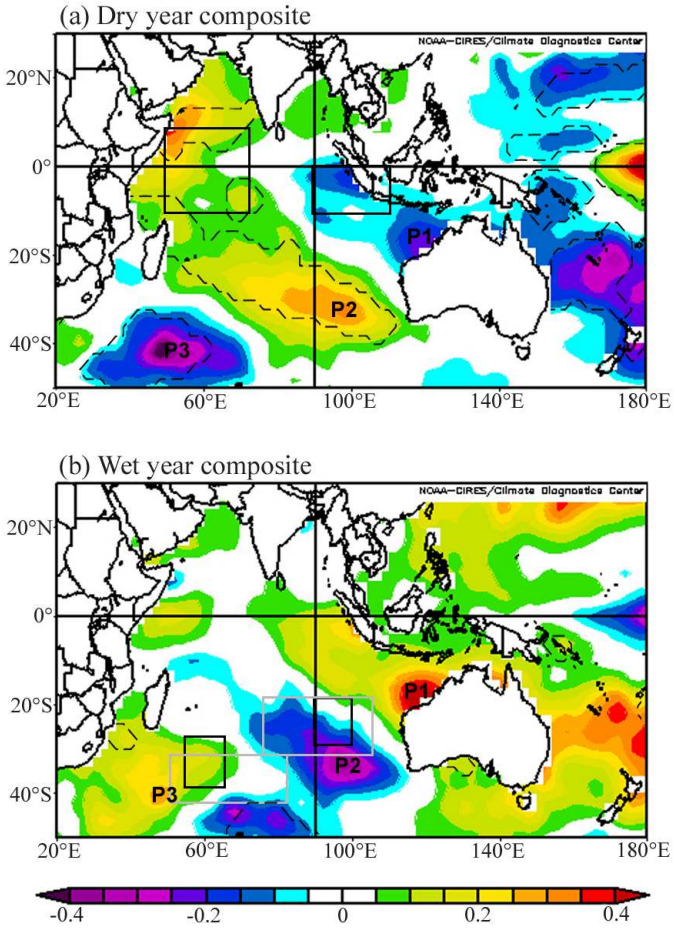

Figure 2.5. Composites of anomalous annual NOAA extended reconstructed SST (°C) for (a) dry and (b) wet years in SWWA, as compared to the long-term climatological mean. The areas traditionally associated with the Indian Ocean dipole (Saji *et al.*, 1999) and the subtropical Indian Ocean dipole (Behera and Yamagata (2001), solid boxes; Suzuki *et al.* (2004), gray boxes) are marked in (a) and (b), respectively. Labeled in each panel is the location of the temperature poles P1, P2 and P3 as discussed in the text. The dashed contours indicate where anomalies exceed the 90% significance level as estimated by a two-tailed *t*-test.

The SST pole south of Indonesia (P1) can be explained by the anomalous wind fields of Fig. 2.4. During dry years, strong easterly wind anomalies (Fig. 2.4a) cause a shoaling of the thermocline (forced by increased Ekman transport away from the equator), resulting in anomalously cold upwelled waters. The opposite occurs during wet years (Fig. 2.4b), with weaker easterly winds allowing local SST to warm via reduced upwelling. During dry years, a warm pole in SST is also seen in the equatorial western Indian Ocean off Africa reminiscent of the IOD, likely a result of anomalous eastward advection of warm tropical waters originating from the eastern Indian Ocean. This results in a positive air-sea feedback of anomalous SST fields reinforcing the overlying anomalous winds. A signature of negative IOD

phase is, however, only marginally apparent in the composite analysis of wet SWWA years (as noted below, only some wet years coincide with a strongly negative phase of the IOD).

The temperature pole located in the southeast Indian Ocean (P2; near 30°S, 100°E) corresponds with the anomalous meridional wind fields discussed in Section 2.4.3. For example, during dry years (Fig. 2.5a), the warm SST pole coincides with anomalous winds from the north (in fact, except for 2002, individual years show either anomalously weak southerly winds, or indeed, a mean northerly wind stream at this location). In contrast during wet years, the cold SST pole coincides with enhanced southerly winds. This suggests that this second pole in SST is forced by local air-sea heat fluxes (unlike the tropical pole that appears to be the result of anomalies in wind-driven ocean advection). This is confirmed by composite analyses of observed air-sea heat fluxes (Fig. not shown), which show enhanced ocean heat loss over pole P2 during wet years (cool SST), and weakened ocean heat loss at pole P2 during dry years (warm SST). The air-sea coupling at P2 is apparent in the composite analyses of surface air temperature (Fig. 2.6), which show a prominent anomaly in heat content of the air mass overlying the southeast Indian Ocean SST pole. This confirms that the second SST pole is associated with anomalous warming (dry years) and cooling (wet years) forced by air-sea heat fluxes via meridional wind anomalies.

The third SST pole in Figure 2.5 lies in the southwest Indian Ocean off southern Africa (P3). The SST anomalies in this region may be explained by anomalous wind-driven ocean advection during dry years (the cool water there is consistent with a stronger Ekman transport from the south), and anomalous air-sea heat fluxes during wet years (an anomalous northerly air stream flows toward P3 in the wet year composite).

It is finally worth noting that the SST composite signatures shown in Fig. 2.5 bear some similarity to previous analyses of surface temperature patterns in the Indian Ocean. For example, Nicholls (1989) found a significant correlation between northwest Western Australian (NWWA) winter rainfall and a pattern of SST reminiscent of poles P1 and P2 in our analysis. Surprisingly, Nicholls (1989) found no significant connection between his SST dipole and SWWA rainfall. Instead, his SST dipole was shown to correlate to rainfall over a region stretching from NWWA through central Australia and down to the southeast of the continent (matching the approximate trajectory of a northwest cloud band originating off NWWA). Ansell *et al.* (2000a) found that a similar SST dipole to Nicholls (1989) was correlated to Victorian rainfall in the southeast of Australia. More recently, Saji and Yamagata (2003b, their Fig. 2) plotted a composite map of the Indian Ocean SST anomaly

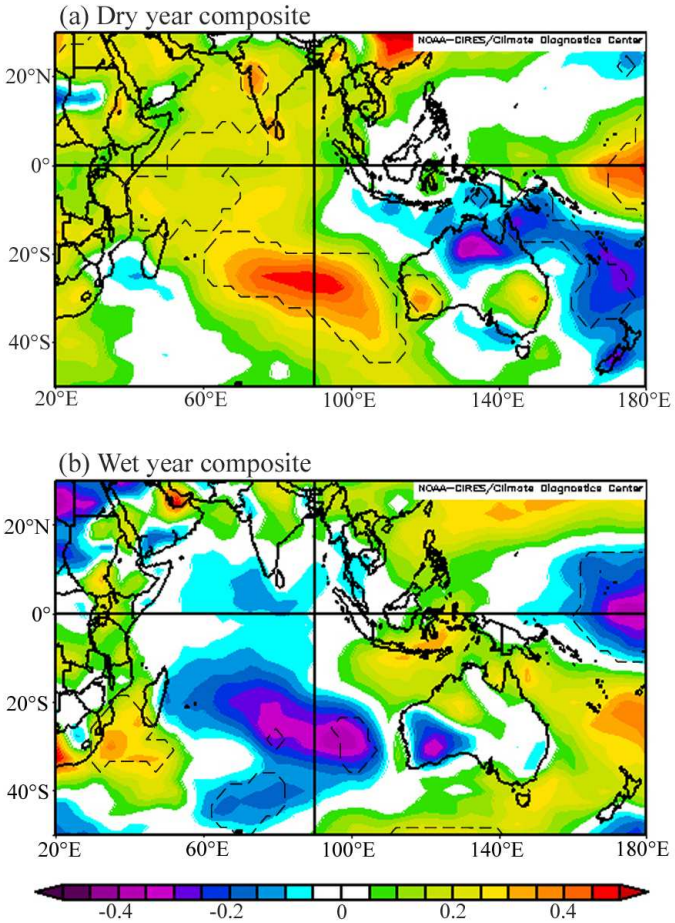

Figure 2.6. NCEP/NCAR reanalysis composite of anomalous annual surface air temperature (°C) for (a) dry and (b) wet years in SWWA, as compared to the long-term climatological mean. The dashed contours indicate where anomalies exceed the 90% significance level as estimated by a two-tailed *t*-test.

during September–November based on seven of the coolest SST anomaly years at 7°S, 105°E, which sits over the eastern pole of the IOD (to the northwest of P1). While the resulting SST composite shows only a weak cool signature at our pole P1, it reveals a warm band of SST spanning from the western pole of the IOD off Africa southeastwards towards SWWA (reminiscent of the pattern of SST seen in our Fig. 2.5a). This correspondence reflects the IOD component in our composite dry year analysis for SWWA rainfall.

2.4.5. Relation to the IOD and SIOD

It has already been mentioned that in some years the IOD is associated with SWWA rainfall via the reinforcement of SST anomalies at pole P1. The IOD may also affect SWWA rainfall by other means, such as via a modification of the tropical wind field as is suggested by the anomalies seen in Fig 2.4. To investigate the

IOD-SWWA rainfall link further we calculate the Indian Ocean dipole mode index (DMI), an indication of IOD strength, and plot its annual mean against SWWA rainfall anomalies in Fig. 2.7. All properties shown in Fig. 2.7 represent the annual mean of monthly values. In particular, we calculate the monthly DMI using monthly SST values before forming the annual mean. The DMI definition is as described by Saji *et al.* (1999); namely, the difference is taken between spatially averaged NOAA reconstructed SST anomalies of two areas in the Indian Ocean (shown in Fig. 2.5a), one in the western Indian Ocean (50°–70°E, 10°S–10°N) and the other in the tropical eastern Indian Ocean (90°–110°E, 0°–10°S). In the DMI, the eastern SST anomaly is subtracted from the western SST anomaly.

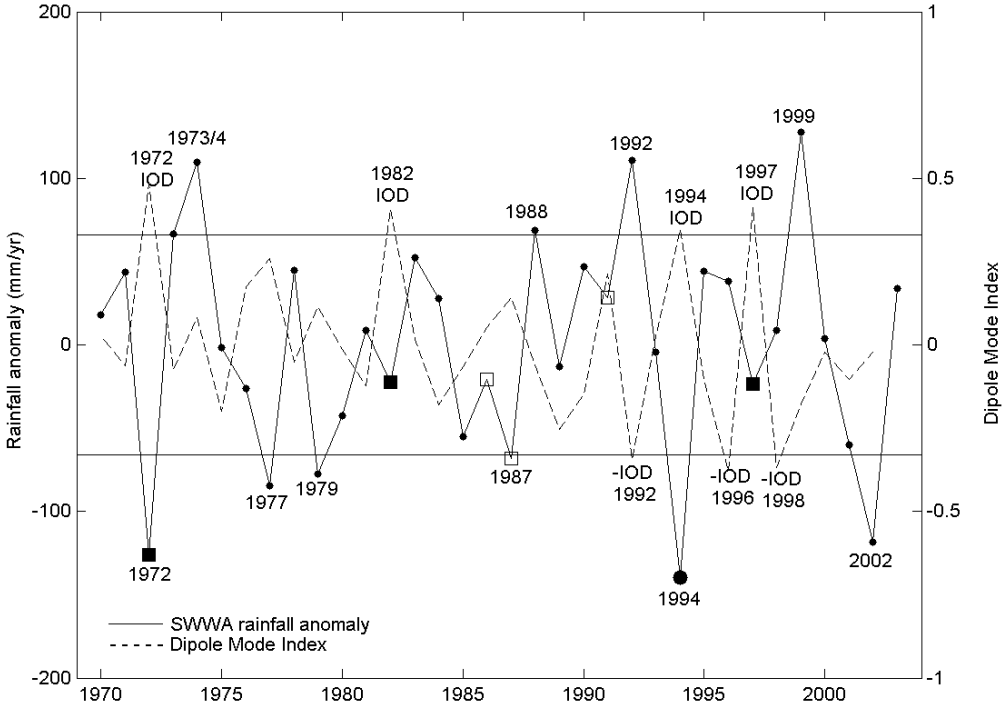

Figure 2.7. Observed annual rainfall anomaly (solid line, mm yr^{-1}) for SWWA during 1970–2003 overlaid with the annual mean Indian Ocean dipole mode index (dashed line, as defined by Saji *et al.*, 1999). The Indian Ocean dipole mode index is calculated using the regions indicated in Fig. 2.5a and the NOAA extended reconstructed sea surface temperature climatology. Years identified as positive Indian Ocean Dipole (IOD) years and positive ENSO years are indicated (■ = both IOD and ENSO; □ = ENSO only; • = IOD only). ENSO year definitions are taken from Meyers *et al.* (2007). Years of significant negative IOD phase are also indicated. The criteria used for wet/dry SWWA years are included (i.e., one standard deviation above/below the mean).

The most obvious aspect of Fig. 2.7 is that the DMI and SWWA rainfall are

strongly out of phase. However, not all IOD events force anomalously dry conditions over SWWA, and indeed some dry years occur in the absence of an anomalously positive IOD phase. The DMI is correlated negatively with rainfall in SWWA, with a Pearson correlation coefficient of -0.534 and an associated P-value of 0.001. The connection between the IOD and SWWA rainfall is most apparent, however, during dry years, with the dry year SST composite anomaly pattern typical of an IOD event (Fig. 2.5a) yet only a weak signature of negative IOD phase during wet years (Fig. 2.5b). Nonetheless, several of the anomalous wet years coincide with a negative phase in the DMI, most notably 1992 (Fig. 2.7). During such years the IOD acts to strengthen the SST anomalies south of Indonesia as well as enhancing wind anomalies along the northern flank of the Indian Ocean anticyclone, thereby affecting the mean subtropical ridge that drives winds and moisture onto the coast of SWWA.

The combination of SST anomalies at P2 and P3 is reminiscent of the subtropical Indian Ocean dipole (SIOD), although as indicated in Fig. 2.5 the location of these anomalies does not match previous definitions of the SIOD. For example, Suzuki *et al.* (2004)) investigate a subtropical dipole of SST at 50°–80°E, 42°–30°S (southwestern pole) and 75°–105°E, 29°–17°S (northeastern pole). Neither of these two poles overlies the regions of high SST anomaly identified above. It is not surprising then, that the subtropical dipole index (SDI) of Suzuki *et al.* (2004) is not significantly correlated with SWWA rainfall (Pearson correlation coefficient of 0.238, and an associated P-value of 0.183). Similar correlation levels are obtained between SWWA rainfall and the SDI of Behera and Yamagata (2001). We further investigated time-series of the seasonal mean SDI indices versus seasonal mean SWWA rainfall, and again found no significant correlation.

In spite of this, it is clear that extremes in SWWA rainfall are associated with subtropical and midlatitude Indian Ocean SST and SLP anomalies, which in turn modulate the subtropical high and thereby alter the local atmospheric circulation (Figs. 2.3, 2.4). In the context of our study region, SWWA rainfall extremes are related to subtropical SST anomalies at locations to the east of previous definitions of the SIOD (e.g., as depicted in Fig. 2.5). This is supported by the magnitude of anomalous winds in the southwest Indian Ocean shown in Fig. 2.4, which are weaker than those in the east, particularly during dry years. Anomalies in the southwest Indian Ocean (near P3) are thus likely symptomatic of other basin-scale adjustments in the Indian Ocean anticyclone during dry and wet years, and not essential to the control of SWWA rainfall.

2.4.6. Modulation by ENSO

The focus of this paper is on the link between interannual SWWA rainfall variability and climate over the Indian Ocean. However, it is of interest to assess whether the link to Indian Ocean climate variability is in some way modulated by ENSO. If not stated otherwise, an ENSO year/event refers to the positive phase of the ENSO cycle, i.e. an El Niño event. Fig. 2.7 highlights years during the 1970–2003 observational record that can be identified as IOD years, those identified as ENSO years (using the definition of Meyers *et al.*, 2007), and those identified as both IOD and ENSO years. For comparison the annual rainfall anomaly for SWWA is included in Fig. 2.7, and years of significant negative IOD phase are also shown. SWWA rainfall extremes exhibit no obvious link to ENSO events. For example, when an ENSO event occurs in the absence of a strongly positive IOD phase (1986, 1987, 1991), SWWA rainfall is not significantly different to the long-term mean. Rainfall can be anomalously low during combined ENSO-IOD years (e.g., 1972), but it can also be average in such years (1982, 1997). It is true that ENSO events tend to be associated with drier SWWA years, although the connection is by no means robust and could just be symptomatic of the known ENSO-IOD connection (e.g., just over 40% of IOD events during 1876–1999 have coincided with ENSO events; Meyers *et al.*, 2007). The teleconnection of ENSO to the IOD remains a topic of vigorous debate, and separating their projection onto SWWA rainfall is beyond the scope of the present study. Nonetheless, it is possible that ENSO directly plays a role in SWWA rainfall, for example via a continent-wide SLP response through the downward branch of the Walker circulation.

2.5. Modeled climate during extreme years

One of the limitations of the above analyses of the observed and reanalysis records is that there are only 5–6 years characterized by anomalously high or low SWWA rainfall (Fig. 2.1b). This means that in general, only the high amplitude signatures of the observed composite analyses are statistically significant (e.g., the SST poles, the SLP anomalies over Australia, and the tropical and extratropical wind anomalies). A much longer observational record is required to obtain detailed statistically significant patterns of Indian Ocean climate during wet and dry years over SWWA. It is therefore useful to revisit our analyses in the context of a long-term multi-century natural simulation of the global coupled climate system. To this end we examine 1000 years of model data from the latter stages of a 10,000-year integration of the CSIRO coupled climate model under constant CO_2 forcing. The model used is an updated version of the climate simulation described by Hirst *et al.* (2000),

consisting of coupled atmospheric, oceanic, sea-ice and land-surface submodels. All components of the model have a horizontal spectral resolution of R21 (approximately 5.6° longitude x 3.2° latitude), while on the vertical scale the ocean GCM has 21 geopotential levels and the atmospheric GCM 9 sigma levels. The climate model employs seasonally varying heat and freshwater flux adjustment terms to keep the simulation near to a present-day steady state. Further details on the model physics and numerics, as well as its ability to simulate the present-day global climate, can be found in Gordon and O'Farrell (2004) and Hirst *et al.* (2000). Details of the model's representation of global climate variability and precipitation can be found in Walland *et al.* (2000) and Hunt (2001).

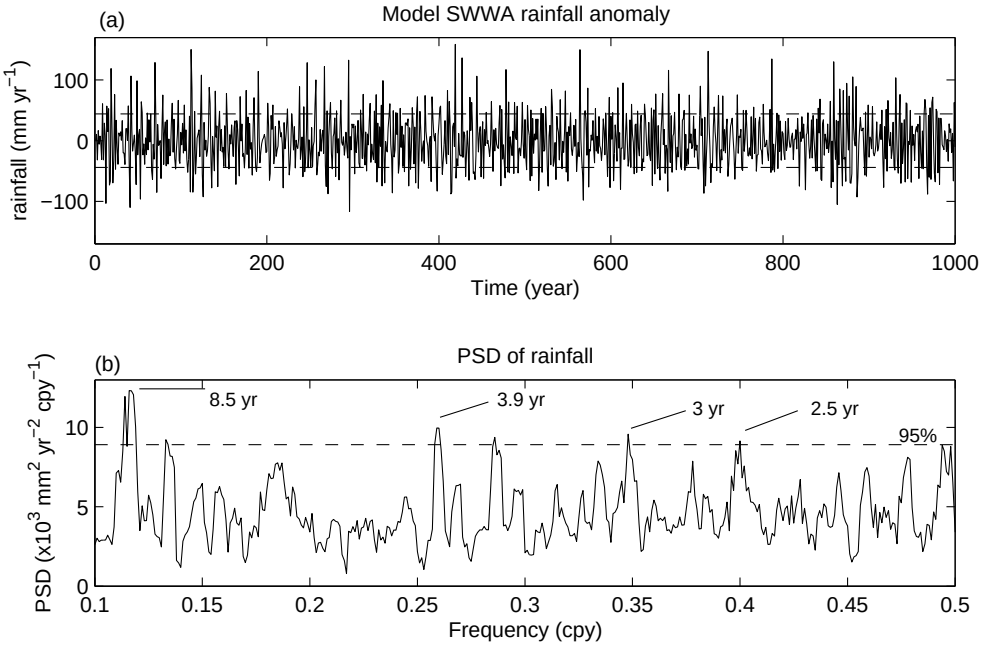

Figure 2.8. (a) Time-series of annual precipitation anomaly (mm yr^{-1}) in SWWA over the 1000-year climate model simulation. The dashed lines indicate one standard deviation (44 mm yr^{-1}) above and below the 1000-year mean, which is used to define anomalously dry and wet years. The model SWWA precipitation is defined as the average over the area indicated by the box at 115°–120°E, 30°–35°S (see Fig. 2.9a, b for the location). (b) Power spectral density (PSD) of SWWA precipitation. The dashed line represents the estimated white noise spectrum at 95% confidence level.

Since the focus of this study is on rainfall variability on interannual timescales, a high-pass filter is applied to the model data to retain signals with periods of 2–10 years. The model variables analyzed here include the annual mean SWWA rainfall (shown as a time-series over 1000 years in Fig. 2.8a, using rainfall averaged over the area indicated in Fig. 2.9a, b), as well as global SST, rainfall, surface wind stress, air-sea heat fluxes and surface ocean currents. The SWWA rainfall shown in

Fig. 2.8a is calculated using linear interpolation involving a total of 12 model grid points that span the domain of interest, matching the nearest model grid boxes to the analyzed observational domain of 115°–120°E, 30°–35°S. There are only 2 model grid points wholly enclosed by the box shown in Fig. 9a and 9b, but another 10 points adjacent to the region that come into the calculation of SWWA rainfall via an area-weighted linear interpolation.

The coupled climate model SWWA rainfall variability is weaker than that seen in the BoM observations, with a standard deviation of 44 mm yr^{-1} compared to the observed 66 mm yr^{-1}. This is typical of coarse resolution climate models wherein extreme events tend to be weakly damped compared to observations. The extremes in model SWWA rainfall (Fig. 2.8a) are defined as those in which the rainfall anomaly exceeds one standard deviation above and below the long-term mean (i.e. $\pm$44 mm yr^{-1}), resulting in $\sim$150 instances of each of anomalously wet and dry years. The dominant periods of interannual variability of the model SWWA rainfall appear similar to the observations from a cursory comparison of Figs. 2.1b and 2.8a, which is confirmed by PSD analyses (Fig. 2.1c, 2.8b). The dominant variability in the model rainfall occurs at a broad range of periods, including 3–4 years and $\sim$8.5 years (these peaks are significantly different at 95% confidence level from a white noise signal, see Fig. 2.8b). The PSD analysis of observed rainfall (Fig. 2.1c) shows much less structure than the model (to be expected given the short data record), although the observed peaks at 2.4, 3.9 and 8 years are in good agreement with three of the significant peaks shown in the model analysis. The dominant period of variability seen in the observed SWWA rainfall ($\sim$4 years, Fig. 2.1c) contrasts multiple significant peaks in the model (at $\sim$2.5, 3, 3.5, 4, 7, 8.5 years). It also contrasts the variability of the model's IOD, which exhibits a dominant period of $\sim$3 years (figure not shown). The model IOD variability also exhibits a signal with a period of $\sim$2 years, although not of magnitude significantly different from background noise. Damped higher frequency climate variability is a problem common to coarse-resolution models; it is likely to be why the simulation does not capture the primary biennial peak in the IOD noted in observations (e.g., Ashok *et al.*, 2003b).

Composite anomalies of the model regional rainfall patterns during dry and wet SWWA years are shown in Fig. 2.9a, b. Anomalies are only shown where they exceed the 90% significance level as estimated by a two-tailed t-test. The composite patterns of model precipitation correspond closely to those formed based on the observed 1979–2003 CMAP climatology (Fig. 2.2), though with reduced amplitude. Anomalous rainfall extends from SWWA and the eastern Indian Ocean into Asia in both dry and wet years, with a general reversal of sign over the western Indian

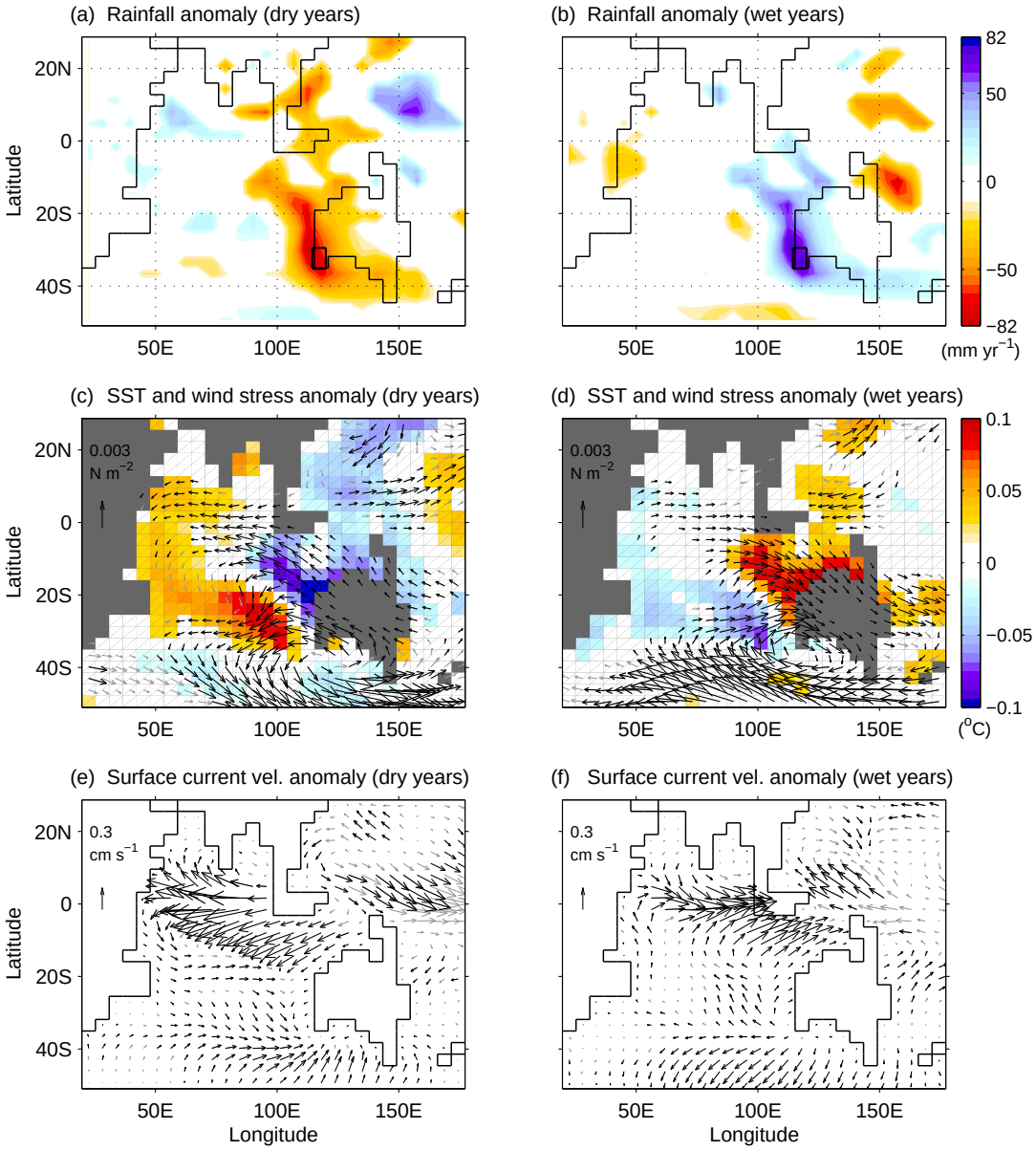

Figure 2.9. Composite maps of (a, b) rainfall anomaly (mm yr^{-1}), (c, d) SST (°C) overlaid on vectors of wind stress anomaly (N m^{-2}), and (e, f) ocean surface current anomaly (cm s^{-1}) during dry (a, c, e) and wet (b, d, f) years in the climate model. Anomalies are only shown where they exceed the 90% significance level as estimated by a two-tailed *t*-test. Anomalous wind stress and surface current velocities below the significance level are displayed as gray vectors in (c–f). Wind anomaly vectors of magnitude less than 0.5 x 10^{-3} N m^{-2} are not shown. The highlighted box in (a, b) marks the SWWA location used to define years of anomalous model rainfall (i.e., the dry and wet years of Fig. 2.8a).

Ocean and Africa, as well as in the western Pacific. Unlike the observed, however, the composite patterns exhibit highest anomaly magnitudes over SWWA, not Asia. This indicates a greater variety of rainfall scenarios over Asia in the model during dry and wet SWWA years. It is also noted that the model under-represents tropical ocean-atmosphere variability, including ENSO and the IOD, owing to its coarse resolution and possibly the use of flux-adjustment terms. In this context we repeated the model composite analyses within the non-flux-adjusted NCAR climate system model, and found similar patterns to those described here (figures not shown).

Composites of the model SST and wind vector anomalies during dry and wet SWWA years are presented in Fig. 2.9c, d (as above, only shown where they exceed the 90% significance level). This shows that during dry years a pole of cold SST sits in the tropical eastern Indian Ocean off Northwest Australia alongside a pole of anomalously warm SST to the south extending northeast towards Central Africa. During wet years this SST pattern is reversed, with the dipole of temperature anomalies nearly a mirror image of the dry year scenario. These dry and wet year patterns are remarkably similar to the reanalysis SST composite anomalies shown in Fig. 2.5, although the magnitude of the SST anomalies is smaller in the model compared to the observations ($\pm 0.1^{\circ}$C versus $\pm 0.4^{\circ}$C, respectively). This reduced SST variability is likely due to a combination of the model's coarse resolution, the model flux adjustment terms, and the fact that we composite $\sim$150 model years for each of the low rainfall and high rainfall scenarios. Like the observational analyses (Fig. 2.5), the model SST dipole reaches peak amplitude in the tropical and subtropical eastern Indian Ocean, adjacent to western Australia (and to the east of previous definitions of the SIOD). Furthermore, the model composite of dry years shows a stronger magnitude IOD pattern compared to the model wet years, similar to the observed composite SST signals of Fig. 2.5.

The model composite winds are also for the most part consistent with the reanalysis data. There is a strengthening (weakening) of the subpolar westerlies during dry (wet) SWWA years (Fig. 2.9c, d). In addition, dry (wet) years are accompanied by acceleration (deceleration) of the tropical easterlies, with strongest anomalies off the Indonesian coast. As with the reanalysis data, this forces the oceanic heat anomalies at pole P1 via fluctuations in the surface Ekman transport away from the equator (this can be confirmed for the model in Fig. 2.9e, f). In addition, local evaporative fluxes also play a role in regulating the model's SST anomalies at P1. Winds over the southeast Indian Ocean SST pole (P2) include anomalously northward (southward) components during cold (warm) phases. These features again show excellent agreement between the reanalyzed and climate model data. As in the observed analyses, anomalies in the model air-sea heat exchange at pole P2 are controlling

SST fluctuations via anomalous meridional winds (composite heat flux patterns not shown). Ocean advection also contributes to SST variability at P2, with meridional flow anomalies altering local ocean heat transport (Fig. 2.9e, f). The model wet (dry) years experience an increase (decrease) in onshore winds over SWWA near 30°S (Fig. 2.9c, d), which is also apparent albeit localized in the NCEP/NCAR data (Fig. 2.4). Anomalous ocean current fields (Fig. 2.9e, f) mostly reflect adjustments in Ekman transport as forced by the wind stress anomalies symptomatic of wet and dry years. These ocean circulation changes are important for forcing SST anomalies at pole P1 (via divergence of water from the equator) and in the extratropics under the subpolar westerlies.

2.6. Seasonal development of climate anomalies

The focus of this paper is on year-to-year precipitation anomalies over SWWA. Nonetheless, with the majority of SWWA rainfall occurring during austral winter (e.g., McBride and Nicholls, 1983; Drosdowsky, 1993b), it is of interest to assess the intra-annual development of climate anomalies associated with extreme wet and dry years. Fig. 2.10 shows the mean monthly precipitation over SWWA over the 1000-yr model integration and during 1970–2003 in the observed. Both model and observed show peak rainfall occurring during June-July-August (JJA), declining gradually to minimum rainfall during December-January-February (DJF). In both model and observed, approximately 45% of the total annual precipitation over SWWA occurs during JJA. To assess the seasonal development of climate anomalies associated with extreme wet and dry years, Fig. 2.11 shows the evolution of NCEP/NCAR SLP anomalies during dry and wet years for the period 1970–2003. A corresponding analysis for NOAA extended reconstructed SST is presented in Fig. 2.12. In these analyses, the seasonal composites are formed using the extreme rainfall years to elucidate the seasonal evolution of annual climate anomalies, rather than looking at extremes of any given season in isolation (we undertake such an analysis for wintertime later in this section).

Fig. 2.11 reveals that on average, extreme SWWA rainfall years are characterized by a progressive strengthening of anomalous SLP during the progression from summer to late winter months. This is not unexpected as peak rainfall occurs during austral winter, with DJF precipitation less than 25% of that received during JJA. In fact, summertime SLP anomalies in DJF (Fig. 2.11a, b) bear only weak resemblance to the peak wintertime pressure anomalies seen in Fig. 2.11e, f. Autumn (MAM), winter (JJA) and spring (SON) anomalies are all reminiscent of the annual patterns shown in Fig. 2.3. In contrast, SST anomalies (Fig. 2.12) show

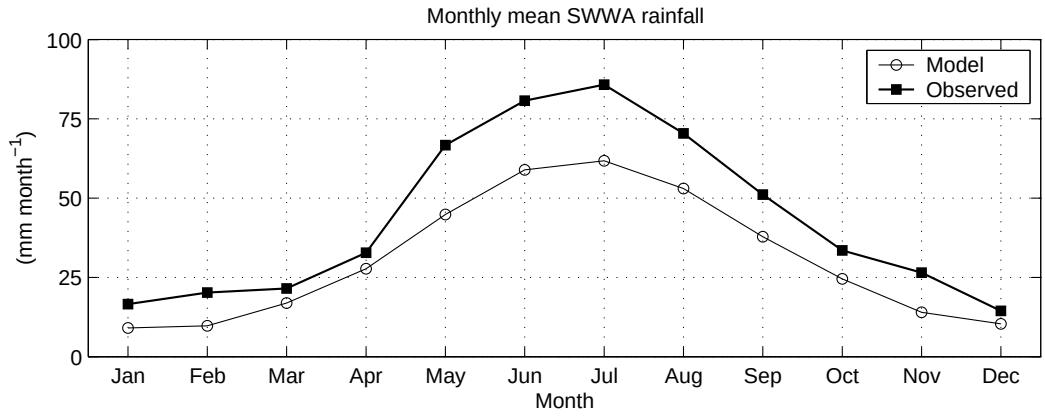

Figure 2.10. Observed and modeled mean monthly precipitation over southwest Western Australia in mm month^{-1}. The observed is derived from the Australian Bureau of Meteorology gridded rainfall climatology during 1970–2003. The model seasonal cycle is derived from the CSIRO 1000-yr integration. The regions of analysis used to construct the observed and model means are shown in Figs. 2.1a and 2.9a respectively.

greater persistence, with summertime SST patterns in DJF already exhibiting the characteristic three-pole structure noted in the annual composites (Fig. 2.5). The two areas of anomalous SST adjacent to SWWA (P1, P2 of Fig. 2.5) reach peak magnitudes in wintertime (JJA) and spring (SON), but their genesis appears as early as the preceding summer.

With our focus on interannual SWWA rainfall fluctuations, an analysis of extremes in seasonal precipitation is mostly beyond the scope of the study. We note, nonetheless, that composite analyses of seasonal rainfall extremes reveal similar Indian Ocean climate states to the wet and dry scenarios described in sections 2.4 and 2.5, particularly during April–November. For example, an analysis of extended wintertime (May–September) rainfall during 1970–2003 identifies six anomalously dry winters (1976, 1977, 1979, 1987, 2000, 2002) and seven anomalously wet winters (1973, 1974, 1983, 1988, 1992, 1996, 1999), using the ± 1 SD criterion adopted previously. Fig. 2.13 shows composite SLP, winds, and SST during the wet and dry winters identified above.

The overall pattern of anomalous SLP and SST during extreme winters is very similar to the annual composite anomalies described previously, despite a different selection of years in the composite statistics. Some notable differences appear in the wind composites, which are now dominated by anomalous patterns of onshore and offshore winds at the latitude of SWWA. Overall, the peak in surface pressure anomalies appears to be shifted slightly to the south compared to the annual composites, with a weakened tropical influence on SWWA during wintertime. This

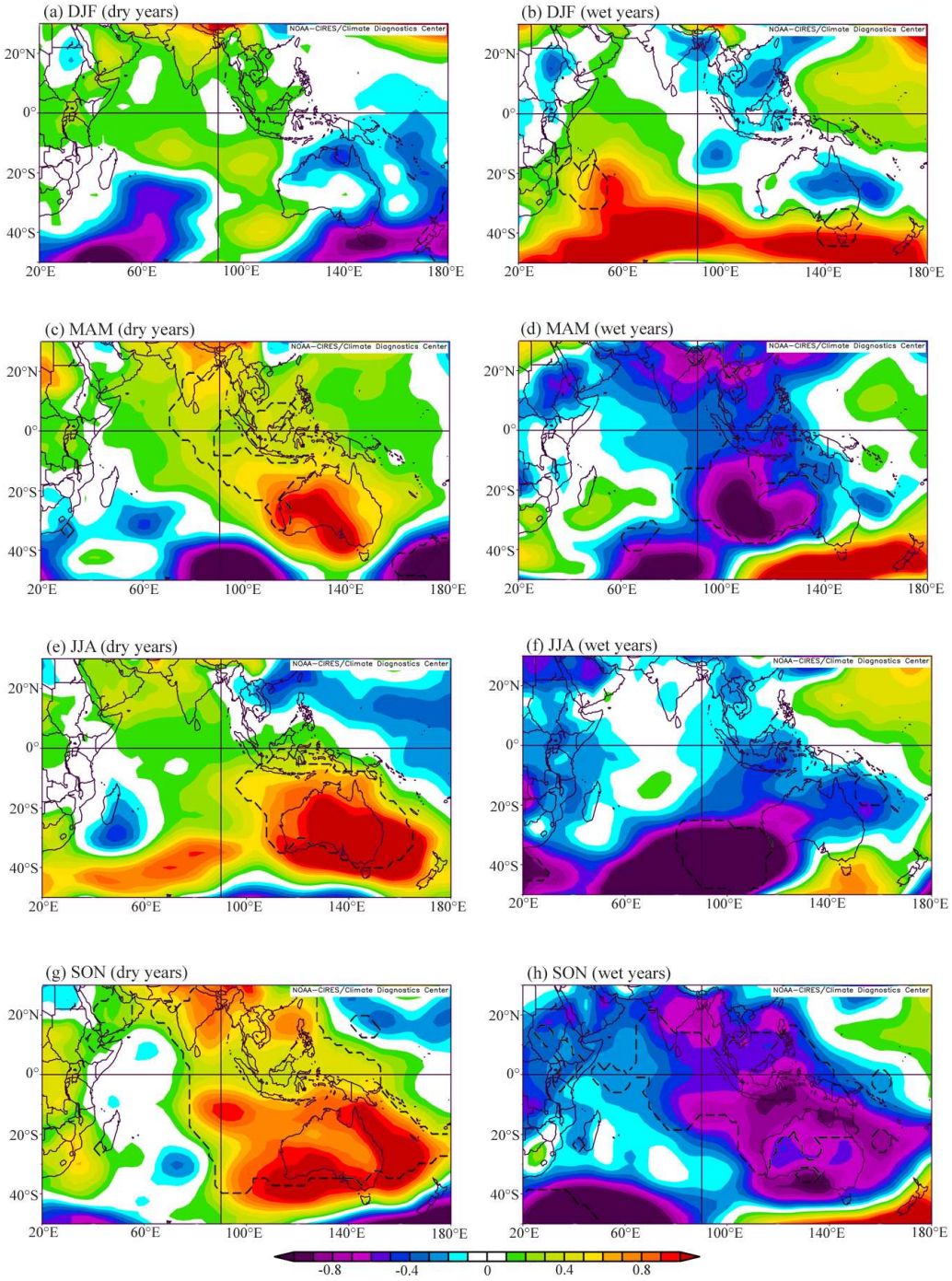

Figure 2.11. Seasonal evolution of NCEP/NCAR reanalysis SLP anomalies (mb) for dry (left) and wet (right) SWWA years for the period 1970–2003, as compared to the long-term climatological seasonal mean. The dashed contours indicate where anomalies exceed the 90% significance level as estimated by a two-tailed *t*-test.

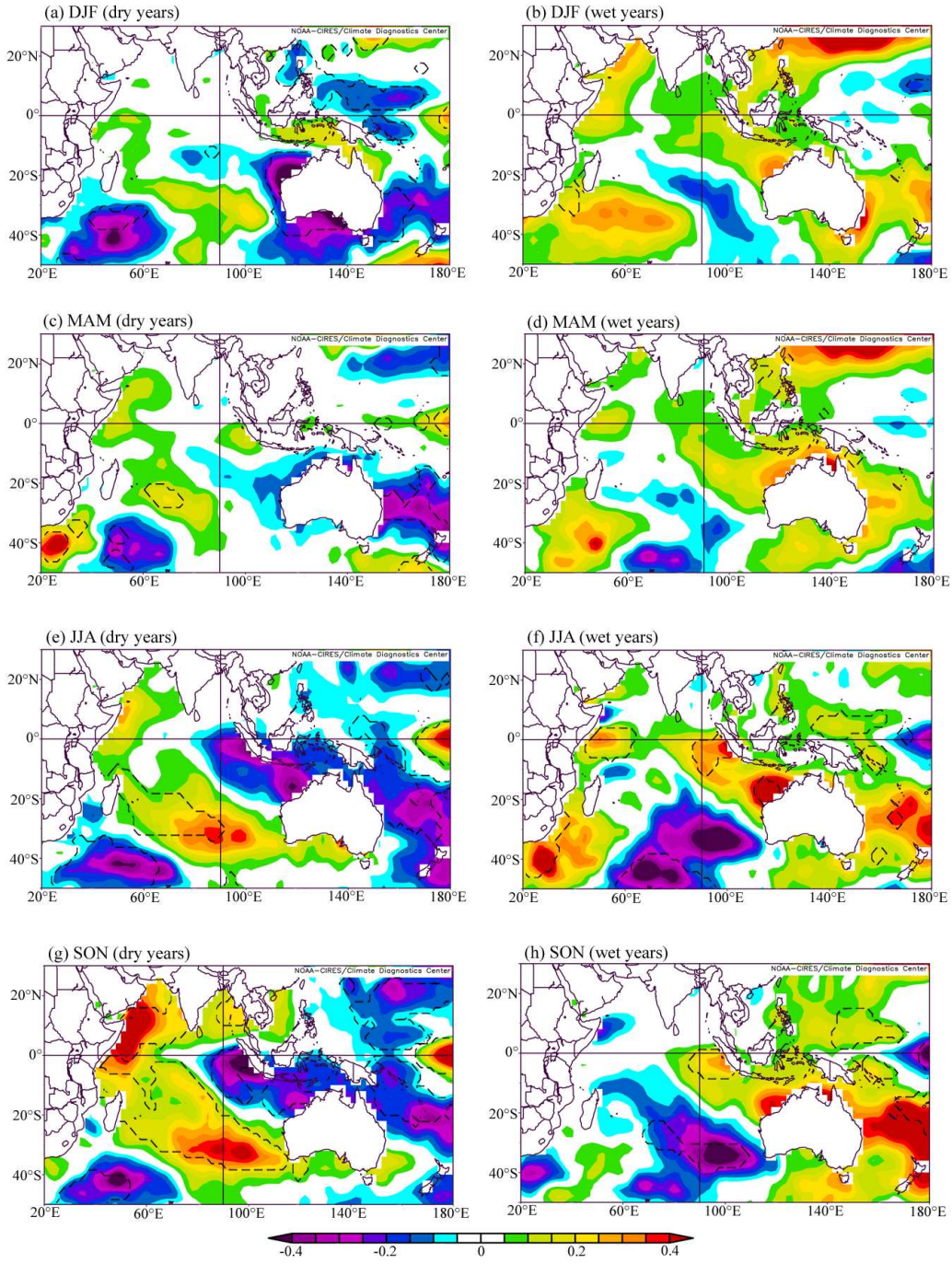

Figure 2.12. Seasonal evolution of NOAA extended reconstructed SST anomalies (°C) for dry (left) and wet (right) SWWA years for the period 1970–2003, as compared to the long-term climatological seasonal mean. The dashed contours indicate where anomalies exceed the 90% significance level as estimated by a two-tailed *t*-test.

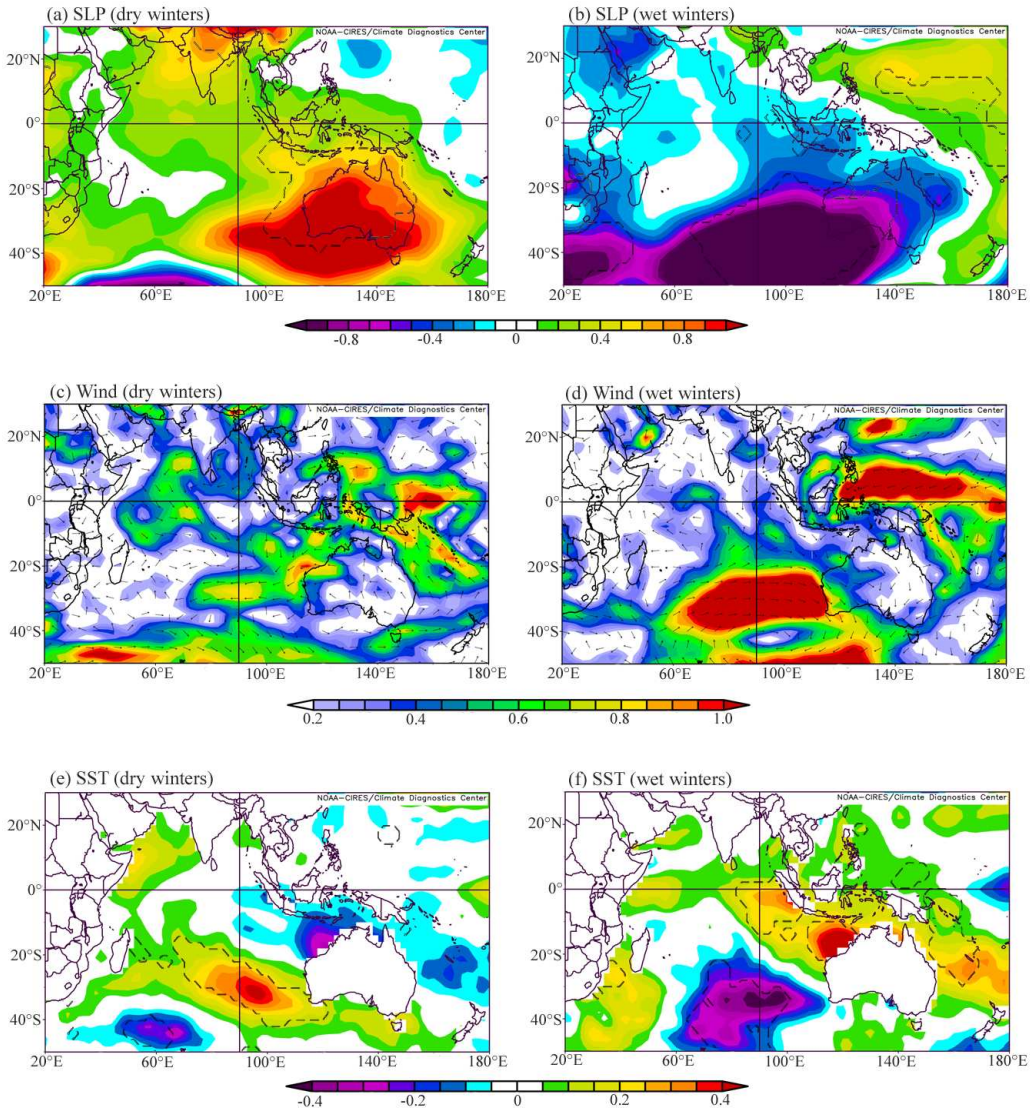

Figure 2.13. Composite analyses of (a, b) SLP (mb), (c, d) vector winds (m s^{-1}) and (e, f) SST (°C) for dry (a, c, e) and wet (b, d, f) winters in SWWA. The extreme winter rainfall events are defined as one standard deviation below/above the mean rainfall during May–September (inclusive). Years included in the composite winter analysis are given in the text. The dashed contours indicate where anomalies exceed the 90% significance level as estimated by a two-tailed *t*-test. Wind anomalies in excess of 0.5 m s^{-1} are significant at the 90% confidence level, as estimated by a two-tailed *t*-test.

is likely due to the increased role of extratropical cyclones during winter in feeding moisture to SWWA, as compared to other seasons when northwest cloud bands may dominate. Apart from these differences in composite winds, the overall patterns of SST and SLP characteristic of SWWA winter rainfall extremes exhibit strong similarity to the annual composites detailed in Section 2.4. Thus, our results for the Indian Ocean climate states associated with annual SWWA rainfall extremes are

robust when applied to an analysis of SWWA winter rainfall extremes. While not shown here, analyses of SST, SLP and winds during austral autumn (MAM) and spring (SON) extremes also exhibit robust features compared to those described for the annual extremes. In contrast, composite analyses based on extreme summertime (DJF) rainfall events show robust patterns of SST, similar to the features revealed in Fig. 2.5, and largely robust patterns in SLP and winds during dry summers, but significant differences in SLP and winds for anomalously wet summers (figure not shown).

An analysis of the climate model's seasonal evolution of SST and wind anomalies during wet and dry years is presented in Fig. 2.14. Like the evolution of climate anomalies within observed wet/dry years (Figs. 2.11, 2.12), the model exhibits a progressive amplification of anomalies in SST and atmospheric circulation towards a wintertime peak during JJA. The composite plots suggest ocean temperature anomalies begin to develop as early as summertime, with a weak SST dipole appearing at P1 and P2 in the mean DJF conditions. Wind anomalies then develop during the ensuing months (MAM), amplifying to a pronounced large-scale acceleration (deceleration) of the Indian Ocean mean anticyclone by wintertime (JJA) during dry (wet) years. The wind anomalies reinforce the SST anomalies via Ekman transport at P1 and air-sea fluxes at P2, yielding peak amplitude SST anomalies during JJA. The Indian Ocean climate anomalies then begin to weaken gradually during austral spring (SON). Thus in summary, both the model and observed extreme years exhibit a seasonally-evolving climate signal over the Indian Ocean, appearing to initiate in SST as early as summertime, rapidly increasing to a peak amplitude in atmospheric circulation and SST during winter, then abating gradually during austral spring.

2.7. Discussion and conclusions

We have assessed interannual rainfall extremes over SWWA using 34 years of observations and reanalysis data as well as 1000 years of model output from a global coupled climate model integration. The study area is limited in its spatial extent but is chosen due to its unique rainfall characteristics, which are confirmed in this study to be of a highly localized nature. Both the reanalysis data and the climate model suggest SWWA rainfall extremes are linked to a reorganization of the large-scale wind field over the eastern and southeastern Indian Ocean. The wind field alters SST via anomalous Ekman transport in the tropical Indian Ocean and via anomalous air-sea heat fluxes in the subtropics, as well as changing the large-scale advection of moisture onto the SWWA coast. The resulting dipole in SST seesaws

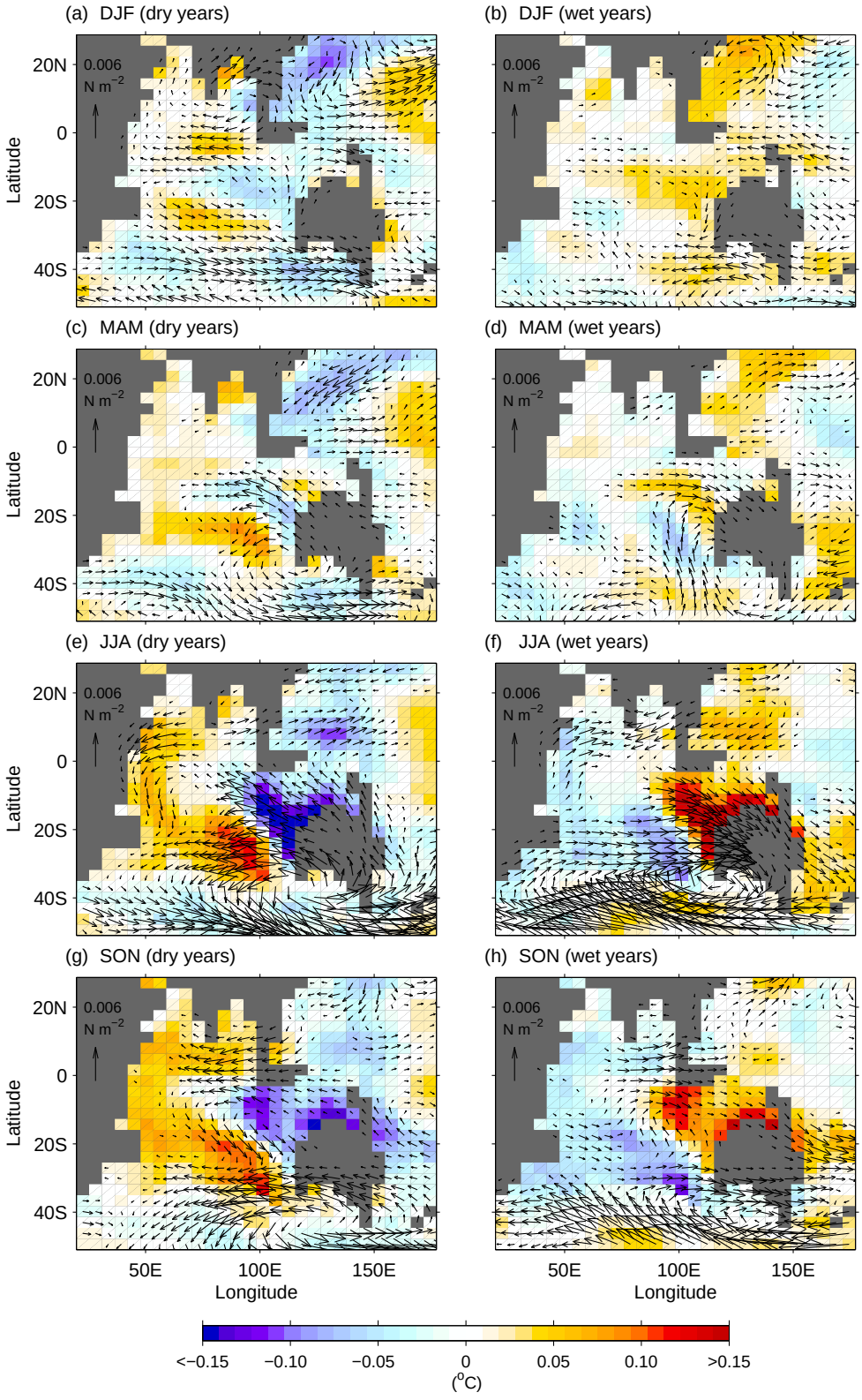

Figure 2.14. Seasonal evolution of SST (°C) and wind stress (N m^{-2}) anomalies presented as composite maps based on extreme years of SWWA rainfall in the coupled climate model. Wind anomaly vectors of magnitude less than 0.5 x 10^{-3} N m^{-2} are not shown. Anomalies are only shown where they exceed the 90% significance level as estimated by a two-tailed *t*-test.

in sign between dry and wet years, and is different from most previous definitions of SST dipoles in the region. In particular, the dipole we linked to SWWA rainfall exhibits peak amplitudes in the eastern Indian Ocean adjacent to the west coast of Australia. During dry years, the SST pattern is characterized by anomalously cool waters in the tropical eastern Indian Ocean (P1; Fig. 2.5), adjacent to a region of unusually warm water in the subtropics off SWWA (P2). In some of the dry years, the cool temperatures in the tropical eastern Indian Ocean are reinforced by an IOD event. Notably, however, not all IOD events force anomalously dry conditions over SWWA, and indeed some dry years occur in the absence of an anomalously positive IOD phase (Fig. 2.7). In a similar manner, some (but not all) wet SWWA years are reinforced by a negative phase in the IOD.

The fact that there is no simple relationship between interannual variability in SWWA rainfall and the IOD suggests that other low-frequency processes are also at play. These include the modes of subtropical and extratropical variability that have already been described above. In addition, the proximity of the first SST pole (P1) to the Indonesian Archipelago suggests that variations in the Indonesian throughflow (ITF) will also drive substantial SST variability at P1. In addition, the Leeuwin Current propagates heat content anomalies from P1 polewards along the west coast of Western Australia, offshore of the SWWA region, and so it too likely impacts on local wind and moisture advection anomalies in the region. These modes of variability cannot be examined using observational data, however, as direct ocean current measurements are too sparse. In addition, coupled climate model resolution is inadequate to resolve the structure and speed of the Leeuwin Current. Hence, we cannot easily assess the role of the ITF and Leeuwin Current variability in determining SWWA rainfall in the present study.

As noted above, anomalous winds during extreme years alter SST via Ekman transport in the tropical Indian Ocean and via air-sea heat fluxes in the subtropics. The winds also change the large-scale advection of moisture onto the SWWA coast. At the basin scale, the anomalous winds can be interpreted as an acceleration (deceleration) of the Indian Ocean climatological mean anticyclone during dry (wet) years. In addition, dry years see a strengthening and coinciding southward shift of the subpolar westerlies, which results in a similar southward shift of the rain-bearing fronts associated with the subpolar front. A link is also noted between extreme rainfall years and winds over the tropical margin of the Indian Ocean anticyclonic, which reinforces the tropical eastern pole of SST described above. In this manner, both tropical and extratropical processes in the Indian Ocean generate SST and wind anomalies off western Australia, which are linked to moisture transport and rainfall extremes in the region.

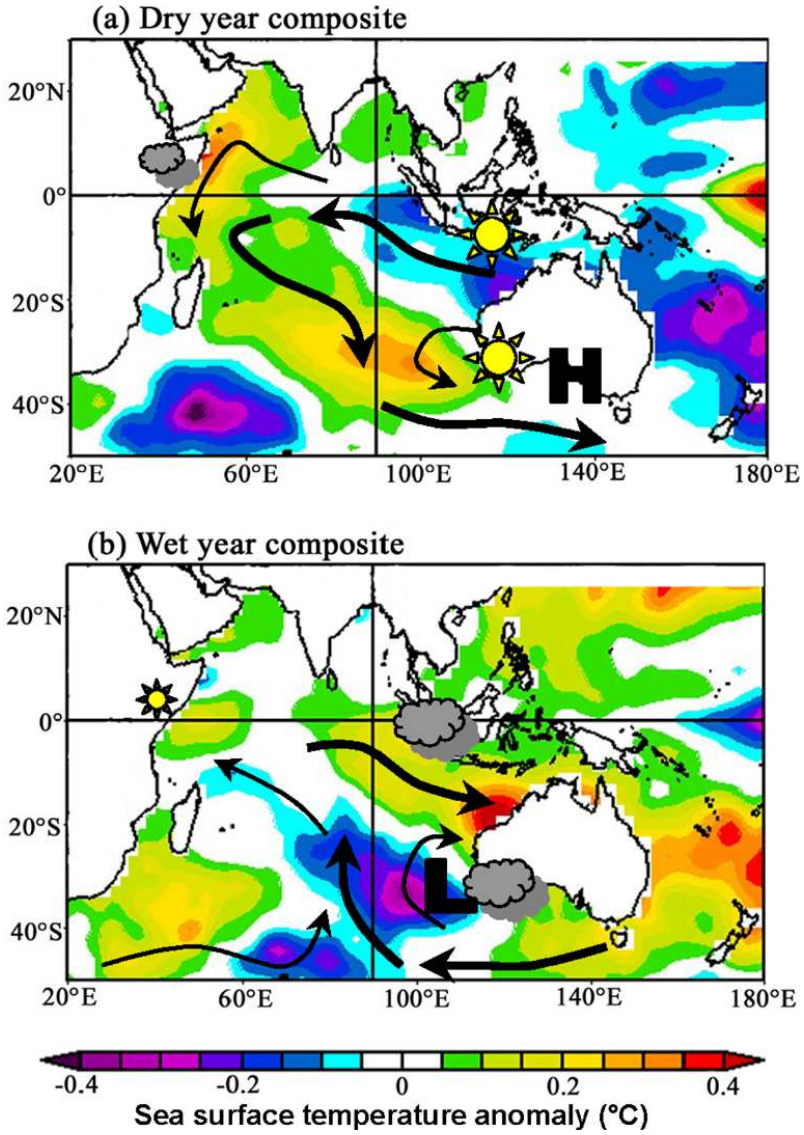

Figure 2.15. Schematic diagram showing the connection between Indian Ocean climate variability and (a) dry and (b) wet years over SWWA. SST anomalies are shown as actual composite fields as in Fig. 2.5 (color shaded in °C). Wind anomalies are shown schematically as bold arrows, pressure anomalies are indicated by H (high) and L (low), and rainfall anomalies are shown using sun/cloud symbols.

A schematic diagram depicting the major climate anomalies during dry and wet years over SWWA is shown in Fig. 2.15. During dry years, a strengthening of the northern flank of the anticyclonic wind field across the equatorial Indian Ocean causes a shoaling of the thermocline and cool upwelled SST off the Indonesian coast, accounting for the simultaneously dry conditions in southeast Asia. This is sometimes reinforced by an IOD event. The cool SST anomalies exhibit highest magnitude adjacent to the west Australian coast (P1 of Fig. 2.5). In addition, dry

years coincide with an anomalous southward air stream over the eastern subtropical Indian Ocean, leading to warmer air, anomalous air-sea heat fluxes, and warmer SST centered near 100°E and 30°S (pole P2 of Fig. 2.5). Further south, the dry year climate exhibits a strengthening and coinciding southward shift of the subpolar westerlies, which results in a similar southward shift of the rain-bearing fronts associated with the subpolar front. This leads to reduced moisture transport onto the SWWA region. The dry year climate dynamics are more-or-less reversed during wet years, although only a weak IOD signal is noted in the composite analyses. During wet years, anomalously low air pressure extends over much of the region, driving a deceleration of the Indian Ocean subtropical anticyclone. In the immediate vicinity of SWWA, winds are anomalously stronger onshore, forcing increased moisture transport into the region. Wright (1974) found dominant winter rainfall in SWWA to be prefrontal with moisture inflow from the ocean to the northwest, also shown by Hope and Nicholls (2004) for wet conditions in SWWA. These findings are consistent with the anomalous signal in SST, winds, and moisture transport in this study during wet SWWA years.

A 1000-year integration of a coupled climate model was used to reassess the results of the 34-year reanalysis record, particularly in view of the low number of extreme events available in the short observational record. Analysis of the ∼150 extreme dry and wet SWWA years in the climate model simulation revealed surprisingly similar composite anomaly patterns as those seen in the observations. The proposed dynamics linking large-scale Indian Ocean climate to SWWA rainfall extremes, as derived from the reanalysis data, appear robust in the coupled model. In particular, composite model patterns of Indian Ocean winds, rainfall and SST are broadly similar to those seen in the reanalyses and observations. The model anomalies have smaller magnitudes than in the reanalysis fields, which is likely due to a combination of the coarse model resolution, the model flux adjustment terms, and the fact that we composite 150 events for each of dry and wet years. We had initially assumed that the model would be too coarse in resolution to capture the dynamics of interannual rainfall variability over SWWA. However, given the close correspondence between composite climate patterns in the coupled model and the observed (both on the annual average as well as during their seasonal evolution), and given that these features are basin-scale in their extent, it appears that the model is resolving regional southeast Indian Ocean climate variability rather well. Indeed, the finding that the model agrees with the observed, despite its coarse resolution, is symptomatic of the fact that the driving mechanisms for SWWA rainfall variability are large in scale.

An analysis of the seasonal evolution of SST, winds, and SLP during wet and dry years revealed a progressive amplification of anomalies towards a wintertime peak

during JJA. In both the model and observed, ocean temperature anomalies can begin to develop as early as summertime, with an SST dipole appearing at P1 and P2 in the composite mean DJF conditions. Wind anomalies then develop during the ensuing months, amplifying to a pronounced large-scale acceleration (deceleration) of the Indian Ocean mean anticyclone by wintertime during dry (wet) years. The wind anomalies act to reinforce the SST anomalies via Ekman transport at P1 and air-sea fluxes at P2, yielding peak amplitude SST anomalies during JJA. Both the model and observed extreme years exhibit this seasonally-evolving climate signal over the Indian Ocean: genesis in SST as early as summertime, rapidly increasing to maximum amplitude in atmospheric circulation and SST during winter (the season of highest SWWA rainfall), and then gradually abating during austral spring.

Because there is evidence of a net decrease in wintertime SWWA rainfall since the mid-1970s relative to the pre-1975 period (e.g., IOCI, 2002), it is of interest to briefly assess whether recent multi-decadal trends in SST and SLP bear any resemblance to the dry-year composite fields obtained in our study. We have plotted the JJA difference in SST and SLP during the 25-yr period 1980–2004 relative to 1951–1975 in Fig. 2.16. The change in SLP is dominated by a positive trend in the SAM, associated with an intensification of the subpolar westerly winds. In addition, a large-scale increase in SLP has occurred at subtropical latitudes, with changes of up to 1.4 mb centered over Western Australia - of the same sign and of higher magnitude than the SLP anomaly seen during dry years in Fig. 2.3a. The changes in SST during 1980–2004 relative to 1951–1975 show a pronounced warming over the Indian Ocean, with peak magnitude near pole P2, and cooling near pole P3 – that is, temperature trends of the same sign as the characteristic SST anomaly pattern found during dry years (Fig. 2.5a). However, the observed temperature at P1 has warmed as well, so that the P1-P2 dipole is only $\sim$0.3°C more pronounced during 1980–2004 as compared to the pre-1975 period. With greater warming at P2 than at P1, the sense of this SST trend at the P1-P2 dipole should favor drier conditions over SWWA. In summary, there is some evidence that the post-1970 decrease in wintertime SWWA rainfall has been accompanied by a trend toward the dry-year scenario described in this paper. This is consistent with the proposed decadal modulation of the IOD noted by Ashok *et al.* (2004a). However, other factors, such as the documented positive trend in the SAM (e.g., see analysis in Karoly, 2003) and shifts in synoptic systems (Hope *et al.*, 2006), are perhaps also playing a dominant role.

The observed relationship between SWWA rainfall and Indian Ocean winds and SST might be modulated by other phenomena, such as ENSO and the ACW. While we did not establish a direct link between ENSO-related variability and SWWA

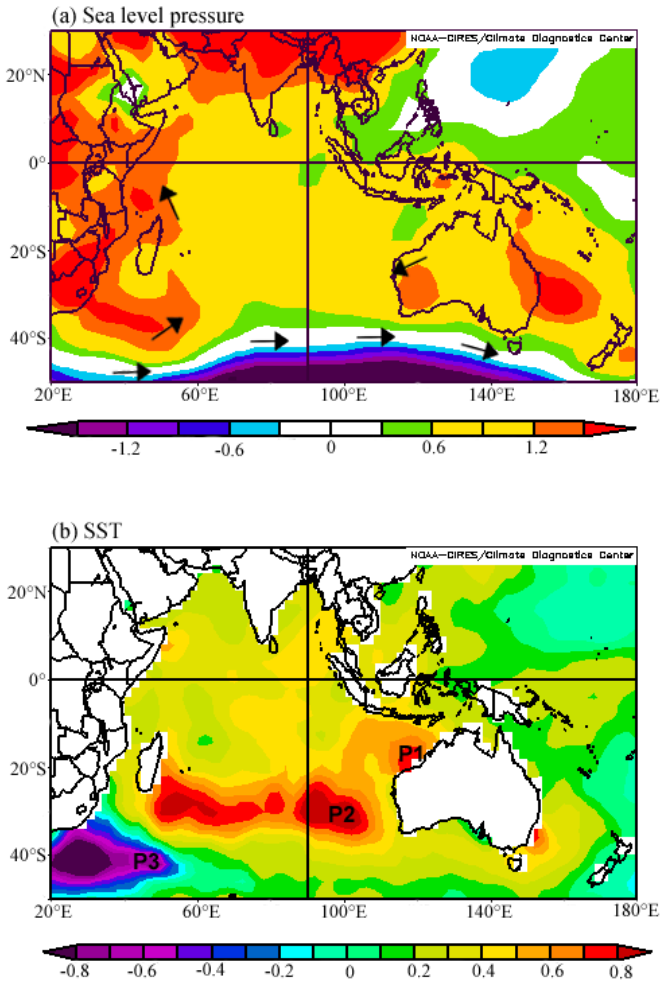

Figure 2.16. Difference in the climatological mean wintertime (JJA) (a) SLP (mb), and (b) SST (°C) during 1980–2004 relative to 1951–1975. Geostrophic wind directions are indicated in (a) and the locations of poles P1–P3 are shown in (b).

precipitation, there are numerous climate teleconnections from the Pacific to Indian Ocean, and so an indirect ENSO influence is quite likely. For example, the Indonesian throughflow is thought to directly influence Indian Ocean variability (Lee *et al.*, 2002; Xie *et al.*, 2002), thereby likely affecting IOD characteristics (Saji and Yamagata, 2003b) as well as the heat content at pole P1. The sensitivity of the Indonesian throughflow to ENSO (Meyers, 1996; Behera *et al.*, 2000; England and Huang, 2005) means that it is likely the climate of the tropical Pacific Ocean will impact on SWWA rainfall via the Indian Ocean connection established in our study. There is anecdotal evidence for this, with several of the dry years coinciding with ENSO years in both the observations and the coupled climate model. However, in both model and observed, the influence of ENSO on SWWA rainfall is much less obvious than the Indian Ocean connection, and quite possibly an artifact of

the IOD-ENSO link. Similarly, Simmonds and Rocha (1991) pointed out that the SST pattern in the Indian Ocean region that Nicholls (1989) linked to Australian rainfall and which is broadly reminiscent of the anomalies described here is largely independent of ENSO.

The suggestion that the ACW impacts on Australian rainfall (White, 2000) was not apparent in this study for the localized SWWA region. In particular, we observed no clear circumpolar propagation of anomalies leading up to anomalous SWWA rainfall years in either the model or reanalysis data. In spite of this, we cannot exclude the possibility that the pressure field across the south Indian Ocean is in some way responding to oscillations associated with the ACW or the SAM. Large-scale changes in extratropical air pressure affect the location and intensity of the subpolar westerlies, which in turn control SST and moisture advection near SWWA. Separating this extratropical forcing from the tropical and subtropical signals described in this paper is difficult as they are ultimately linked via the anticyclonic pressure system over the Indian Ocean. We have shown how interannual rainfall extremes over southwest Western Australia are linked to large-scale ocean-atmosphere variability over the Indian Ocean. Future work should address the formation and evolution of these ocean-atmosphere anomalies with a view to improving predictability of rainfall extremes in the region.

Acknowledgments. Access to historical data from the NCEP/NCAR reanalysis project and its graphical representation was provided by the Climate Diagnostics Center (CDC) at Boulder, Colorado, USA, and obtained via the webpage http://www.cdc.noaa.gov. Observational rainfall data were provided by the Australian Bureau of Meteorology courtesy of Scott Power. We thank Barrie Hunt for access to 1000 yrs of data from a 10,000-year integration of the CSIRO coupled climate model. Chris Reason, Saji Hameed, and two anonymous reviewers provided helpful comments on an earlier draft of the manuscript. This research was supported by the Australian Research Council.

Chapter 3

Anomalous Rainfall over Southwest Western Australia Forced by Indian Ocean Sea Surface Temperatures

Caroline C. Ummenhofer[1], Alexander Sen Gupta[1], Michael J. Pook[2], and Matthew H. England[1]

[1] Climate Change Research Centre, University of New South Wales, Sydney, Australia
[2] CSIRO Marine and Atmospheric Research, Hobart, Tasmania, and Wealth from Oceans National Research Flagship, CSIRO, North Ryde, New South Wales, Australia

Manuscript for: Journal of Climate
Status: revised (accepted)

3.1. Abstract

The potential impact of Indian Ocean sea surface temperature (SST) anomalies in modulating mid-latitude precipitation across southern and western regions of Australia is assessed in a series of atmospheric general circulation model (AGCM) simulations. Two sets of AGCM integrations forced with a seasonally evolving characteristic dipole pattern in Indian Ocean SST consistent with observed "dry-year" (P_{DRY}) and"wet-year" (P_{WET}) signatures are shown to induce precipitation changes across western regions of Australia. Over Western Australia, a significant shift occurs in the winter and annual rainfall frequency with the distribution becoming skewed towards less (more) rainfall for the P_{DRY} (P_{WET}) SST pattern. For southwest Western Australia (SWWA), this shift is due primarily to the large-scale stable precipitation. Convective precipitation actually increases in the P_{DRY} case over SWWA forced by local positive SST anomalies. A mechanism for the large-scale rainfall shifts is proposed, by which the SST anomalies induce a reorganization of the large-scale atmospheric circulation across the Indian Ocean basin. Thickness (1000–500 hPa) anomalies develop in the atmosphere mirroring the sign and position of the underlying SST anomalies. This leads to a weakening (strengthening) of the meridional thickness gradient and the subtropical jet during the austral winter in P_{DRY} (P_{WET}). The subsequent easterly offshore (westerly onshore) anomaly in the thermal wind over southern regions of Australia, along with a decrease (increase) in baroclinicity, result in the lower (higher) levels of large-scale stable precipitation. Variations in the vertical thermal structure of the atmosphere overlying the SST anomalies favor localized increased convective activity in P_{DRY} due to differential temperature lapse rates. In contrast, enhanced widespread ascent of moist air masses associated with frontal movement in P_{WET} accounts for a significant increase in rainfall in that ensemble set.

3.2. Introduction

The seasonal to interannual variability in precipitation in mid-latitudes is generally assumed to be predominantly driven by internal atmospheric dynamics. In contrast to the strong air-sea coupling in the tropics, the ocean's role in forcing extratropical atmospheric variability is often regarded to be of minor importance. Kushnir *et al.* (2002) review the present understanding of the extratropical ocean's role in modulating atmospheric circulation. They find that in addition to a direct thermal response in the atmospheric boundary layer to sea surface temperature (SST) anomalies, there is also evidence for a significant modulation of the large-scale atmospheric circulation. However, relative to the atmosphere's internal variability the ocean-induced changes are small. Nevertheless, a wealth of studies have been inspired by the possibility of utilizing the longer persistence of anomalies in the ocean, which in turn might modulate extratropical atmospheric variability, for improving seasonal to interannual climate forecasts (Kushnir *et al.*, 2002, and references therein). Few of these studies show clear evidence that the extratropical ocean has a major effect on the large-scale atmospheric circulation (e.g., Czaja and Frankignoul, 1999; Rodwell *et al.*, 1999; Sterl and Hazeleger, 2005). Many more studies demonstrate the overriding importance of the atmosphere's internal variability, particularly in controlling precipitation on interannual to seasonal timescales (e.g., Harzallah and Sadourny, 1995; Rowell, 1998; Watterson, 2001). There is general agreement that a marked contrast exists between the tropics, where 60%–80% of climate variability is SST-forced, and the mid-latitudes where only about 20% can be attributed to SST-forcing (Kushnir *et al.*, 2002). In this study, we present evidence for regional mid-latitude precipitation being significantly affected by extratropical SST on seasonal to interannual timescales in an atmospheric general circulation model (AGCM). This study is motivated by previous observational and model work by England *et al.* (2006) who find that precipitation over southwest Western Australia (SWWA) can be linked to a recurring SST dipole pattern in the Indian Ocean.

The first proposed link between Australian rainfall variability and SST was made by Priestley and Troup (1966) and further explored by Streten (1981, 1983). Nicholls (1989) describes a gradient in SST between the Indonesian region and the central Indian Ocean highly correlated with winter rainfall extending from the northwest to the southeast of Australia. However, he cautioned against assuming a causality, i.e. that the SST pattern was *forcing* the rainfall changes. To determine whether SST anomalies could be regarded as the *cause* of rainfall variations, Voice and Hunt (1984) carried out AGCM experiments where the atmosphere was forced by SST

anomalies similar to those found by Streten (1981, 1983). However, they find conflicting results, especially in southern regions of Australia. In contrast, in AGCM experiments with idealized positive SST anomalies to the north of Australia by Simmonds (1990), warm anomalies to the northwest of Australia result in increased precipitation over much of the country. In further experiments, by introducing an additional cold SST anomaly to the southwest of Australia south of the warm anomalies Simmonds and Rocha (1991) strengthen the rainfall response over Australia. The induced SST anomalies in the AGCM experiments impact on Australian rainfall via changes in the atmospheric circulation, rather than directly via the warmer ocean temperatures (Simmonds *et al.*, 1992). Frederiksen *et al.* (1999) use multidecadal AGCM simulations forced with observed global SST to split the rainfall variance over Australia into components due to SST forcing and due to internal variability. In their experiments, the SST forcing seems to be most influential over the tropical northern part of the country. Ansell *et al.* (2000b) find that observed rainfall in southern regions of Australia has a stronger link with variations in mean sea level pressure (MSLP) than with Indian Ocean SST. However, Frederiksen and Balgovind (1994) use an enhanced SST gradient reminiscent of the one described by Nicholls (1989) in AGCM simulations and record increased frequency of northwest cloud bands and associated winter rainfall over an area extending from the northwest to the southeast of the country. For similar regions over Australia, Ashok *et al.* (2003a) link positive Indian Ocean Dipole (IOD) events with a reduction in winter rainfall due to a baroclinic response in the atmosphere resulting in anomalous subsidence. Applying an enhanced meridional SST gradient in the eastern Indian Ocean, Frederiksen and Frederiksen (1996) demonstrate an equatorward shift of storm track instability modes over the Australian region and an increase in the baroclinicity.

For SWWA, Smith *et al.* (2000) find neither Indian Ocean SST nor MSLP to be closely linked with observed interannual rainfall variability (though they propose that both play a role in long-term trends in the region). More recently, England *et al.* (2006) identify a characteristic SST pattern and a reorganization of the large-scale wind field over the Indian Ocean region associated with anomalous rainfall years in SWWA in both observations and a multi-century coupled climate model simulation. They find dry (wet) years in SWWA associated with cold (warm) SST anomalies in the eastern Indian Ocean off the northwest shelf of Australia and warm (cold) anomalies in the subtropical Indian Ocean. Concurrently an acceleration (deceleration) of the anticyclonic basin-wide wind field exists with anomalous offshore (onshore) moisture advection over SWWA. However, it could not be determined if the SST anomalies played a role in forcing the SWWA rainfall anomalies, or were just symptomatic of the changed wind field. In this latter case, the wind field

changes would be the primary cause of both the precipitation and SST anomalies (for SST, air-sea heat flux anomalies would also play a role). The goal of this study is to address the question of whether the SST patterns described by England *et al.* (2006) are capable of driving SWWA precipitation anomalies using an ensemble set of AGCM simulations.

SWWA is characterized by a Mediterranean-type climate dominated by wet winters and dry summers (Drosdowsky, 1993a). During summer, the influence of the subtropical high-pressure belt dominates over this region. The axis of the subtropical ridge moves equatorward in autumn and is located near the northern boundary of SWWA (approximately 30°S) during the winter months (Gentilli, 1972). As a consequence, moist westerly winds prevail over SWWA from late autumn into spring. Rainfall associated with the maritime westerlies is enhanced by topography and by the regular passage of cold fronts and associated depressions (e.g., Gentilli, 1972; Wright, 1974; IOCI, 2001). There is a general decrease in rainfall rate from south to north over the SWWA region, but rainfall increases slightly from west to east across the coastal plain, before declining steadily inland of the Darling Scarp (Wright, 1974).

SWWA and its surrounds maintain a considerable proportion of Australia's agricultural production, which is heavily dependent on the winter rainfall. Since the 1970s, a dramatic decrease of about 20% has occurred in autumn and early-winter rainfall. This is associated with an even bigger (about 40%) drop in stream inflow into dams (IOCI, 2001). The rainfall decline in SWWA, which is the topic of many observational and modeling studies, has been linked to changes in large-scale MSLP (Allan and Haylock, 1993; IOCI, 2001; Li *et al.*, 2005a), shifts in synoptic systems (Hope *et al.*, 2006), changes in baroclinicity (Frederiksen and Frederiksen, 2005b, 2007), the Southern Annular Mode (Li *et al.*, 2005b; Cai and Cowan, 2006; Li, 2007), land cover changes (Pitman *et al.*, 2004; Timbal and Arblaster, 2006), and anthropogenic forcing (Cai and Cowan, 2006; Timbal *et al.*, 2006), amongst others, with a combination of several factors most likely playing a role. In light of these exacerbated conditions and the need for difficult water management decisions, a better understanding of seasonal to interannual rainfall variability in the region is imperative. This is particularly the case as traditional Australian predictors for rainfall variability such as the Southern Oscillation Index have very limited skill over SWWA (Smith *et al.*, 2000; IOCI, 2001). Improvements in seasonal rainfall forecasting, as provided potentially by the greater persistence of oceanic versus atmospheric precursors, could therefore prove valuable.

The existence of Indian Ocean precursors for seasonal forecasting of Australian climate has been proposed in previous studies. Ashok *et al.* (2003a) suggest that

links between the IOD and anomalous rainfall in affected regions could help improve predictions in those areas. To improve seasonal forecasts for better agricultural management in a southeastern Australian cropping region, McIntosh *et al.* (2007) incorporate information on the combined states of the IOD and El Niño-Southern Oscillation (ENSO). The only skillful forecast application of the ENSO-IOD configuration they found is in the transition from an El Niño with positive IOD phase (e.g., in 2006), which gives approximately 90% likelihood of moving to a more favorable rainfall pattern over southeastern Australia in the following year (Peter McIntosh 2007, personal communication). In a coupled general circulation model simulation, Watterson (2001) finds that the wind anomalies driving rainfall variability over Australia are not associated with any long-term oceanic precursor. Accordingly, he argues, little predictability can be gained from SST-rainfall relationships, as rainfall in Australia is, excepting associations with ENSO, not forced by SST (Watterson, 2001). In this study, we will show using AGCM simulations that Indian Ocean SST anomalies can indeed give rise to changed thermal properties in the atmosphere, modulating the large-scale atmospheric circulation, and thus ultimately causing precipitation changes on seasonal to interannual timescales. AGCM simulations forced by SST anomalies representative of a dry-case (wet-case) scenario for SWWA allows us to identify causative links which might not be possible using correlation analyses alone.

The remainder of the paper is structured as follows: In Section 3.3, the reanalysis data and the climate model are described, as is the experimental setup and the statistical techniques for analyzing the model output. Section 3.4 provides an assessment of the suitability of the model for the present study. Section 3.5 describes the seasonal evolution of SST anomalies used in the perturbation experiments. The induced changes in precipitation in the experiments are presented in Section 3.6. In Section 3.7, changes in thermal properties of the atmosphere and circulation anomalies forced by the perturbations are described, and a mechanism is proposed explaining the shifts in the rainfall distribution. Section 3.8 summarizes the findings.

3.3. Data and data analysis

3.3.1. Reanalysis data

To assess the model's suitability for the present study, long-term mean fields in the model are compared to observations across the region for sea level pressure (SLP), surface winds, atmospheric thickness, and precipitation. Data from the European Centre for Medium-Range Weather Forecasting (ECMWF) 40-year reanalysis (ERA-40) at a 2.5° latitude/longitude resolution is used for monthly SLP and sur-

face wind fields for the period 1960–2001 (Uppala *et al.*, 2005). The performance of the ECMWF operational forecasts over the Indian Ocean region is assessed by Nagarajan and Aiyyer (2004). The thickness data for 1000–500 hPa and total and convective precipitation are taken from the National Center for Environmental Prediction (NCEP) and National Center for Atmospheric Research (NCAR) reanalysis (NNR; Kalnay *et al.*, 1996; Kistler *et al.*, 2001) for the same period 1960–2001. The large-scale monthly precipitation data is taken from the Climate Prediction Center Merged Analysis of Precipitation (CMAP; Xie and Arkin, 1996) climatology at a 2.5° latitude/longitude resolution for the period 1979–2001. It combines several diverse data sets, including gauge-based analyses from the Global Precipitation Climatology Center, predictions by the operational forecast model of ECMWF, and three types of satellite estimates. Across the Australian continent, precipitation observations are based on the gridded SILO data produced by the Australian Bureau of Meteorology with 0.5° latitude/longitude resolution described in detail by Jeffrey *et al.* (2001).

3.3.2. Climate model

The climate model used for our experiments is the NCAR Community Climate System Model, version 3 (CCSM3), run in uncoupled atmosphere-only mode. The atmospheric component of CCSM3, the Community Atmosphere Model (CAM3), uses a spectral dynamical core, a T42 horizontal resolution (approximately 2.8° latitude/longitude), and 26 vertical levels. The CCSM3 model, its components, and configurations are described in Collins *et al.* (2006), with more CAM3 specific details described in Hurrell *et al.* (2006). Several studies assess the model's performance and suitability for applications in climate research relevant for the present study, in particular in regard to the representation of the hydrological cycle (Hack *et al.*, 2006), tropical Pacific climate variability (Deser *et al.*, 2006), ENSO variability (Zelle *et al.*, 2005), and monsoon regimes (Meehl *et al.*, 2006). Several biases in the model have been documented: most notably associated with tropical Pacific climate, i.e. the Intertropical Convergence Zone (ITCZ), South Pacific Convergence Zone (SPCZ; e.g., Zhang and Wang, 2006), and ENSO spatial and temporal variability (e.g., Deser *et al.*, 2006). These issues will be revisited and assessed in the context of this study in Section 3.4.

3.3.3. Experimental setup

The perturbation experiments were conducted using the NCAR CCSM3 run with the monthly SST climatology after Hurrell *et al.* (2006), which is based on Reynolds

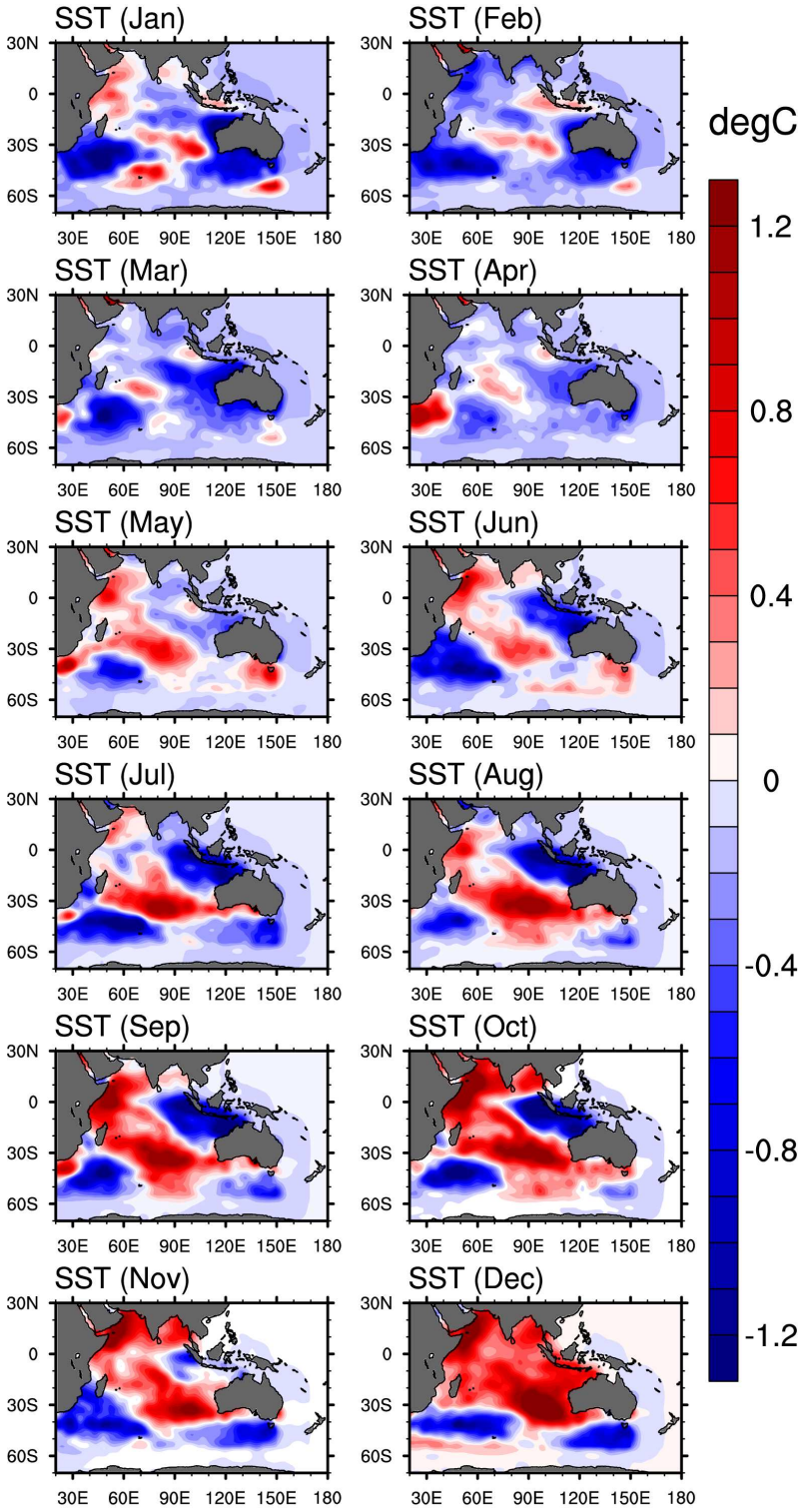

Figure 3.1. Monthly SST anomaly (in °C) superimposed as a perturbation on the climatological SST in the dry-year case (P_{DRY}). Perturbation values outside the Indian Ocean domain are set to zero, i.e. forcing in those regions simply follows the climatological SST.

SST (Smith and Reynolds, 2003, 2004) and Hadley Centre anomalies (Rayner *et al.*, 2003). An 80 year integration forced by the 12-month climatology was taken as the control experiment (CNTRL). Two sets of perturbation experiments were carried out where anomalous SST patterns were superimposed onto the climatology. These perturbations were derived from composites of observed average monthly SST anomalies for years defined as being extremely dry/wet over SWWA (30°–35°S, 115°–120°E) by England *et al.* (2006), i.e. exceeding ±1 standard deviation in their rainfall time-series. Due to the expectation that the resultant atmospheric response would be small compared to the natural variability, the anomalies of England *et al.* (2006) were scaled by a factor of 3. Scaling the composite SST pattern by this factor more closely represents the magnitude of SST anomalies encountered during any particular extreme year (for details, see Section 3.5). The seasonal evolution of the SST anomalies thus derived for the perturbed dry-year case (P_{DRY}) is shown as an example in Fig. 3.1. No perturbations are applied outside the Indian Ocean domain, i.e. the magnitude of the SST anomalies is zero there, as seen in Fig. 3.1. Though not an exact mirror image of P_{DRY}, anomalies for the wet-year case (P_{WET}; figure not shown) demonstrate the same general features of the opposite polarity. Perturbation runs were started from a variety of years spanning the control run and integrated from the start of January for one year. The ensemble set consisted of 60 positive and 60 negative one-year integrations.

3.3.4. Data analysis and statistical methods

For the purposes of our analysis, two regions are defined over which climate variables are averaged. The first represents the southwest corner of the state of Western Australia (SWWA), delimited by lines of latitude and longitude at 30°S, 35°S, 115°E, and 120 °E (as indicated in Fig. 3.3c). This limited region contains 11x11 observational and 3x3 model grid boxes. A second region more broadly representative of the subtropical area of Western Australia (WA) is delimited by lines of latitude and longitude at 21°–35°S, 115°–130°E (this larger area contains 6x6 model grid points; see Fig. 3.3d). The tropical north of WA is excluded for the analysis, as it is characterized by a very different rainfall regime dominated by summer monsoons.

The nonparametric Mann-Whitney rank test is used to determine the significance level at which the rainfall frequency distribution in a particular region (SWWA and WA) in the perturbed cases differs from the control (von Storch and Zwiers, 1999). Throughout the study, we use a two-tailed t-test to determine the significance of the spatial anomaly fields. This test estimates the statistical significance at which the anomalies in P_{DRY} and P_{WET} are distinguishable from the CNTRL at each grid point.

3.4. Model validation and assessment

3.4.1. Atmospheric circulation

To assess the suitability of the model for the present study, the mean annual and seasonal state of key atmospheric variables across the Indian Ocean region is compared between observations and the model. Annual SLP, surface winds, and thickness are shown in Fig. 3.2. Seasonal long-term means of these variables were also evaluated and generally demonstrated good qualitative agreement with observations (figures not shown).

The long-term annual mean SLP field in the model captures the overall Southern Hemisphere patterns with a distinct meridional SLP gradient (Fig. 3.2a, b). However, the pattern is overly zonally symmetric (across all seasons) in mid-latitudes compared to the observations (Sen Gupta and England, 2006), resulting in an exaggerated meridional SLP gradient (Hurrell *et al.*, 2006). The seasonal cycle in the movement of the subtropical high pressure belt and the circumpolar trough agrees well with observations, though the latter is too deep and positioned too far equatorward in winter (Hurrell *et al.*, 2006). The overall pattern of subtropical easterlies and mid-latitude westerlies at the surface across the Indian Ocean region is captured in the model (Fig. 3.2c, d). However, as before the zonal component in the model is slightly overestimated with a positive bias in the mid-latitude westerlies for the latitude band 35°–60°S compared to the observations, especially south of Australia and toward New Zealand (Hurrell *et al.*, 2006) and an overly strong easterly wind field across the central Indian Ocean, over northern parts of Australia and extending eastward. In the subtropical easterlies this is especially apparent in the winter half of the year (figure not shown). The meridional wind field in the model closely matches observations (Fig. 3.2e, f), with only a slightly enhanced northerly (southerly) component in the latitude band 40°–60°S (along eastern Africa). The observed seasonal cycle of strengthening southerly winds across much of the Indian Ocean during the winter months is also well represented in the model (figure not shown). The meridional gradient in thickness is captured very well by the model and the differences to the observations are small (Fig. 3.2g, h).

Several biases in the model have been documented previously: most notably a spurious second ITCZ south of the equator in the Pacific and hence a poor simulation of the SPCZ (Zhang and Wang, 2006). This is a problem common to many atmospheric general circulation models (Meehl and Arblaster, 1998; Hurrell *et al.*, 2006). The positive bias in the tropical Pacific rainfall in both branches of the ITCZ signifies an overly vigorous hydrological cycle there (Collins *et al.*, 2006). The double ITCZ problem has been linked to a bias in SST in the equatorial Pacific region

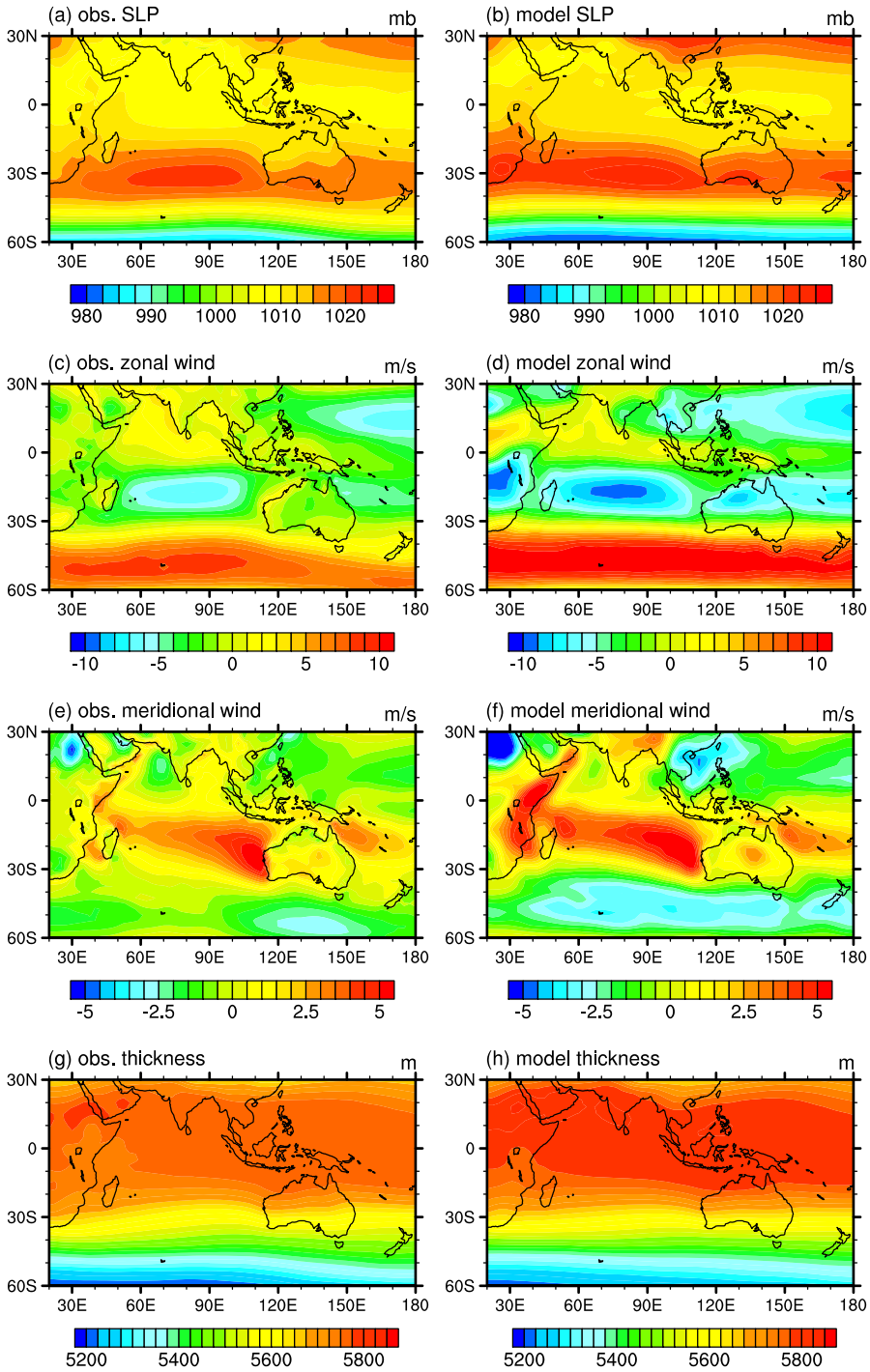

Figure 3.2. Annual long-term mean of (a, b) SLP (in mb), (c, d) zonal and (e, f) meridional wind (in m s^{-1}), and (g, h) thickness (in m for 1000–500 hPa) fields with observed (model) on the left (right). The long-term mean in the observations is based on ERA-40 (thickness on NCEP/NCAR reanalysis) data for the period 1960–2001, the model fields on the 80-year control run.

(Arblaster *et al.*, 2002; Zhang and Wang, 2006). This relates to the spatial pattern of ENSO in the coupled model extending too far west in the Pacific Ocean and being too narrowly confined to the equator (Deser *et al.*, 2006). In the atmosphere-only mode, these biases are less pronounced and Deser *et al.* (2006) speculate that they contribute to the ENSO frequency in the coupled mode being too high (2–2.5 years; e.g., Collins *et al.*, 2006; Deser *et al.*, 2006) relative to observed frequencies (3–8 years; e.g., Collins *et al.*, 2006; Kiehl and Gent, 2004; Zelle *et al.*, 2005). So, for the scope of the present study and considering our focus on Indian Ocean variability, the general structure and variability in the tropical Pacific is sufficiently well captured by the model.

3.4.2. Precipitation

In Fig. 3.3, the model precipitation across the Indian Ocean basin is compared to observed estimates based on CMAP data (Xie and Arkin, 1996). As climatologies of observed rainfall differ considerably on regional and local scales, differences to the model should be taken as qualitative only (Hurrell *et al.*, 2006). The model represents broad patterns of annual mean precipitation across the Indian Ocean basin well, with increased rainfall in the tropics and lower rainfall in the region of the subtropical high pressure belt across the eastern Indian Ocean and over Australia, as well as Africa (Fig. 3.3a, b). However, the model shows excessive rainfall over the Indonesian Archipelago and the Bay of Bengal compared to observations, as the tropical maximum remains north of the equator throughout the year (Hurrell *et al.*, 2006). In contrast, the high rainfall region in the central equatorial Indian Ocean receives too little rainfall. The latter discrepancy is associated with the simulation of a double ITCZ, i.e. the persistence of ITCZ-like precipitation north of the equator throughout the year (Hack *et al.*, 2006), a problem common to many general circulation models (e.g., Meehl and Arblaster, 1998; Hurrell *et al.*, 2006; Zhang and Wang, 2006; Zhang *et al.*, 2007). The low-rainfall region in the eastern subtropical Indian Ocean is too dry in the model to the west of Australia, while south of 40°S the model is too wet across the entire Indian Ocean basin compared to the observations, related to a positive bias poleward of the extratropical storm tracks (Hack *et al.*, 2006). Meehl *et al.* (2006) assess the seasonally varying rainfall associated with monsoonal regimes across the tropical Indian Ocean in CCSM3 in detail. They find the major monsoonal wind features and associated precipitation maxima to be well simulated in the model. Future work will explore impacts of the characteristic SST pattern used in this study on precipitation across the wider Indian Ocean region.

Across Australia (Fig. 3.3c, d) the overall rainfall distribution, with wetter coastal

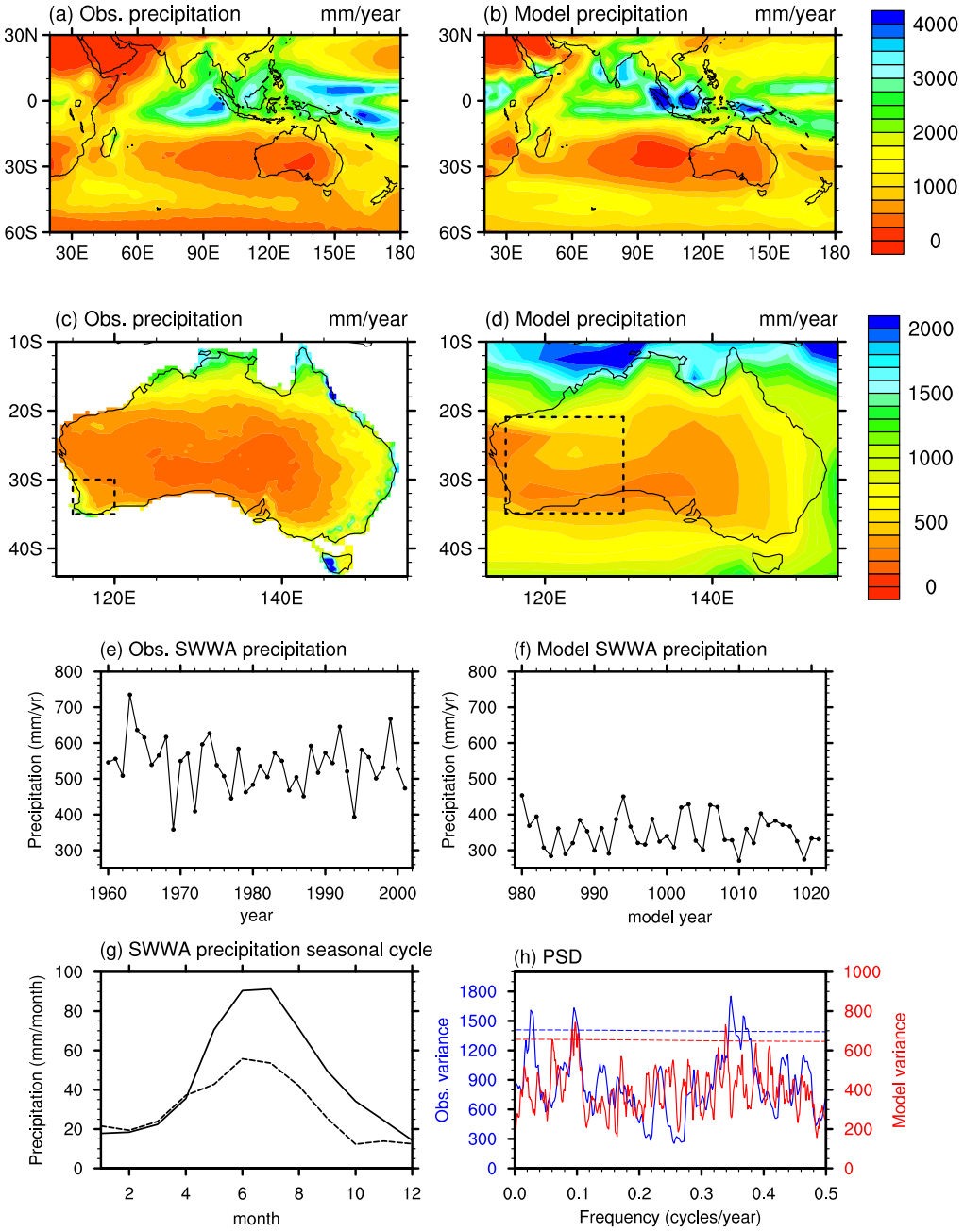

Figure 3.3. Annual long-term mean of (a–d) rainfall (in mm yr^{-1}) fields across the Indian Ocean basin (a, b) and magnified over the Australian continent (c, d) with observed (model) on the left (right). The long-term mean in the observations in (a) is based on CMAP data for the period 1979–2001, in (c) on the SILO data for 1960–2001, and in (b, d) on the model fields from the 80-year control run, though for ease of comparison between observed and model, only the first 40 years of the control are shown). The dashed box in (c) indicates the area used to derive the observed and model SWWA precipitation time-series shown as annual values in (e, f). The dashed box in (d) depicts the area termed WA. (g) presents the long-term seasonal cycle in precipitation for the observed (solid) and model (dashed). The power spectral density in (h) shows the observed (model) variance for the dominant cycles in blue (red), with the dashed lines indicating a 95% confidence level according to white noise.

regions especially along the northern and eastern coastline, and a very dry interior, is simulated well, although the contrast is weaker than observed. In particular, the increased rainfall in the tropical north extends too far inland, as can be seen in Fig. 6b of Meehl *et al.* (2006). Notwithstanding these shortcomings, the seasonal cycle with the associated precipitation regimes across the Australian continent (i.e. winter rainfall in the south, summer monsoonal rainfall in the north) compare very favorably with observations (figure not shown). Despite a few regional rainfall deficiencies in the model, useful inferences can still be made regarding mechanisms for change in the simulations.

The time-series for SWWA rainfall in the observations and the model (Fig. 3.3e, f) were derived for the region outlined by the boxes in Fig. 3.3c, d (for details also see Section 2.4). The SWWA region records on average 540 mm yr^{-1} in the observations, while only 360 mm yr^{-1} are received in the model. The lower rainfall in the model is characteristic of climate models, considering its coarser resolution relative to the observations. The standard deviation of 74 mm yr^{-1} in the observations compares with 48 mm yr^{-1} in the model. However, a more appropriate metric of variability, the coefficient of variation (i.e. ratio of standard deviation and mean), demonstrates good agreement with 0.137 and 0.133 for observations and model, respectively. This indicates a comparable variability in SWWA rainfall on interannual timescales between observations and CAM3.

In line with the modeled annual mean precipitation, the amplitude of the seasonal cycle in the total precipitation is reduced over a large part of the year (May–November) in the model relative to the observations (Fig. 3.3g). However, the phase of the seasonal cycle with the majority of the rainfall falling in May–September is well reproduced. Model precipitation is given as the combination of stable large-scale and convective components. While the SILO data set does not distinguish these components, they are available as part of the NNR and compared to the model components (figure not shown). For both model and reanalysis, the contribution of large-scale precipitation is considerably less than that due to convection. In the reanalysis, convective rainfall occurs predominantly in winter (April–October), while it is more evenly distributed across the year in the model due to overestimated summer levels. The model large-scale precipitation in contrast is slightly higher than the reanalyzed throughout the year, though it reproduces the reanalyzed seasonal cycle of enhanced rainfall during April–August. Overall, the model has a higher proportion of total rainfall due to large-scale precipitation. Further investigation into the parametrization of precipitation in the model for convective and large-scale rainfall, and a detailed comparison with the NNR is beyond the scope of this study. As broad features of the relative contribution of the two components and their sea-

sonal cycle agree between model and reanalysis, it seems reasonable to assume that the model is sufficiently realistic in terms of SWWA precipitation to be a useful tool to investigate precipitation characteristics. This is further suggested by a spectral analysis of SWWA rainfall showing coincident peaks in model and observed time-series (Fig. 3.3h; peaks at 2–3 and 10 years are significant at the 95% confidence level).

3.5. Seasonal evolution of the SST perturbation

The SST anomalies used in the perturbation experiments are based on characteristic observed SST patterns identified by England *et al.* (2006). The monthly varying SST anomalies averaged across their anomalous dry years in SWWA are shown in Fig. 3.1. They form the basis for the P_{DRY} run. England *et al.* (2006) found a characteristic tripole pattern in Indian Ocean SST (for specific location of the poles see Fig. 5 in England *et al.*, 2006), consisting of one pole off the shelf to the northwest of Australia extending northwestwards to Sumatra (named P1; centered near 15°S, 120°E), a second pole of opposite polarity in the central subtropical Indian Ocean (P2; near 30°S, 100°E), and a third pole of the same sign as P1 to the southeast of Madagascar (P3; near 40°S, 50°E). In the remainder of the paper we will refer to those poles as P1, P2, and P3. This pattern gradually forms over the course of the year becoming most prominent in late winter/early spring. Though not yet fully formed, the cold SST anomalies at P1 appear as early as January. In contrast, the warm anomalies at P2 are briefly revealed during January and February, but then weaken again until in May when they re-emerge and become a persistent feature. The anomalies in all three poles intensify until October. From November onwards, anomalies in P1 decline, while the warm SST of P2 extends northwards and covers the entire Indian Ocean north of 30°S by December. The seasonal evolution of the SST perturbation during P_{WET} shows a similar spatial and temporal development to P_{DRY}, with SST anomalies of opposite polarity (figure not shown).

It is of interest to compare the seasonal evolution of the pattern and magnitude of the composite SST anomalies used in the P_{DRY} simulation (Fig. 3.1) with the SST anomalies in a particular dry year in SWWA, namely 2006. The SWWA growing season (May to October) in 2006 was the driest ever recorded for many of the agricultural areas in Western Australia (DAFWA, 2006). The SST anomalies of that specific dry year were not incorporated into the P_{DRY} forcing field, as only extreme years prior to 2003 were included in the England *et al.* (2006) composites. The seasonal evolution of SST anomalies in 2006 (Fig. 3.4) broadly matches those in Fig. 3.1, both spatially and temporally, and in magnitude. In 2006, the SST

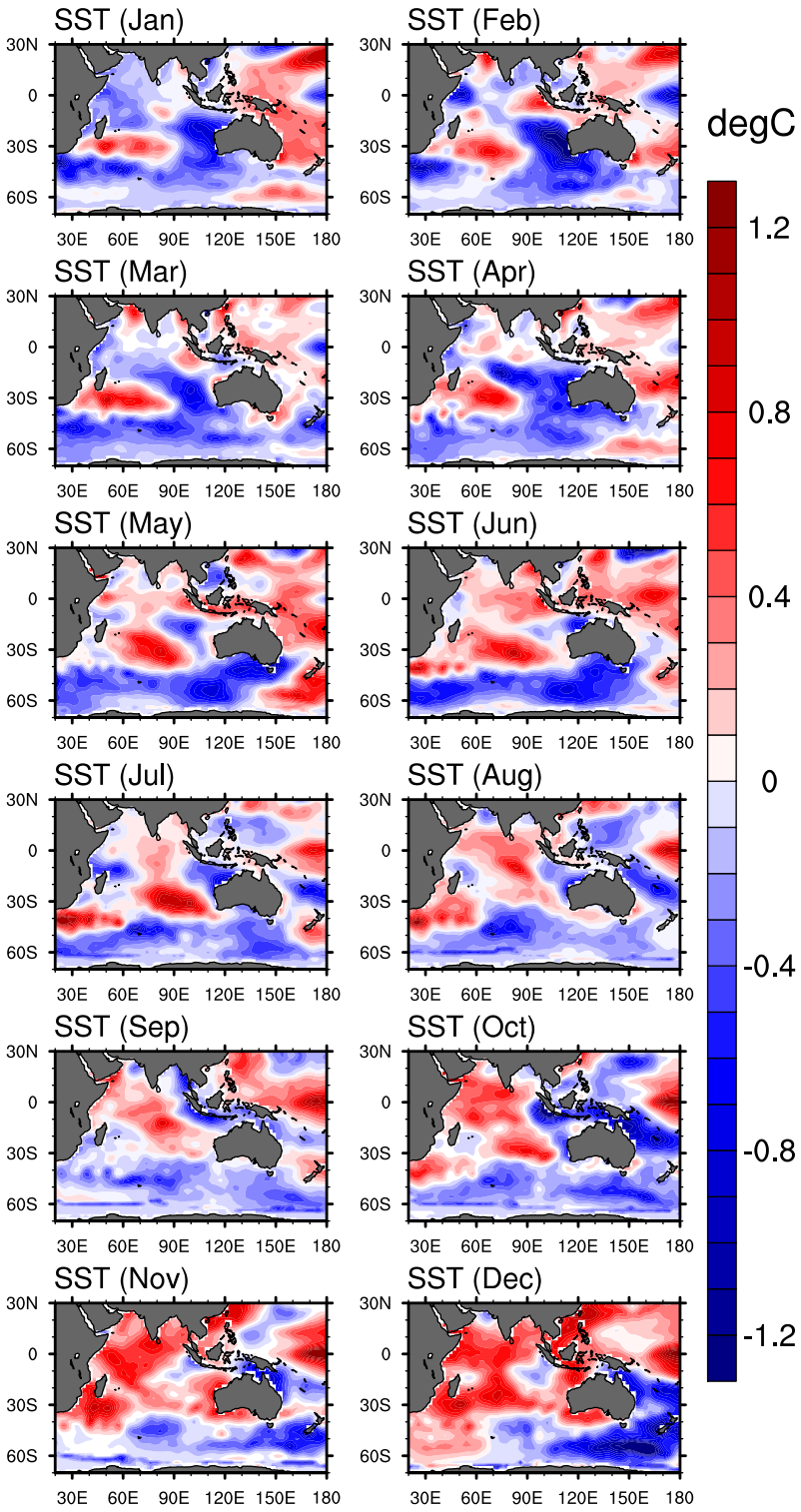

Figure 3.4. Observed monthly SST anomaly (in °C) during 2006, which was a dry year in SWWA.

anomalies at P1 and P2 intensified over the course of the year reaching maximum values of up to ±1°C in winter/early spring, which is of comparable magnitude to the perturbations in the same months (up to ±1.2°C). The close match between the composite SST anomalies used as forcing and the 2006 SST anomalies demonstrates that the forcing is not of an unrealistically large magnitude. The use of the composite pattern for the forcing, rather than the pattern of a single year, allows more general inferences about other anomalous dry/wet years to be made. Similarly in 2005, a year with above-average precipitation across SWWA, the monthly SST anomalies across the Indian Ocean closely mirror the P_{WET} SST pattern (figures not shown), both temporally and spatially, and with anomalies of comparable magnitude. This provides some limited evidence that the SST perturbations we apply represent a recurring SST pattern over the Indian Ocean. Correlation of the SWWA rainfall and Indian Ocean SST also reveals a qualitatively similar pattern with the three poles apparent (figure not shown). An empirical orthogonal function analysis of observed Indian Ocean SST (not shown) confirms this, with the second mode (the first mode represents the warming of the Indian Ocean) explaining 16% of the total variance in SST (Santoso, 2005). This is of the same order of magnitude as the SST variance accounted for by the IOD (12%; Saji *et al.*, 1999). The identification of the effects of this pattern on regional climate conditions is therefore of considerable importance.

As pointed out by England *et al.* (2006), the location and evolution of the poles in Indian Ocean SST shown here (Fig. 3.1, 3.4) are distinct from previous definitions of characteristic SST patterns, some of which have been linked to Australian rainfall. However, some similarities with previous SST patterns exist both in the tropics and subtropics of the Indian Ocean. The evolution of P1 in P_{DRY} is similar to the eastern pole of the tropical IOD shown by Saji *et al.* (1999) in their Fig. 2, especially in the second half of the year. The subtropical Indian Ocean Dipole (SIOD) of Behera and Yamagata (2001) in their Fig. 4 is displaced to the west relative to our poles, with their warm SST anomalies located over the western edge of P2 and overlapping P3, and their cold pole to the west of P1 and less clearly defined. In addition, their SIOD SST anomalies reach their maximum earlier in the year (around February/March) compared to July–October in this study. The broad features of SST anomalies associated with the first rotated principal component of Australian annual precipitation in Fig. 3 in Nicholls (1989) broadly agree with our P_{DRY} perturbation pattern (Fig. 3.1), though most closely during the August–October period. In light of the distinctiveness of our SST patterns from previous studies, both spatially and temporally, and their link to SWWA rainfall (England *et al.*, 2006), it is of interest to explore the precipitation anomalies across western

regions of Australia induced by these SST perturbations in an AGCM.

3.6. Precipitation changes

3.6.1. SWWA

We first assess the impact of the changed SST fields in the perturbation experiments on the rainfall distribution in the more limited SWWA region (Fig. 3.3c). The model rainfall distributions over SWWA across the ensemble members in P_{DRY} and P_{WET} relative to CNTRL are shown in Fig. 3.5 and 3.6, summed over different months. The model separates large-scale and convective precipitation providing a first indication of likely causes in any shift in the rainfall distribution (based on all months) between P_{DRY} and P_{WET}. The large-scale annual rainfall distribution is shifted towards low (high) rainfall amounts for P_{DRY} (P_{WET}) relative to the CNTRL, both significant at the 99% confidence level (Fig. 3.5a, b). This is especially apparent at the upper end of the rainfall distribution for years receiving in excess of 150 mm yr^{-1}: while in the CNTRL case 8% of the years receive 150–170 mm yr^{-1}, none of the years in P_{DRY} record more than 150 mm yr^{-1}, but in 25% of the years in P_{WET} this threshold is passed (annual rainfall of 150–170 mm yr^{-1} occurring in 13% of the years, 70–190 mm yr^{-1} in 7%, and 190–210 mm yr^{-1} in 5%). When focusing on the main rainfall season for SWWA, the period May–September during which 70% of the annual rainfall occurs, the same trends are observed: namely, a significant reduction (increase) is seen in the number of ensemble members receiving in excess of 100 mm of rainfall during May–September for the P_{DRY} (P_{WET}) case (Fig. 3.5c, d). For austral winter (June–August; Fig. 3.5e, f), only 5% of winters in the P_{DRY} case receive more than 65 mm, while this occurs in 9% of winters in the CNTRL and 32% in the P_{WET} case. Overall, a consistent shift in the large-scale annual and seasonal rainfall distribution is observed, with the upper end of the distribution losing (gaining) a disproportionate number of events for the dry (wet) cases.

The frequency distribution for convective rainfall over SWWA shows less consistent shifts (Fig. 3.6), with an apparent asymmetry between P_{DRY} and P_{WET}. An increase in the number of years with high convective precipitation is observed for the P_{DRY} case (Fig. 3.6a, c, e). This trend is significant at the 99% confidence level for the period January–December, May–September, and June–August. In contrast, the convective rainfall distribution for P_{WET} does not differ significantly from the CNTRL. A mechanism explaining this asymmetry whereby the P_{DRY} forcing actually induces an *increase* in convective rainfall will be proposed in Section 3.7.

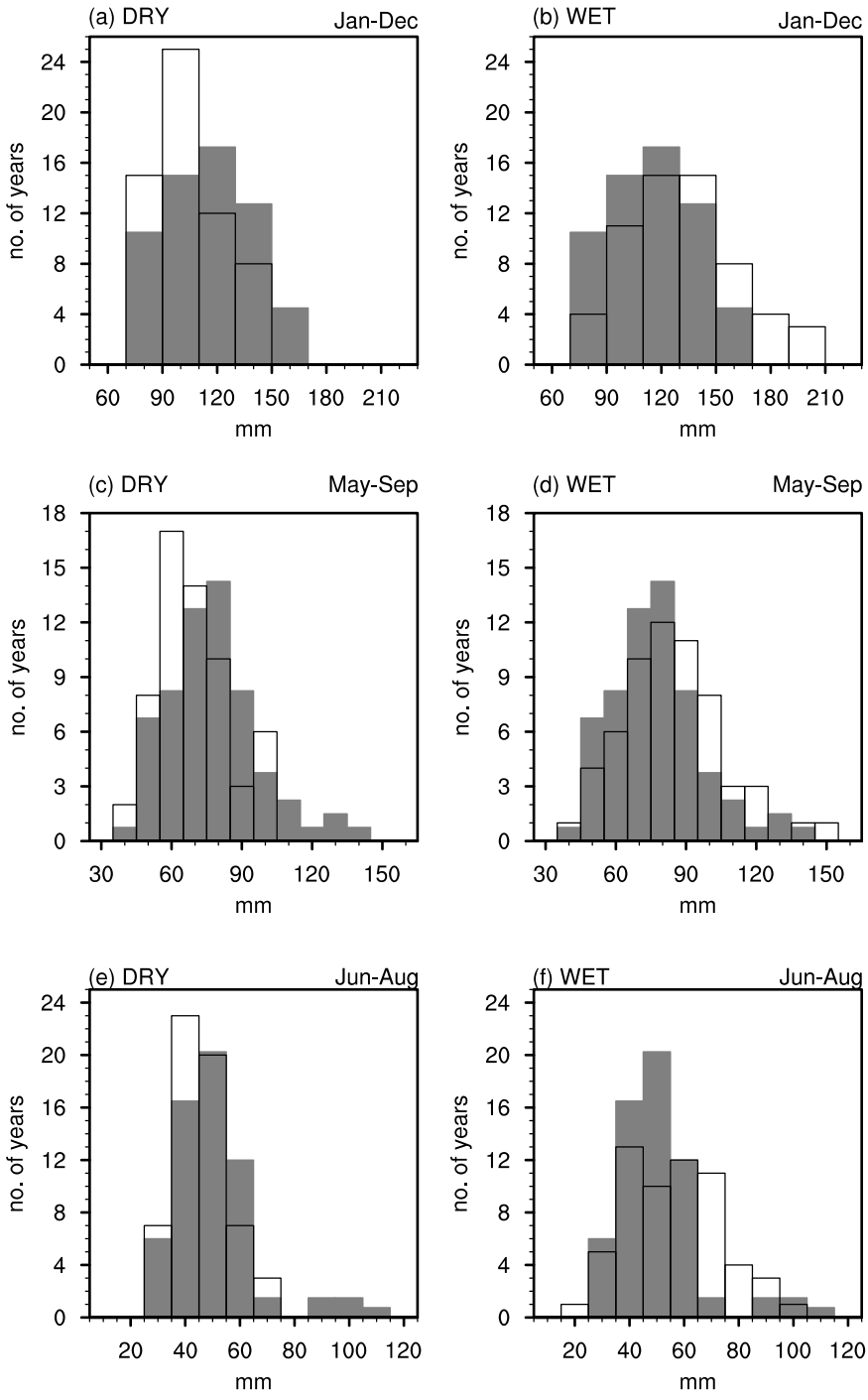

Figure 3.5. Frequency distribution of large-scale rainfall spatially averaged across SWWA: rainfall amount (in mm) summed for the months Jan.–Dec. (top), May–Sep. (middle), and June–Aug. (bottom) for P_{DRY} (left) and P_{WET} (right) cases. The shaded gray rainfall distribution represents the CNTRL (normalized to the number of ensemble members in P_{DRY}/P_{WET}), while P_{DRY} and P_{WET} are indicated with black outlines. The following significance levels hold, as determined by a Mann-Whitney test: (a) 99%, (b) 99%, (c) 99%, (d) 95%, (e) 90%, (f) 95%.

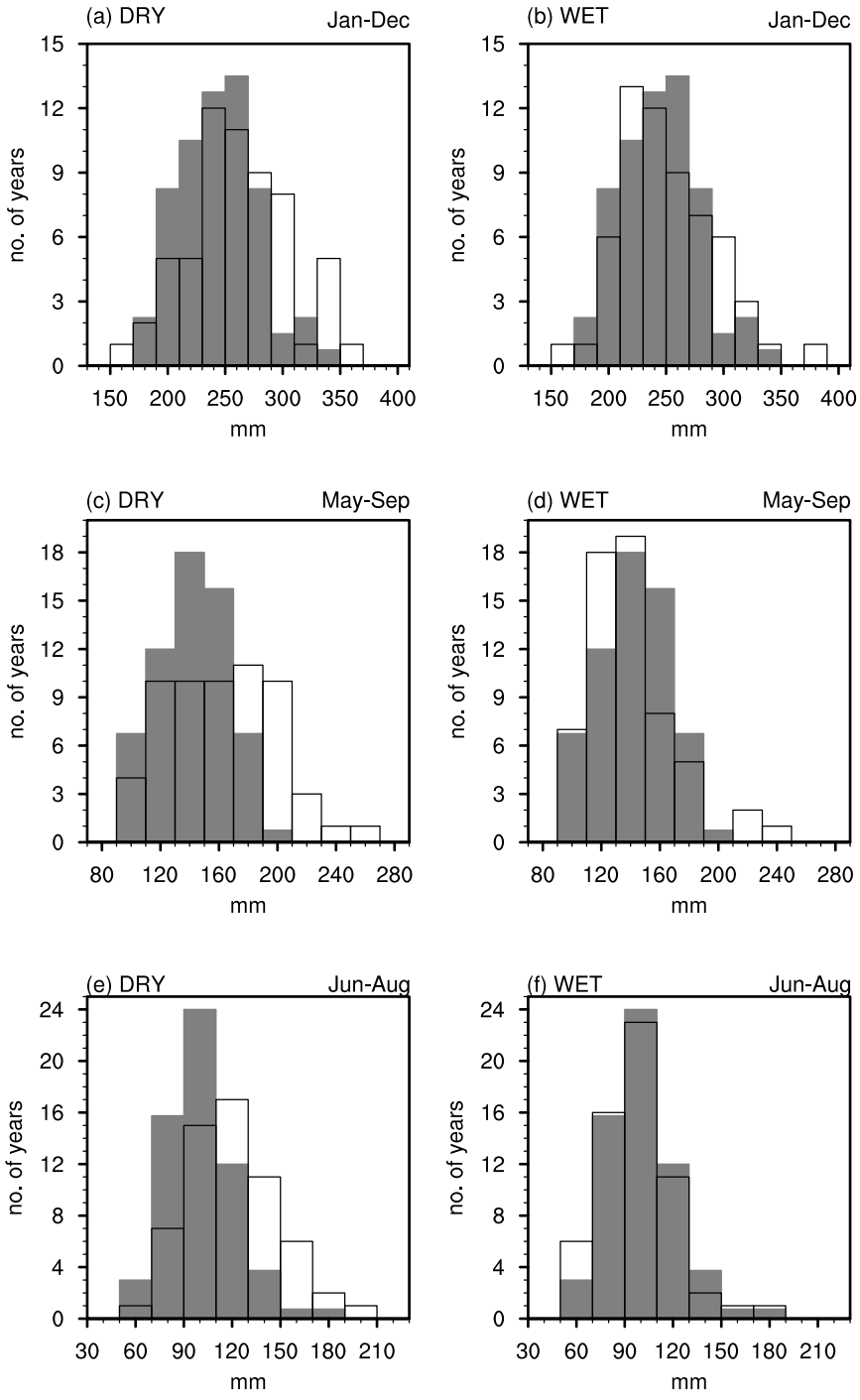

Figure 3.6. Frequency distribution of convective rainfall spatially averaged across SWWA: rainfall amount (in mm) summed for the months Jan.–Dec. (top), May–Sep. (middle), and June–Aug.(bottom) for P_{DRY} (left) and P_{WET} (right) cases. The shaded gray rainfall distribution represents the CNTRL (normalized to the number of ensemble members in P_{DRY}/P_{WET}), while P_{DRY} and P_{WET} are indicated with black outlines. The following significance levels hold, as determined by a Mann-Whitney test (if nothing indicated, below 80%): (a) 99%, (c) 99%, (d) 80%, (e) 99%.

3.6.2. Western Australia

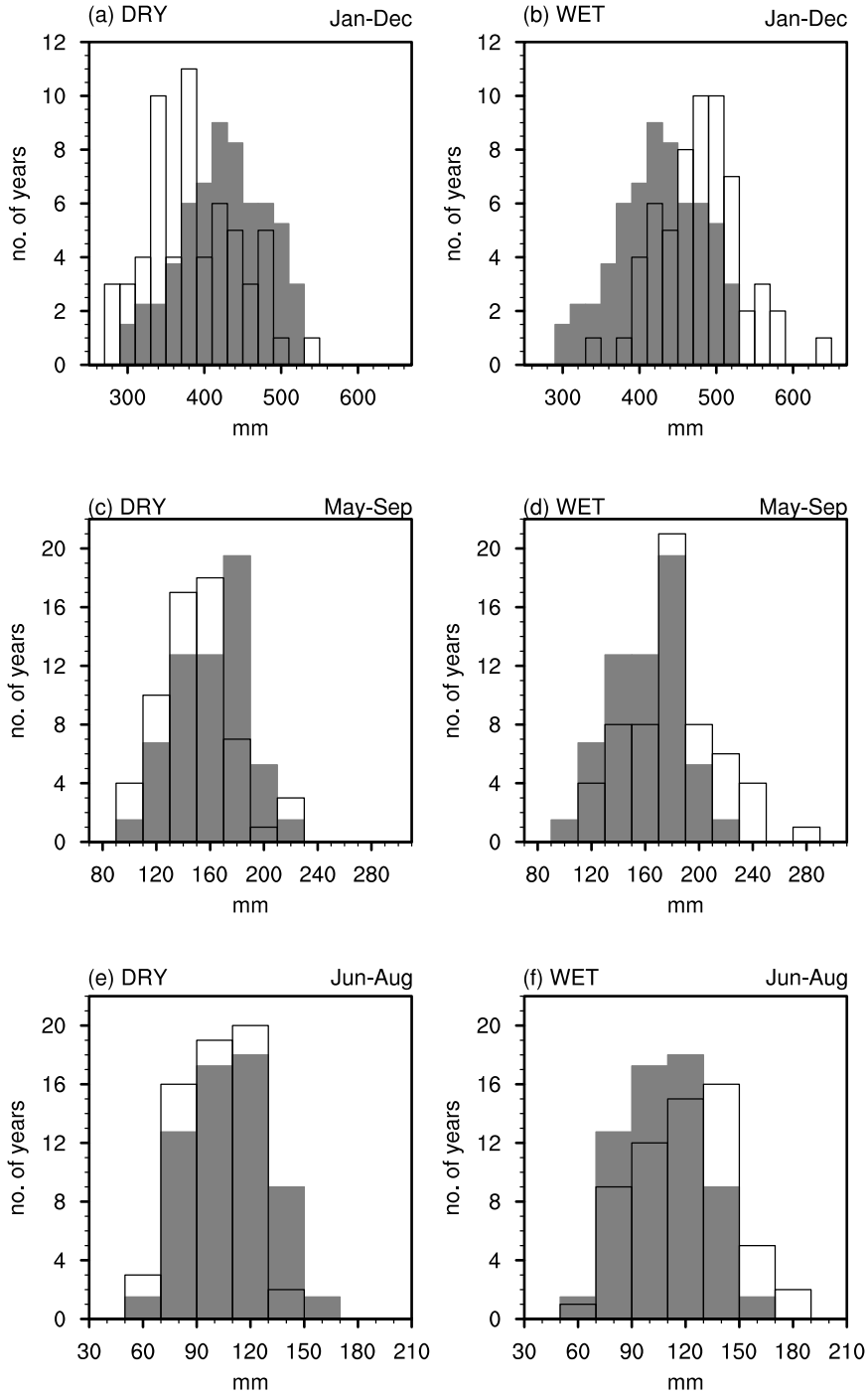

Figure 3.7. Frequency distribution of total rainfall spatially averaged across WA: rainfall amount (in mm) summed for the months Jan.–Dec. (top), May–Sep. (middle), and June–Aug. (bottom) for P_{DRY} (left) and P_{WET} (right) cases. The shaded gray rainfall distribution represents the CNTRL (normalized to the number of ensemble members in P_{DRY}/P_{WET}), while P_{DRY} and P_{WET} are indicated with black outlines. The following significance levels hold, as determined by a Mann-Whitney test: (a) 99%, (b) 99%, (c) 95%, (d) 99%, (e) 90%, (f) 99%.

We focus now on a larger area across WA excluding the tropical north of the state (see Fig. 3.3d). For this larger region, shifts in rainfall distribution are evident for both the large-scale and convective precipitation and are of the same sign. Fig. 3.7 presents the frequency distribution of total rainfall for WA. Now, the entire frequency distribution pattern for the annual total rainfall is clearly shifted towards lower (higher) rainfall amounts in the P_{DRY} (P_{WET}) case relative to the CNTRL (significant at the 99% confidence level; Fig. 3.7a, b). The shifts for the May–September and June–August are less prominent, though still significant as indicated (Fig. 3.7c–f). This can be attributed to the fact that as we extend the investigated area farther inland, we move from a region with predominant winter precipitation towards a more uniform distribution throughout the year. This means that the prominent shifts in annual rainfall distribution (Fig. 3.7a, b) are accumulated over the whole year. Furthermore, the opposing trends in convective and large-scale precipitation seen in SWWA are not apparent for the larger region WA. This relates most likely to the fact that with increasing distance inland, the impact of the warm SST at P2 giving rise to localized convective upward motion and enhanced convective rainfall in SWWA during P_{DRY} is averaged away. The asymmetry in the convective rainfall over SWWA, not seen in the analysis for WA, will be investigated in more detail in Section 3.7, when the atmospheric dynamics leading to the changed rainfall distribution are explored.

3.6.3. Seasonal variability

The seasonal cycle in SWWA and WA rainfall in the perturbed cases is further investigated for the different rainfall types. The total monthly large-scale rainfall over each region is presented in Fig. 3.8, showing a notable reduction (increase) in P_{DRY} (P_{WET}). In contrast, when including convective events, the total rainfall (figure not shown) in P_{DRY} shows an intensification of the seasonal cycle with enhanced winter precipitation (May–August) and a reduction in autumn, relative to the CNTRL. This amplification of the seasonal cycle in P_{DRY} can be attributed to the positive (negative) changes in the convective winter (autumn) rainfall, while the annual cycle in large-scale rainfall remains unchanged. In contrast, P_{WET} is characterized by slightly wetter conditions in both rainfall types throughout the year, particularly in summer and autumn. So, in the P_{DRY} case, a further enhancement of the predominant winter precipitation occurs, driven largely by an increase in convective rainfall, while the amplitude of the seasonal cycle in P_{WET} rainfall is reduced. As above, the seasonal cycle of SWWA large-scale precipitation in the perturbed cases overall follows the CNTRL (Fig. 3.8a), though with a notable reduction (increase) in P_{DRY} (P_{WET}). For WA, although the seasonal cycle for large-scale precipitation

also remains unchanged in the perturbed cases relative to the CNTRL, the rainfall amounts in each month deviate considerably more from the CNTRL than for the smaller region of SWWA. That is, in all months prior to November the large-scale precipitation in P_{DRY} (P_{WET}) consistently lies below (above) the CNTRL fields (Fig. 3.8b).

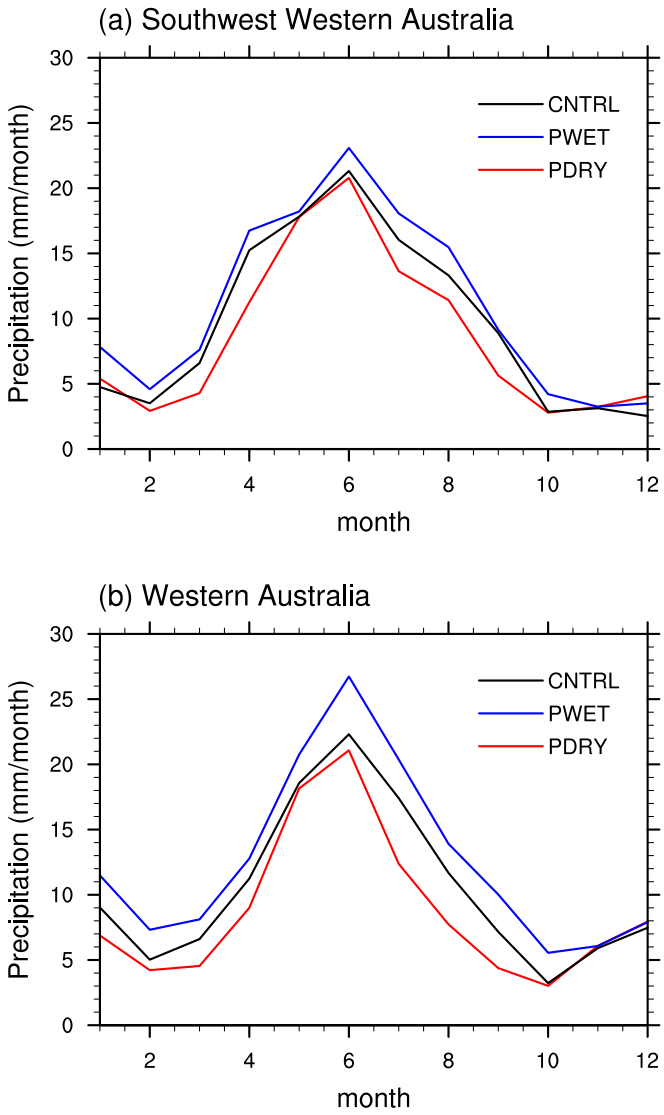

Figure 3.8. Long-term seasonal cycle in model large-scale precipitation in the CNTRL (black), P_{DRY} (red), and P_{WET} (blue) runs over (a) SWWA and (b) WA.

3.7. Mechanisms and atmospheric dynamics

To understand the mechanism responsible for the observed local and regional rainfall changes we now investigate large-scale atmospheric anomalies. Both thermal properties and circulation characteristics are explored across the Indian Ocean and

adjacent land masses during the dry and wet ensemble of experiments.

3.7.1. Thermal anomalies in the atmosphere

The seasonal thickness anomalies in Fig. 3.9 provide a measure of the thermal properties in the lower atmosphere and resultant atmospheric flow. The seasonal evolution of the P_{DRY} thickness anomalies (Fig. 3.9a, c, e) follows the evolution of the underlying SST anomalies (Fig. 3.1). In concert with the cold SST anomalies, negative thickness anomalies occur over the eastern Indian Ocean, south of Australia, and across parts of Australia during the first three months of the year. Warm SST anomalies in the central subtropical Indian Ocean start establishing the characteristic dipole pattern (P1 and P2) from May onwards (Fig. 3.9; although individual months are not shown). This is followed by the formation of a positive thickness anomaly extending from the central subtropical Indian Ocean across southern regions of Australia, including SWWA, from July onwards. During the winter months until October, the pattern of negative, positive, and negative thickness anomalies across the Indian Ocean (extending from northeast towards southwest), reflects the sign and positions of P1, P2, and P3 in SST anomalies, respectively. The combination of the three poles leads to an easterly anomaly in the thermal wind across the SWWA region. This would lead to a weakening of the subtropical jet which normally reaches peak strength during the winter months, resulting in weaker interactions with low pressure disturbances and cold fronts moving through the region. This could account for the reduction in large-scale rainfall during P_{DRY} and is particularly prominent during the winter months (Fig. 3.5c, e). The positive thickness anomaly over SWWA persists until October.

The development of the thickness anomalies during P_{WET} over the eastern Indian Ocean and Australia (Fig. 3.9b, d, f) is, on a broad scale, the reversal of the P_{DRY} evolution. Positive thickness anomalies dominate until April across the Indian Ocean region and Australia. Simultaneous with a strengthening of the P_{WET} SST dipole structure in May (figure not shown), warm thickness anomalies strengthen over the P1 location to the northwest of Australia. At the same time, cold thickness anomalies develop in the subtropical Indian Ocean off the coast of SWWA. The meridional gradient in thickness between the tropics (P1) and subtropics (P2) further intensifies over the following months. This represents an intensification of the underlying seasonal cycle. The intersecting line between positive and negative anomalies to the north and south, respectively, passes through SWWA, extending towards the southeast. It moves further north in September, with negative anomalies covering all southern regions of Australia.

The monthly thickness anomalies in both P_{DRY} and P_{WET} show the greatest re-

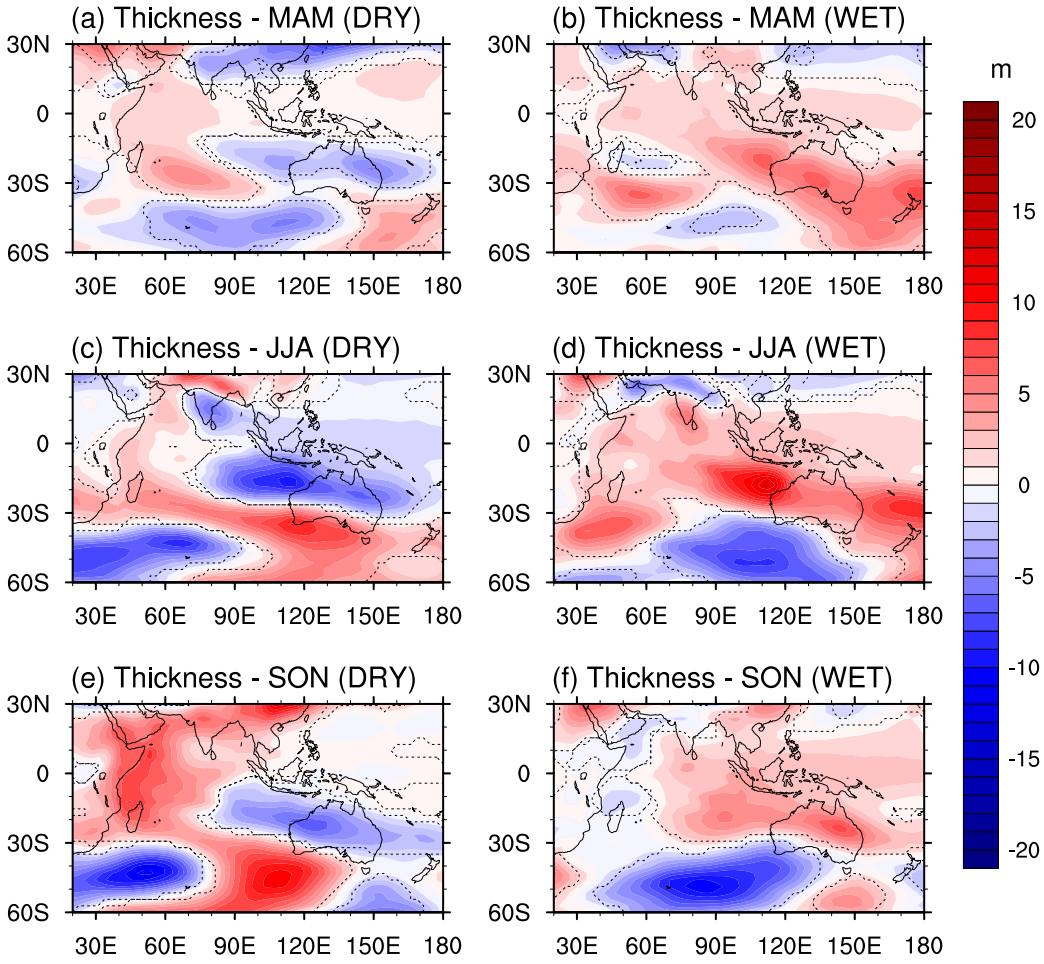

Figure 3.9. Average seasonal thickness (in m for 1000–500 hPa) anomaly for (left) P_{DRY} and (right) P_{WET}, relative to the CNTRL for the (a, b) MAM, (c, d) JJA, and (e, f) SON seasons. Dashed lines indicate significant anomalies at the 90% confidence level as estimated by a two-tailed t-test.

sponse in the May–September period when the majority (close to 75%) of the annual SWWA precipitation falls. Hence, for the remainder of this study, we will focus on the May–September months. The thermal structure through the atmosphere arising from the SST perturbations is shown in cross-sections at 32°S in Fig. 3.10 averaged over the May–September period. The characteristic structure of cold (warm) SST anomalies at P1, warm (cold) at P2, and cold (warm) at P3 for P_{DRY} (P_{WET}) is apparent (Fig. 3.10a, b). The location of the cross-section at 32°S is indicated by the black line in Fig. 3.10a, b and directly traverses the center of P2, while also showing some influences of P3. The warm temperature anomalies at P2 in P_{DRY} penetrate to a height of more than 4 km (Fig. 3.10c), with the maximum increases in temperature below 2 km (about 800 hPa). In contrast, the cold anomalies at P2 in P_{WET} only reach to a height of 2 km and are capped by warm anomalies aloft (Fig.

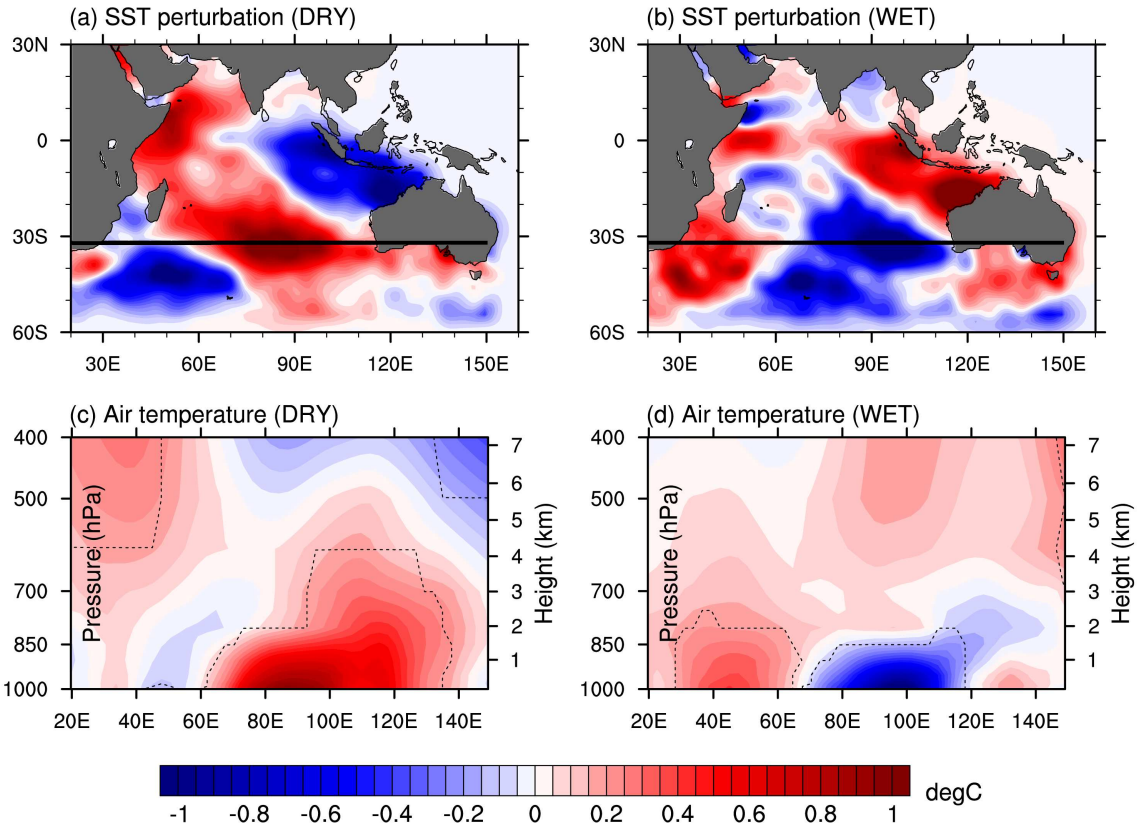

Figure 3.10. (a, b) SST perturbation and (c, d) cross-section of air temperature anomalies for the P_{DRY} (left) and P_{WET} (right) case averaged over the May–September period (all in °C). The 32°S location of the cross-section in (c, d) is marked by black lines in (a, b). Dashed lines in (c, d) indicate significant anomalies at the 90% confidence level as estimated by a two-tailed t-test.

3.10d). This asymmetry seems reasonable, as warm surface anomalies will produce a more unstable air column that has the ability to mix the warm air higher into the atmosphere than the cold anomalies. This may explain the increase in convective rainfall over SWWA seen in P_{DRY} (Fig. 3.6c), but not in P_{WET} (Fig. 3.6d), as the convective activity in the former would be stronger likely due to the enhanced temperature lapse rate through a deep atmospheric column. By way of contrast, the thermal structure in Fig. 3.10d seems more favorable for episodes of slow widespread ascent and associated rain, as warm moist air is forced to move southwards over the cold SST anomaly by an eastward moving trough. The asymmetry may additionally affect circulation anomalies arising from changes in the thermal properties of the atmosphere. This is investigated below.

3.7.2. Circulation anomalies in the atmosphere

Circulation anomalies in the atmosphere are shown in Fig. 3.11 for horizontal winds at 500 hPa and vertical velocity at 700 hPa during the May–September period for P_{DRY} and P_{WET}, respectively. Broadly speaking, anomalies in the horizontal winds relate to changes in the large-scale stable precipitation, while vertical velocity anomalies mostly are associated with convective rainfall. During P_{DRY}, there is a weakening of the anticyclonic circulation over the Indian Ocean basin (Fig. 3.11a). This is especially apparent in a reduction in the easterly wind field over the eastern Indian Ocean at 10°–20°S. Over southern regions of Australia, easterly anomalies occur as well, resulting in anomalous offshore flow over SWWA. In contrast during P_{WET}, enhanced onshore flow and westerly anomalies dominate over the Australian continent south of 20°S (Fig. 3.11b). The weakened (strengthened) onshore wind anomalies are consistent with the sign and position of the reduced (enhanced) gradient in thickness resulting from the underlying cold (warm) SST anomalies at P1 and warm (cold) anomalies at P2 during P_{DRY} (P_{WET}). The surface horizontal circulation anomalies induced by the SST perturbations in this study (figure not shown) closely mirror anomalous surface winds associated with dry/wet SWWA rainfall years in observations (England *et al.*, 2006).

Significant anomalies in vertical velocity (Fig. 3.11c, d) are mainly confined to the tropics, being positive (negative) over the equatorial eastern Indian Ocean and parts of the Indonesian Archipelago during P_{DRY} (P_{WET}). This reduction (enhancement) in rising motion over the equatorial Indian Ocean during P_{DRY} (P_{WET}) is located above the underlying cold (warm) SST anomalies at P1. Significant vertical velocity anomalies over the P2 pole occur in the P_{DRY} case only. This indicates a reduction in subsidence off the SWWA coast (Fig. 3.11c). Again, this helps to explain the significant increase in convective rainfall over SWWA for P_{DRY} (Fig. 3.6c), but not for P_{WET} (Fig. 3.6d).

A further indication of stability in the atmosphere is provided by the Eady growth rate, a measure of the baroclinic instability in the atmosphere. The Eady growth rate was calculated according to Paciorek *et al.* (2002), using the vertical gradient in horizontal wind speed and the Brunt-Väisälla frequency as a measure of static stability. It provides an indication of the development of low pressure systems (Risbey *et al.*, 2007), which are associated with increased rainfall. Mean states of the Eady growth rate in the model during winter (figure not shown) compare well with observations (e.g., Fig. 5 in Risbey *et al.*, 2007). During the May–September period in P_{DRY}, negative anomalies in Eady growth rate extending across southern regions of Australia indicate a reduction in baroclinicity and hence a lower formation rate of

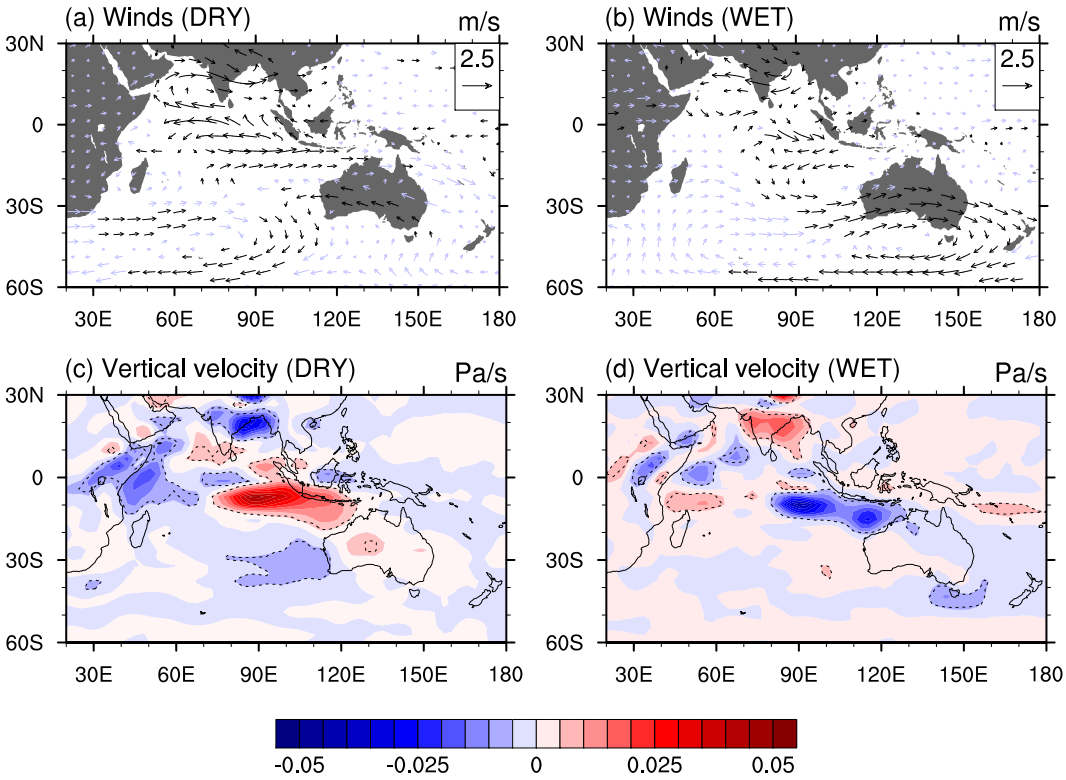

Figure 3.11. Anomalies of (a, b) winds at 500 hPa (in m s^{-1}) and (c, d) vertical velocity at 700 hPa (in Pa s^{-1}) for the P_{DRY} (left) and P_{WET} (right) case averaged over the May–September period (positive, being downwards). Black vectors in (a, b) and dashed lines in (c, d) indicate significant anomalies at the 90% confidence level as estimated by a two-tailed t-test.

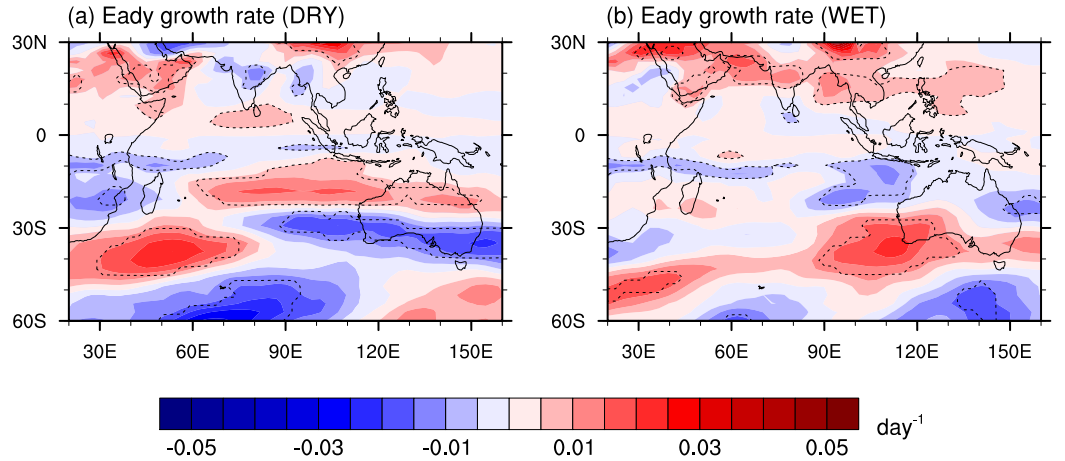

Figure 3.12. Anomalies of Eady growth rate (in day^{-1}) for the (a) P_{DRY} and (b) P_{WET} case averaged over the May–September period. Dashed lines indicate significant anomalies at the 90% confidence level as estimated by a two-tailed t-test. Positive (negative) values indicate an increase (decrease) in baroclinicity and development of more (less) instabilities.

instabilities (Fig. 3.12a). An increase in instabilities is seen over northern regions of Australia and the eastern Indian Ocean over the latitude band 10°–20°S, coinciding with the westerly wind anomalies there (Fig. 3.11a). The positive anomalies in Eady growth rate during P_{WET} are centered over SWWA and the adjacent Indian Ocean region, representing a local enhancement of baroclinicity with increased instabilities just offshore of SWWA (Fig. 3.12b). The location of the increased baroclinicity over the P2 cold SST anomalies during P_{WET} hints at their role in forcing the increased large-scale rainfall recorded over SWWA. In contrast, reduced instability is observed overlying the P1 region off the northwest shelf of Australia. Under an enhanced SST gradient in the eastern Indian Ocean reminiscent of the P_{WET} forcing, Frederiksen and Frederiksen (1996) find increased baroclinicity and an equatorward shift of storm track instability modes over southern regions of Australia. This is consistent with the results presented here.

3.8. Summary and conclusions

In this study we have used AGCM simulations to assess the way Indian Ocean SST anomalies modulate mid-latitude precipitation across southern and western regions of Australia. This represents an extension of previous work by England *et al.* (2006) who find extremes in SWWA rainfall associated with characteristic SST patterns and a reorganization in the large-scale atmospheric circulation across the Indian Ocean. Here, we have presented evidence that these composite SST patterns significantly affect SWWA and WA precipitation in ensemble sets of AGCM simulations. We have also proposed a mechanism for the observed rainfall shifts due to changes in the large-scale general circulation.

Good agreement between the model mean fields and reanalysis data on annual and seasonal timescales indicates that the model represents the general atmospheric circulation across the Indian Ocean region suitably well. Over the Australian continent, the seasonal rainfall distribution associated with the monsoons in the north in summer and winter rainfall in the south of the country are well captured, though some regional biases exist (e.g., Meehl *et al.*, 2006). Over the study region of SWWA, interannual variability and the seasonal cycle of the observed and model rainfall is comparable, although the long-term means in the model are lower than observed. Despite certain biases in the model regarding tropical Pacific climate (e.g., Zhang and Wang, 2006; Deser *et al.*, 2006) and a slight enhancement of zonal flow at mid-latitudes (Sen Gupta and England, 2006; Hurrell *et al.*, 2006) the model performs sufficiently well over the Indian Ocean and Australian region to justify its use in the present study.

The monthly-varying Indian Ocean SST composite patterns used as perturbations in the AGCM simulations appear to represent a realistic and recurring SST pattern (Santoso, 2005). This is also evidenced by the close match in the spatial and temporal evolution of the dry-year SST perturbation (Fig. 3.1) and the SST anomalies during 2006 - not included in the composite fields (Fig. 3.4). The characteristic dipole pattern, which is distinct in location and temporal evolution from previous definitions of dipoles in the Indian Ocean (e.g., Saji *et al.*, 1999; Behera and Yamagata, 2001), develops with cold (warm) SST anomalies in the eastern Indian Ocean over the northwest shelf of Australia (P1) and warm (cold) anomalies in the central subtropical Indian Ocean (P2) during dry (wet) years in SWWA, reaching maximum values in late winter/early spring (Fig. 3.1).

Significant changes occur in the distribution of SWWA and WA precipitation in the perturbation experiments with the modified SST patterns (P_{DRY} and P_{WET}). In particular:

1. A consistent shift in winter and annual large-scale stable precipitation over SWWA is recorded, with the upper end of the distribution losing (gaining) a disproportionate number of events in P_{DRY} (P_{WET}).

2. An apparent asymmetry is seen in the response of winter and annual *convective* precipitation in SWWA, with an increase in P_{DRY} convective rainfall, while no significant changes are apparent in P_{WET}.

3. For WA, a shift of the entire rainfall distribution towards the low (high) end of the distribution is observed for P_{DRY} (P_{WET}), for both convective and large-scale precipitation.

To understand the mechanism(s) responsible for these rainfall changes, we investigated anomalies in thermal properties of the atmosphere and in the general circulation. Thickness anomalies of the same sign and position as the underlying SST anomalies at P1 and P2 develop in the perturbation experiments, intensifying towards late winter and extending across southern regions of Australia (Fig. 3.9). This leads to a weakening (intensification) of the meridional thickness gradient and the subtropical jet during the winter in P_{DRY} (P_{WET}), with a coincident easterly (westerly) anomaly in the thermal wind over southern regions of Australia. The anomalously offshore (onshore) winds over SWWA (Fig. 3.11a, b) could thus contribute to a reduction (increase) in large-scale rainfall. In the observed record, Ansell *et al.* (2000b) similarly associate variations (and trends) in SWWA rainfall with modulations in the subtropical high pressure belt and a shift of the circumpolar trough. However in their study, links with Indian and Pacific Ocean SST are

weak compared to the variability of the large-scale atmospheric circulation, while we demonstrate that the reorganization in the general atmospheric circulation arises as a *result* of the changed SST fields in the AGCM simulations.

A measure of the baroclinic stability in the atmosphere, and hence its disposition towards the development of rain-bearing low pressure systems, is provided by the Eady growth rate (Paciorek *et al.*, 2002). A reduction (increase) in the Eady growth rate (Fig. 3.12) indicates a lower (higher) formation rate of baroclinic instabilities over southern and western regions of Australia during P_{DRY} (P_{WET}), consistent with the large-scale rainfall changes. Hope *et al.* (2006) also linked trends in baroclinicity and reduced frequency of passing troughs across the region with the observed rainfall decrease in SWWA. Similarly, Frederiksen and Frederiksen (2005b, 2007) suggest that these decreases resulted from changes in the intensity and southward deflection of regions of cyclogenesis due to a decline in mid-latitude baroclinicity. Over the Australian region, they find a 30% decrease in the growth rate of leading Southern Hemisphere cyclogenesis modes associated with a reduction in the vertical mean meridional temperature gradient, and in the peak upper tropospheric jetstream zonal winds at 30°S. Here, we have demonstrated that such changes can be forced by anomalous SST patterns over the Indian Ocean.

The asymmetry in convective precipitation can be related to anomalies in the thermal properties of the atmosphere (Fig. 3.10), with the warm underlying SST at P2 during P_{DRY} penetrating higher into the atmosphere (due to an enhanced temperature lapse rate) than the cold P_{WET} anomalies. The vertical thermal structure in P_{DRY} thus could favor localized increases in convective activity, as seen in the increase in convective rainfall over SWWA and the reduction in large-scale rainfall. On the other hand, both the circulation and thermal anomalies in P_{WET} may enhance widespread ascent of moist air masses associated with frontal movement, as evidenced by increases in large-scale precipitation in that ensemble set.

Considering the significant drop in precipitation in SWWA since the 1970s (e.g., Allan and Haylock, 1993; IOCI, 2001; Timbal *et al.*, 2006) and the projections for its continuation over the coming decades (Cai *et al.*, 2003b; Timbal, 2004; Cai and Cowan, 2006; Hope, 2006), it is of interest to relate our findings on interannual rainfall variations in SWWA to long-term trends. Recent changes in the large-scale Southern Hemisphere general circulation have been described in several studies. These include trends in the SAM towards its high-index phase (e.g., Li *et al.*, 2005b; Cai and Cowan, 2006; Hendon *et al.*, 2007), a consistent poleward shift in the zones of strong baroclinicity (Yin, 2005), reductions in the density of low pressure systems (Smith *et al.*, 2000), shifts in the subtropical jet (Frederiksen and Frederiksen, 2005a), reduced intensity of cyclogenesis (Frederiksen and Frederiksen, 2005b,

2007), amongst others. In this study, we have identified mechanisms by which these factors, driven by SST, modulate precipitation, both at a regional scale for SWWA and over interannual timescales. It is thus possible that the ocean plays a vital role in driving these atmospheric circulation changes that have led to longer-term trends in SWWA rainfall, especially as recent Indian Ocean SST trends favor a tendency toward the P_{DRY} thermal gradient (England *et al.*, 2006). This is supported by other studies. For example Smith *et al.* (2000) suggest that long-term SWWA rainfall variability is influenced by coupled air-sea interactions across the South Indian Ocean linking SST and MSLP. Frederiksen and Balgovind (1994) demonstrated a connection between the frequency of northwest cloud bands and Indian Ocean SST gradients.

In summary, we have presented evidence that Indian Ocean SST is indeed instrumental in *forcing* mid-latitude rainfall changes over regions of southern and western Australia. The characteristic SST pattern we investigate is thus not simply symptomatic of the changed wind field, but could also play an important role in modulating the atmospheric circulation and rainfall anomalies. These findings are in contrast with some previous work on mid-latitude rainfall in general (Kushnir *et al.*, 2002, and references therein) and for the Australian region in particular (Watterson, 2001, though his experiments do not employ a scaled SST forcing). We do not dispute the main hypothesis of Watterson (2001) that interannual variations in seasonal rainfall are primarily driven by internal atmospheric mechanisms. However, this does not rule out the possibility of significant modulation by Indian Ocean SST forcing. Indeed Watterson (2001) refers to other GCM studies that find a proportion of the rainfall variance being explained by SST variability. Our results suggest a modest, yet significant, change in the frequency distribution for rainfall (i.e. the extreme events) due to SST anomalies, which is not necessarily captured by a total rainfall metric. It still remains an open question as to what initially drives the formation of the characteristic SST anomaly pattern (e.g., internal ocean dynamics, ocean-atmosphere coupling), but this is beyond the scope of the present study and will be explored elsewhere. In a separate study, we will further investigate the implications of the present findings on improving predictability of SWWA rainfall. Considering the longer persistence of temperature anomalies in the ocean, as opposed to the higher-frequency variability in the atmosphere, we are hopeful that the mechanism presented here can help improve seasonal rainfall predictions, and thus ultimately aid in water management decisions in SWWA. In addition, the relative influence of the individual SST poles and the lead-time of predictability warrant further investigation; these will be explored separately in a future study.

Acknowledgments. Use of the NCAR's CCSM3 model is gratefully acknowledged. The CMAP precipitation, NNR data, and NOAA_ERSST_V2 SST data was provided by NOAA/OAR/ESRL PSD, Boulder, Colorado, USA, through their website http://www.cdc.noaa.gov, and the ERA-40 data by the ECMWF. The model simulations were run at the Australian Partnership for Advanced Computing National Facility. The manuscript benefitted from helpful discussions with Peter McIntosh and James Risbey, and comments by three anonymous reviewers. CCU was supported by the University of New South Wales under a University International Postgraduate Award, ASG and MHE by the Australian Research Council, and MJP partially by the Managing Climate Variability Program of Land and Water, Australia, and the CSIRO Wealth from Oceans National Research Flagship.

Chapter 4

Contributions of Indian Ocean Sea Surface Temperatures to Enhanced East African Rainfall

Caroline C. Ummenhofer[1], Alexander Sen Gupta[1], Matthew H. England[1], and Chris C. J. Reason[2]

[1] Climate Change Research Centre, University of New South Wales, Sydney, Australia
[2] Department of Oceanography, University of Cape Town, Rondebosch, Cape Town, South Africa

Manuscript for: Journal of Climate
Status: to be submitted

4.1. Abstract

Links between extreme wet conditions over East Africa and Indian Ocean sea surface temperatures (SST) are investigated during the "short rain" season in October–November. During periods of enhanced East African rainfall, Indian Ocean SST anomalies reminiscent of a tropical Indian Ocean Dipole (IOD) event are observed. Ensemble simulations with an atmospheric general circulation model (AGCM) are used to understand the relative effect of local and large-scale Indian Ocean SST anomalies on above-normal East African precipitation. The importance of the various tropical and subtropical IOD SST poles, both individually and in combination, is quantified. In the simulations, enhanced East African "short rains" are predominantly driven by the local warm SST anomalies in the western equatorial Indian Ocean, while the eastern cold pole of the tropical IOD is of lesser importance. The changed East African rainfall distribution can be explained by a reorganization of the atmospheric circulation induced by the SST anomalies. A reduction in sea level pressure over the western half of the Indian Ocean and converging wind anomalies over East Africa lead to moisture convergence and increased convective activity over the region. The seasonal cycle of various indices related to the SST and the atmospheric circulation in the equatorial Indian Ocean are examined to assess their potential usefulness for seasonal forecasting.

4.2. Foreword

The main focus of this PhD thesis is on regional Southern Hemisphere climate variability. Despite this, it is of interest to investigate the response of a characteristic Indian Ocean SST pattern at other locations around the Indian Ocean, as there are basin-wide reorganizations in the large-scale atmospheric circulation. This chapter explores the contributions of local and large-scale SST to enhanced equatorial East African precipitation.

4.3. Introduction

Much of the African continent faces frequent and devastating climate extremes with far-reaching economic and social consequences. These extremes are mainly related to a lack or an excess of rainfall over wide regions, often affecting the livelihood of millions, with a profound impact on rain-fed agriculture and pastoralism (Verdin *et al.*, 2005), water and food security (Funk *et al.*, 2005; Verdin *et al.*, 2005), and public health (Epstein, 1999). Over the past few decades, such events that caused havoc across wide parts of Africa included the devastating droughts of the 1960s to 1980s in the Sahel region (e.g., Giannini *et al.*, 2003), the drought-associated famine in Ethiopia in 1984/1985 (Broad and Agrawala, 2000), and the disastrous floods in East Africa in 1961, 1994, and 1997 (e.g., Birkett *et al.*, 1999). Across the Horn of Africa, Linthicum *et al.* (1999) and Epstein (1999) directly link tens of thousands of new cases of Rift Valley fever, cholera, and malaria in 1998 to periods of heavy rainfall in late 1997 and the ensuing expansion of mosquito-prone habitats. Improved forecasts through a better understanding of the mechanisms in the climate system responsible for above-normal rainfall in the region could reduce the severity of such outbreaks and ameliorate human suffering: a 2–5 month lead time would be sufficient for preventive measures such as vaccinating domestic animals and pre-treating mosquito habitats with insecticides (Linthicum *et al.*, 1999).

Several studies have focused on a particular extreme event in an attempt to understand the mechanisms involved for that specific case: e.g., recent El Niño events in southern Africa (Reason and Jagadheesha, 2005; Lyon and Mason, 2007); and for East Africa, the drought in 2005 (Hastenrath *et al.*, 2007) and floods in 1994 (Behera *et al.*, 1999) and in 1997 (Birkett *et al.*, 1999; Latif *et al.*, 1999; Webster *et al.*, 1999). Over East Africa, previous studies present clear evidence of the importance of the tropical Indian Ocean in modulating rainfall variability in observations (e.g., Black *et al.*, 2003; Clark *et al.*, 2003a) and in climate model simulations (e.g, Goddard and Graham, 1999; Latif *et al.*, 1999). SST patterns associated with the zonal mode of variability, the Indian Ocean Dipole (IOD; Saji *et al.*, 1999; Webster *et al.*,

1999), and associated changes in the basin-wide atmospheric circulation, are implicated in several flooding events (e.g., Behera *et al.*, 1999; Latif *et al.*, 1999; Black *et al.*, 2003; Hastenrath, 2007). However, the question of which particular region(s) of anomalous SST, with coincident atmospheric circulation changes, is sufficient to induce rainfall changes over East Africa has yet to be considered. In this study, we use ensemble experiments with an atmospheric general circulation model (AGCM) to quantify the contribution of SST anomalies (associated with a characteristic Indian Ocean dipole pattern discussed in previous studies) to extreme wet conditions over East Africa.

4.3.1. Mean state

Precipitation across the African continent is highly variable in its temporal and spatial distribution. It is modulated by a multitude of factors. Of major importance are oceanic influences that include local forcing by sea surface temperatures (SST) in the adjacent Atlantic and Indian Oceans, as well as remote teleconnections from the tropical Pacific (e.g., Giannini *et al.*, 2003). The atmospheric circulation is characterized by the annual progression of the Intertropical Convergence Zone (ITCZ), the seasonally varying monsoon winds, and extratropical influences to the south (e.g., Reason and Roualt, 2005). The interactions between these components and the continent's many orographic features makes for complex dynamics controlling African rainfall (Janowiak, 1988). The present study focuses on precipitation in equatorial East Africa, a region dominated by the migration of the ITCZ and the monsoon circulation. The rainy seasons in East Africa occur during the transitions between winter and summer monsoons, when airflow from both hemispheres converges near the equator (Hastenrath, 2007). The timing of the rains associated with the ITCZ lags the migration of the sun by approximately one month (Black *et al.*, 2003). The so-called "long rains" bring several weeks of heavy rainfall during April and May associated with the relatively slow northward movement of the ITCZ. In contrast, during the "short rains" in October and November, the southward migration of the ITCZ is more rapid (Black *et al.*, 2003) and precipitation is particularly variable (Hastenrath, 2007).

4.3.2. Interannual variability

Interannual variations in East African rainfall have been linked to variability in both the Indian (Goddard and Graham, 1999; Latif *et al.*, 1999; Webster *et al.*, 1999; Black *et al.*, 2003; Clark *et al.*, 2003a; Hastenrath, 2007) and Pacific Oceans (Janowiak, 1988; Mutai *et al.*, 1998; Reason *et al.*, 2000; Clark *et al.*, 2003a). In

empirical orthogonal function (EOF) analyses of rainfall observations for the period 1979–2001, Bowden and Semazzi (2007) show the leading mode of variability in October–December (OND) East African rainfall to be associated with El Niño-Southern Oscillation (ENSO)-IOD covariability. During El Niño events, Janowiak (1988) finds rainfall in eastern Africa, east of 20°E, to be increased (decreased) by 10–25% for the region 0°–10°S (15°–30°S). Ogallo (1988) further explores links between ENSO and seasonal East African rainfall and finds strongest correlations during the latter half of the year. For precipitation in northern Tanzania, Kijazi and Reason (2005) link wet (dry) conditions during the OND season to El Niño (La Niña) events, and to enhanced (reduced) convection and easterly (westerly) anomalies over the western equatorial Indian Ocean. However, several studies have proposed that the relationship between East African rainfall and ENSO is actually more the result of an indirect forcing by ENSO on the Indian Ocean (e.g., Goddard and Graham, 1999; Latif *et al.*, 1999; Black *et al.*, 2003). A close coupling between the tropical Pacific and Indian Oceans during an ENSO cycle allows anomalies from the Pacific to modulate Indian Ocean variability via changes to the atmospheric Walker circulation (Black *et al.*, 2003) and in the ocean via the Indonesian Throughflow (Meyers, 1996).

The impact of the Indian Ocean is much more immediate in its influence on East African rainfall. For the short rain season, rainfall in East Africa seems to be closely linked to the strength of the Wyrtki Jet in the upper tropical Indian Ocean, driven by the surface westerly winds, which re-enforce the westward oceanic temperature gradient and form part of the equatorial zonal-vertical circulation cell (Hastenrath, 2007). Hastenrath (2007) links an uncharacteristic weakening of the westerlies over the central Indian Ocean with floods in 1961, 1994, and 1997 over East Africa. For 1994, Behera *et al.* (1999) report unusual conditions in the ocean-atmosphere system of the tropical Indian Ocean, with cold (warm) SST anomalies in the eastern (western) Indian Ocean and anomalous moisture transport across the Indian Ocean region. Black *et al.* (2003) find years with enhanced short rains in East Africa linked to Indian Ocean SST anomalies reminiscent of the IOD. This association is nonlinear, however: only extreme IOD years with persistent changes in the SST pattern and a concurrent easterly anomaly in the surface zonal wind field show a robust relationship with excessive East African short rains. The easterly anomalies in surface winds reduce the normal moisture transport away from East Africa, similarly shown for Tanzania by Mapande and Reason (2005a,b). Black *et al.* (2003) further propose that remote forcing from the Pacific associated with ENSO can predispose the Indian Ocean to an IOD event. Coupled ocean-atmosphere processes between the tropical Pacific and Indian Ocean as part of the tropospheric biennial oscillation and with effects on the Asian-Australian monsoon are explored

by Meehl *et al.* (2003). Feng and Meyers (2003) associate both local winds and remote forcing with the formation of the eastern pole of the IOD. Similarly, Wijffels and Meyers (2004) find that surface winds from both the Pacific and Indian Ocean act to modulate the depth of the thermocline in the eastern Indian Ocean. Both upwelling-favorable easterly winds and a shallow thermocline in the Java-Sumatra region play an essential role in the formation phase of the IOD (Meyers *et al.*, 2007). These indirect effects from the Pacific via the Indian Ocean could thus result in the statistical relationship between East African rainfall and ENSO described in earlier studies (cf., Janowiak, 1988; Ogallo, 1988).

Goddard and Graham (1999) use AGCM experiments to assess the relative contribution of the Indian and Pacific Ocean to East African rainfall variability. They force an AGCM with realistic SST variability in the Indian Ocean and Pacific Ocean separately and then compare results to a simulation with realistic SST variability globally. In the Indian Ocean simulations, convergent westerly (divergent easterly) flow results from warm (cool) SST anomalies in the western tropical Indian Ocean enhancing (reducing) moisture flux over central East Africa. Increased rainfall over East Africa occurs due to enhanced convective heating causing anomalous cyclonic circulation conditions to the southeast of Africa with southeasterly moisture flux onto East Africa (Goddard and Graham, 1999). The influence of the Indian Ocean can be modulated by remote forcing from the central and eastern tropical Pacific Ocean with warm (cool) Pacific SST associated with anomalous eastward (westward) surface zonal winds and downward (upward) vertical motion over equatorial Africa and the tropical Indian Ocean. This situation increases (reduces) convection over the African tropics and the western Indian Ocean, shifting the ITCZ polewards (equatorwards; Goddard and Graham, 1999). Latif *et al.* (1999) find similar results in their AGCM simulations forced with 1997/1998 SST patterns in the Indian and Pacific Ocean separately to explain the excessive rainfall in East Africa during that period. The anomalous Indian Ocean SST of 1997/1998 with unusually warm (cold) SST in the western tropical Indian Ocean are sufficient to induce the observed East African rainfall changes. In contrast, Pacific Ocean SST are not directly responsible for the increased rainfall over East Africa. However, as previously discussed, there are indications that the unusual Indian Ocean SST patterns at the time were remotely forced by the Pacific Ocean via anomalous surface heat fluxes (Latif *et al.*, 1999).

4.3.3. Interdecadal variability

On interdecadal timescales, Clark *et al.* (2003a) find that the influence of ENSO and the tropical Indian Ocean on OND East African rainfall varies, modulated by

a regime shift in the warming of the Indian Ocean and in the ENSO evolution apparent in 1976. Allan *et al.* (2003) suggest that a quasi-decadal ENSO-like signal can account for low-frequency variations in Indian Ocean climate. Black *et al.* (2003) propose that the indirect ENSO-East African rainfall relationship via modulation of the tropical Indian Ocean can explain interdecadal variations in East African rainfall, with both ENSO and the IOD suppressed during the mid-1940s to the early 1960s. They further hypothesize that improved long-term predictability of East African rainfall could be gained from an understanding of ENSO's influence on tropical Indian Ocean dynamics.

4.3.4. Seasonal forecasting

Rocha and Simmonds (1997a) find both the SOI and an index focused on pressure differences across the Indian Ocean to be potential predictors, used best in conjunction as they are largely independent, for austral summer rainfall in southeastern Africa with several months lead-times. Mutai *et al.* (1998) use rotated EOF analysis of global SST anomalies to predict interannual variability in the East African short rains for the OND season. They find the dominant SST modes to be associated with large-scale changes in the tropical atmospheric circulation with anomalies in the near-surface divergence/convergence over the three ocean basins and ultimately with continental African rainfall. Strong correlations between these SST modes and East African rainfall are evident at zero lag, however, only one of the EOF predictors promised any predictive skill at longer lead-times (Mutai *et al.*, 1998). In contrast, Hastenrath *et al.* (2004) investigate the skill of atmospheric circulation indices over the tropical Indian Ocean region to help in forecasts of the East African short rains. This approach attempts to exploit the tight relationship between equatorial surface westerlies over the Indian Ocean and the coastal East African short rains (Hastenrath *et al.*, 1993). However, as the Indian Ocean boreal autumn zonal circulation cell, despite its intensity, develops very rapidly without any long-lived precursors, the predictive potential gained from any circulation indices is very limited (Hastenrath *et al.*, 2004). In this study, we aim to gain a better understanding of the influence of local Indian Ocean SST on the regional atmospheric circulation. This would help in pinpointing more long-lived oceanic precursors that predispose the Indian Ocean to extreme situations, as occurred in 1961, 1994, and 1997 with excessive short rains over East Africa. Even a two-month lead time, which is not unrealistic with oceanic precursors, could allow preventive measures to greatly reduce the economic and social impacts over East Africa (Linthicum *et al.*, 1999).

Interestingly, Hastenrath *et al.* (2004) and Hastenrath (2007) report a decline in the strength of the relationship between the equatorial zonal circulation and the East

African short rains over the period 1978–1996 relative to the earlier period 1958–1977, despite the zonal equatorial circulation cell retaining its previous strength. Landman and Mason (1999) also describe a weakening of the ENSO signal in Indian Ocean temperatures since the late 1970s. As a result, relationships between tropical Indian Ocean variability and summer rainfall over South Africa and Namibia may have changed, with warm (cold) SST anomalies in the western tropical Indian Ocean associated with wet (dry) conditions over northeastern South Africa and Namibia over the last few decades (Landman and Mason, 1999).

4.3.5. Projected precipitation changes

The impact of future projected changes in precipitation patterns on surface water availability and drainage across Africa is assessed by de Wit and Stankiewicz (2006). Since large regions of Africa lie in an unstable to dry regime, even small changes in rainfall can have considerable impacts on water availability due to the non-linear relationship of rainfall and surface drainage. While drought-stricken areas of southern Africa are unlikely to experience improved conditions, East Africa might expect increases in surface water availability due to small projected increases in precipitation translating into a shift from the unstable to the wet regime (de Wit and Stankiewicz, 2006). Similarly, from a suite of Intergovernmental Panel of Climate Change (IPCC) Third Assessment Report model simulations with enhanced greenhouse gas forcing for the 21st Century, Hulme *et al.* (2001) suggest increases (decreases) in East African December–February (DJF; June–August, JJA) rainfall, with the amount of change highly dependent on the emission scenarios. Over the last century, Nicholson (2001) reports slight increases in East African rainfall. However, following on from the extreme precipitation event in 1961, there has been a steady decline in lake levels over the past few decades, although levels have still not returned to their pre-1960 state (Birkett *et al.*, 1999). On longer millennial timescales, links between shifts in the ITCZ and thus tropical African rainfall have been associated with reorganizations of the large-scale atmospheric circulation over the Indian Ocean (Tierney and Russell, 2007) and the North Atlantic (Johnson *et al.*, 2002; Brown *et al.*, 2007) region. The overarching goal of the present study is to explore the contributions of local and large-scale SST to enhanced East African short rains via changes of the atmospheric circulation across the Indian Ocean.

The remainder of the paper is structured as follows: Section 4.4 describes the data sets (observational and reanalysis), the climate model and the model experiments used in the study. In Section 4.5, observed and model rainfall characteristics are described over the African continent and locally for the East African region. The

observed SST anomalies associated with extremes in the East African short rains are explored in Section 4.6 and related to the SST anomalies used in the model simulations. Section 4.7 presents the changes in the atmospheric circulation in the model simulations and a mechanism for the induced shifts in the rainfall distribution is proposed. The main results are summarized in Section 4.8.

4.4. Data sets and climate model

4.4.1. Observational and reanalysis data

A suite of observation- and reanalysis-based precipitation products are used to assess the model's representation of precipitation over the African continent and the Indian Ocean region. Monthly precipitation data for the post-1979 period is taken from several products, when these products generally become more reliable. All products are provided at a 2.5° latitude/longitude resolution. Brief details are given in Table 4.1.

4.4.2. Climate model

The climate model used for the experiments is the NCAR Community Climate System Model, version 3 (CCSM3; Collins *et al.*, 2006), run in the atmospheric-only mode. The atmospheric component of CCSM3, the Community Atmosphere Model (CAM3), uses a spectral dynamical core at a T42 horizontal resolution (approximately 2.8° latitude/longitude), and 26 vertical levels. The CCSM3 model, its components, and configurations are described in Collins *et al.* (2006), and more specifically the atmospheric component, CAM3, by Hurrell *et al.* (2006). Several studies assess the model's performance and suitability for applications in climate research relevant for the present study, in particular in regard to the representation of the hydrological cycle (Hack *et al.*, 2006), tropical Pacific climate variability (Deser *et al.*, 2006), ENSO variability (Zelle *et al.*, 2005), and monsoon regimes (Meehl *et al.*, 2006). Several biases in the model have been documented: most notably associated with tropical Pacific climate, i.e. the Intertropical Convergence Zone (ITCZ), South Pacific Convergence Zone (SPCZ; e.g., Zhang and Wang, 2006), and ENSO spatial and temporal variability (e.g., Deser *et al.*, 2006). These issues and their relevance for the Indian Ocean region have been explored in detail by Ummenhofer *et al.* (2007c).

4.4.3. Experimental setup

In complementary studies, England *et al.* (2006) and Ummenhofer *et al.* (2007c) investigate the link between southwest Western Australian (SWWA) precipitation

Table 4.1. Summary of observation- and reanalysis-based precipitation products used and the period analyzed in this study.

Product	Description	Period	Reference
NNR	Reanalysis data product from the National Center for Environmental Prediction (NCEP) and the National Center for Atmospheric Research (NCAR) reanalysis. Precipitation is not constrained by observations, but derived completely from model 6-h forecasts.	1979–2006	Kalnay *et al.* (1996); Kistler *et al.* (2001)
CAMSOPI	National Oceanic and Atmospheric Adminstration (NOAA) NCEP CPC Climate Anomaly Monitoring System-Outgoing longwave radiation Precipitation Index. Merged analysis product that combines raingauge data with satellite-derived OLR Precipitation Index estimates.	1979–2006	Janowiak and Xie (1999)
GPCC	Global Precipitation Climatology Center product. Incorporates global data from 10,000–43,000 stations, depending on the time coverage.	1979–2004	Fuchs *et al.* (2007)
CMAP	Climate Prediction Center Merged Analysis of Precipitation product. Combines several diverse data sets, including gauge-based analyses from GPCC, predictions by the operational forecast model of European Centre for Medium-Range Weather Forecasting (ECMWF), and three types of satellite estimates.	1979–2006	Xie and Arkin (1996)

and anomalous Indian Ocean SST. Ummenhofer *et al.* (2007c) find that the frequency distribution of precipitation in this region is associated with a characteristic SST tripole pattern very similar to the dominant mode of SST variability in the Indian Ocean (defined through an EOF analysis; Santoso, 2005). England *et al.* (2006) in observations and Ummenhofer *et al.* (2007c) in model experiments demonstrate that in addition to SWWA, there is also a strong link between this SST pattern and precipitation over regions including East Africa. In the present study, the perturbation experiments of Ummenhofer *et al.* (2007c) are further analyzed, now focusing on the East African region, and additional experiments are performed in which the

original perturbation pattern is broken into its regional component poles.

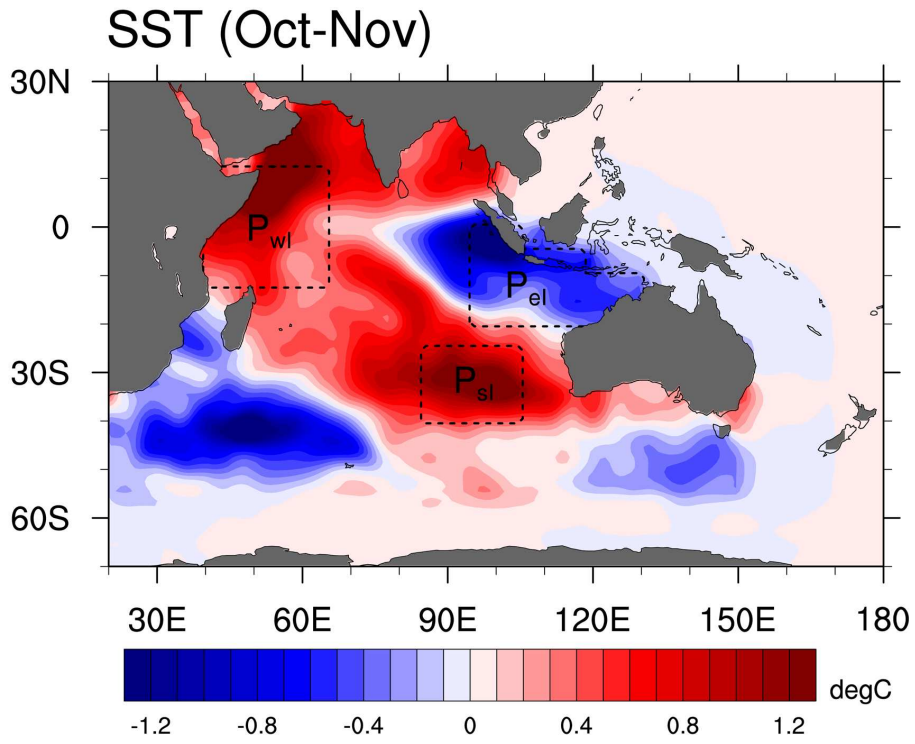

Figure 4.1. Average Oct.–Nov. SST anomaly (in °C) superimposed as a perturbation on the climatological SST across the entire Indian Ocean (P_I) and for individual poles separately, with the poles indicated by the dashed boxes as P_{wI}, P_{eI}, and P_{sI}.

In the control experiment the CCSM3 in atmosphere-only mode is forced with the monthly SST climatology, which is based on Reynolds SST (Smith and Reynolds, 2003, 2004) and Hadley anomalies (Rayner *et al.*, 2003). For a more detailed description of the SST climatology see Hurrell *et al.* (2006). A set of 80 one-year ensemble runs, each starting on January 1 from different initial atmospheric conditions and using this SST climatology, comprises the control experiment set (CNTRL). In the perturbation experiments, monthly-varying SST anomalies are added to the standard climatology across the Indian Ocean region. The full seasonally evolving SST perturbation pattern is described in Ummenhofer *et al.* (2007c) and features components of both a tropical IOD and a subtropical IOD (SIOD) signal. Additional experiments are also carried out using various regional subsets of the poles evident in the full pattern (see below). The average Oct.–Nov. SST anomalies, when the anomalous SST are generally most pronounced, used in the perturbation runs are shown in Fig. 4.1 (for the detailed monthly-varying SST anomalies, see Fig. 1 in Ummenhofer *et al.*, 2007c). A set of 60 one-year ensemble runs are carried out for each of the perturbation fields applied. The entire anomalous SST pattern shown

in Fig. 4.1 over the Indian Ocean region is termed P_I. To assess the importance of local SST anomalies in modulating East African rainfall, and to quantify their separate contributions, perturbation experiments are also conducted with particular local poles of SST anomalies only: P_{eI} with the eastern tropical IOD pole only (centered at 10°S, 110°E), P_{wI} with the western tropical IOD pole only (centered at 0°, 50°E), P_{eI+wI} with the eastern and western tropical IOD poles only, the SIOD pole P_{sI} (centered at 30°S, 95°E), and P_{eI+sI} with the eastern and southern poles only. The location of the poles used in the different experiments are indicated as dashed boxes in Fig. 4.1. To reduce spurious atmospheric circulation set up by unrealistic gradients at the "edges" of the poles, smoothing has been applied. For more details see Section 4.6.

4.5. Observed and model rainfall characteristics

The spatial and temporal characteristics of precipitation in the model are assessed across the African region and compared to observations (Fig. 4.2). The observed large-scale features of annual precipitation with the arid areas across northern and southern Africa are well represented in the model (Fig. 4.2a, b). However, in the model, the high-rainfall region in western and central equatorial Africa receives an excess of precipitation of the order of 20–30% compared to observations. Over tropical eastern Africa, the band of high rainfall also extends too far east into the Ethiopian highlands. In addition, the observed low-rainfall regime over the Horn of Africa is confined too close to the coast in the model. Over the equatorial Indian Ocean, the observed high-rainfall region associated with the ITCZ is split into two in a classical double-ITCZ configuration, a common problem in general circulation models (Meehl and Arblaster, 1998; Hurrell *et al.*, 2006). The excessive precipitation in the model over the Bay of Bengal is due to the fact that the tropical maximum remains north of the equator throughout the year (Hack *et al.*, 2006; Hurrell *et al.*, 2006). The major spatial and temporal features of the monsoonal precipitation patterns are suitably well represented by the model (Meehl *et al.*, 2006).

Focusing on East Africa, the Oct.–Nov. precipitation time-series are shown spatially averaged over the region delimited by 9°N–1°S and 29°–46°E (10°N–1°S and 31°–45°E) for the observed (model) in Fig. 4.2c (d), shown as standardized anomalies for ease of comparison. The study area in the observations is chosen to match the one in the model that recorded the largest response to the SST perturbations in the simulations. For the Oct.–Nov. months during 1979–2006, East Africa received on average 77 mm month^{-1} with a standard deviation of 26 mm month^{-1} (figure not shown). The years 1983 and 1997, and less so 2006, in the East African rainfall

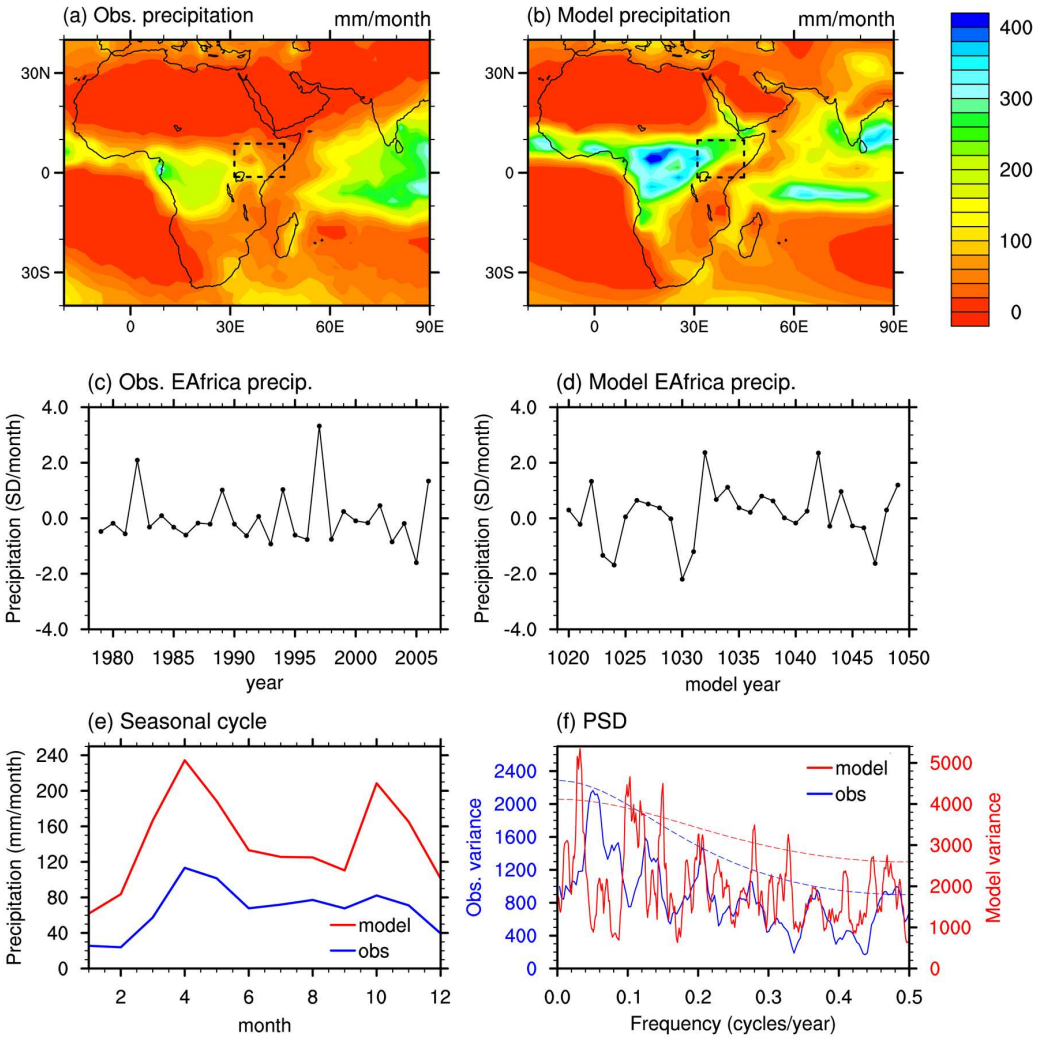

Figure 4.2. Oct.–Nov. long-term mean of (a, b) rainfall (in mm month^{-1}) across the African continent and the Indian Ocean region with observed (model) on the left (right). The long-term mean in the observations in (a) is based on CAMSOPI data for the period 1979–2006, the model field in (b) on the 80-year control run. The dashed boxes in (a, b) indicate the area used to derive the observed and model East Africa Oct.–Nov. precipitation time-series shown as standardized anomalies in (c, d). (e) presents the long-term seasonal cycle in precipitation for the observed (blue) and model (red). The power spectral density in (f) shows the observed (model) variance for the dominant cycles in blue (red), with the dashed lines indicating a 95% confidence level according to a theoretical Markov spectrum.

time-series stand out as years with enhanced short rains (Fig. 4.2c). A pronounced long-term decline in East African rainfall is apparent when focusing on the period since 1960, with a steady drop in lake levels (Birkett *et al.*, 1999). However, due to the sparse station data coverage over the region (e.g., Verschuren *et al.*, 2000), we limit our comparison to the post-1979 period with good satellite estimates, and no significant (at 90% confidence level) observed rainfall trend. As mentioned previ-

ously, the simulated East African rainfall is substantially higher at 187 mm month^{-1} and with a standard deviation of 19 mm month^{-1} (figure not shown). However, with a direct comparison of the model and observed rainfall time-series, one has to be mindful that the model is forced with SST climatology, which could account for the damped variability. For the same length of record, the standardized anomalies of East African precipitation in the model show, as in the observed, two years with enhanced short rains above 2 standard deviations month^{-1} (Fig. 4.2d). However, negative excursions with rainfall below 1 standard deviation are more common in the model than in the observed (Fig. 4.2c, d).

The seasonal cycle of East African rainfall exhibits distinct maxima in the March–May and Oct.–Nov. months, termed the "long" and "short" rains, respectively (e.g., Black *et al.*, 2003). The modeled precipitation captures the double peaked seasonal cycle (Fig. 4.2e), although the peaks, particularly the one associated with the short rains, are overly pronounced. Details of the model's representation of the monsoon circulation and precipitation are described by Meehl *et al.* (2006). The observed East African rainfall exhibits dominant periodicity at 5 and 2 years, compared to the model 10, 6.5, 3.5, 3, and 2 years.

4.6. Observed and model SST anomalies

Composites of SST during years of anomalous short rains are shown in Fig. 4.3. For different observation- and model-based precipitation products (details see Table 4.1), years with extreme short rains are defined as those exceeding ±1 standard deviation in the area-averaged, detrended time-series of East African precipitation (Fig. 4.3a, d, g, j). With the exception of the NNR, all products show a positive trend in precipitation during the Oct.–Nov. season of 0.6–0.8 mm month^{-1} yr^{-1}. Two years with very excessive short rains are common to all precipitation products, namely 1983 and 1997. Extensive flooding during the latter year has inspired previous work (e.g., Birkett *et al.*, 1999; Latif *et al.*, 1999). In addition, 2006 is recorded as a wet short rain season in all products that cover that period (GPCC is only available up to 2004). In contrast, short rain seasons with very much reduced precipitation are more variable across the products, with relatively few years qualifying as extreme dry short rains. Among the years receiving very much reduced short rains, 2003 and 2005 feature in most of the precipitation products. The low number of dry short rains is in part due to the non-Gaussian nature of the precipitation distribution, reducing the validity of the standard deviation measure for identifying extreme years. However, the metric is successful in identifying years with wet Oct.–Nov. rain seasons. Furthermore, despite small variations in the set of years chosen

for the composites of SST anomalies, robust SST features across the Indian Ocean are evident for the dry and wet extremes (described below).

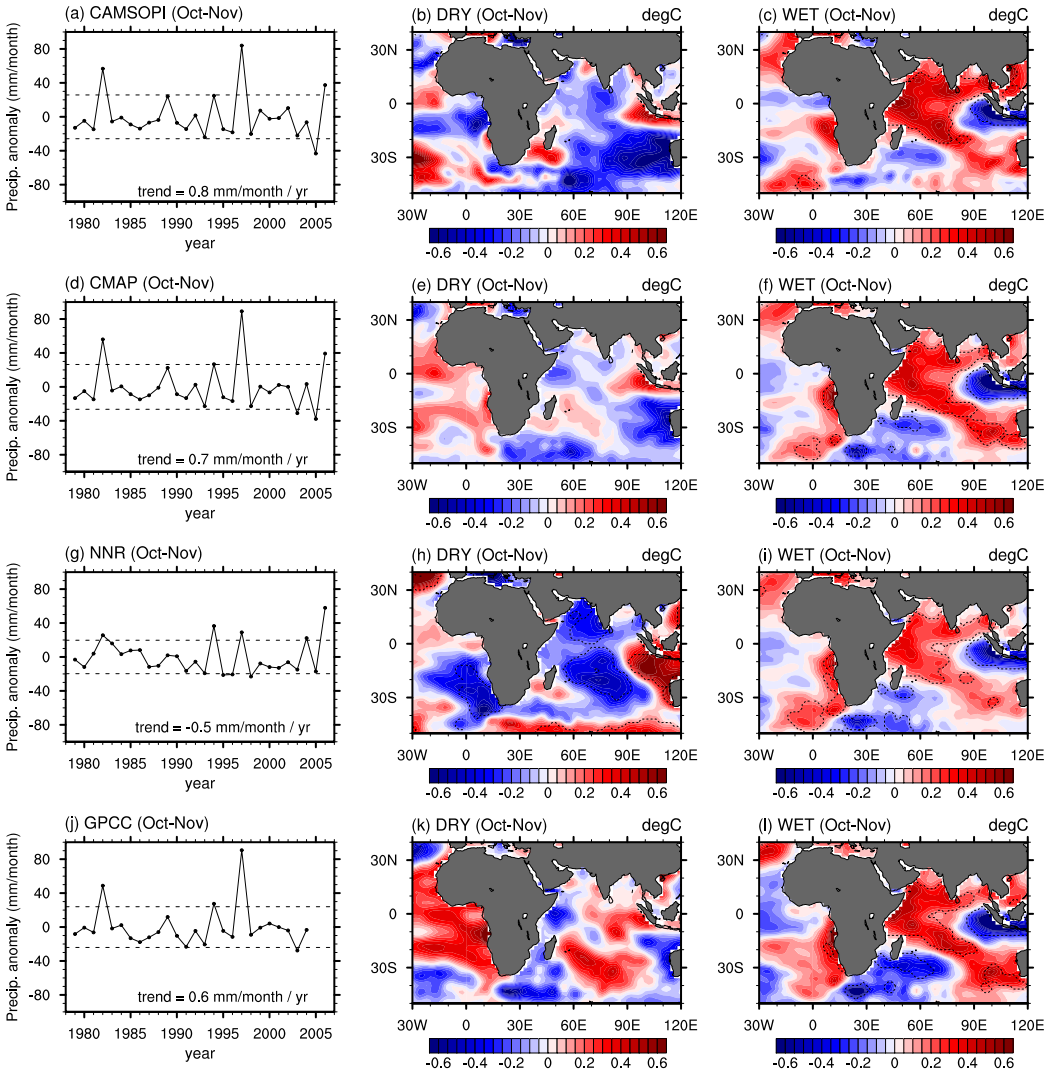

Figure 4.3. (Left) Time-series of East African rainfall averaged over Oct.–Nov. for the period 1979–2006, with ±1 standard deviation indicated (dashed horizontal lines). SST anomaly (in °C) for the extreme dry (middle) and wet (right) years, determined as those exceeding ±1 standard deviation in the respective rainfall time-series. From top to bottom for different precipitation products as CAMSOPI, CMAP, NNR, and GPCC, with the linear trend removed from each time-series indicated at the bottom of the left-hand panels. Dashed lines over the SST panels indicate significant anomalies at the 90% confidence level as estimated by a two-tailed t-test.

The Indian Ocean during dry short rains in East Africa is characterized by localized warm SST anomalies in the eastern Indian Ocean off Sumatra, consistent across the different precipitation products (Fig. 4.3b, e, h, k). Across the remainder of the Indian Ocean during dry Oct.–Nov. seasons the composite patterns are less

consistent, although there is a tendency towards below-average SST in the western region of the Indian Ocean. Similarly, for the 2005 drought in East Africa, Hastenrath *et al.* (2007) describe anomalous cold (warm) SST anomalies in the northwest (southeast) of the equatorial Indian Ocean, a steepened eastward pressure gradient, and strengthened westerlies. SST anomalies over the Atlantic show no consistent pattern across the dry composites. In contrast, during anomalous wet short rains, an area of warm SST anomalies in the western Atlantic off Angola, Namibia and South Africa is common across all the SST composites. Colberg *et al.* (2004) link a similar warming in the South Atlantic to changes in the trade winds and surface heat fluxes associated with El Niño. Over the Indian Ocean, Oct.–Nov. SST anomalies are cold off Sumatra in the tropical eastern Indian Ocean, while warm anomalies extend over much of the western half of the Indian Ocean and the subtropical region towards Australia (Fig. 4.3c, f, i, l). Indian Ocean SST anomalies are significant over much of the domain and the overall pattern is very robust across all the wet composites (and for individual composite members; figure not shown). The pattern of Indian Ocean SST anomalies closely matches those associated with heavy East African SON precipitation for the period 1900–1997 in Black *et al.* (2003, their Fig. 3). The magnitude of SST anomalies in Fig. 4.3 is larger than in Black *et al.* (2003), as we focus on the Oct.–Nov. months and a much smaller number of extreme years in the composite. So, despite the short record and sparsity of high-quality observations over the East African region, persistent features in Indian Ocean SST anomalies concurrent with excessive short rains can be identified. These observed Indian Ocean SST anomalies associated with excessive East African short rains are now compared to the SST forcing fields used for a set of AGCM experiments.

The model simulations with the anomalous SST perturbations across the entire Indian Ocean (P_I) are taken from experiments described in previous work by Ummenhofer *et al.* (2007c). They use composite patterns of observed monthly SST anomalies across the Indian Ocean for extreme dry (and wet) years over southwest Western Australia (SWWA; England *et al.*, 2006; Ummenhofer *et al.*, 2007c). Ummenhofer *et al.* (2007c) show extreme rainfall years in SWWA to be associated with a basin-wide reorganization of the atmospheric circulation across the Indian Ocean in response to the anomalous SST forcing. In observations, England *et al.* (2006) find hints of an out-of-phase relationship between rainfall in SWWA and East Africa, linked to the changed large-scale atmospheric circulation across the Indian Ocean region. This link is further strengthened by model experiments in the CCSM3 described in Ummenhofer *et al.* (2007c), in which a highly significant shift is seen in East African rainfall intensity resulting from this SST pattern. While derived for an analysis of Australian precipitation, these SST patterns are very similar

to a dominant EOF mode in Indian Ocean variability (see Santoso, 2005; Ummenhofer *et al.*, 2007c), containing features characteristics of both the IOD and SIOD. As such, the present study effectively examines the links between anomalously wet short rain seasons in East Africa and a characteristic mode of Indian Ocean SST variability identified in previous work by the authors. We investigate the effect of both local and large-scale Indian Ocean SST anomalies on above-average rainfall in East Africa. In addition, we attempt to quantify the respective contributions of anomalous SST in various regions and propose a mechanism for the changed rainfall distribution.

The average Oct.–Nov. SST anomalies used in the perturbation AGCM simulations were shown previously in Fig. 4.1. In addition to the SST anomalies across the entire basin, simulations with individual SST poles are conducted, with the pole locations indicated as dashed boxes in Fig. 4.1 (for latitude/longitude coordinates see Section 4.4.3). The Oct.–Nov. SST anomalies are characterized by warm (cold) temperatures in the western and central (eastern) tropical Indian Ocean (Fig. 4.1). An area of anomalously cold SST is located south of Madagascar. The SST pattern in Fig. 4.1 resembles anomalies associated with above-average rainfall in East Africa (Fig. 4.3; Black *et al.*, 2003). In an AGCM, Reason (2002) investigates the impact of South Indian Ocean SST anomalies reminiscent of the forcing used here in the P_I case, i.e. cold (warm) SST anomalies in the southwest Indian Ocean south of Madagascar (in the southeast Indian Ocean off the west coast of Australia), on the atmospheric circulation over southern Africa. Despite using characteristic basin-wide Indian Ocean SST anomalies extending across both the tropics and the subtropics, the focus in the present study is on tropical East African rainfall. In addition, a *quantification* of the relative influence of individual (and combined) poles to excessive East African short rains is attempted.

4.7. Changed atmospheric circulation in model experiments

4.7.1. Rainfall distribution

The simulated total precipitation during the short rain season is spatially averaged across East Africa (subregion indicated in Fig. 4.2) for each of the ensemble members in the control and the perturbed cases. The rainfall frequency distribution for each of the perturbed cases with the control distribution superimposed is shown in Fig. 4.4. A nonparametric Mann-Whitney rank test (von Storch and Zwiers, 1999) is used to determine the significance level at which the rainfall frequency distribution over East Africa in the perturbed cases differs from the control. For P_I with the SST anomalies applied over the entire Indian Ocean, the rainfall distribution over

East Africa is shifted significantly (at 99% confidence level) relative to the CNTRL during the Oct.–Nov. period (Fig. 4.4a). In fact, the rainfall distribution for the CNTRL and P_I barely overlap, which represents an increase in mean Oct.–Nov. rainfall of over 35% from 410 mm to 560 mm. This increase in P_I seems to be predominantly driven by the SST anomalies in the local western pole: both of the other experiments that contain a perturbed western pole (i.e. P_{eI+wI} and P_{wI}) show an increase in precipitation of comparable magnitude (Fig. 4.4c, f). In contrast, the ensemble sets with only the eastern and/or southern pole show no significant changes in rainfall over East Africa (Fig. 4.4b, d, e).

The spatial distribution of the precipitation anomalies across the Indian Ocean basin are assessed in Fig. 4.5. Throughout the study, we use a two-tailed t-test to determine the significance of the spatial anomaly fields. This test estimates the statistical significance at which the anomalies in the perturbed experiments are distinguishable from the control at each grid point. The rainfall response over East Africa in the P_I case forms a band of increased precipitation extending from the Horn of Africa to the southwest towards the Atlantic coast (Fig. 4.5a). Again, the enhanced rainfall over the African continent seems to be linked to the warm SST anomalies in the western Indian Ocean, as both P_{eI+wI} and P_{wI} show a similar signal (Fig. 4.5c, f). All three cases with warm western Indian Ocean SST also record increased precipitation overlying the area with above-normal SST. In P_I, anomalous dry conditions occur over southeastern Africa, as linked to warm SST in the tropical Pacific and Indian Ocean in AGCM experiments by Rocha and Simmonds (1997b). Interestingly, they find the drought conditions over southeastern Africa to be exacerbated with co-occurring cool SST in the South Indian Ocean, consistent with a stronger response in P_I than P_{wI} here (Fig. 4.5a, f). Over the eastern equatorial Indian Ocean, reduced precipitation occurs over the region with anomalous cold SST and the adjacent Indonesian Archipelago (Fig. 4.5a, b, d). In the model, these results demonstrate a strong precipitation response related to tropical SST anomalies, but no such response from the subtropical forcing (Fig. 4.5e).

In summary, enhanced East African short rains in the AGCM experiments seem to be predominantly driven by the local warm SST anomalies in the western equatorial Indian Ocean, while the eastern cold pole is of lesser importance. The mechanisms by which the different poles change the large-scale atmospheric circulation and thus contribute to changed East African rainfall will be investigated in detail below.

4.7.2. Circulation anomalies

The large-scale and local SST anomalies can give rise to changes in the overlying atmosphere, modulating its thermal and circulation characteristics. An extensive

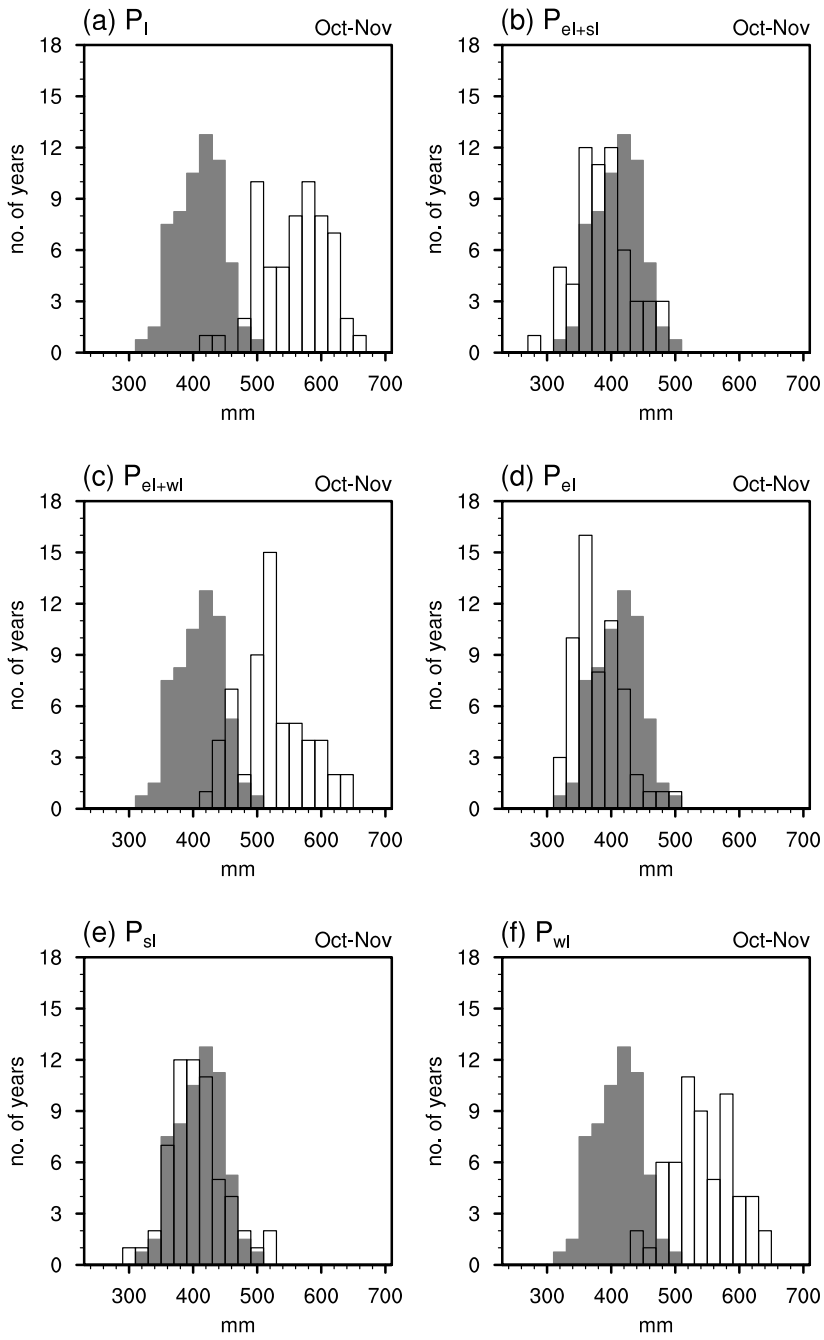

Figure 4.4. Frequency distribution of total precipitation spatially averaged across East Africa (subregion indicated in Fig. 4.2a, b): cumulative rainfall amount (in mm) summed for the months Oct.–Nov. for the following experiments: (a) P_I, (b) P_{eI+sI}, (c) P_{eI+wI}, (d) P_{eI}, (e) P_{sI}, and (f) P_{wI}. The shaded gray rainfall distribution represents the CNTRL (normalized to the number of ensemble members in the perturbed cases), while the perturbed cases are indicated with black outlines. The following significance levels hold, as determined by a Mann-Whitney test: with the exception of (e) all significant at 99% level.

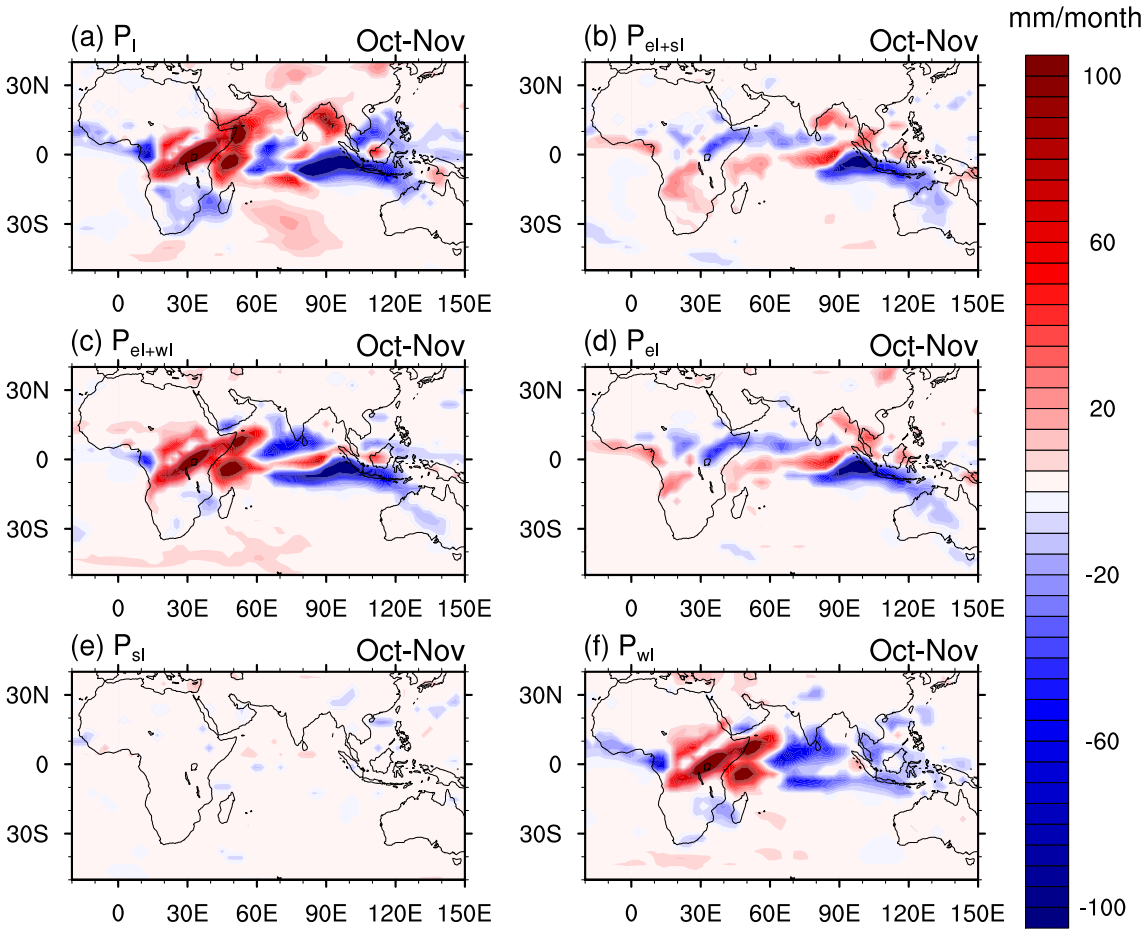

Figure 4.5. Precipitation anomalies (in mm month^{-1}) for (a) P_I, (b) P_{eI+sI}, (c) P_{eI+wI}, (d) P_{eI}, (e) P_{sI}, and (f) P_{wI}, averaged over the Oct.–Nov. months. Only anomalies are shown that are significant at the 90% confidence level as estimated by a two-tailed t-test.

area of negative SLP anomalies (in excess of 2 hPa below normal) is seen over the warm western half of the Indian Ocean and the adjacent central and east African continent in the P_I case (Fig. 4.6a). The reduced SLP extends to the south of Africa, west across the South Atlantic, and to the north over the Arabian Peninsula, India, and central Asia. In contrast, positive SLP anomalies occur in the P_I case in the eastern equatorial Indian Ocean associated with the cold SST pole (Fig. 4.6a). The positive SLP anomalies in the eastern Indian Ocean are a consistent feature across all the perturbed cases with a cold eastern SST pole (Fig. 4.6a–d). Locally reduced SLP anomalies are centered over the western Indian Ocean warm pole and the East African coast, and also extend west to the south of Africa in the P_{eI+wI} and P_{wI} cases (Fig. 4.6c, f). This response in anomalous SLP seems to be primarily driven by the western pole.

The SLP anomalies result in an adjustment of the large-scale circulation seen in

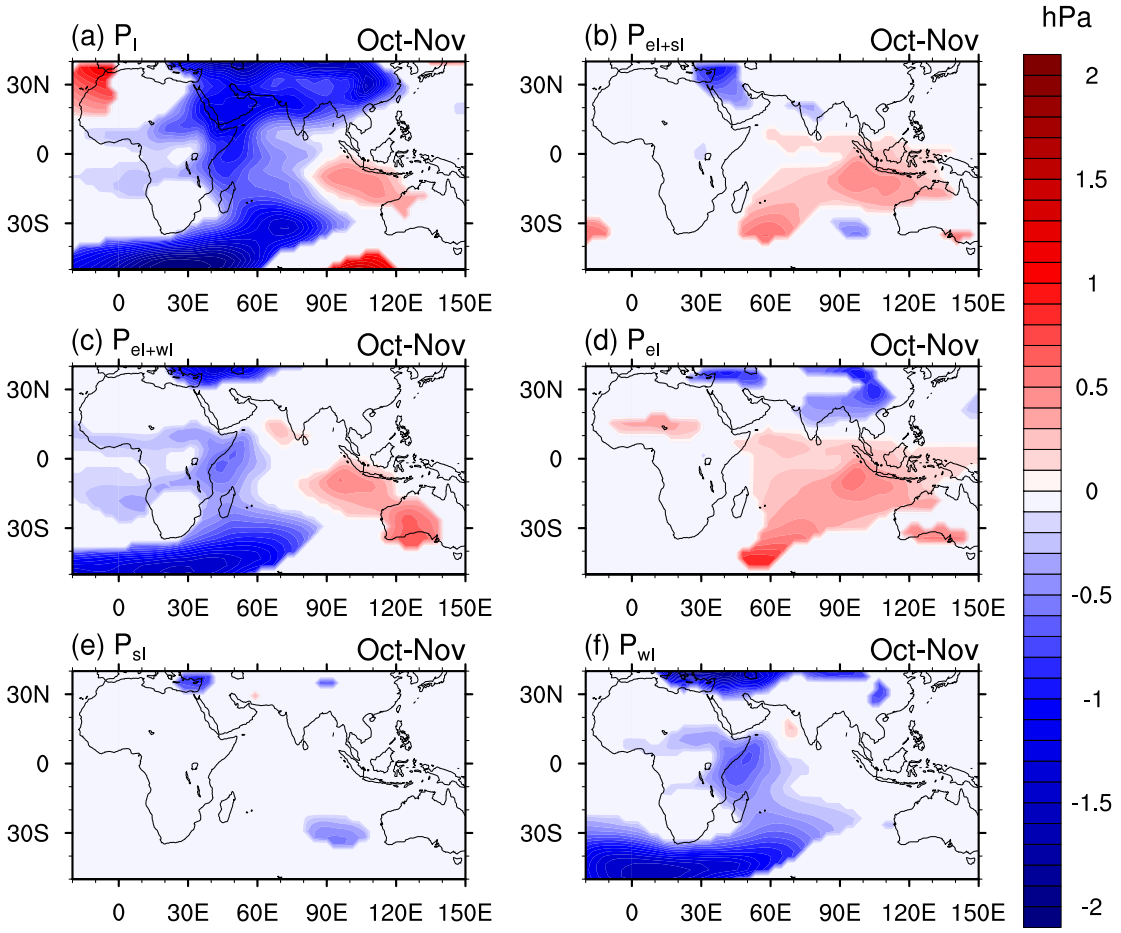

Figure 4.6. Sea level pressure anomalies (in hPa) for (a) P_I, (b) P_{eI+sI}, (c) P_{eI+wI}, (d) P_{eI}, (e) P_{sI}, and (f) P_{wI}, averaged over the Oct.–Nov. months. Only anomalies are shown that are significant at the 90% confidence level as estimated by a two-tailed t-test.

anomalous surface (Fig. 4.7) and mid-level (Fig. 4.8) wind anomalies. A surface wind convergence over East Africa is seen for the P_I simulation during Oct.–Nov. (Fig. 4.7a). Strengthened westerly airflow over central Africa and easterly onshore anomalies from the Indian Ocean intersect over the coast of equatorial East Africa. Easterly anomalies dominate over the entire width of the equatorial Indian Ocean basin, while the westerly anomalies are confined to central and eastern Africa. The presence of the cold eastern Indian Ocean SST pole determines the extent of the zonal easterly anomalies. In contrast, the western pole alone is sufficient for the local surface wind response over the East African coast, though with a more northerly component than seen in P_I (Fig. 4.7f), which is further confirmed in the wind anomalies at 500 hPa (Fig. 4.8). In contrast to the surface winds, the airflow convergence at 500 hPa occurs further inland towards central Africa. Earlier studies confirm this surface to mid-level wind anomaly pattern associated with enhanced

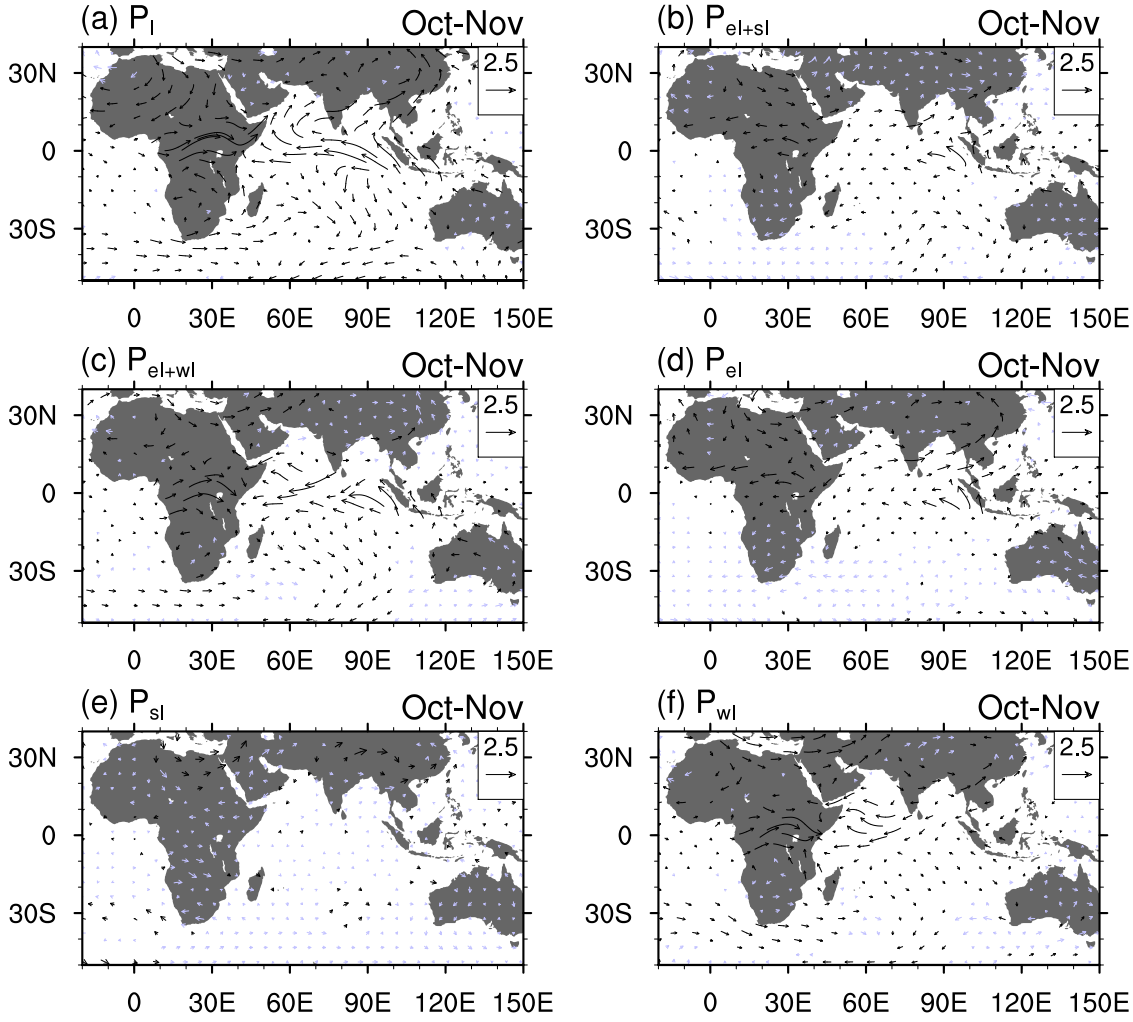

Figure 4.7. Surface wind anomalies (in m s^{-1}) for (a) P_I, (b) P_{eI+sI}, (c) P_{eI+wI}, (d) P_{eI}, (e) P_{sI}, and (f) P_{wI}, averaged over the Oct.–Nov. months. Black arrows indicate significant anomalies at the 90% confidence level as estimated by a two-tailed t-test.

East African precipitation in observations (Black *et al.*, 2003; Hastenrath, 2007) and model simulations (Goddard and Graham, 1999). However, previous work tends to link these wind anomalies to the enhanced zonal pressure gradient due to the presence of both the western and eastern SST poles of the IOD. Here, we find that the wind, and thus moisture, convergence over East Africa is predominantly driven by the local warm SST anomalies in the western equatorial Indian Ocean.

In response to the underlying warm SST anomalies in the western equatorial Indian Ocean, changes in vertical velocity anomalies ω are recorded for P_I, P_{eI+wI}, and P_{wI} (Fig. 4.9a, c, f). Anomalous upward velocities occur over the western Indian Ocean and over East Africa, extending towards the southwest. The regions with upward vertical velocity anomalies closely match the areas recording increased

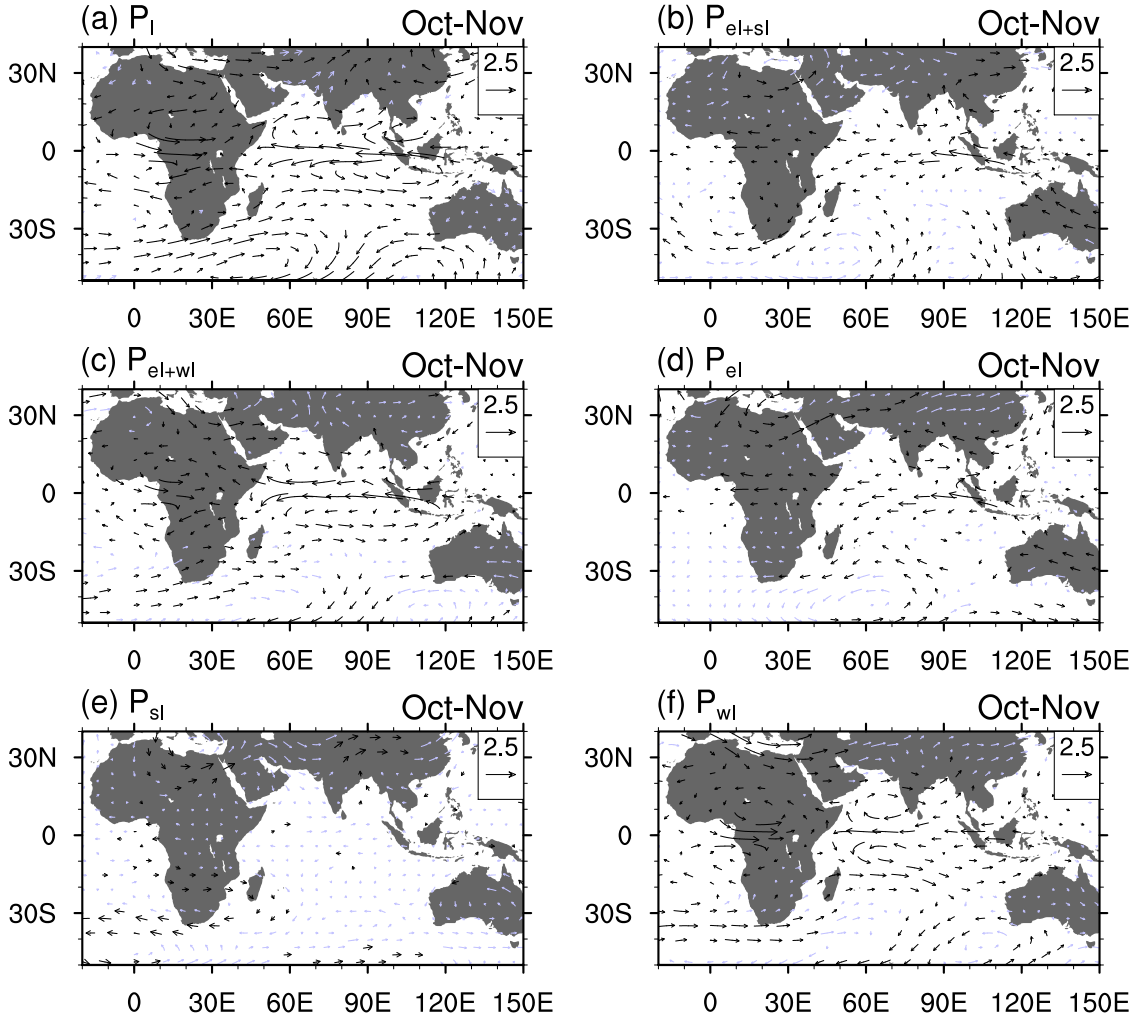

Figure 4.8. Wind anomalies at the 500 hPa level (in m s^{-1}) for (a) P_I, (b) P_{eI+sI}, (c) P_{eI+wI}, (d) P_{eI}, (e) P_{sI}, and (f) P_{wI}, averaged over the Oct.–Nov. months. Black arrows indicate significant anomalies at the 90% confidence level as estimated by a two-tailed t-test.

precipitation (compare to Fig. 4.5a, c, f). In contrast, anomalous subsidence is associated with the cold SST anomalies in the eastern equatorial Indian Ocean and the Indonesian Archipelago (Fig. 4.9a–d).

4.7.3. Thermal anomalies

It is of interest to explore the structure of the thermal anomalies throughout the atmosphere induced by the anomalous SST. Latitudinal cross-sections of air temperature anomalies centered at the equator and at 20°S are shown in Fig. 4.10 extending across the Indian Ocean basin and the adjacent continents. Following on from previous results, only the P_I, P_{eI+wI}, and P_{wI} cases are presented, as these provide distinct responses to the underlying SST anomaly forcing. The low-level air

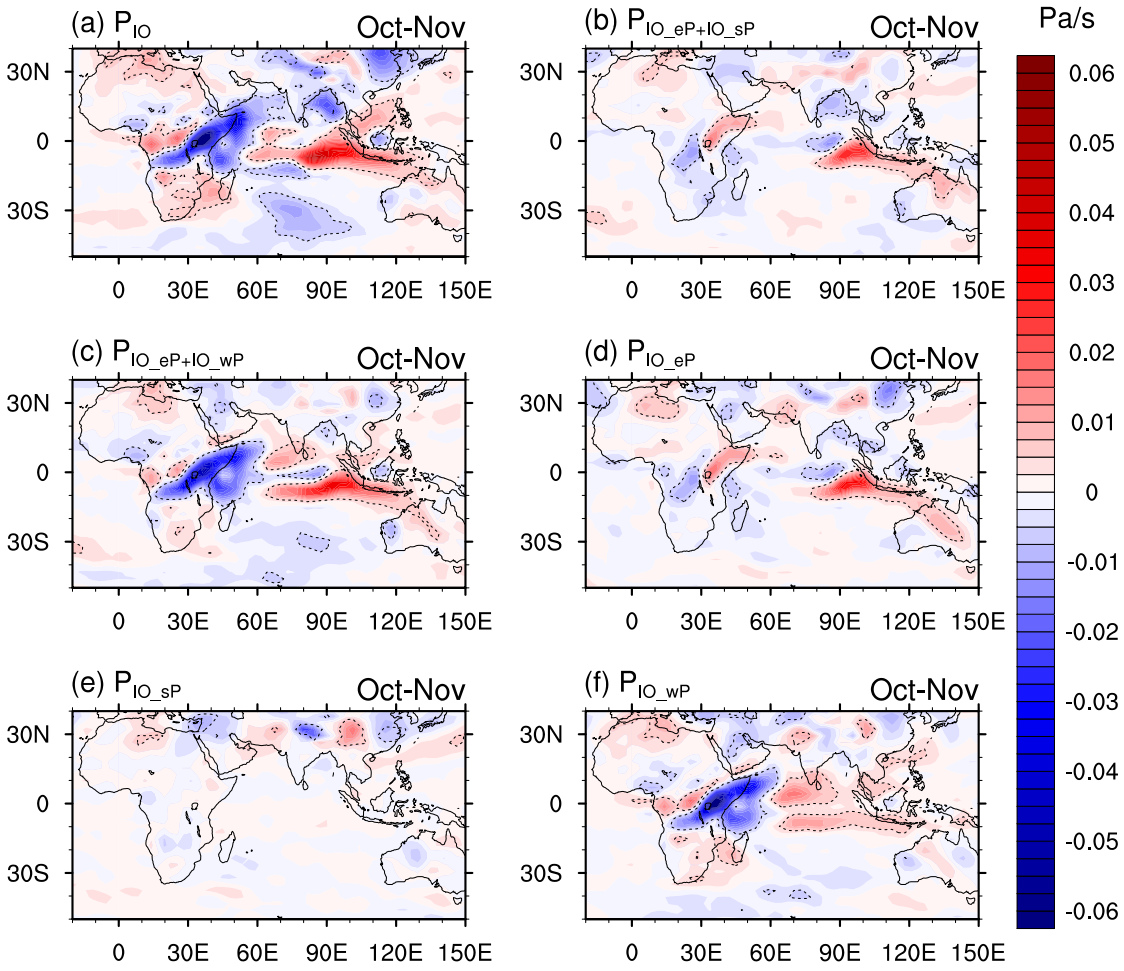

Figure 4.9. Vertical velocity ω anomalies at the 700 hPa level (in Pa s^{-1}) for (a) P_I, (b) P_{eI+sI}, (c) P_{eI+wI}, (d) P_{eI}, (e) P_{sI}, and (f) P_{wI}, averaged over the Oct.–Nov. months. Dashed lines indicate significant anomalies at the 90% confidence level as estimated by a two-tailed t-test.

temperatures reflect the sign and position of the underlying SST anomalies, with positive (negative) temperature anomalies over the western (eastern) Indian Ocean (Fig. 4.10a–d). However, along the equator, the vertical extent of the warm and cold anomalies differs considerably: the cold anomalies associated with the eastern pole are limited to the lower 2 km (below 850 hPa) of the atmosphere, while the signature of the warm temperature anomalies is seen up to a height of 14 km (150 hPa; Fig. 4.10a, c). This higher penetration is due to local convective effects driven by increased gravitational instability over the warm SST region.

While warm temperature anomalies occur over the western Indian Ocean, over equatorial central and eastern Africa cold low-level temperature anomalies are evident (Fig. 4.10a, c, e). These seem to be directly related to the western Indian Ocean warm pole, as they remain apparent in the P_{wI} case (Fig. 4.10e). The cold

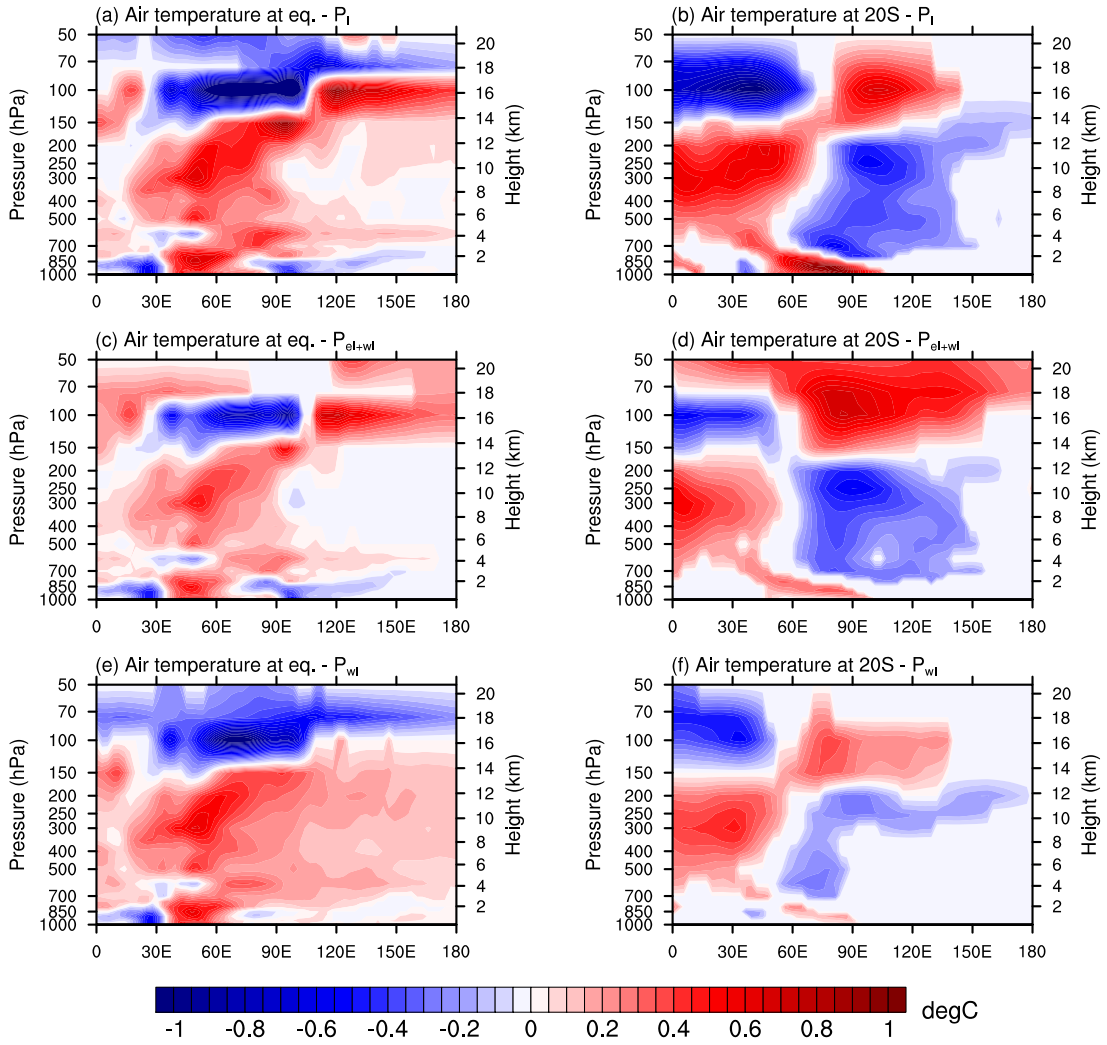

Figure 4.10. Cross-section of air temperature anomalies centered at (left) the equator and (right) at 20°S for (a, b) P_I, (c, d) P_{eI+wI}, and (e, f) P_{wI}, averaged over the Oct.–Nov. months (all in °C). Colors indicate significant anomalies at the 90% confidence level as estimated by a two-tailed t-test.

anomalies most likely result from reduced incoming solar radiation due to increased cloud cover associated with the enhanced convective activity (Fig. 4.9f). Mapande and Reason (2005b) find a similar reduction in observed outgoing longwave radiation, implying increased cloud cover, during anomalous wet seasons in Tanzania. Along the equator, the structure and magnitude of the thermal anomalies in the atmosphere in the P_I case can be mainly attributed to the western warm pole, as demonstrated by the close match with the anomalies in the P_{wI} case, while the eastern pole on its own has a small moderating effect (figure not shown). To explain the large-scale atmospheric structure in the temperature anomalies, however, the zonal gradient in SST becomes more important (Fig. 4.10b, d, f). For example,

the cross-section of the temperature anomalies at 20°S in the P_I case show warm anomalies associated with the western pole extending up and westward to a height of 14 km, and cold mid-level anomalies over the eastern Indian Ocean (Fig. 4.10b). The structure and magnitude of these thermal anomalies at 20°S rely on the zonal gradient in SST, as only the P_{eI+wI} case reproduces the temperature anomalies (Fig. 4.10d), while neither the western pole on its own (Fig. 4.10f) nor the eastern pole (figure not shown) represent these features adequately.

4.7.4. Seasonal development of Indian Ocean anomalies

While we have thus far focused on the Oct.–Nov. climate response to the year-long forced SST perturbations, it is of interest to assess their seasonal development. To better understand the atmospheric circulation response to the evolving SST anomalies, we investigate here the seasonal development of indices characterizing the state of the equatorial Indian Ocean zonal circulation. The indices, representing an averaged zonal pressure difference and the zonal surface wind, are adapted from Hastenrath (2007). Details of the calculation of these indices is provided below. Shown first in Fig. 4.11a are the SST anomalies for the perturbation simulations relative to the CNTRL. In general, the spatially averaged SST anomalies for the various poles used in the perturbation experiments are small until April, after which they increase in magnitude (Fig. 4.11a). Negative SST anomalies develop gradually at the cold eastern pole (P_{eI}) from May onwards, reaching a minimum value of around -0.4°C in October, after which time the anomaly rapidly decays. This is consistent with earlier findings for the seasonal evolution of the IOD (e.g., Saji *et al.*, 1999; Webster *et al.*, 1999; Li *et al.*, 2003; Meyers *et al.*, 2007). Increasingly warm anomalies occur at the western and southern poles, with a maximum of around 0.4°C for the western pole in October, while the temperatures at the southern pole continue to rise to reach around 0.5°C above normal in December. The zonal (meridional) gradient in SST anomalies, i.e. the difference of SST anomalies between the western and eastern (southern and eastern) pole are also indicated in Fig. 4.11a as dashed lines. Both the zonal and meridional gradient in SST anomalies increase from April onwards and reach a maximum in October.

The zonal SLP gradient (pressure over the western Indian Ocean minus pressure in the east for the latitude band 7°N–7°S; SLP_{W-E}) determines the strength of the zonal circulation anomalies in the equatorial Indian Ocean (Hastenrath, 2007). The annual cycle of SLP_{W-E} is characterized by a maximum in JJA due to an inverse relationship between the pressure in the west and the east of the Indian Ocean, declining to a minimum in austral summer (Fig. 3c in Hastenrath, 2007). For the P_I experiment, a drop relative to the CNTRL occurs in SLP_{W-E} between April and

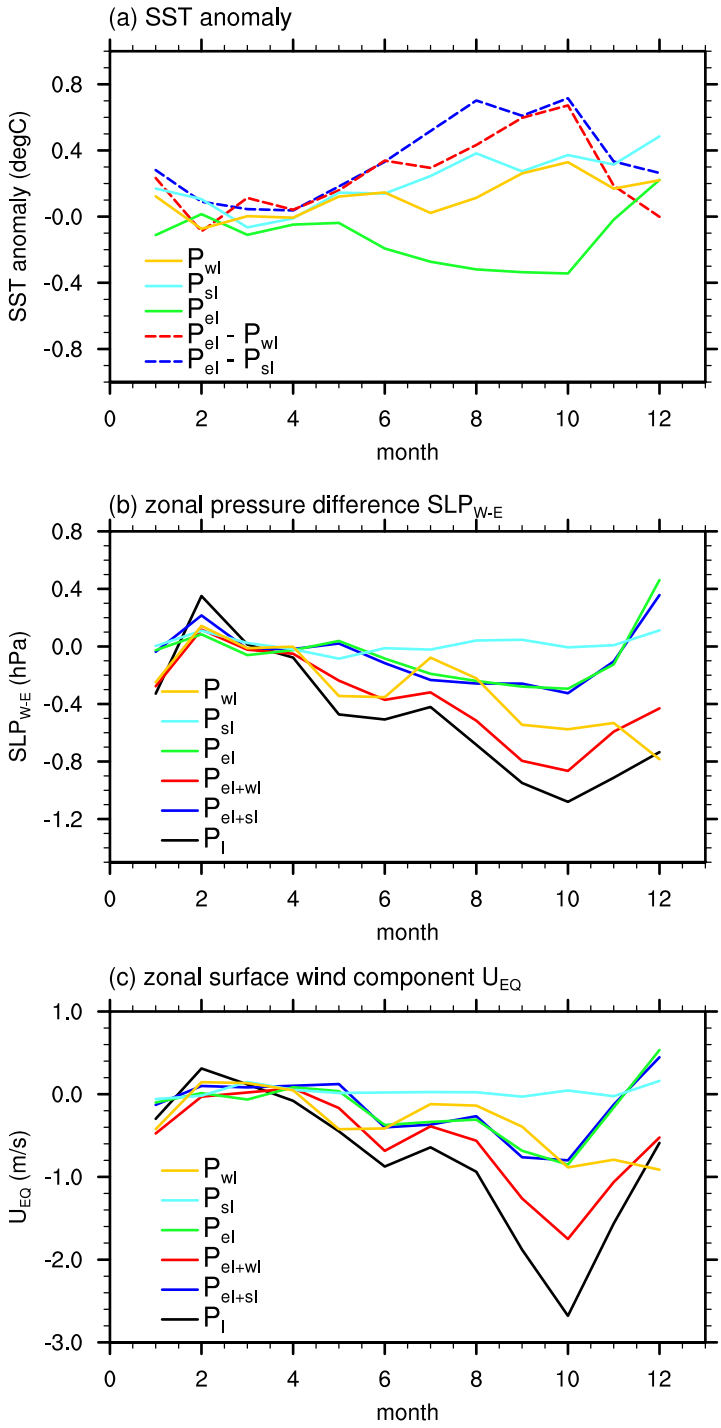

Figure 4.11. (a) Seasonal cycle of SST anomalies (in °C) spatially averaged over the poles used in the perturbation experiments (solid lines) and for the difference in SST anomalies for P_{wI} - P_{eI} and P_{sI} - P_{eI} (dashed lines). Seasonal cycle of the anomaly of the perturbation experiments relative to the CNTRL for (b) zonal sea level pressure difference SLP_{W-E} (in hPa) for 7°N–7°S, 39°–51°E minus 7°N–7°S, 90°–101°E and (c) zonal surface wind component U_{EQ} (in m s^{-1}) averaged over 4°N–4°S, 59°–90°E.

May, followed by a steeper decrease from July to a minimum in October (Fig. 4.11b). This represents an intensification of the seasonal decrease in SLP_{W-E} after August. The magnitude and seasonal evolution of this pressure difference anomaly in P_I is reproduced most closely by the P_{eI+wI} case, although the full perturbation values are slightly higher. The pressure difference is mostly due to the negative anomalies at the western pole (P_{wI} in Fig. 4.11b; see also Fig. 4.6f), while the contributions of the eastern pole (P_{eI} in Fig. 4.11b) are minimal. The zonal pressure difference SLP_{W-E} is instrumental in driving the zonal surface wind component along the equator (U_{EQ}), measured for the latitude band 4°N–4°S (Fig. 4.11c). The seasonal progression of U_{EQ} shows peaks with zonal mean westerly winds of almost 3 m s^{-1} during May and the Oct.–Nov. months (Fig. 3b in Hastenrath, 2007). In the P_I case, the U_{EQ} anomaly relative to the CNTRL becomes increasingly negative after February. Strengthening of the easterly anomalies in the surface wind is especially rapid from August to October, reaching easterly wind anomalies in excess of 2.5 m s^{-1}. These U_{EQ} anomalies are of comparable magnitude to the U_{EQ} seasonal mean of 3 m s^{-1} in Hastenrath (2007) and thus represent a considerable weakening (or even a reversal, in some instances) of the overall westerly flow.

In observations, Black *et al.* (2003) find extreme IOD events associated with a weakening of the predominant westerly flow, a reduction of moisture transport away from East Africa, and thus enhanced short rains. Similarly for Tanzania, Mapande and Reason (2005a,b) indicate that easterly flow anomalies slow eastward propagation of intraseasonal anomalies and thus allow rain-inducing convection to remain over Tanzania for longer periods of time. In our experiments, the P_{eI+wI} case also shows strengthened easterly anomalies in the second part of the year, though of lower magnitude than those seen in P_I. Only moderate easterly anomalies develop for the P_{wI} and P_{eI} cases. As previously demonstrated, the easterly anomalies in surface wind are closely linked to enhanced East African rainfall (Fig. 4.7; see also Goddard and Graham, 1999; Black *et al.*, 2003; Mapande and Reason, 2005a; Hastenrath, 2007). The development and magnitude of U_{EQ} in the different experiments presented here could thus provide an indication of the importance of the individual (and combined) SST anomaly poles.

4.8. Summary and conclusions

We have investigated the effect of a characteristic Indian Ocean SST pattern, with signatures of both the IOD and SIOD, on equatorial East African rainfall during the Oct.–Nov. season in AGCM ensemble experiments. In observations, enhanced East African precipitation is associated with Indian Ocean SST anomalies closely

resembling a tropical IOD event (Fig. 4.3; see also Black *et al.*, 2003; Clark *et al.*, 2003a). The SST anomaly pattern used in the AGCM simulations in this study is very similar to that obtained when compositing SST for years with extreme wet short rains over East Africa. In addition to employing SST anomalies over the entire Indian Ocean, we also assessed the contributions of individual (and combined) poles of the IOD and SIOD to above-average precipitation over East Africa.

Enhanced short rains in East Africa are driven predominantly by the local warm SST anomalies in the western Indian Ocean, while the eastern cold pole is of lesser importance (Fig. 4.4 and 4.5). The SST anomalies result in locally reduced SLP anomalies centered over the western Indian Ocean warm pole and the East African coast, and also extending west to the south of Africa. The SLP anomalies induce strengthened westerly airflow over central Africa and easterly onshore anomalies from the Indian Ocean intersecting over the coast of equatorial East Africa, enhancing local convective activity. Previous work linked enhanced East African rainfall and changed zonal flow anomalies to the zonal SST and zonal pressure gradient across the equatorial Indian Ocean associated with an IOD event (e.g., Saji *et al.*, 1999; Webster *et al.*, 1999; Black *et al.*, 2003). However, we demonstrate that the wind, and thus moisture, convergence over equatorial East Africa is a predominantly local response forced by the warm SST anomalies in the western tropical Indian Ocean. Despite the importance of the western pole shown here in AGCM simulations, observations suggest that the western warm pole generally occurs in concert with a cold eastern pole. Therefore, the importance placed on the zonal gradient in SST, pressure, and winds in previous observational studies seems justified. We also find that large-scale features of thermal anomalies in the atmosphere extending towards subtropical Africa seem to require the zonal gradient in SST (Fig. 4.10).

The seasonal development of characteristic indices of the zonal circulation in the equatorial Indian Ocean for the different experiments further confirms the importance of the western Indian Ocean warm pole in modulating East African rainfall. The SST anomalies associated with the various poles and the zonal gradient across the Indian Ocean intensify over the course of the year to peak during the Oct.–Nov. season. Similarly, the zonal circulation anomalies, in response to the gradually intensifying SST anomalies and to the seasonal cycle in the Indian Ocean Walker circulation, reach maximum values at the time of the East African short rains. The results suggest that the development of the anomalies in the zonal pressure gradient and especially the surface wind component is very rapid over the two months prior to the short rain season in East Africa. This has implications for the usefulness of these indices as predictors in seasonal forecasting of East African rainfall due

to a short lead time. Hastenrath *et al.* (2004) find that the sudden development of the zonal circulation cell and the lack of long-lived precursors seriously hampers its usefulness as predictors for East African rainfall. The results of the present study regarding the importance of the local western SST pole suggest that future work into predictors for western Indian Ocean SST anomalies might benefit seasonal forecasting of East African rainfall.

Acknowledgments. Use of the NCAR's CCSM3 model is gratefully acknowledged. The model simulations were run at the Australian Partnership for Advanced Computing National Facility. The CMAP precipitation, NNR data, and NOAA_ERSST_V2 SST data was provided by NOAA/OAR/ESRL PSD, Boulder, Colorado, USA, through their website http://www.cdc.noaa.gov, the GPCC data by the DWD, and CAMSOPI from NOAA NCEP CPC through the IRI data library. CCU was supported by the University of New South Wales under a University International Postgraduate Award, ASG and MHE by the Australian Research Council.

Chapter 5

Interannual Extremes in New Zealand Precipitation Linked to Modes of Southern Hemisphere Climate Variability

Caroline C. Ummenhofer and Matthew H. England

Climate and Environmental Dynamics Laboratory, School of Mathematics and Statistics, University of New South Wales, Sydney, Australia

Manuscript for: Journal of Climate
Status: published in 2007, Vol. 20, pp. 5418–5440

5.1. Abstract

Interannual extremes in New Zealand rainfall and their modulation by modes of Southern Hemisphere climate variability are examined in observations and a coupled climate model. North Island extreme dry (wet) years are characterized by locally increased (reduced) sea level pressure (SLP), cold (warm) sea surface temperature (SST) anomalies in the southern Tasman Sea and to the north of the island, and coinciding reduced (enhanced) evaporation upstream of the mean southwesterly airflow. During extreme dry (wet) years in South Island precipitation, an enhanced (reduced) meridional SLP gradient occurs, with circumpolar strengthened (weakened) subpolar westerlies and an easterly (westerly) anomaly in zonal wind in the subtropics. As a result, via Ekman transport, anomalously cold (warm) SST appears under the subpolar westerlies, while anomalies of the opposite sign occur further north. The phase and magnitude of the resulting SST and evaporation anomalies cannot account for the rainfall extremes over the South Island, suggesting a purely atmospheric mode of variability as the driving factor, in this case the Southern Annular Mode (SAM). New Zealand rainfall variability is predominantly modulated by two Southern Hemisphere climate modes, namely the El Niño-Southern Oscillation (ENSO) and the SAM, with a latitudinal gradation in influence of the respective phenomena, and a notable interaction with orographic features. While this heterogeneity is apparent both latitudinally and as a result of orographic effects, climate modes can force local rainfall anomalies with considerable variations across both islands. North Island precipitation is for the most part regulated by both local air-sea heat fluxes and circulation changes associated with the tropical ENSO mode. In contrast for the South Island, the influence of the large-scale general atmospheric circulation dominates, especially via the strength and position of the subpolar westerlies, which are modulated by the extratropical SAM.

5.2. Introduction

Located in the Southern Hemisphere in the path of the subpolar westerlies and relatively remote from other land masses, atmospheric circulation dominates New Zealand's weather and climate. Rainfall over New Zealand is influenced by the interaction of the orography of an essentially mountainous country with the atmospheric circulation (Salinger *et al.*, 1995; Salinger and Mullan, 1999). Situated in the mid-latitudes, the country experiences tropical and subtropical influences from the Pacific as well as high-latitude effects from the southern Pacific and Southern Oceans. Tropical convection in the equatorial Pacific impacts on large-scale Southern Hemisphere circulation and therefore New Zealand climate, especially during extreme years of the El Niño-Southern Oscillation (ENSO; Kidson and Renwick, 2002). Similarly, the strength and position of the subtropical jet, the subtropical high pressure belt and the subpolar westerlies influence New Zealand's climate (Clare *et al.*, 2002), as do extratropical storm tracks (Simmonds and Keay, 2000; Keable *et al.*, 2002). Interannual variability in New Zealand climate has been linked to a number of large-scale Southern Hemisphere climate modes, including the Antarctic Circumpolar Wave (ACW; White and Cherry, 1999), ENSO (Kidson and Renwick, 2002; Carleton, 2003), the high-latitude mode, more commonly termed the Southern Annular Mode (SAM; Clare *et al.*, 2002), and the Interdecadal Pacific Oscillation (IPO; Salinger *et al.*, 2001).

The complex interactions between tropical/subtropical and high-latitude influences, along with the synoptic nature of atmospheric circulation at mid-latitudes, make New Zealand's climate difficult to predict over seasonal to interannual timescales. This is exacerbated by the sparse data coverage over the Southern Hemisphere prior to 1970, which precludes analysis of a long, high-quality data record. In this study, we combine observations and reanalysis data with output from a 200-year unforced natural variability run of a coupled climate model, an approach not used for the region to date, to investigate factors influencing interannual variations in New Zealand rainfall. In a future study, we will separately investigate long-term trends in New Zealand rainfall during the second half of the 20th Century and their relation to trends in Southern Hemisphere climate modes. For the present study, our focus remains on the interannual timescale.

Previous work on New Zealand climate concentrate on the use of station (Madden *et al.*, 1999; Salinger and Mullan, 1999; Salinger and Griffiths, 2001) and reanalysis data (Mullan, 1998). To our knowledge only Renwick *et al.* (1998) use model data, in their case the Commonwealth and Scientific Industrial Research Organisation (CSIRO) limited-area model, DARLAM, nested in the CSIRO Mark 2 model

to examine spatial properties of precipitation and surface temperature across New Zealand. Their results were highly dependent on model resolution, especially the frequency of extreme events, and the authors identify deficiencies linked to an overly vigorous zonal flow in the model. In the present study, we combine direct observations, reanalysis data, and output from coupled climate models to explore New Zealand's interannual rainfall variability.

The high proportion of mountainous regions over the country's surface area, especially on the South Island, leads to considerable heterogeneity in climate fields over short distances (e.g., rainfall; Fig. 5.1). Nonetheless, attempts have been made to explain local characteristics in New Zealand climate as a result of the large-scale general circulation and its variability. For example, Mullan (1998) investigates lag associations between reanalyzed sea surface temperature (SST) and New Zealand station data of temperature, precipitation, and mean sea level pressure (MSLP) for the second half of the 20th Century. On seasonal timescales, he finds several lag relationships, some of which relate to ENSO and Indian Ocean SST, that suggest the SST surrounding New Zealand responds to variability in the general circulation. Further connections to ENSO are described by Fitzharris *et al.* (1997), relating positive (negative) New Zealand glacial mass balance to El Niño (La Niña) events. In addition, Salinger *et al.* (2001) investigate the effect of the IPO on South Pacific climate during the period 1931–1998, finding a modulating influence of the IPO on ENSO teleconnection patterns around Australia and New Zealand. By modulating the South Pacific Convergence Zone (SPCZ), the IPO is found to favor stronger ENSO teleconnections in the northeast of New Zealand during its positive phase, with El Niño (La Niña) periods being drier (wetter) since 1977. In contrast to other studies, White and Cherry (1999) relate variations in New Zealand temperature and precipitation directly to SST anomalies associated with the ACW. They find empirical orthogonal function (EOF) patterns of autumn-winter station data over New Zealand for the period 1982–1995 to vary in phase with SST anomalies. They argue that ACW-driven anomalies in SST and surface winds around New Zealand set up anomalous low-level wind convergence and cyclonicity during years of increased autumn-winter precipitation. However, their study period 1982–1995 is very short and will be extended in the present analysis and combined with output from a multi-century coupled climate model.

Apart from the above study by White and Cherry (1999), only Clare *et al.* (2002) have made a link between New Zealand rainfall and high-latitude climate modes. Clare *et al.* (2002) found a modulating influence of the SAM on end-of-summer snowlines in the Southern Alps, New Zealand. They suggest that the SAM affects snowlines via weakened (strengthened) zonal flow carrying a reduced (increased)

number of depressions over the New Zealand region during its low (high) phases. SAM influences on rainfall in other mid-latitude regions have been shown previously: e.g., for southwest Western Australia by shifting the position of the maximum temperature gradient and modulating baroclinic instability (Cai *et al.*, 2005b), across the Australian continent (Meneghini *et al.*, 2006), for South America via changes to the upper-level atmospheric circulation and moisture convergence (Silvestri and Vera, 2003), and for South Africa via shifts in the position of the subtropical jet and associated moisture flux (Reason and Roualt, 2005).

This is the first study to investigate the impact of the SAM on New Zealand interannual precipitation. In addition, we assess the respective influence of two prominent Southern Hemisphere climate modes (SAM and ENSO) on New Zealand rainfall variability, along with the associated atmospheric circulation, by using an extended simulation from a coupled climate model in combination with available observations and reanalysis data. High-quality observations in the mid- to high-latitudes of the Southern Hemisphere are sparse, especially over the oceans, and data coverage has only increased in recent years. We therefore have no high-quality extended data record for our analyses, which results in only a relatively small number of anomalously dry and wet years employed in composites. Using output from a 200-yr unforced natural variability coupled climate model run provides an additional means of assessing modes of New Zealand rainfall variability. In particular, the model time-series includes approximately 30 anomalously dry and wet years in the composites, which allows an independent assessment of the robustness of the reanalysis findings. This is an approach used successfully in previous studies for other regions of the Southern Hemisphere (e.g., England *et al.*, 2006). Of particular interest in this study are the relative roles of the SAM and ENSO in controlling interannual New Zealand rainfall variability via changes to the large-scale ocean and/or atmospheric circulation. This will be investigated in more detail with composites during extreme phases of ENSO and the SAM, complementing the approach of compositing anomalously high/low rainfall years across New Zealand.

The rest of the paper is outlined as follows: Section 5.3 describes the data sets and the model, as well as the methods and techniques used. Section 5.4 details precipitation observations across New Zealand and composites of reanalysis and model data during years of anomalously high and low precipitation. In Section 5.5, relationships between New Zealand precipitation and Southern Hemisphere climate patterns are investigated in more detail. Section 5.6 summarizes the results of the study.

5.3. Data and data analysis

5.3.1. Observational data

The observational New Zealand precipitation data analyzed in this study is taken from the National Institute of Water and Atmospheric Research (NIWA) Climate Database. It comprises daily New Zealand station data that has been interpolated to give a gridded data set with a 0.05° latitude/longitude (approximately 5 km) resolution for the entire country. The daily gridded precipitation data is converted to monthly and annual rainfall totals for the time period 1960–2004.

The data for regional and large-scale analysis of atmospheric parameters, such as sea level pressure (SLP), surface winds, and surface heat and moisture fluxes, amongst others, is part of the National Center for Environmental Prediction (NCEP) and National Center for Atmospheric Research (NCAR) reanalysis project (Kalnay *et al.*, 1996; Kistler *et al.*, 2001). The NCEP/NCAR reanalysis assimilates land- and ocean-based observations and satellite measurements and, by employing a global spectral model, generates a data set with global coverage for a wide set of climatic parameters with a horizontal resolution of T62 (approximately 2° latitude/longitude) going back to 1948. However, we only analyze monthly data for the same time period as the rainfall observations, i.e. 1960–2004. Problems regarding data coverage and quality in the high latitudes of the Southern Hemisphere prior to 1979 have been documented (Hines *et al.*, 2000; Marshall and Harangozo, 2000; Kistler *et al.*, 2001; Marshall, 2002, 2003; Renwick, 2004). However, on seasonal to interannual timescales the NCEP/NCAR reanalysis fields are in overall good agreement with observations (Hines *et al.*, 2000; Kistler *et al.*, 2001). In addition, for comparison, the analyses are repeated with the European Centre for Medium-Range Weather Forecasting (ECMWF) 40-year reanalysis (ERA-40) for the period 1960–2001 (Uppala *et al.*, 2005). Monthly SST is employed for 1960–2002 from the extended reconstructed data set developed by the National Oceanic and Atmospheric Administration (NOAA) with a 2° latitude/longitude resolution (Smith and Reynolds, 2003, 2004). All analyses are performed on annually averaged data.

5.3.2. Climate model

Apart from analyzing the above climatologies, we also examine the mechanisms controlling New Zealand rainfall within a 200-year unforced natural variability run of the NCAR Community Climate System Model, version 2 (CCSM2; Kiehl and Gent, 2004). The atmospheric component of CCSM2 uses a spectral dynamical core, a T42 horizontal resolution (approximately 2.8° latitude/longitude), and 26 vertical levels. The ocean component is based on the Parallel Ocean Program (POP)

and its grid uses spherical coordinates in the Southern Hemisphere. Its horizontal resolution is constant in longitude (1.125°), but varies with latitude from 0.27° in the tropics to 0.5° at mid- to high latitudes. In the vertical there are 40 geopotential levels at 10 m resolution from the surface down to 50 m, and increasing towards 250 m intervals in the abyssal ocean. For further information on the CCSM2 model and its components see Kiehl and Gent (2004) and Boville and Gent (1998). Key model analyses are repeated with the latest version of the NCAR's coupled climate model, CCSM3, details of which can be found in Collins *et al.* (2006). The mean annual model rainfall for the New Zealand region is compared to the Climate Prediction Center (CPC) Merged Analysis of Precipitation (CMAP; Xie and Arkin, 1996) climatology for the period 1979–2004. The CMAP data set has an approximately 2.5° latitude/longitude resolution and combines satellite measurements, gauge-based analyses from the Global Precipitation Climatology Center, and operational forecast data from ECMWF.

5.3.3. Data analysis and statistical methods

Given the relatively large latitudinal extent of New Zealand, we have stratified our analyses separately for the North and South Islands. For each island, time-series are calculated of the monthly and annual mean precipitation as a spatial area-average. For the observed annual rainfall records, the least squares linear trend (-8.13 mm yr^{-1} and -0.03 mm yr^{-1} for the North and South Island, respectively) is removed, along with the mean, to give a detrended time-series of anomalies. This time-series forms the basis for our analysis of anomalously dry and wet years in New Zealand rainfall.

Due to the coarser resolution of the coupled CCSM2 model two slightly larger regions are formed for the South and North Islands, respectively (see boxes in Fig. 5.1). The first region (40.5°–46.0°S, 165.9°–174.4°E, consisting of 3 x 4 grid boxes) coincides with the South Island of New Zealand and the other one (34.9°–43.3°S, 171.6°–180.0°E, consisting of 4 x 4 grid boxes, though the southwestern most grid box overlapping the South Island has been excluded) with the North Island. Though not all gridboxes used to form the model rainfall time-series for the two islands are exclusively land-points, most are covered by at least some fraction of land. Only a negligible linear trend is discernible for the model precipitation time-series for both regions, so the time-series are not detrended. This contrasts the observations, particularly for the North Island, where a clear multi-decadal decline is apparent. However, with the model data resulting from an unforced natural variability simulation, we expect and are reassured by the absence of any long-term trends.

For both observations and model, composites of anomalies are formed for years

of extreme precipitation from the anomalous precipitation time-series for the two islands of New Zealand. Years exceeding the cut-off value of ±1 standard deviation are considered wet and dry years, respectively. While we stratify our analyses into North and South Island rainfall, we do not propose *a priori* that one island will uniformly respond to any given mode of climate variability, nor that a given climate mode projects onto each island distinctly. Indeed, we will see later that dry (wet) years for each island are also associated with significant regions of below (above) average rainfall for the adjacent New Zealand island. Throughout the study, we use a two-tailed t-test to determine the significance of the spatial composite fields. This test estimates the statistical significance by which the mean of the composite anomalies for extreme years is distinguishable from zero at each grid point.

Extreme year composites of anomalous New Zealand rainfall observations are compared to patterns associated with ENSO and the SAM. The years taken as El Niño and La Niña years are taken to be those defined by Meyers *et al.* (2007) for the period 1960–1999. All eight El Niño years occurring during this period were defined as certain while this was true for only four out of ten La Niña years. However, as separate analyses for certain and debatable La Niña years gave very similar results, composites for all ten La Niña events are presented here. There is no general consensus on ENSO years after 1999, but increased Niño-3 temperatures occurred during 2002 (Gary Meyers 2006, personal communication). Thus, the year 2002 was included as an additional El Niño year. The monthly SAM index used here (Todd Mitchell 2006, personal communication) is the principal component (PC) time-series of the leading EOF of NCEP/NCAR reanalyzed SLP anomalies south of 20°S, standardized with respect to the period 1979–2004. The index is highly correlated with that of Thompson and Wallace (2000), which is based on 850 hPa geopotential height, for the period in common, i.e. for 1958–1997 (Todd Mitchell 2006, personal communication). For details see http://www.jisao.washington.edu/aao/slp. A SAM index based on NCEP/NCAR reanalyzed SLP has been used previously (e.g., Gong and Wang, 1999) and Jones and Widmann (2003) further discuss its validity. As described above, the monthly SAM index is converted to annual values and detrended before determining extreme years of the SAM; i.e. those exceeding ±1 standard deviation from the detrended mean. This results in eight extreme positive and eight extreme negative SAM years. It is noted that we also analyzed composite properties derived from monthly extremes in the SAM, and obtained qualitatively similar results, as would be expected when the SAM directly controls New Zealand rainfall via internal atmospheric variability. For the model, ENSO and SAM years were determined similarly as those exceeding ±1 standard deviation in the time-series. The ENSO years were derived from an annual Niño-3.4 index calculated from SST

anomalies for the region 5°N–5°S, 120°–170°W. The SAM years were calculated from the annual PC time-series of the first leading EOF performed on SLP anomalies south of 20°S. Both time-series were detrended and normalized by dividing by their standard deviation.

5.4. Results

5.4.1. Precipitation observations

The NIWA precipitation observations show high spatial variability in rainfall over New Zealand. Precipitation patterns for the North and South Island are distinctly different both in overall rainfall amounts and their seasonal distribution (Fig. 5.1, 5.2). The high-rainfall region along the mountainous west coast of the South Island is dominant throughout the year with mean annual values in excess of 6000 mm yr^{-1} (Fig. 5.1). The eastern part of the South Island receives considerably less rainfall at an average of about 600–1500 mm yr^{-1}. The North Island does not show such a clear gradation in either the east-west or north-south sense. Rainfall there is mostly in the range 900 and 3000 mm yr^{-1}, with a few highly localized high-rainfall regions in excess of 4000 mm yr^{-1}.

For the period 1960–2004, the area-averaged annual mean rainfall for the North Island (1600 mm yr^{-1}) is comparatively lower than the South Island (2085 mm yr^{-1}). A prominent trend (-8.13 mm yr^{-1}) of overall decreasing precipitation is observed over the North Island for the period 1960–2004 (removed in Fig. 5.2b). In contrast, only a negligible trend (-0.03 mm yr^{-1}) appears in the area-integrated South Island precipitation record. Anomalously dry and wet years for both the South and North Islands are indicated in Fig. 5.2a, b as those years exceeding one standard deviation from the annual mean. For the period 1960–2004, only very few extreme years are shared between the two islands, namely 1961 (dry), 1968 (wet), and 1995 (wet) (see also Table 5.1). One year, 1983, appears as an extreme year of opposite sign; being anomalously dry for the North Island and wet for the South Island. Extreme years for the North (South) Island include seven (eight) dry and eight (ten) wet years during the length of the record investigated (Table 5.1).

The characteristics of the two islands also differ in their respective seasonal cycles (Fig. 5.2c, d): the South Island precipitation occurs more or less uniformly throughout the year, while the North Island shows slightly increased monthly rainfall during austral winter (May–October). Precipitation in anomalous high and low rainfall years for the South Island deviates mostly from the mean rainfall distribution during early austral spring (August–October), and less so for autumn (March–May; Fig. 5.2c). In contrast, for the North Island, the seasonal rainfall distribution dur-

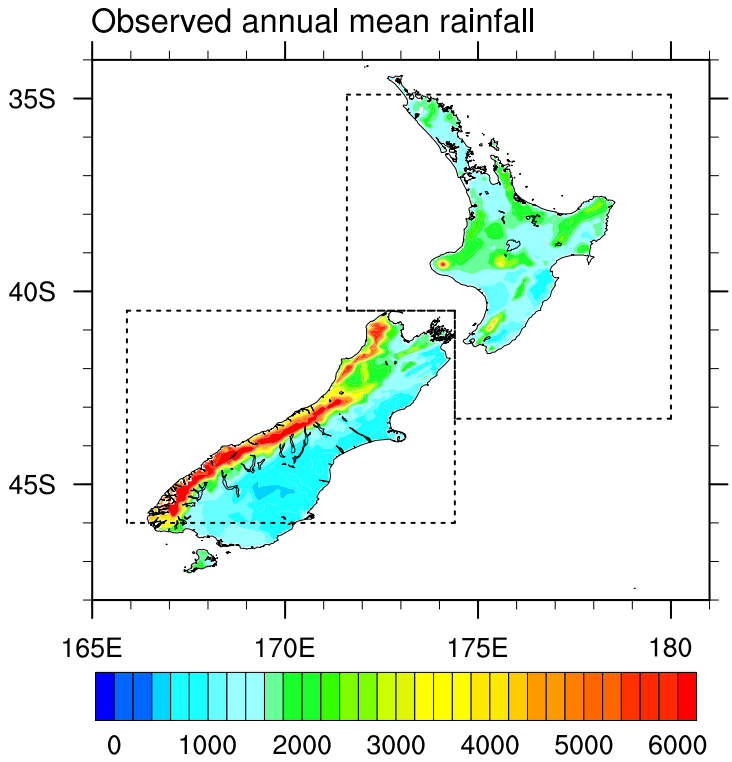

Figure 5.1. Annual mean precipitation map for New Zealand for the period 1960–2004 (in mm yr^{-1}). The thin dashed boxes indicate the areas over which a spatial average was employed to calculate the model precipitation time-series for the North and South Island, respectively, in the NCAR CCSM2 unforced natural variability simulations.

ing dry and wet years mirrors the average seasonal cycle closely (Fig. 5.2d). The distribution of rainfall is not significantly different from a uniform value (at 90% confidence level) for both the North and South Island. This allows us to concentrate our analyses on the annual mean fields.

A power spectral density analysis is performed for both observed and model annual precipitation time-series as follows: the mean and least squares linear trend are removed, smoothing is applied, and 10% of the data is tapered. A theoretical "white noise" spectrum is calculated to determine frequencies dominant at the 90% significance level. The power spectral density analysis reveals no high-frequency variability to be significant for either of the two islands (Fig. 5.2e, f), confirming that sub-annual variability is weak compared to year-to-year fluctuations. This lends further support to an analysis of interannual, not intra-annual rainfall variability over New Zealand. At longer timescales, broad peaks occur at approximately 4 years for the South Island and at approximately 4.5 and 3 years for the North Island.

In addition to the temporal variability, the spatial variation of rainfall across New Zealand during extreme years for both islands is presented in Fig. 5.3. It shows

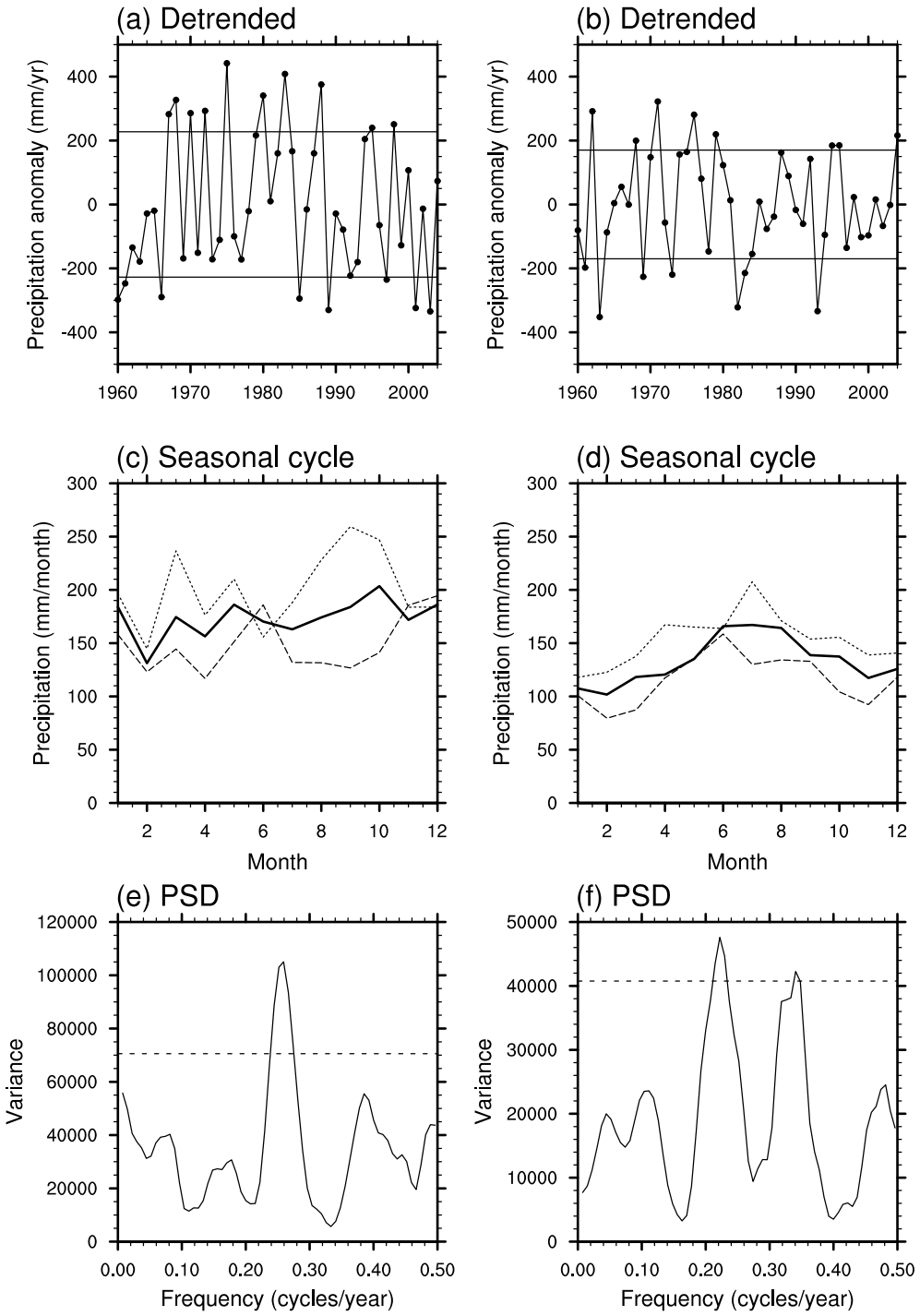

Figure 5.2. Characteristics of observed precipitation time-series for the South (left) and North Island (right): (a, b) detrended annual anomalies in mm yr^{-1} with horizontal lines indicating cutoff values for extreme years; (c, d) seasonal cycle (mm $month^{-1}$) averaged over all years (solid line) or only dry (dashed) and wet (dotted) years, respectively; (e, f) power spectral density with theoretical white noise spectrum at the 90% confidence level.

Table 5.1. Years of anomalous precipitation for the South and North Islands of New Zealand for the period 1960–2004 (determined as those years exceeding the cut-off value of ±1 standard deviation). ±EN indicates El Niño and La Niña years (as defined by Meyers *et al.*, 2007) and ±SAM indicates positive and negative years for the Southern Annular Mode.

Island	Dry	Wet
South Island	1960	1967
	1961	1968
	1966	1970
	1985 (+SAM)	1972 (+EN, -SAM)
	1989 (+SAM)	1975 (-EN)
	1997 (+EN)	1980 (-SAM)
	2001	1983
	2003 (-SAM)	1988 (-EN)
		1995
		1998 (+SAM)
North Island	1961	1962 (+SAM)
	1963 (+EN)	1968
	1969	1971
	1973 (-EN, +SAM)	1976
	1982 (+EN)	1979 (+SAM)
	1983	1995
	1993 (+SAM)	1996
		2004

extreme years for both the North and South Island to be consistently dry/wet for the entire island. During dry years in the South Island, the entire southern island and southern regions of the North Island receive 100–400 mm yr^{-1} below normal precipitation (Fig. 5.3a). Wetter conditions in excess of 200 mm yr^{-1} only prevail along the very northern and eastern coast of the North Island. South Island wet years are characterized by wetter conditions for the entire western and southern regions of the two islands, with negligible changes along the eastern coastlines (Fig. 5.3b). For the North Island dry (wet) years, anomalously low (high) rainfall in excess of 200 mm yr^{-1} occurs for the entire North Island and northern and eastern regions of the South Island (Fig. 5.3c, d). In contrast along the west coast of the South Island, dry conditions dominate in both dry and wet North Island years. Overall though, the anomalous patterns of rainfall indicate "all-island" responses for both dry and wet years for each island. That is, each island exhibits a coherent below- and above-average rainfall pattern, on average, during years of anomalous total island rainfall.

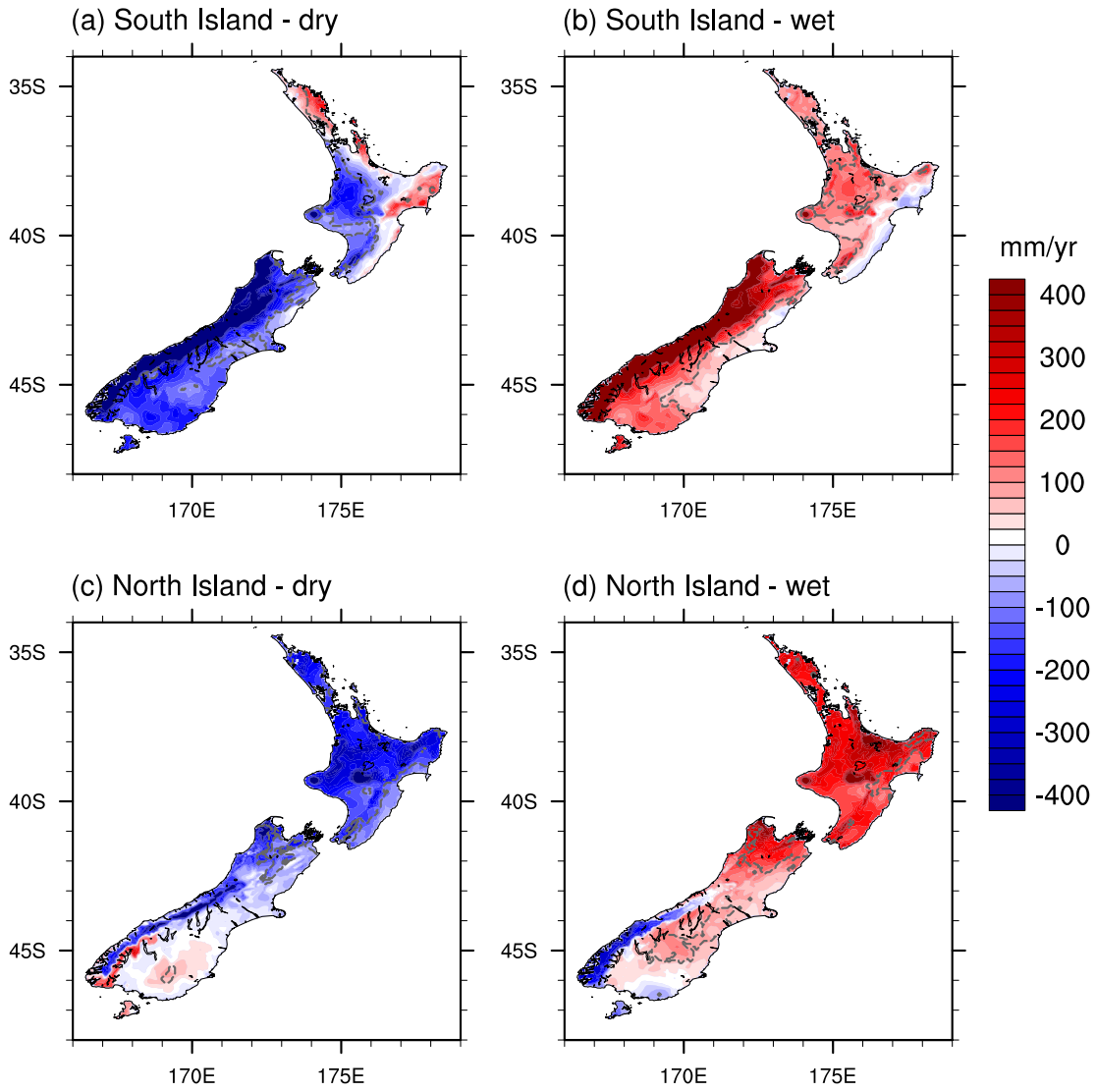

Figure 5.3. Composites of observed precipitation anomalies for (a, b) South Island and (c, d) North Island anomalously dry (left) and wet (right) rainfall years. Gray dashed lines indicate significant anomalies at the 90% confidence level as estimated by a two-tailed *t*-test.

5.4.2. Climate during New Zealand extreme years

5.4.2.1. Reanalysis fields. Composites of various atmospheric NCEP/NCAR reanalyzed fields are investigated for anomalous rainfall years in the two New Zealand islands during the period 1960–2004 (Fig. 5.4, 5.5). During South Island dry (wet) years, an intensification (weakening) of the meridional SLP gradient occurs (Fig. 5.4a, b). Significant positive (negative) anomalies (in excess of ±1.5 hPa) appear across a latitude band 30°–60°S from the subtropical Indian Ocean to the middle of the Pacific basin. Composites for anomalous rainfall years over the North Island show less of a circumpolar pattern in SLP anomalies (compare Fig. 5.4a, b to

5.5a, b), instead exhibiting a dipole pattern. One significantly positive (negative) pole during dry (wet) years occurs across New Zealand and eastern Australia, and the other negative (positive) pole is located to the east of New Zealand across the subtropical south Pacific gyre. The circumpolar nature of the SLP anomalies, especially for the South Island anomalously dry and wet years, is reminiscent of the pattern widely associated with the SAM (e.g., Gong and Wang, 1999; Thompson and Wallace, 2000).

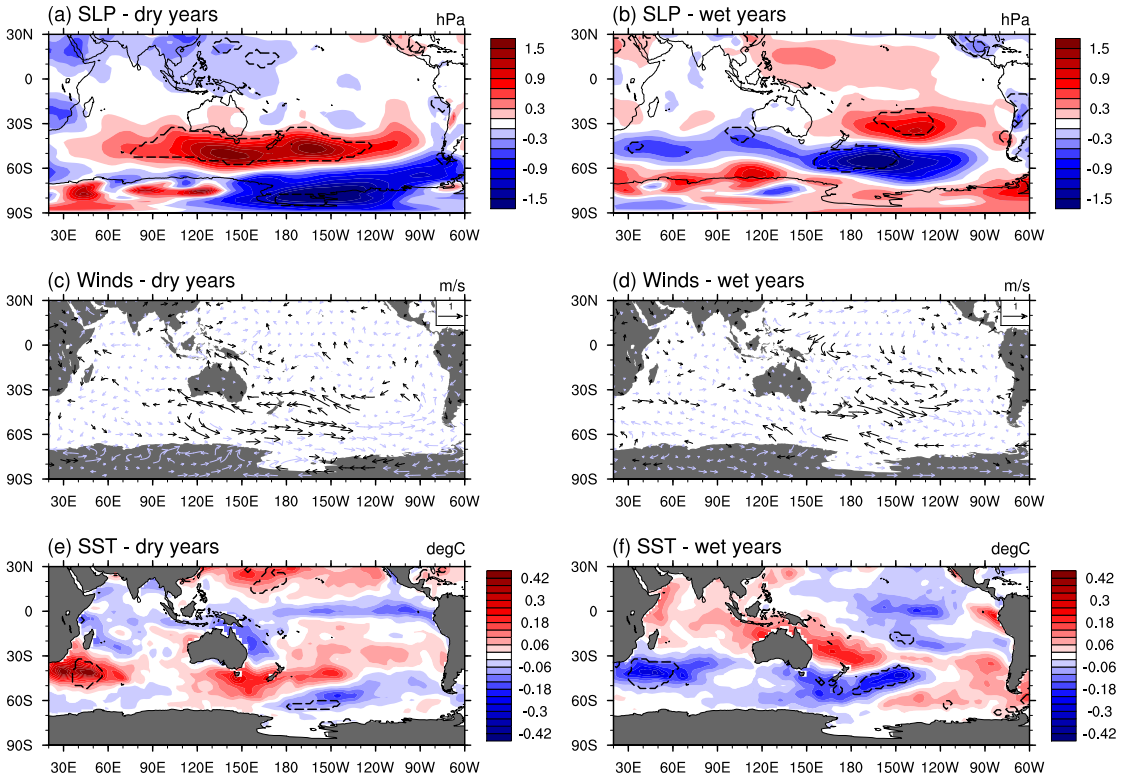

Figure 5.4. Composite anomalies in observed (a, b) SLP, (c, d) winds, and (e, f) SST for the South Island anomalously dry (left) and wet (right) rainfall years. Dashed lines and black vectors indicate significant anomalies at the 90% confidence level as estimated by a two-tailed *t*-test.

The anomalous SLP fields force, according to geostrophy, changed zonal wind fields of a similar circumpolar nature for South Island anomalous rainfall years (Fig. 5.4c, d). A strengthening (weakening) of the subpolar westerlies is observed during years of dry (wet) South Island extremes at 50°–70°S, while a weakening (strengthening) of a similar magnitude (up to ± 0.8 m s^{-1}) is seen to the north for the latitude band 30°–50°S. These changes in zonal wind are again characteristic of the increased MSLP gradient between mid- and high-latitudes linked to the SAM (Thompson and Wallace, 2000; Hall and Visbeck, 2002). Associations between the SAM and extratropical storm tracks, as described by Rao *et al.* (2003), and ob-

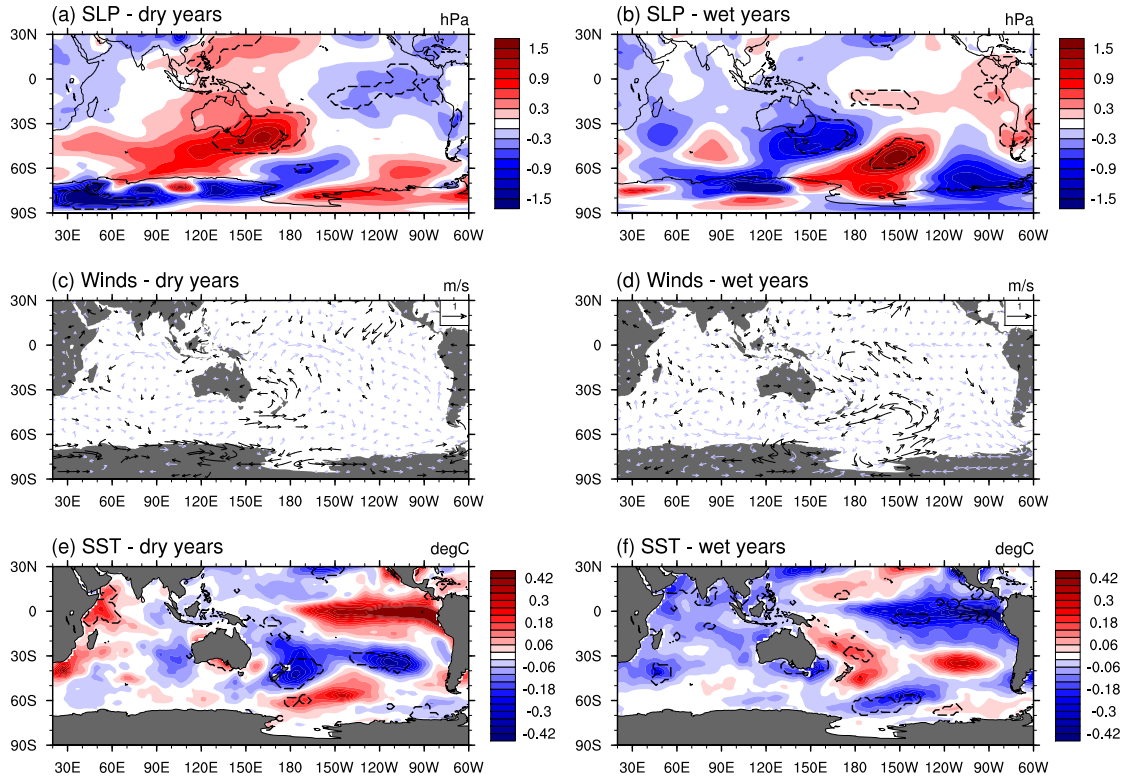

Figure 5.5. Composite anomalies in observed (a, b) SLP, (c, d) winds, and (e, f) SST for the North Island anomalously dry (left) and wet (right) rainfall years. Dashed lines and black vectors indicate significant anomalies at the 90% confidence level as estimated by a two-tailed t-test.

served and projected poleward shifts in the position of the storm tracks under a more positive SAM phase (Fyfe, 2003; Yin, 2005) could account for the reduced rainfall across the South Island during dry years. Dry (wet) years also coincide with more southerly (northerly) wind anomalies across New Zealand, and especially over a region to the northeast of the country (Fig. 5.4c, d), affecting local moisture transport onto the islands. Regions of positive (negative) westerly anomalies across New Zealand during dry (wet) North Island years stretch in a southwest-northeast direction from 120°E–150°W and 30°–70°S (Fig. 5.5c, d). These anomalies are followed further north by a similar band of easterly (westerly) wind anomalies across Tasmania and eastern Australia. The New Zealand region and adjacent ocean also experiences southerly (northerly) wind anomalies during dry (wet) North Island years (Fig. 5.5c, d), varying local moisture fluxes. Composite anomalies of ERA-40 SLP and winds (figures not shown) indicate qualitatively very similar results, though the level of significance differs slightly and the circumpolar character of the anomalies is marginally more pronounced in ERA-40.

Localized changes in moisture flux due to local wind anomalies seem to be more

important for the North Island of New Zealand. Humidity is generally reduced (increased) during dry (wet) years in northern New Zealand over the land itself and the surrounding ocean regions (figure not shown), due to reduced (increased) latent heat flux from the ocean in the immediate vicinity of the island (figure not shown). This, along with the anomalous offshore (onshore) local winds, contributes to dry (wet) conditions over the North Island. In contrast, anomalous composite fields of humidity and latent and sensible heat fluxes during anomalously dry and wet South Island years show no consistent patterns to explain the rainfall anomalies. This issue will be revisited below for the model simulations.

Anomalous composite fields of SST indicate warm (cold), though mainly insignificant, anomalies (up to ± 0.3°C) around New Zealand and the Tasman Sea during dry (wet) South Island years (Fig. 5.4e, f). Smaller anomalies of the opposite sign, i.e. cold (warm) during dry (wet) years occur to the north of New Zealand and across the Coral Sea. The small area of statistically significant SST anomalies in the composites is in part symptomatic of the short observational record (1960–2002), resulting in few extreme years (7–10 anomalously dry/wet years). This signal has to then be compared in significance to the natural year-to-year variability in SST (Fig. 5.6c). So, small areas of significance do not necessarily imply that rainfall over the two islands is largely atmospheric driven. To resolve this issue we investigate latent heat fluxes and employ output from a 200-yr natural variability run of the CCSM2 model, providing approximately 30 anomalously dry and wet years (see next section). As seen in composites of latent heat fluxes (figure not shown) these SST anomalies are indeed not significantly contributing to the observed rainfall anomalies via changes in the evaporation. The SST anomalies are rather symptomatic of the changed general atmospheric circulation during dry (wet) South Island years: the poleward (equatorward) shift and strengthening (weakening) of the subpolar westerlies south of 50°S and easterly (westerly) anomaly to the north for the latitude band 30°–50°S lead to anomalously warm (cold) SST for the latitude band 40°–60°S (Fig. 5.4e, f) likely due to anomalous wind-driven Ekman transport. In contrast, during North Island dry (wet) years, cold (warm) anomalies around New Zealand dominate, with a small area of opposite sign along the east Australian coast (Fig. 5.5e, f). These SST anomalies can account for the anomalous latent heat fluxes described earlier and thereby contribute via reduced (increased) evaporation and changed local wind fields to dry (wet) conditions for northern New Zealand. These results suggest that northern New Zealand climate is influenced by local air-sea heat fluxes. In contrast, rainfall anomalies over the South Island are controlled by the large-scale general circulation. In addition, a prominent, though non-significant, El Niño- (La Niña-) type warming (cooling) in excess of ± 0.4°C is observed in the eastern tropical Pacific

Ocean during dry (wet) North Island years, suggestive of a possible ENSO influence on the northern island's precipitation.

5.4.2.2. Model. To assess the suitability of the CCSM2 model for this study, we compare the model variability in SST and SLP in the region to observations (Fig. 5.6). This simple analysis helps reveal the relative intensity and patterns of ENSO and SAM in comparison to the observations.

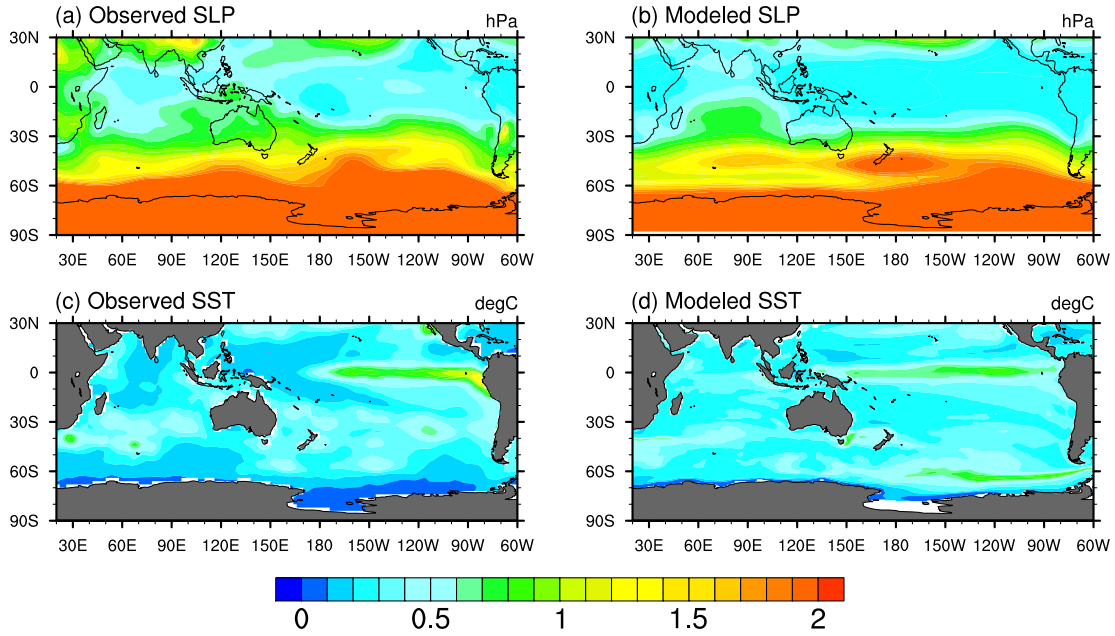

Figure 5.6. Standard deviation in observations (left) and the CCSM2 model (right) of (a, b) annual mean SLP (hPa) and (c, d) annual mean SST (°C). The observations cover the period 1960–2004 for SLP and 1960–2002 for SST, the model output is for 200 years.

The standard deviation of SLP shows a latitudinal gradient in the observations with higher variability (in excess of 1.8 hPa) in the high latitudes south of 60°S, diminishing to 1–1.5 hPa in the mid-latitudes and less in the tropics (Fig. 5.6a). The broad features of the latitudinal gradient of the SLP standard deviation is reproduced well in the model (Fig. 5.6b). However, over New Zealand and the Tasman Sea, the model shows slightly higher variability than the observations, while a band of lower variability in the model extends across the Indian Ocean sector of the Southern Ocean between 50°–60°S. Sen Gupta and England (2006) found that the SAM projects too strongly onto SST, but the effect on winds (especially zonal flow) is well captured in the model. They suggest that the disagreement in the SST response to the SAM forcing between the model and observations is due in part to the short observational record and sparse data coverage in the high latitudes

of the Southern Hemisphere. The SST variability in the equatorial Pacific Ocean in the model and observed differ in their magnitude, with the observed showing greater variance in the eastern equatorial Pacific, and lower variance in the western Pacific warm pool region compared to the model (Fig. 5.6c, d). The extension of the model's ENSO pattern too far west in the Pacific Ocean (Fig. 5.6d) was described in detail by Kiehl and Gent (2004) and Collins *et al.* (2006). The ENSO in the model also has a dominant frequency of around 2–3 years (e.g., Kiehl and Gent, 2004; Collins *et al.*, 2006), which compares with the longer period of 3–5 (Collins *et al.*, 2006), 3–7 (Kiehl and Gent, 2004), or 3–8 (Zelle *et al.*, 2005) years in the observed. However, for the scope of this study, reasonable agreement between the model and observations is found on interannual timescales for the spatial and temporal variability of the SAM and ENSO, as shown previously by Sen Gupta and England (2006) and Hack *et al.* (2006), respectively. To further corroborate this we repeated key analyses with output from the CCSM3 model and ERA-40 and found qualitatively similar results and conclusions.

Comparison of the annual mean CCSM2 model precipitation with the CMAP climatology shows that the model reproduces the large-scale features in rainfall over the southwestern Pacific region reasonably well (Fig. 5.7). The high-rainfall region over the equatorial western Pacific is captured, as is the low-rainfall domain over the interior of the Australian continent. The extent and position of the Intertropical Convergence Zone (ITCZ) and SPCZ in the model show some deficiencies. Details of the model's performance in the ITCZ and SPCZ in the western Pacific region can be found in Kiehl and Gent (2004), Collins *et al.* (2006) and Hack *et al.* (2006). Biases in the characteristics of the Pacific ITCZ are common to many coupled climate models (Kiehl and Gent, 2004; Zhang and Wang, 2006), particularly those without flux adjustments (Meehl *et al.*, 2001). In CCSM3 as in previous versions, a persistent bias exists towards a double ITCZ and too strong a SPCZ extending too far to the southeast into the central Pacific Ocean (Collins *et al.*, 2006; Hack *et al.*, 2006). However, Hack *et al.* (2006) conclude that the hydrological cycle in the atmospheric component of CCSM3 more closely resembles observations compared to previous model versions and captures the major features of the water cycle well on seasonal to interannual timescales, also as associated with ENSO. After comparing our results for both the CCSM2 and CCSM3 models, we conclude that the precipitation representation in the southern Pacific is sufficiently good on interannual timescales. Nonetheless, we have carefully assessed our results for CCSM2 and compared them to both reanalyses and observations over the New Zealand region, as well as CCSM3 results. Over New Zealand, the very localized region of enhanced precipitation along the mountainous west coast of the South Island in CMAP is apparent in the model

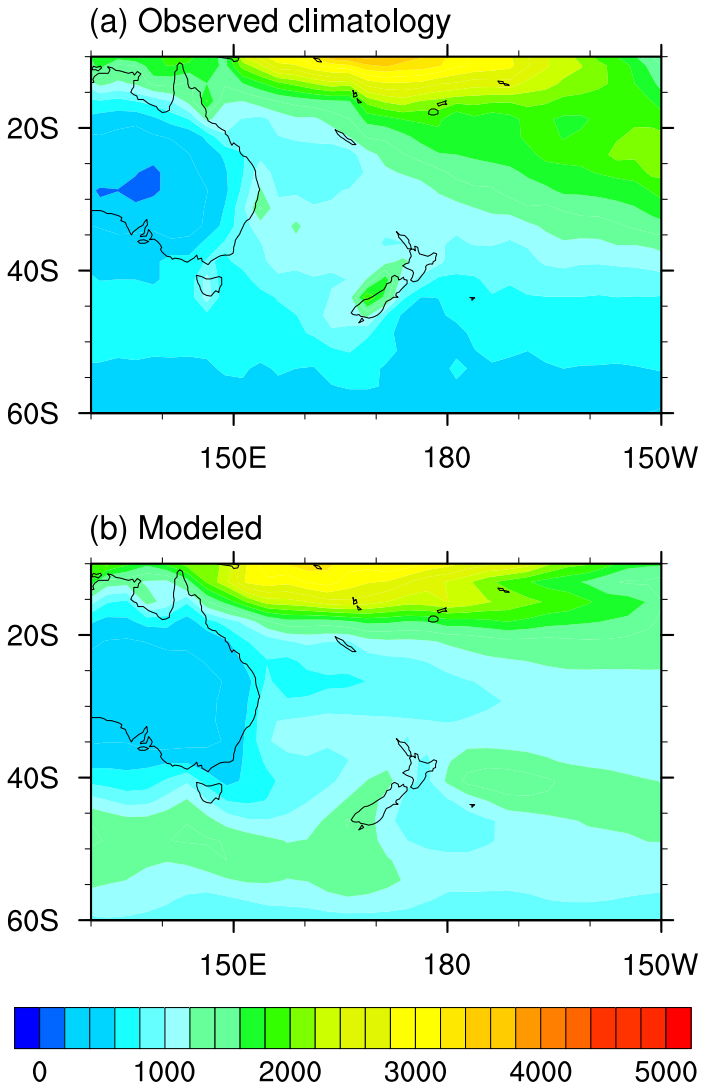

Figure 5.7. Annual mean precipitation for (a) the CMAP climatology for the period 1979–2004 and (b) the model (both in mm yr^{-1}).

as well, though lower in magnitude and extending over a wider area. The difference in observed rainfall between the North and South Islands are also reproduced in the model (Fig. 5.7b), even if the absolute rainfall amounts are reduced for both islands compared to the observations.

A detailed analysis of the time-series of the 200 years of New Zealand precipitation fluctuations (Fig. 5.8) also shows the model captures two different regimes over the two New Zealand islands. Though the model rainfall anomalies for the two islands are smaller, they are of similar magnitude in relation to the annual precipitation as in the observed (i.e. 13–15% of the mean annual precipitation). The annual mean precipitation for the South and North Island is 1150 mm yr^{-1} and 1060 mm yr^{-1}, respectively. Following the method described above, years with anomalous high

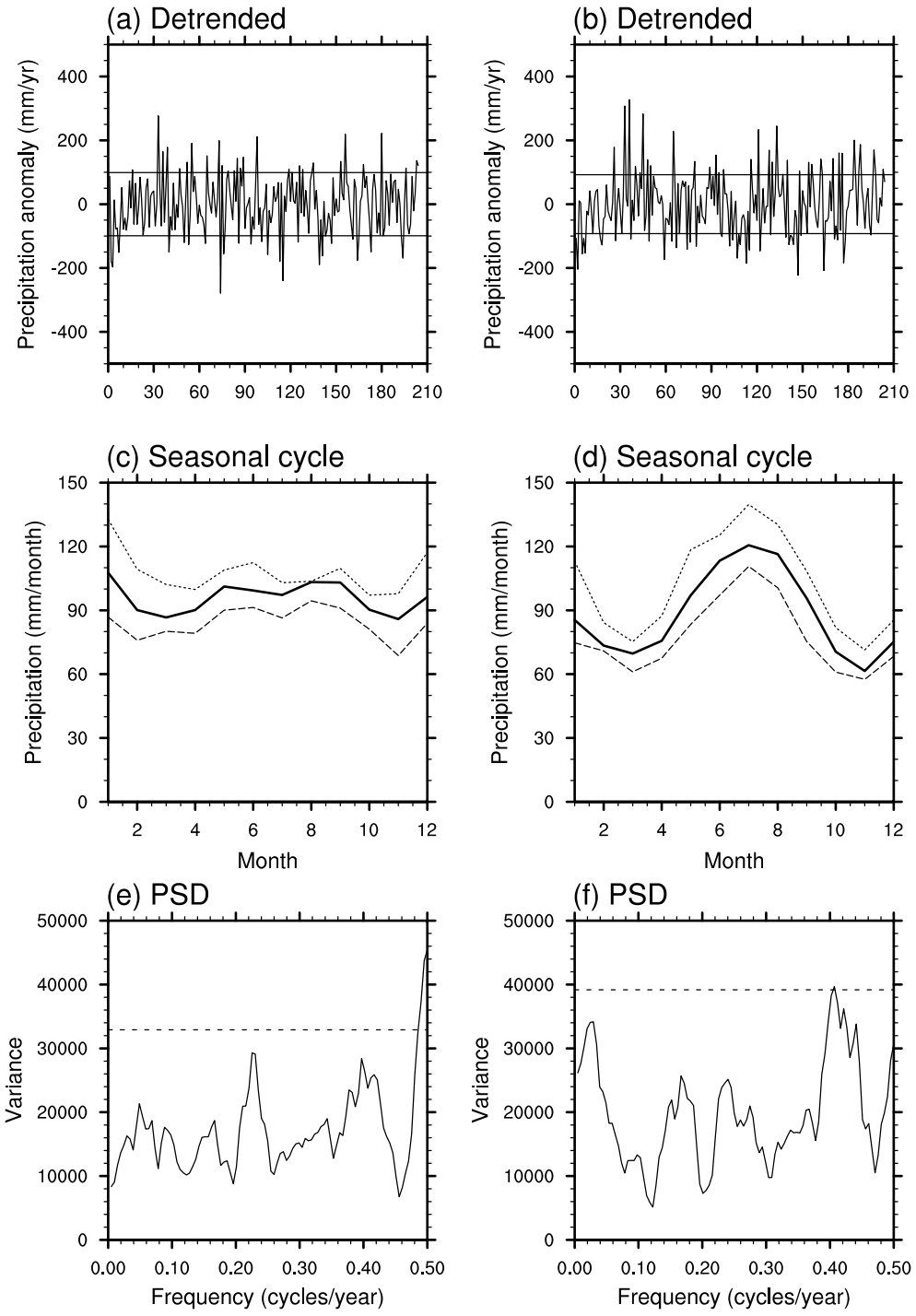

Figure 5.8. Characteristics of model precipitation time-series for the South (left) and North Island (right): (a, b) annual anomalies in mm yr^{-1} with horizontal lines indicating cutoff values for extreme years; (c, d) seasonal cycle (mm $month^{-1}$) averaged over all years (solid line) or only dry (dashed) and wet (dotted) years, respectively; (e, f) power spectral density with theoretical white noise spectrum at the 90% confidence level.

and low precipitation are chosen as those exceeding ±1 standard deviation of the mean, resulting in 30 (31) anomalously low (high) rainfall years for the South and 32 (30) anomalously dry (wet) years for the North Island (Fig. 5.8a, b). The relative proportion of extreme events is comparable with about 8 dry/wet years each in 45 years of observations and about 31 of each in 200 years of model time. Like the observed, the precipitation over the southern part of New Zealand is more or less uniform throughout the year, varying between 90 and 110 mm month^{-1} (Fig. 5.8c). As also seen in the observed, there is a noticeable seasonal cycle in the North Island precipitation data (Fig. 5.8d), with mean peak rates of up to 120 mm month^{-1} during austral winter, declining steadily to a low-rainfall season of only 75–90 mm month^{-1} for austral summer. The seasonal cycle in North Island rainfall might be enhanced in the model due to the previously mentioned bias in the ITCZ and an excessively strong SPCZ, which is most prominent during June–August (Hack *et al.*, 2006; Zhang and Wang, 2006), when the observed SPCZ normally weakens (Collins *et al.*, 2006). However, as is generally accepted, New Zealand rainfall occurs essentially uniformly throughout the year (Garnier, 1958), with neither the model nor observed seasonality being statistically significant at the 90% confidence level. Spectral analysis (Fig. 5.8e, f) also indicates a difference in dominant frequencies for the two regions: for the South Island, peaks occur at approximately 4.3 and 2 years, while the North Island shows a significant peak at approximately 2.9 years, which happens to be in the range of the frequency associated with ENSO in the model (e.g., Kiehl and Gent, 2004; Collins *et al.*, 2006). Overall, considering the coarse resolution of the coupled climate model and the very localized nature of New Zealand precipitation, the model represents the overall regional rainfall characteristics surprisingly well (Fig. 5.7 and 5.8).

The spatial distribution of significant precipitation anomalies during dry and wet South and North Island years in the model shows considerable large-scale features centered over the respective islands (Fig. 5.9). Naturally, the model's coarse grid cannot resolve the rich orography of each island, so our comparison is focused on large spatial scales, where they agree broadly with the observations (refer to Fig. 5.3). Dry (wet) South Island years are characterized by below (above) normal rainfall (in excess of 200 mm yr^{-1}) across the country with the exception of the very northern coast of the North Island experiencing wet (dry) conditions (Fig. 5.9a, b). This out-of-phase relationship of the north coast rainfall with the remaining country during South Island dry years is encountered in the observations as well, though over a slightly larger area (Fig. 5.3a). For North Island anomalous rainfall years, a clear latitudinal gradation in rainfall anomalies is seen, with southern regions of the South Island experiencing progressively smaller anomalies (Fig. 5.9c, d). Again, the very

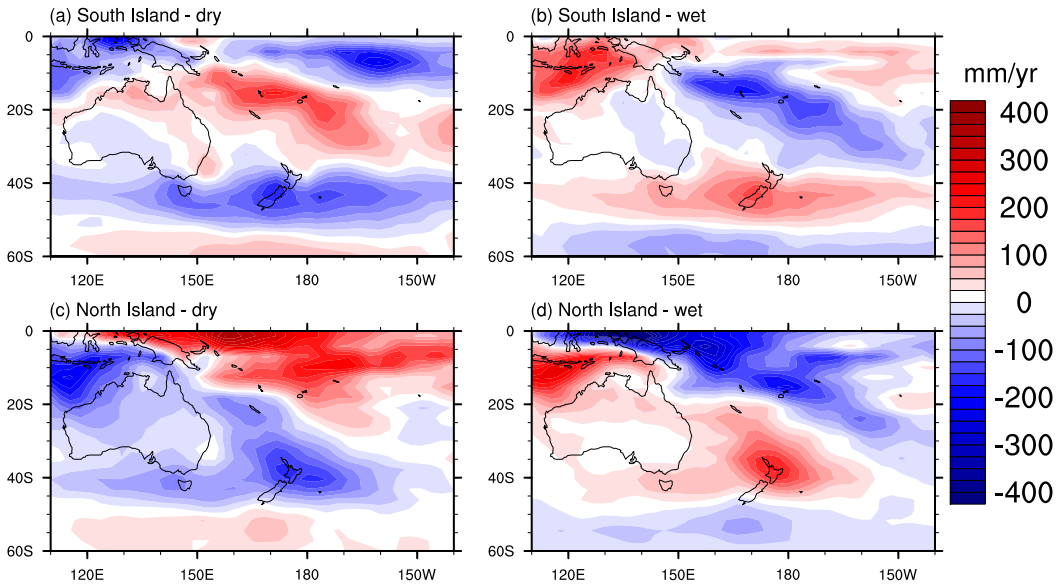

Figure 5.9. Composites of model precipitation anomalies for (a, b) South Island and (c, d) North Island anomalously dry (left) and wet (right) rainfall years. Color shaded regions indicate significant anomalies at the 90% confidence level as estimated by a two-tailed t-test.

southern tip of the South Island shows out-of-phase rainfall anomalies with the rest of the country, reminiscent of the observations (Fig. 5.3c, d). Meridional gradients in rainfall anomalies for New Zealand extreme years are well represented in the model, while it does not capture observed zonal features due to the inability to resolve the rich orography of the north-south oriented mountain ranges across New Zealand.

Composites of anomalies of a range of variables in the model during years of anomalous precipitation are shown in Figs. 5.10, 5.11, and 5.12. During dry (wet) years for the South and North Island, an intensification (weakening) of the meridional SLP gradient is observed (Fig. 5.10a, b and 5.11a, b). However, the SLP anomalies for the North Island are weaker (only up to ± 1 hPa) and more localized in nature, concentrated over the Australian-New Zealand region, while those for the South Island are stronger (in excess of ± 1.5 hPa) and truly circumpolar. This agrees well with the observed composite SLP patterns described above, although overall the model composite fields appear more zonal. The SLP composites for both the North and South Island are reminiscent of the pattern of SLP anomaly associated with the SAM (Hall and Visbeck, 2002; Sen Gupta and England, 2006), though more so for the case of the South Island. The intensified (weakened) SLP gradient during dry (wet) South and North Island years leads to increased (decreased) westerlies south of 45°S and more easterly (westerly) anomalies for the latitude band

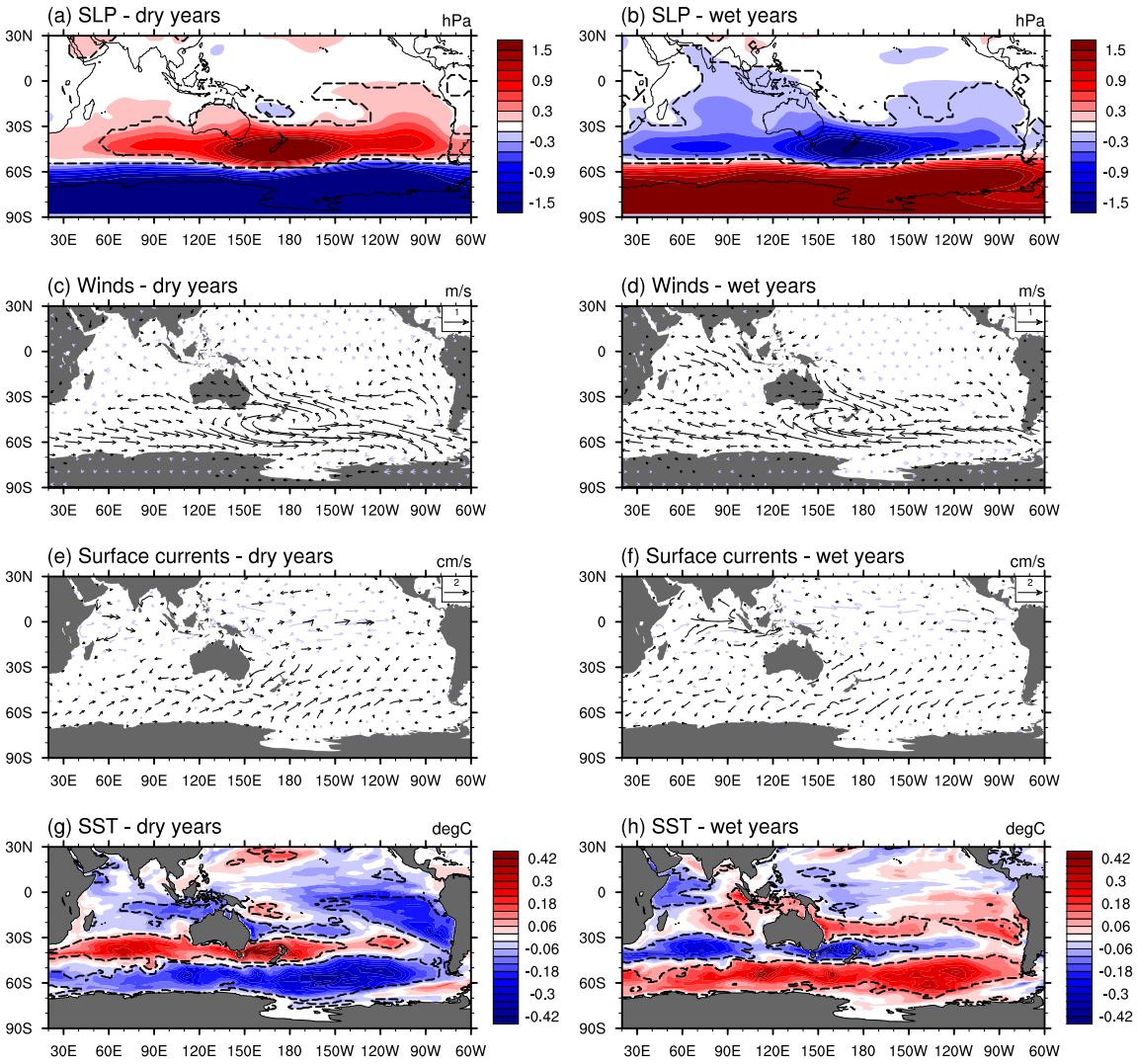

Figure 5.10. Composite anomalies in model (a, b) SLP, (c, d) winds, (e, f) surface currents, and (g, h) SST for the South Island anomalously dry (left) and wet (right) rainfall years. Dashed lines and black vectors indicate significant anomalies at the 90% confidence level as estimated by a two-tailed t-test.

20°S–40°S (Fig. 5.10c, d and 5.11c, d). For the South Island, the anomalies in the westerlies (in excess of ±0.8 m s^{-1}) are again circumpolar, while the zonal wind anomalies in the subtropics are less extensive. The North Island zonal wind anomalies are weaker and focus on the Australian-New Zealand region, especially during wet years over northern New Zealand. The meridional winds show more northerly (southerly) anomalies to the south of Australia and across southern New Zealand for dry (wet) South and North Island years, and southerly (northerly) wind anomalies over northern New Zealand and to the northeast of Australia (Fig. 5.10c, d and 5.11c, d). The meridional wind anomalies for the South Island are again stronger (up to ±0.5 m s^{-1}) and more extensive than the corresponding anomalies for the

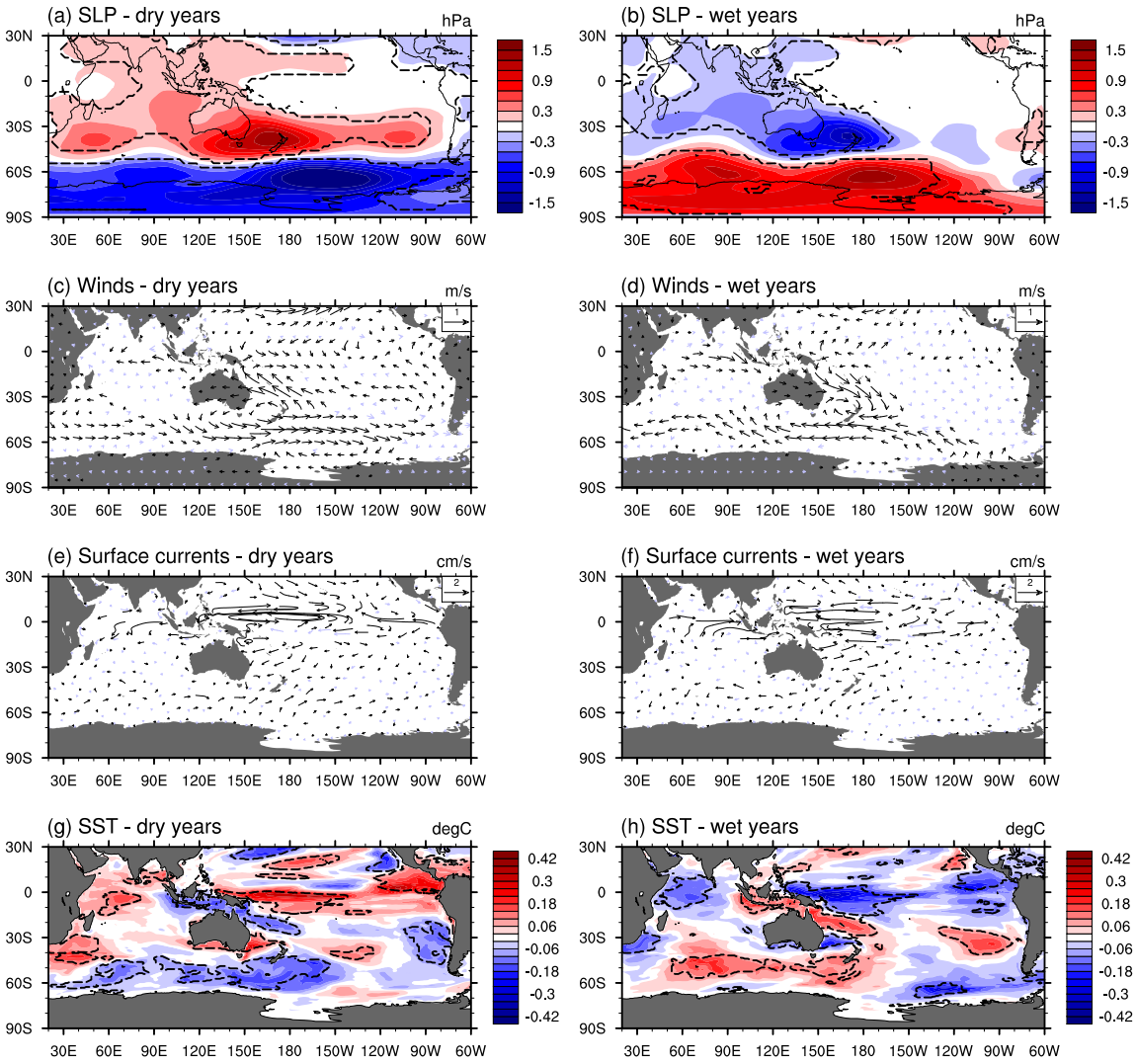

Figure 5.11. Composite anomalies in model (a, b) SLP, (c, d) winds, (e, f) surface currents, and (g, h) SST for the North Island anomalously dry (left) and wet (right) rainfall years. Dashed lines and black vectors indicate significant anomalies at the 90% confidence level as estimated by a two-tailed t-test.

North Island (only up to ± 0.3 m s^{-1}). Both zonal and meridional wind anomalies essentially follow the SLP distribution according to geostrophy.

Composites of anomalous surface ocean velocity fields (Fig. 5.10e, f and 5.11e, f) depict ocean currents responding to the changed wind fields via Ekman transport and geostrophic adjustment. During dry (wet) South and North Island years, significantly enhanced (weakened) northeastward zonal currents occur south of 45°S, agreeing well with the intensification (weakening) of the westerlies. The anomalies in surface zonal current velocity for anomalously dry and wet years over the South Island are circumpolar in extent and stronger (in excess of ± 2 cm s^{-1}) than the weaker (only up to ± 1 cm s^{-1}) anomalies for northern New Zealand. Northern

New Zealand dry and wet years show alternating bands of eastward and westward anomalies in surface currents in the western tropical Pacific Ocean that are missing in the case of southern New Zealand. The strong and significant current anomalies in the western equatorial Pacific suggest the role of tropical processes in North Island rainfall variability. In contrast, during South Island dry/wet years, strong ocean current anomalies in the latitude band 30°–60°S underlying the subpolar westerlies hint at a modulating effect in the extratropics.

SST anomalies are affected by the changed wind and current fields, with composites showing a band of cold (warm) SST for dry (wet) years for 50°–70°S (Fig. 5.10g, h and 5.11g, h). For South Island dry and wet years, this band of anomalous SST is in excess of ±0.4°C and circumpolar in extent, while it is weaker (only up to ±0.3°C) and more localized just to the south of New Zealand and Australia in the case of northern New Zealand anomalous rainfall years. Furthermore, a band of warm (cold) SST during dry (wet) years for 30°–45°S of similar magnitude (in excess of ±0.4°C) is only seen for southern New Zealand years, being only marginally apparent in North Island years. The warm (cold) SST anomalies for the latitudes 30°–45°S are established by anomalous Ekman transport due to the changed wind fields leading to a mass and heat convergence (divergence) at the interface of the easterly (westerly) to the north and westerly (easterly) zonal wind anomaly to the south. This is as would be expected during the positive (negative) phase of the SAM (e.g., Hall and Visbeck, 2002; Sen Gupta and England, 2006). This suggests a modulating influence of the SAM for the South Island anomalous rainfall years. In contrast, during North Island anomalous years, significant anomalies in SST occur in the tropical western equatorial Pacific Ocean, with the area 0°–10°S anomalously warm (cold) and the Coral Sea region unusually cold (warm) during dry (wet) years. This suggests ENSO plays a role in varying western Pacific SST anomalies and the regional atmospheric circulation via a northward displacement of the subpolar westerlies (Trenberth and Shea, 1987) and changes to the SPCZ, which migrates eastward during El Niño years (Carleton, 2003) and thus affects North Island rainfall. Almost no significant anomalies appear in the same areas for anomalously dry and wet years over the South Island, suggesting no direct influence of ENSO on that island's rainfall.

Anomalous surface air temperature (SAT; in excess of ±0.4°C; figure not shown) of warmer (cooler) anomalies over New Zealand occur during dry (wet) years over the South Island. Also apparent is anomalous cold (warm) SAT to the south of 45°S during dry (wet) years in southern New Zealand, most likely a result of underlying anomalous SST due to the strengthened (weakened) westerlies driving increased (decreased) anomalous northward Ekman transport (Fig. 5.10). The composites of

anomalous SAT for North Island dry and wet years (figure not shown) indicate almost no significant anomalies across New Zealand, but cold (warm) anomalies to the south of the country, congruent with the SST anomalies (e.g., Mullan, 1998) for dry (wet) North Island years. A stronger signal over the tropical Pacific, mirroring the underlying SST anomalies, can be seen in the western Pacific warm pool region (figure not shown), again suggestive of the greater importance of tropical processes in North as compared to South Island precipitation. The congruence of SAT to underlying SST contrasts findings by Basher and Thompson (1996), who suggested that both SAT and SST anomalies on interannual timescales are solely responses to the *meridional* wind component (i.e. southerly airflow resulting in colder temperatures), a result clearly not found in this study. Instead, we find that *zonal* wind anomalies and ensuing anomalous meridional Ekman transport contribute considerably to the SST anomaly, and in turn SAT, patterns.

Composites of anomalies in relative humidity during South Island anomalous rainfall years (figures not shown) across New Zealand, the Tasman Sea and southeast Australia show no consistent pattern of significant anomalies and do not vary in phase with the rainfall patterns (i.e., dry/wet year composites do not necessarily see drier/moister air over the adjacent oceans). In contrast, during dry (wet) North Island years, relative humidity is significantly decreased (increased) over the North Island of New Zealand and the surrounding ocean to the northwest of the island (figure not shown). Total cloud cover for dry (wet) South and North Island years is significantly reduced (increased) across all of New Zealand and the adjacent oceans (figures not shown). The composite anomalies in cloud cover during anomalous rainfall years in northern New Zealand vary in phase with those of tropical Australia, which is clearly not the case for those of the South Island.

To determine the respective role of the ocean anomalies in accounting for the rainfall anomalies over the two islands, anomalous surface heat flux (figures not shown) and evaporation (Fig. 5.12) composites are investigated. Emphasis is placed on evaporation anomalies, as evaporation most clearly differentiates the influence of oceanic versus atmospheric processes on rainfall. During dry (wet) South Island years, reduced (enhanced) evaporation anomalies appear in the Tasman Sea in a band extending from east of Tasmania across to the south of the South Island, and along the east coast of the South Island (Fig. 5.12a, b). This region of anomalous evaporation is at the interface of the westerly and easterly wind anomaly at 45°S, characterized by subsiding air masses and reduced cloud cover (figure not shown) during South Island dry years, while the situation is reversed during wet years. The location of anomalous evaporation for the South Island is hence determined directly by the wind anomalies and not by the SST anomaly pattern (compare

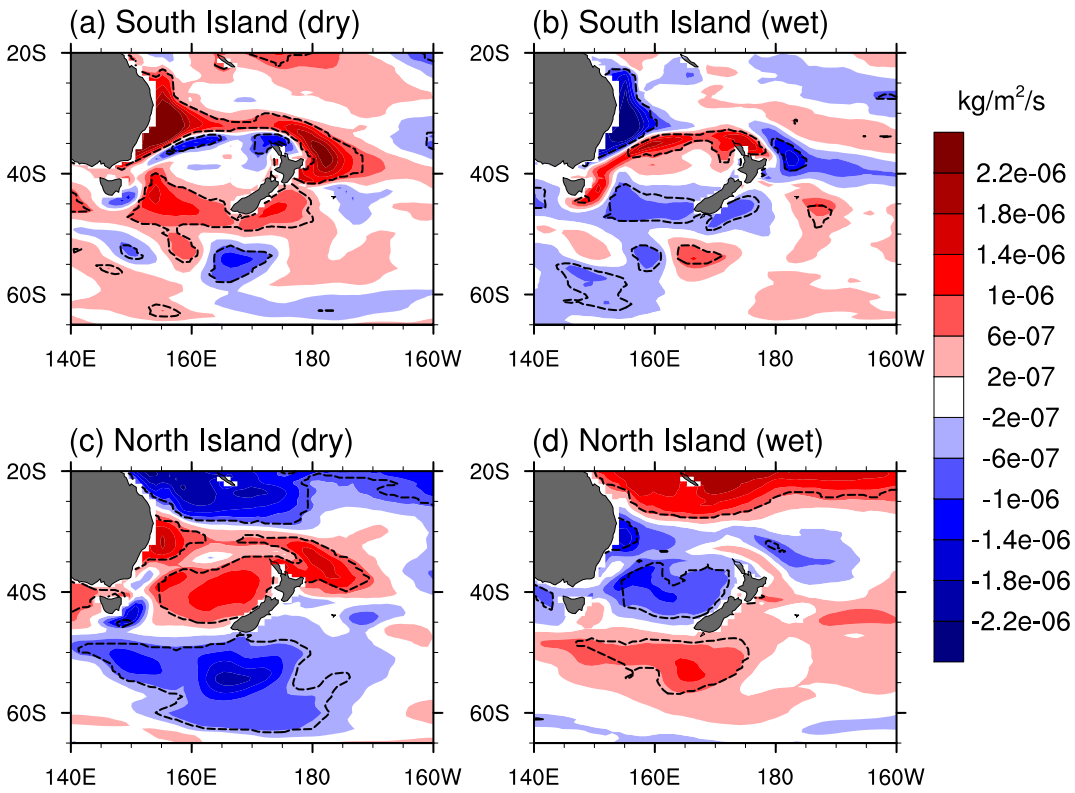

Figure 5.12. Composite evaporation anomalies (in kg m^{-2} s^{-1}) in the model for the (a, b) South and (c, d) North Island for anomalously dry (left) and wet (right) rainfall years. Dashed lines indicate significant anomalies at the 90% confidence level as estimated by a two-tailed *t*-test. Positive (negative) values indicate reduced (increased) evaporation out of the ocean.

Fig. 5.12a, b to Fig. 5.10g, h). Since the evaporation anomalies do not mirror SST anomalies, we can confirm that the anomalous SST is only symptomatic of the changed wind field and resultant anomalous Ekman transport, as proposed earlier, and not a driving factor influencing South Island rainfall during dry and wet years. In contrast, evaporation composites for North Island dry (wet) years depict reduced (enhanced) evaporation to occur for much of the Tasman Sea, while anomalies of the reverse sign appear south of New Zealand between 50°–60°S (Fig. 5.12c, d). This corresponds closely to the patterns of anomalous SST seen in Fig. 5.11g, h, with high (low) evaporation overlying anomalously warm (cool) SST. This demonstrates the role of local air-sea heat fluxes driven by anomalous SST on North Island precipitation anomalies.

5.5. Links to Southern Hemisphere climate modes

From the results presented thus far, there appears to be a higher influence of the tropical Pacific Ocean region on the North Island climate, while southern New

Zealand seems to be mostly affected by the atmospheric circulation in the mid-latitudes. The circumpolar character of the South Island anomalies, both in the reanalyses and the model, suggests a dominant role of the SAM. To evaluate this further we now analyze composites of New Zealand precipitation during El Niño and La Niña years and extreme years in the SAM during the recent observational record for 1960–2004 and in the 200-yr natural variability model run.

Composite anomalies of New Zealand precipitation during El Niño and La Niña years reveal very different influences by the respective ENSO phases (Fig. 5.13). During El Niño years, drier conditions occur for much of the North Island and the very northern edge of the South Island (Fig. 5.13a). The decrease in rainfall is significant in the northeast of the North Island with annual precipitation levels dropping by almost 400 mm yr^{-1}. The very southern and southwestern regions of the South Island experience moderately wetter conditions (up to 200 mm yr^{-1}), though only partially significant. The anomalous rainfall distribution during El Niño years (Fig. 5.13a) is very reminiscent of that of the North Island dry years (Fig. 5.3c), of which two were El Niño years (Table 5.1). Enhanced southwesterly airflow across the country during El Niño years (Fig. 5.13e; see also Waugh *et al.*, 1997; Kidson and Renwick, 2002) due to a northward displacement of the westerlies and higher incidence of cold fronts (Trenberth and Shea, 1987) accounts for wetter southern and western regions, while reducing rainfall further north. These southwesterly anomalies across the country resemble the anomalous winds seen during North Island dry years (Fig. 5.5c), as expected during times of below average precipitation. In contrast, during La Niña years, no significant anomalies appear for the North Island and eastern regions of the South Island, while along the entire west coast of the South Island, significant above average precipitation occurs (up to 400 mm yr^{-1} above normal; Fig. 5.13b). In turn, the rainfall anomalies during La Niña years (Fig. 5.13b) appear similar to South Island wet years (Fig. 5.3b), with two of the latter categorized as La Niña years (Table 5.1). The distribution of anomalous rainfall during La Niña years is caused by anomalous northerly winds (Fig. 5.13f; see also Waugh *et al.*, 1997; Kidson and Renwick, 2002), as already seen during wet North Island years (Fig. 5.5d), depositing increased moisture onto the mountainous west coast of the South Island and parts of the North Island. The respective anomalies in precipitation and circulation across the Southern Alps confirm those found by Fitzharris *et al.* (1997) for glacial mass balances for the shorter period 1977–1993. Across the entire country, the precipitation changes during ENSO years agree in principle with those of Kidson and Renwick (2002) for the period 1979–2001, though they furthermore stratified their analysis by season and distinguished between moderate and strong El Niño years, which is beyond the scope of this study.

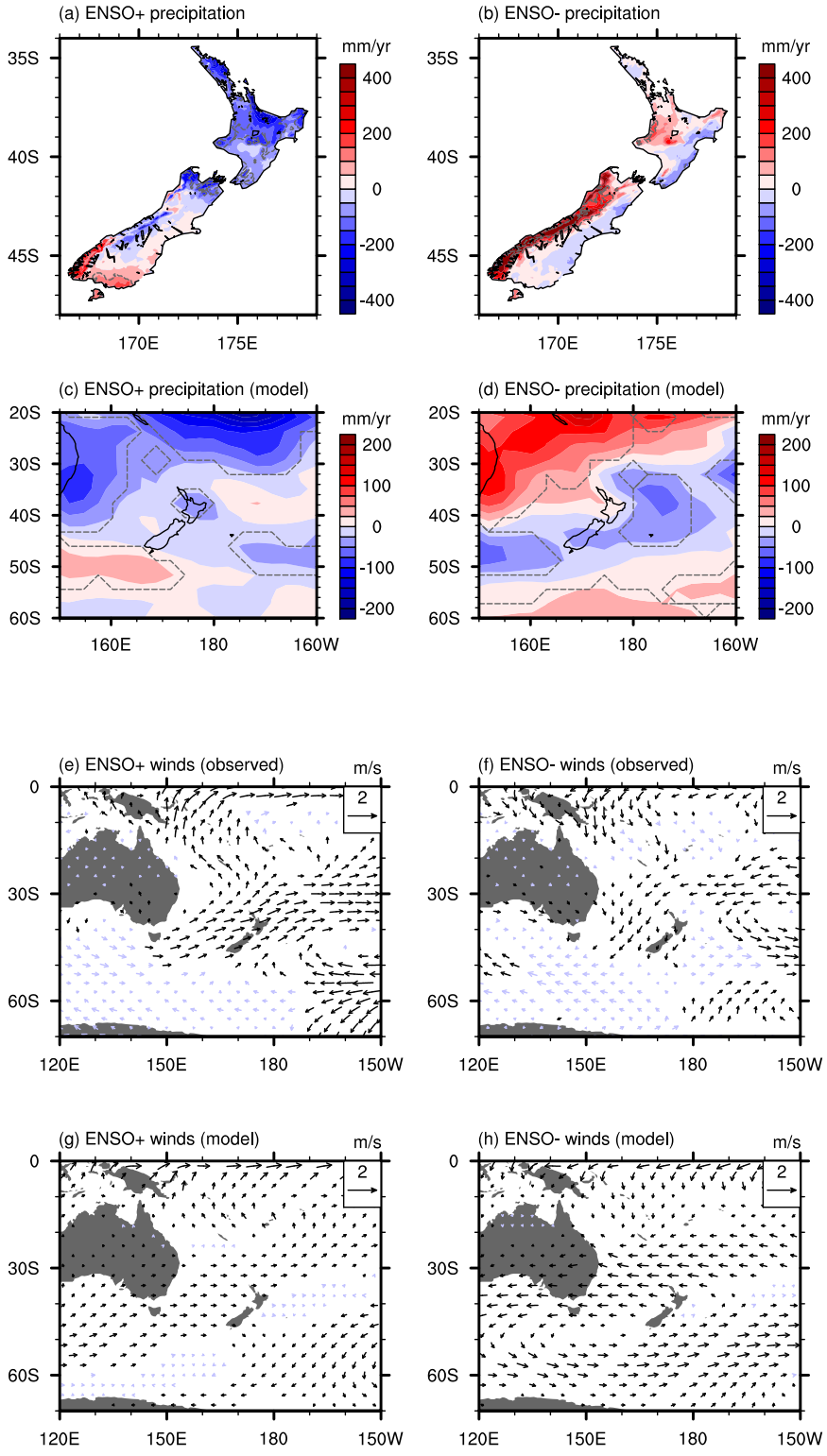

Figure 5.13. Composite anomalies of annual (a, b) observed and (c, d) model New Zealand precipitation (in mm yr^{-1}) and (e, f) NCEP and (g, h) model winds (in m s^{-1}) during El Niño (left) and La Niña (right) years for the period 1960–2004. Dashed lines in (a)–(d) and black vectors in (e)–(h) indicate significant anomalies at the 90% confidence level as estimated by a two-tailed *t*-test. Vector scale is indicated in (e)–(h) in m s^{-1} at top right of the diagram.

The model precipitation anomalies during El Niño years (Fig. 5.13c), though of smaller magnitude, agree well in their spatial distribution with the observed (Fig. 5.13a): i.e., anomalous dry conditions across New Zealand except over the southernmost tip of the South Island. The model winds during El Niño years (Fig. 5.13g) also show enhanced westerly flow across New Zealand, though their magnitude is only half of the observed. In contrast during La Niña years, the model does not capture the northerly flow anomalies across New Zealand (Fig. 5.13h), which explains the poor agreement between the observed and model precipitation anomalies, especially over the South Island (Fig. 5.13b, d). The poor representation of the situation during La Niña years in the model might be due in part to the simple method used to determine model La Niña years (i.e., as those below one standard deviation in the Niño-3.4 index).

The patterns of anomalous New Zealand precipitation and wind fields over the region during anomalous SAM years are presented in Fig. 5.14. It should be noted that the phase of the SAM indicates not only the location of the subpolar westerlies (and the associated moisture advection), it also acts as a proxy for the latitude of extratropical storm tracks (e.g., Fyfe, 2003). During positive SAM years, much of New Zealand experiences drier than normal conditions, with the exception of the very northernmost edges of both islands, which see slightly enhanced rainfall by up to 200 mm yr^{-1} (Fig. 5.14a). The decrease in precipitation everywhere else in the country lies generally around 100–250 mm yr^{-1}, although in the high-rainfall region along the mountainous west coast of the South Island anomalies reach in excess of 400 mm yr^{-1}. However, considering the anomalies in terms of a variation coefficient of rainfall (not shown), the reduction in rainfall is of a similar order of magnitude across both islands.

The anomalous rainfall distribution during positive SAM years can be understood as a response to the changed wind fields with enhanced northeasterly flow over the country (Fig. 5.14e), supplying the northern edges of the two islands with increased rainfall, while precipitation levels elsewhere are lowered. The anomalous wind field agrees with the circulation changes described by Hall and Visbeck (2002) during the high-index phase of the SAM and is similar to those seen for South Island dry years in this study (Fig. 5.4c). The distribution of anomalous rainfall during the positive SAM phase is very similar to the situation evident during anomalously dry South Island years (Fig. 5.3a), of which two are positive SAM years (Table 5.1). It is reversed during negative SAM years, with increased rainfall in the Southern Alps, the southern tip of the South Island and much of the North Island (Fig. 5.14b). Again, the northernmost edges of the two islands are out of phase with the rest of the country, being anomalously dry with annual rainfall up to 300 mm yr^{-1} below average.

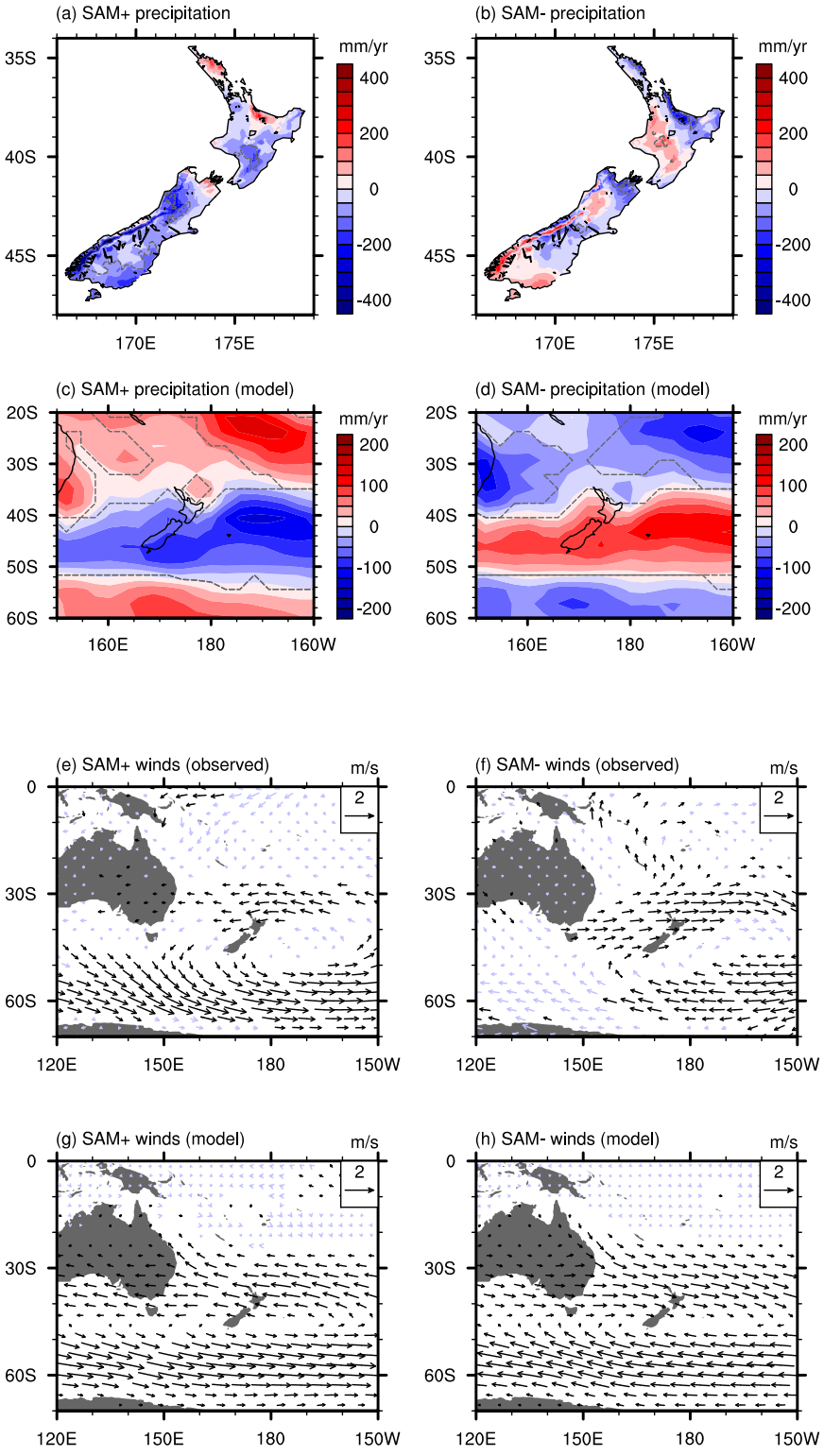

Figure 5.14. Composite anomalies of annual (a, b) observed and (c, d) model New Zealand precipitation (in mm yr^{-1}) and (e, f) NCEP and (g, h) model winds (in m s^{-1}) during positive (left) and negative (right) SAM years for the period 1960–2004. Dashed lines in (a)–(d) and black vectors in (e)–(h) indicate significant anomalies at the 90% confidence level as estimated by a two-tailed *t*-test. Vector scale is indicated in (e)–(h) in m s^{-1} at top right of the diagram.

While the rainfall distribution across the North Island closely approximates reversed conditions between the positive and negative phase of the SAM, the South Island shows more asymmetry between these extreme phases: during the positive SAM, the South Island experiences dry conditions everywhere (Fig. 5.14a). In contrast for the negative SAM, the South Island is characterized by greater heterogeneity and fine-scale structure in the precipitation anomalies (Fig. 5.14b). The anomalous westerly/southwesterly winds across the country (Fig. 5.14f) correspond with the described rainfall changes and are reminiscent of the changed wind field during South Island wet years (Fig. 5.4d). The anomalously low (high) rainfall along the west coast of the South Island during positive (negative) SAM years, with weakened (enhanced) westerlies and enhanced (weakened) northerly airflow, agree with the findings of Clare *et al.* (2002) for glacial mass balances in the Southern Alps. The above analyses were repeated with a monthly time-series for the SAM, giving robust results, as would be expected given the short timescale for the atmosphere to respond to the annular mode.

The situation during model SAM years agrees very well with observations during the positive phase: dry conditions occur across the country except along the very northern coast of the North Island (Fig. 5.14c) and easterly flow anomalies dominate (Fig. 5.14g), as seen during South Island dry years (Fig. 5.10c), though they extend further south in the model compared to the observations (Fig. 5.14e). The model precipitation and wind anomalies during the negative SAM phase (Fig. 5.14d, h) are mirror images of the positive phase. However, the observations show more local intra-island variation in rainfall (Fig. 5.14b), especially over the South Island, which is not resolved by the model due to the fine-scale orography of that island.

The ENSO in the model has a spectral peak of 2–3 years (e.g., Kiehl and Gent, 2004; Collins *et al.*, 2006), a frequency also dominant for the North Island rainfall time-series in the model (Fig. 5.8f). However, the composites do not show as strong a signal in the SST anomalies in the equatorial Pacific Ocean in the model (Fig. 5.11) as they do in the observed (Fig. 5.5). Fig. 5.6c, d shows that the amplitude of ENSO in the model is lower compared to the observed, which may account for the weaker SST signature in the composites.

The difference in seasonal cycle between the two islands (Fig. 5.2e, f and 5.8e, f) can also be understood as a result of the predominant influence of different phenomena for each region; namely tropical/subtropical influences and ENSO for the North Island and the high-latitude SAM for the South Island rainfall. The axis of the subtropical high pressure belt migrates from around 26°S in winter to around 36°S in summer (Mosley and Pearson, 1997) and associated with this anticyclonic conditions dominate during summer over the North Island, accounting for reduced

rainfall then (Fig. 5.2f and 5.8f). North Island seasonal precipitation is modulated by ENSO, with the largest ENSO-related changes occurring in austral winter (Kidson and Renwick, 2002), the high-rainfall season in the North Island. This essentially keeps the seasonal rainfall distribution during anomalous North Island years more-or-less equivalent to average years (Fig. 5.2f and 5.8f). In contrast, the South Island on average displays uniform rainfall distribution throughout the year (Fig. 5.2e and 5.8e), as is typical of a mid-latitude climate dominated by the influence of the subpolar westerlies. However, during dry and wet South Island precipitation years, the deviation in rainfall from the average seasonal distribution occurs predominantly during austral spring (and to a lesser degree also for autumn; Fig. 5.2e), the most active season of the SAM (Thompson and Wallace, 2000). The fact that the model does not show this strong deviation from the average seasonal cycle during anomalously dry and wet years (Fig. 5.8e) could be attributed to a weak seasonal cycle in the SAM in the NCAR CCSM2 model (Alex Sen Gupta 2006, personal communication). An investigation of seasonal rainfall variations in response to the SAM is beyond the scope of this study, although this has been undertaken already for ENSO (e.g., Kidson and Renwick, 2002).

5.6. Summary and conclusions

We have assessed interannual and multi-decadal variability in New Zealand rainfall in both observations and a global coupled climate model. Variability in precipitation across New Zealand was shown to be predominantly modulated by two Southern Hemisphere climate modes, namely ENSO and the SAM, with a latitudinal gradation in influence of the respective phenomena.

1. For the North Island, local air-sea heat fluxes and circulation changes associated with the tropical ENSO mode play an important role. North Island anomalously dry (wet) years are characterized by locally increased (reduced) SLP, cold (warm) SST anomalies in the southern Tasman Sea and to the north of the island and a coinciding reduced (enhanced) evaporation upstream of the southwesterly (northeasterly) airflow.

2. South Island precipitation variability is dominated by the strength and position of the subpolar westerlies, which are modulated by the extratropical SAM. During anomalously dry (wet) years in precipitation for southern New Zealand, an enhanced (reduced) meridional SLP gradient occurs, with circumpolar strengthened (weakened) subpolar westerlies and an easterly (westerly) anomaly in zonal wind north of that. Cold (warm) SST anomalies appear

underlying the subpolar westerlies, while anomalies of the opposite sign occur further north around New Zealand. The easterly (westerly) zonal wind anomaly across the island lead to decreased (increased) moisture transport onto the island. White and Cherry (1999) describe similar anomalies in SST and meridional winds that are associated with above and below average rainfall for New Zealand, associating these anomalies with the ACW. In contrast, we find clear circumpolar anomalies in this study, especially for the South Island, suggesting a dominant influence of the SAM for southern New Zealand rainfall.

3. During El Niño years, drier conditions are apparent for the entire North Island and the northern edge of the South Island, while enhanced precipitation occurs on the southwestern edge of the South Island, due to enhanced southwesterly airflow across the country. The anomalous rainfall distribution during El Niño years is very reminiscent of that of the North Island dry years.

4. In contrast, La Niña leads to increased rainfall solely along the mountainous west coast of the South Island due to anomalous northerly airflow depositing heightened moisture onto the mountains. The rainfall anomalies during La Niña years appear similar to South Island wet years.

5. During the positive (negative) phase of the SAM, via changes to the general atmospheric circulation, reduced (increased) precipitation occurs over much of the South Island and the southern regions of the North Island, while the northern edges of both islands are out of phase with these changes. The distribution of anomalous rainfall during the positive SAM phase is very similar to the situation in anomalously dry South Island years.

As stated previously, the results we have obtained were then reassessed with the recent CCSM3 model and the ERA-40 reanalysis fields and our conclusions were found to be consistent.

The SAM has previously been linked to precipitation variability in mid-latitudes; for example in South America (Silvestri and Vera, 2003) and South Africa (Reason and Roualt, 2005). Thus, it is of little surprise to find rainfall over New Zealand, especially across the South Island which is located in the subpolar westerly wind belt, also modulated by the SAM. Projections of a further trend towards the positive phase of the SAM under enhanced greenhouse forcing (Fyfe *et al.*, 1999; Kushner *et al.*, 2001), coupled with the above described links between the SAM and New Zealand rainfall, suggest future patterns of New Zealand precipitation will be characterized by substantial anomalies from the long-term mean. This issue of recent

trends in New Zealand precipitation will be investigated in more detail in a separate study.

Acknowledgments. We thank the National Institute of Water and Atmospheric Research in New Zealand for providing the precipitation data set used in this study. Use of the CCSM2 and CCSM3 model output from the National Center for Atmospheric Research and their reanalysis data set, jointly developed with the National Center for Environmental Prediction and provided by NOAA/OAR/ESRL PSD, Boulder, Colorado, USA, through their website http://www.cdc.noaa.gov, is gratefully acknowledged. The CMAP Precipitation and NOAA_ERSST_V2 SST data was also provided by NOAA/OAR/ESRL PSD, Boulder, Colorado, USA, and the ERA-40 data by the ECMWF. We would also like to thank Agus Santoso for help with the spectral analysis and three anonymous reviewers for their constructive comments. CCU was supported by the University of New South Wales under a University International Postgraduate Award and MHE was supported by the Australian Research Council and a CSIRO Wealth from Oceans Fellowship.

Chapter 6

Causes of Late Twentieth Century Trends in New Zealand Precipitation

Caroline C. Ummenhofer, Alexander Sen Gupta, and Matthew H. England

Climate and Environmental Dynamics Laboratory, School of Mathematics and Statistics, University of New South Wales, Sydney, Australia

Manuscript for: Journal of Climate
Status: revised

6.1. Abstract

Late twentieth Century trends in New Zealand precipitation are examined using observations and reanalysis data for the period 1979–2006. One of the aims of this study is to investigate the link between these trends and recent changes in the large-scale atmospheric circulation in the Southern Hemisphere. The contributions from changes in Southern Hemisphere climate modes, particularly the El Niño-Southern Oscillation (ENSO) and the Southern Annular Mode (SAM), are quantified for the austral summer season (December–February; DJF). Increasingly drier conditions over much of New Zealand can be partially explained by the SAM and ENSO. Especially over wide parts of the North Island and western regions of the South Island, the SAM potentially contributes up to 80% and 20–50% to the overall decline in DJF precipitation, respectively. Over the North Island, the contribution of the SAM and ENSO to precipitation trends is of the same sign. In contrast, over the southwest of the South Island the two climate modes act in the opposite sense, though the effect of the SAM seems to dominate there during austral summer. The leading modes of variability in summertime precipitation over New Zealand are linked to the large-scale atmospheric circulation. The two dominant modes, explaining 64% and 9% of the overall DJF precipitation variability respectively, can be understood as local manifestations of the large-scale climate variability associated with the SAM and ENSO.

6.2. Introduction

There is much evidence of recent changes to the hydrological cycle with impacts on precipitation patterns across the planet, especially during the late 20th Century (e.g., Oki and Kanae, 2006). Coinciding with these changes, some climate modes have also undergone substantial shifts, such as the annular modes in both hemispheres (e.g., Fyfe *et al.*, 1999; Thompson *et al.*, 2000), the North Atlantic Oscillation (e.g., Hurrell, 1995), and the El Niño–Southern Oscillation (ENSO; e.g., Fedorov and Philander, 2000). In addition, key drivers of precipitation, such as sea surface temperature (SST; e.g., Levitus *et al.*, 2000) and sea level pressure (SLP; e.g., Gillett *et al.*, 2003; Marshall, 2003) are showing wide-spread changes over recent decades. The goal of this study is to examine late 20th Century New Zealand precipitation trends and their association to changes in Southern Hemisphere climate modes.

Over recent decades, large-scale changes to the atmospheric circulation in the Southern Hemisphere have been documented. They include a trend in the meridional SLP gradient between the high- and mid-latitudes and a corresponding strengthening and southward shift in the subpolar westerlies (e.g., Thompson and Solomon, 2002; Renwick, 2004). Model results have shown that these trends are consistent with the observed depletion in stratospheric ozone, which in turn leads to reduced temperatures over the polar cap and a strengthening of the stratospheric polar vortex and circumpolar flow (Thompson and Solomon, 2002; Gillett and Thompson, 2003). Since the photochemical ozone loss is enhanced by solar radiation, the depletion is accelerated in spring and summer (Hartmann *et al.*, 2000) and trends become especially apparent during the December to May period (Thompson and Solomon, 2002). Other studies also implicate enhanced greenhouse gas forcing, as the observed circulation changes also occur in simulations forced solely by increases in atmospheric greenhouse gases (e.g., Fyfe *et al.*, 1999; Kushner *et al.*, 2001; Cai *et al.*, 2003b).

The trends in the Southern Hemisphere circulation can be understood, in large part, as a shift towards the high-index positive phase of the Southern Annular Mode (SAM; Marshall, 2003; Renwick, 2004). The SAM is the leading mode of variability in the extratropical Southern Hemisphere, explaining around 47% of the natural variability of zonal-mean geopotential height for 1000–50 hPa south of 20°S (Thompson and Wallace, 2000). The SAM represents a redistribution of mass between the polar latitudes south of 60°S and the mid-latitudes centered around 45°S, and results in an out-of-phase modulation in the easterly and westerly wind field centered at 35° and 60°S, respectively (Thompson *et al.*, 2000; Sen Gupta and Eng-

land, 2006). The trend in the SAM has been widely documented in observations (Jones and Widmann, 2003; Marshall, 2003; Jones and Widmann, 2004; Marshall *et al.*, 2004), reanalyses (Marshall, 2003), and proxy records (Jones and Widmann, 2003). As described above, trends in the SAM have been linked to both increases in greenhouse gases and stratospheric ozone depletion (Thompson and Solomon, 2002; Gillett and Thompson, 2003). Ensembles of 20th Century simulations separately applying various natural and anthropogenic forcings confirm that natural variability in itself cannot account for the observed trends (Arblaster and Meehl, 2006). Experiments with coupled climate models extending into the 21st Century project that this trend will continue under further increases in greenhouse gases (Fyfe *et al.*, 1999; Kushner *et al.*, 2001) with possible consequences for mid-latitude winds, ocean currents (Cai *et al.*, 2005a; Cai, 2006; Fyfe, 2006), and precipitation (e.g., Cai *et al.*, 2005b).

With the SAM trending towards a more positive phase, atmospheric circulation changes also affect climate conditions over mid-latitudes, including South Africa (Reason and Roualt, 2005), Australia (Cai *et al.*, 2005b; Cai and Cowan, 2006; Hendon *et al.*, 2007; Meneghini *et al.*, 2007), and South America (Silvestri and Vera, 2003). Ummenhofer and England (2007) recently demonstrate that a positive-index SAM is associated with anomalously dry conditions in parts of New Zealand. It is therefore of interest to also analyze the trend in New Zealand precipitation over the past few decades and investigate how much of this can be accounted for by different Southern Hemisphere climate modes, in particular the SAM, but also ENSO.

ENSO has been implicated in various changes to the Southern Hemisphere climate (e.g., Diaz *et al.*, 2001). Over the period 1861–1992, Vecchi *et al.* (2006) describe a weakening of the observed tropical atmospheric circulation across the Pacific Ocean, consistent with theoretical predictions for enhanced greenhouse forcing and reproduced by model simulations incorporating both natural and anthropogenic forcings. Variations in the zonal atmospheric overturning in the tropical Pacific, i.e., the Walker circulation, are closely linked to ENSO (Vecchi *et al.*, 2006), and thus changes in the Walker circulation could impact on the frequency and strength of El Niño and La Niña events. For 1977–2006, Power and Smith (2007) describe a period of unprecedented El Niño dominance, with the lowest 30-year average value on record of the June–December Southern-Oscillation Index (SOI). This coincides with the highest SST and weakest surface wind stresses on record in the equatorial Pacific, all indicative of a weakening of the Walker circulation. Fedorov and Philander (2000) demonstrate a recent increase in the frequency of El Niño events compared to paleoclimate records that they suggest might be due to global warming. Similarly, Verdon and Franks (2006) find El Niño events to be more frequent

during warmer periods, taken from a 400-year paleoclimate record. In a climate model forced by future greenhouse warming, Timmermann *et al.* (1999) show a more frequent occurrence of El Niño-like conditions, but also stronger cold events in the equatorial Pacific. In a multi-model intercomparison, Guilyardi (2006) finds an enhanced El Niño amplitude with increasing greenhouse forcing, though changes in the frequency are much less consistent across the models. For the models used in the Fourth Assessment Report for the Intergovernmental Panel on Climate Change, Meehl *et al.* (2007) comprehensively assess projected changes to interannual ENSO variability and find no consistent indication of future changes to ENSO either in amplitude or frequency. Changes in the El Niño frequency and amplitude are believed to contribute to variations in the regional atmospheric circulation, for example to the migration of the South Pacific Convergence Zone (Juillet-Leclerc *et al.*, 2006).

Salinger and Griffiths (2001) investigated southwest Pacific climate trends for the period 1861–1990 and discovered inconsistent precipitation trends for different decades during the second half of the 20th Century. They suggest that the major 20th Century changes in atmospheric circulation across the New Zealand region occurred around 1950 and 1976. They found more anomalous southerly/southwesterly airflow during the period 1930–1950, followed by anomalously easterly/northeasterly flow between 1951–1975, and then westerly/southwesterly airflow anomalies again during 1976–1998, with a strengthened tropical anticyclonic belt over northern New Zealand. During 1930–1950, Salinger and Mullan (1999) found conditions to be wetter in the northeastern part of the South Island, drier in the north and west of the South Island, and cooler over the entire country. The period 1951–1975 was warmer throughout, wetter in the north of the North Island and drier in the southeast of the South Island. During the latest period of heightened westerly airflow (1976–1998), precipitation has increased for much of the South Island, while it has decreased in the north of the North Island. Hence, trends in New Zealand precipitation over the South Island seem to be associated with changes in the incidence of westerlies, which Salinger and Mullan (1999) attribute to a recent increased frequency of El Niño events. Via modulations of tropical eastern Pacific SST, ENSO was also found to be well correlated with New Zealand surface air temperatures on annual to decadal timescales (Folland and Salinger, 1995). Despite these studies, large-scale 20th Century changes in the atmospheric circulation of the Southern Hemisphere and their link to New Zealand precipitation trends have not been examined in great detail.

On seasonal to interannual timescales, New Zealand precipitation appears to be modulated by the SAM (Clare *et al.*, 2002; Renwick and Thompson, 2006), ENSO (Fitzharris *et al.*, 1997; Kidson and Renwick, 2002; Zheng and Frederiksen, 2006),

and the Interdecadal Pacific Oscillation (IPO; Salinger *et al.*, 2001). Renwick and Thompson (2006) link the positive (negative) phase of the SAM to below (above) normal daily rainfall and warm (cold) maximum daily temperature anomalies over western regions of the South Island of New Zealand. The associations between the SAM, ENSO, and interannual variations in New Zealand precipitation are described in detail by Ummenhofer and England (2007). That study focused on understanding links between New Zealand precipitation and the SAM and ENSO on interannual timescales for the period 1960–2004, using observations, reanalysis data, and output from a multi-century climate model simulation. In this follow-up study, we aim to determine if processes and mechanisms influencing New Zealand precipitation on these shorter interannual timescales can also account for the long-term trends. To our knowledge, this is the first study to *quantify* the contribution of changes in the large-scale Southern Hemisphere climate modes toward recent New Zealand precipitation trends.

The remainder of the paper is structured as follows: Section 6.3 describes the data sets used, both observations and reanalysis. The results in Section 6.4 cover a break-point analysis of seasonal New Zealand precipitation (Section 6.4.1), an analysis of seasonal precipitation trends (Section 6.4.2), an assessment of the links between precipitation trends and the climate modes ENSO and SAM (Section 6.4.3), and an evaluation of the precipitation trends corresponding to the dominant precipitation modes (Section 6.4.4). Associations between different climate modes and the Southern Hemisphere circulation are presented in Section 6.4.5. The final section includes a discussion and a summary of the major findings of this study.

6.3. Observational and reanalysis data

The New Zealand precipitation data set analyzed in this study is from the National Institute of Water and Atmospheric Research (NIWA) Climate Database. It comprises daily New Zealand station data that has been interpolated to give a gridded data set with a 0.05° latitude/longitude (approximately 5 km) resolution for the entire country (http://www.niwa.cri.nz/ncc/mapping/other_products). The daily gridded precipitation data for the period 1960–2006 is converted to seasonal averages.

The data for regional and large-scale analysis of atmospheric parameters, such as SLP and surface winds, is from the National Center for Environmental Prediction (NCEP) and National Center for Atmospheric Research (NCAR) reanalysis project (Kalnay *et al.*, 1996; Kistler *et al.*, 2001). The NCEP/NCAR reanalysis (NNR) assimilates land- and ocean-based observations and satellite measurements and, by

employing a global spectral model, generates a data set with global coverage for a wide set of climatic parameters with a T62 horizontal resolution (approximately 2° latitude/longitude) and covering the period 1948 to the present-day. However, we focus our analyses on seasonal data for the more recent period 1979–2006, after the establishment of satellite records. Problems regarding data coverage and quality in the high latitudes of the Southern Hemisphere prior to 1979 have been documented in several studies particularly for daily fields (e.g., Hines *et al.*, 2000; Marshall and Harangozo, 2000; Kistler *et al.*, 2001; Marshall, 2002, 2003; Renwick, 2004). However, after 1979 on monthly to interannual timescales, the NNR fields are in overall good agreement with observations (Hines *et al.*, 2000; Kistler *et al.*, 2001). Our analyses focus on the austral summer season (December–February, DJF) post-1979, when the skill of the NNR over the Southern Hemisphere high latitudes is much improved over the winter season (June–August, JJA) and, in fact, comparable to the skill over continental areas with denser observational networks during winter (Bromwich and Fogt, 2004). Bromwich and Fogt (2004) do however demonstrate superior skill and reliability in the European Centre for Medium-Range Weather Forecasting (ECMWF) 40-year reanalysis (ERA-40; Uppala *et al.*, 2005) compared to NNR. To check the robustness of our results obtained with the NNR data, we repeat key analyses with the ERA-40 data for the overlapping period 1979–2001. The two reanalysis products produce very similar results and consequently we only present analyses from the longer NNR data set, but refer to ERA-40 where appropriate. Monthly SST for 1979–2006 is obtained from the extended reconstructed data set developed by the National Oceanic and Atmospheric Administration (NOAA) with a 2° latitude/longitude resolution. Smith and Reynolds (2003, 2004) describe the techniques and details for the construction of this historical SST data set.

The monthly SAM index used is described by Marshall (2003) and available at http://www.nerc-bas.ac.uk/icd/gjma/sam.html. It is based on mean SLP observations at 12 stations, with anomalies calculated relative to the 1971–2000 period. The monthly ENSO index is based on the SOI, calculated as the difference in standardized SLP between Tahiti and Darwin, provided by the NOAA Climate Prediction Center (http://www.cpc.ncep.noaa.gov/data/indices/soi). The SOI is used as an indication of ENSO variability, as we focus on changes in the general atmospheric circulation most appropriately represented by an atmospheric, not oceanic, index.

6.4. Results

6.4.1. Breakpoint analysis

The period 1979–2006 is chosen in this study to ensure data quality, as the extratropical Southern Hemisphere suffers from sparse data coverage prior to the satellite era. To further check that this period is also appropriate for investigating New Zealand precipitation trends, we perform a breakpoint analysis of seasonally averaged precipitation data over the country for the period 1960–2006. Seasonal averages of precipitation are calculated for the gridded data with the long-term monthly cycle removed. The breakpoint analysis performs a bilinear regression at each grid point (the two lines are not constrained to be continuous at the breakpoint). The breakpoint is defined as the year with the minimum least squares error. A *t*-test is performed to assess the significance of a particular breakpoint. A breakpoint is only regarded as significant if both the trend before and after the breakpoint differs significantly (at the 95% confidence level) from the trend of the entire time-series (i.e., with no breakpoint).

The breakpoint analysis of New Zealand precipitation trends reveals very different patterns for the four seasons (Fig. 6.1). During the DJF season, much of the mountainous west coast of the South Island experiences a significant breakpoint in the mid- to late-1970s (Fig. 6.1a). This is in accordance with results of Salinger and Mullan (1999) and Salinger and Griffiths (2001), who describe a change in the predominant zonal airflow over the country in the mid-1970s, while Salinger *et al.* (1995) find these local changes to be part of large-scale trends affecting the entire southwest Pacific region. No other spatially consistent breakpoints are found for DJF. All other seasons show high spatial and temporal heterogeneity for significant breakpoints (Fig. 6.1b–d). Locally, some regions along the east coast of the South Island indicate a breakpoint in the mid-1970s for the JJA and September–November (SON) seasons (Fig. 6.1c, d), possibly related to the change in zonal flow regime mentioned above. Overall, the breakpoint analysis reveals large areas of significance for the mid- to late-1970s, locally some early breakpoints in the 1960s, but no substantial areas with breakpoints post-1980. This provides further justification to limit our analyses to the 1979–2006 period, and to the DJF season.

6.4.2. Precipitation trends

Following results from the breakpoint analysis, trends in New Zealand precipitation are stratified by season and their significance determined with a *t*-test for the period 1979–2006. Over the past three decades, New Zealand has undergone considerable changes in precipitation, shown for the four different seasons in Fig.

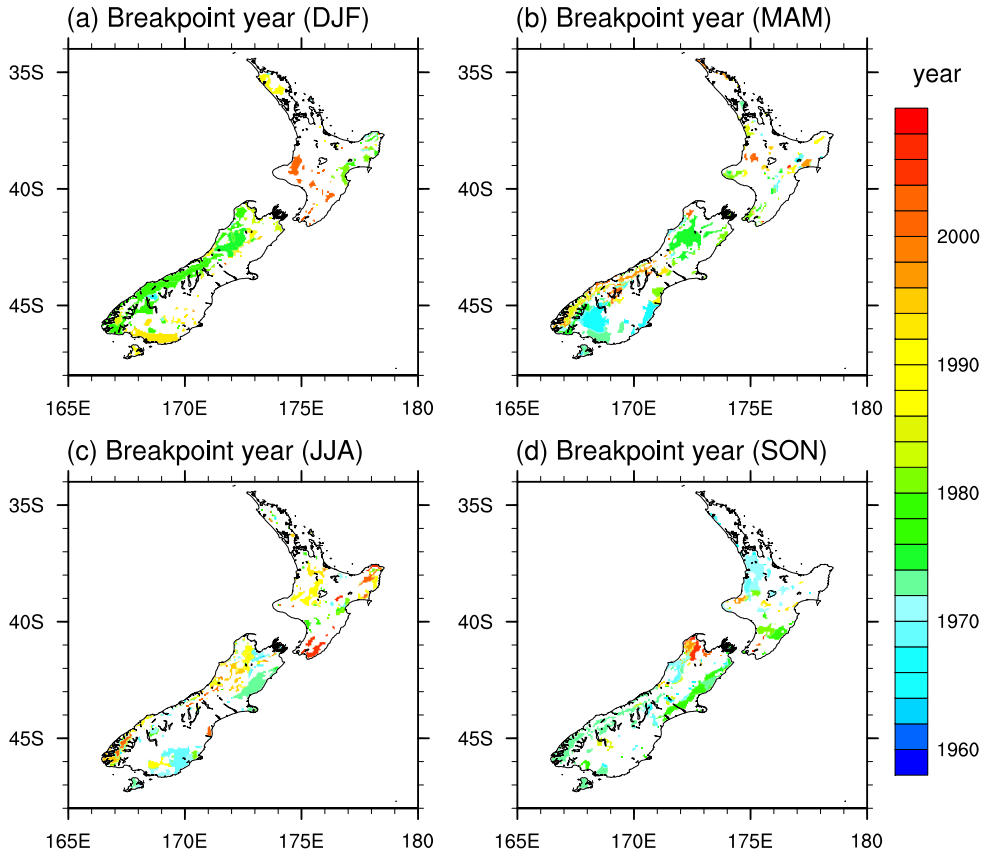

Figure 6.1. Year of breakpoint analysis for New Zealand precipitation for the seasons (a) DJF, (b) MAM, (c) JJA, and (d) SON over the period 1960–2006. Values are only color-shaded where the breakpoint is significant at the 95% confidence level.

6.2. Across all four seasons, a general trend towards drier conditions is observed, especially pronounced over the South Island during DJF (in excess of 5 mm month^{-1} drier), MAM (3–5 mm month^{-1} drier), and JJA (1–3 mm month^{-1} drier) and over the North Island during MAM (2–4 mm month^{-1} drier). Negative trends in North Island autumn rainfall are consistent with Salinger and Mullan (1999) for their analysis period of 1976–1994. However, they find both summer and winter trends considerably wetter for the west coast of the South Island, while our results indicate a very small area there with a positive trend in precipitation for MAM, JJA, and SON, with no significant positive trend for DJF. The southern half of the North Island is the only extensive region of New Zealand with a positive precipitation trend (up to 3 mm month^{-1}), but only during the SON season (Fig. 6.2d).

The magnitude of these precipitation trends is considerable: for example over the 27-year period a drop in precipitation is observed of more than 400 mm overall for much of the South Island during the DJF season. Considering an area-average of 2085 mm yr^{-1} across the South Island (Ummenhofer and England, 2007), a drop of

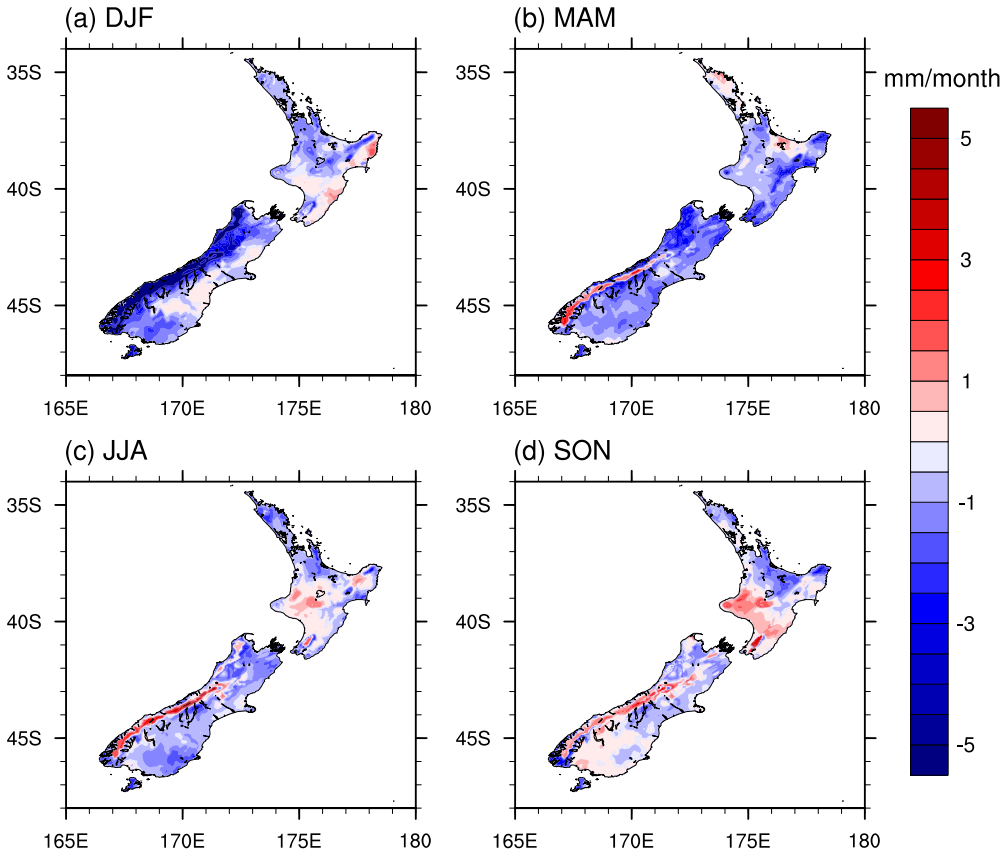

Figure 6.2. Monthly precipitation trends (significant at the 90% confidence level) for New Zealand for the seasons (a) DJF, (b) MAM, (c) JJA, and (d) SON, averaged over the period 1979–2006 (values are shown in mm month^{-1}).

400 mm for the DJF season is considerable. This signifies a 40% reduction in precipitation even if the decrease is mainly concentrated along the high-rainfall region along the west coast, which receives approximately 1500 mm over an average DJF season. It is therefore of interest to explore the mechanism(s) for the observed long-term trends in New Zealand precipitation. DJF precipitation shows a continuous and significant trend after the mid-1970s. In addition, the trend in the SAM is only significant in DJF and the ENSO trend (while not significant at the 90% confidence level) is greatest in the austral summer. As a result we focus our remaining analyses on the trends during the DJF season.

6.4.3. Precipitation trends linked to SAM and ENSO

An attempt is made here to explain and quantify the trends in New Zealand precipitation in relation to long-term changes in the large-scale modes of climate variability. The method used follows that of Thompson *et al.* (2000), who related trends in the Northern Hemisphere extratropical circulation to the Northern Annular

Mode. Due to the short and sparse record of high-quality data in the Southern Hemisphere, Thompson *et al.* (2000) did not attempt the same analysis here. In this present work we are now able to extend their data record by 10 years.

The method divides the observed precipitation trend into a component that is linearly congruent with a specific time-series (e.g., the SAM index) and a residual component that is linearly independent of the index. The linearly congruent component is calculated as the regression coefficient of the standardized and detrended index onto precipitation anomalies (mean, trend, and seasonal cycle removed) multiplied by the previously-removed trend in the index. The fraction of the observed precipitation trend attributable to the index is derived by dividing the component of the trend that is linearly congruent with the index by the overall observed precipitation trend. To avoid artificially high values (resulting when the observed trend is small), fractions are only calculated for those grid points where the observed precipitation trend is significant (at the 90% confidence level). The respective contributions of the SAM and SOI to New Zealand precipitation trends are quantified for the DJF season over the period 1979–2006 in this way.

Recent changes in the extratropical Southern Hemisphere atmospheric circulation have been widely documented (e.g., Salinger *et al.*, 1995; Kushner *et al.*, 2001; Thompson and Solomon, 2002; Fyfe, 2003; Gillett and Thompson, 2003; Marshall *et al.*, 2004; Renwick, 2004; Cai *et al.*, 2006; Cai, 2006) and partially linked to trends in the SAM (e.g., Kushner *et al.*, 2001; Thompson and Solomon, 2002; Gillett and Thompson, 2003; Marshall *et al.*, 2004). These trends in the SAM are strongest during austral summer (e.g., Thompson *et al.*, 2000; Thompson and Solomon, 2002). Fig. 6.3a shows the time-series of the SAM averaged for the DJF season with a trend of 0.048 standard deviation (SD) month^{-1} in the SAM index (significant at the 90% confidence level) over the period 1979–2006. The regression of precipitation onto the SAM time-series is presented in Fig. 6.3c. The SAM is associated with below-average precipitation (Gillett *et al.*, 2006) – in excess of 50 mm month^{-1} for a one SD positive SAM index – along the western and southern regions of both islands (Fig. 6.3a). In contrast, the eastern edges of the two islands experience wetter conditions. These findings are consistent with earlier studies on daily to interannual timescales (Renwick and Thompson, 2006; Ummenhofer and England, 2007). This out-of-phase relationship between eastern and western regions of New Zealand is noted by Salinger *et al.* (1995) and linked to the interaction of the regional circulation, i.e. strength in the prevailing westerlies and frequency of blocking anticyclones east of New Zealand, with the generally north-south aligned orography. The trend in the SAM could thus potentially account for a good proportion of the precipitation trends over New Zealand, especially over the North Island, where in some regions

more than 80% of the precipitation trend is consistent with the SAM (Fig. 6.3e). For the South Island, the SAM trend is congruent with increasingly drier conditions over the mountainous western regions. However, only 20–50% of the precipitation trend is accounted for by the SAM.

The tropical circulation across the Pacific Ocean region has sustained considerable changes over recent decades (e.g., Fedorov and Philander, 2000; Vecchi *et al.*, 2006; Power and Smith, 2007; Vecchi and Soden, 2007). Recent and future changes to ENSO's frequency and amplitude are still debated (e.g., Guilyardi, 2006), and trends in different ENSO indices are only at most marginally significant, dependent on season and study period. Despite these ambiguities, it is still of value to assess the contribution of changes in ENSO to New Zealand precipitation trends (see Fig. 6.3b, d, f). During the DJF season, the SOI indicates a non-significant positive trend of 0.044 SD month^{-1} (Fig. 6.3b). As El Niño events are associated with the negative SOI phase, a significant positive trend in the SOI would indicate a decrease in El Niño incidence. Despite the fact that the trend in the SOI is not distinguishable from zero, we retain the analysis to allow a comparison with the results of the EOF analysis. The positive phase of the SOI is associated with mostly wetter conditions across the northern regions of the North Island, with precipitation in excess of 20 mm month^{-1} above normal (Fig. 6.3d; see also Salinger *et al.*, 1995). Reduced precipitation occurs over the entire mountainous west coast of the South Island (Ummenhofer and England, 2007). The fraction of observed precipitation trends congruent with the SOI is highest for the east coast of the North Island (Fig. 6.3f). The contribution of the SOI trend to the South Island drying along the west coast does not generally exceed 20% of the observed trend.

In summary, changes in New Zealand precipitation could be partially accounted for by trends in the Southern Hemisphere climate modes, the SAM and ENSO. However, there still remain considerable areas over which the magnitude of the observed precipitation trends cannot be explained by these climate modes. To explore the mechanism(s) responsible for the New Zealand precipitation trends not sufficiently explained by the SAM and ENSO, we now examine the leading modes of variability in New Zealand precipitation, their trends, and their associations with the general atmospheric circulation.

6.4.4. Precipitation trends linked to dominant New Zealand precipitation modes

To investigate the leading modes of variability in New Zealand precipitation an EOF analysis (using a covariance matrix) is performed on the gridded seasonal DJF precipitation anomalies. The anomalies were weighted prior to analysis to account

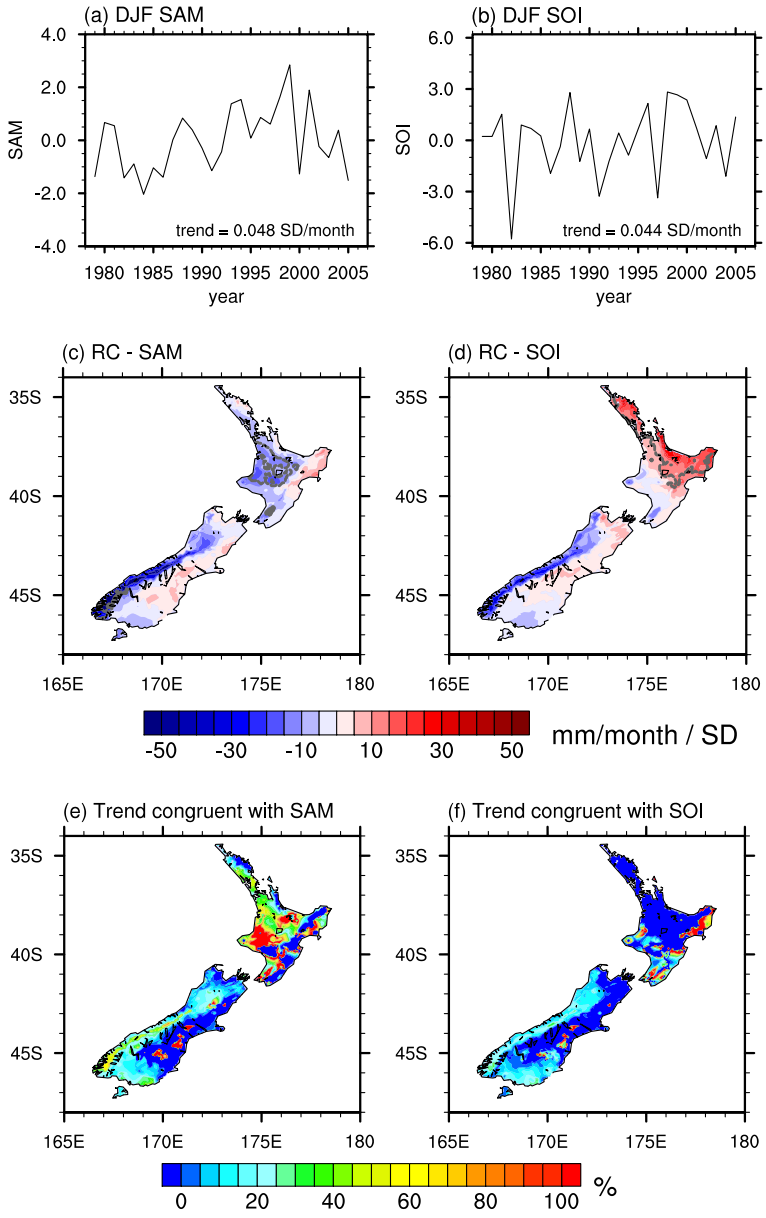

Figure 6.3. (a) SAM and (b) SOI time-series for the DJF season for the period 1979–2006 (with the year given for the first month in the summer season). Regression of the (c) SAM and (d) SOI onto New Zealand precipitation for the DJF season, with gray dashed lines indicating significant regression coefficients at the 95% confidence level as estimated after Sciremammano (1979); DJF trends in New Zealand precipitation linearly congruent with the (e) SAM and (f) SOI, averaged over the period 1979–2006 as a fraction of the monthly DJF precipitation trend. The fractions were only calculated for those grid points in which the DJF precipitation trend was significant at the 90% confidence level. The average monthly DJF trends (in SD month^{-1}) in the SAM and SOI time-series are indicated at the bottom right of (a, b).

for the smaller surface area of grid boxes at higher latitudes. Fig. 6.4 shows the principal component (PC) time-series of the first two EOF modes, the regression of New Zealand DJF precipitation onto the PCs, and their respective contribution to precipitation trends.

The standardized time-series of PC1 of DJF precipitation shows a positive trend of 0.048 SD month^{-1}, significant at the 97% level (Fig. 6.4a). The regression of New Zealand precipitation onto PC1 represents the first EOF mode, which explains approximately 64% of the observed precipitation variability during DJF (Fig. 6.4c). EOF1 is characterized by drier conditions (in excess of 50 mm month^{-1} drier) over much of the western and southern regions of New Zealand (Fig. 6.4c). In contrast, significantly more rainfall occurs for the coastal regions in the northeast of the North Island. This pattern closely resembles the leading mode (based on rotated principal component analysis) of monthly New Zealand precipitation station data for the period 1951–1975 described by Salinger (1980). It is characterized by the strength of the zonal circulation with the passage of eastward-moving wave depressions, and influenced by strong north-south pressure anomalies over New Zealand (Salinger, 1980). The out-of phase relationship between the southwest and northeast regions of the two islands seen in Fig. 6.4c is reminiscent of the projection of New Zealand precipitation onto the SAM (Fig. 6.3c). However, the time-series of SAM and PC1 are not significantly correlated (correlation coefficient of 0.29, P-value of 0.143) during DJF. The trend in PC1 can almost completely account for the observed drier conditions along the west coast of the South Island, and the southwestern regions of the North Island, during austral summer (Fig. 6.4e).

The time-series of PC2 also has a significant (at 95% confidence level) positive trend of 0.044 SD month $^{-1}$ (Fig. 6.4b). EOF2, explaining 9% of the variability, shows drier conditions for much of the country, with precipitation up to 50 mm month^{-1} below normal (Fig. 6.4d). This is especially apparent over the North Island and northern and eastern regions of the South Island. Increases in precipitation are only observed for the mountainous southwestern corner of the South Island. The precipitation distribution associated with EOF2 resembles the pattern linked to El Niño events by Ummenhofer and England (2007). This pattern is due to increased southwesterly airflow over the country (see also Kidson and Renwick, 2002; Waugh *et al.*, 1997), which Salinger and Griffiths (2001) link to increased frequency of showery precipitation events. In contrast, the match with the regression pattern of the SOI (Fig. 6.3d) is rather poor, despite a significant correlation at the 90% level of the SOI and PC2 time-series (correlation coefficient of -0.356). As an El Niño event is associated with the negative phase of the SOI, we would expect Figs. 6.3d and 6.4d to be mirror images. Trends in EOF2 can account for much of the negative

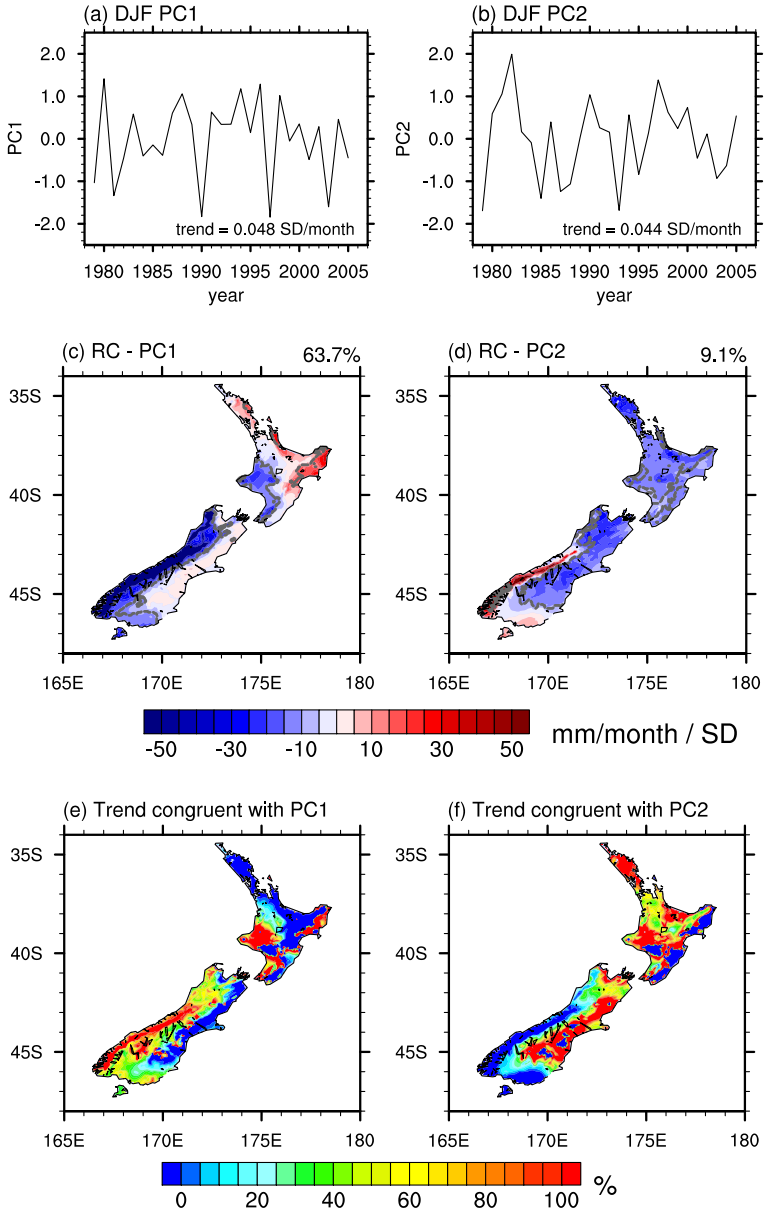

Figure 6.4. (a) PC1 and (b) PC2 time-series of New Zealand precipitation for the DJF season for the period 1979–2006 (with the year given for the first month in the summer season). Regression of the (c) PC1 and (d) PC2 onto New Zealand precipitation for the DJF season, with gray dashed lines indicating significant regression coefficients at the 95% confidence level as estimated after Sciremammano (1979); DJF trends in New Zealand precipitation linearly congruent with the (e) PC1 and (f) PC2, averaged over the period 1979–2006 as a fraction of the monthly DJF precipitation trend. The fractions were only calculated for those grid points in which the DJF precipitation trend was significant at the 90% confidence level. The average monthly DJF trends (in SD month^{-1}) in the PC1 and PC2 time-series are indicated at the bottom right of (a, b), and the fraction of overall variability explained by EOF1 and EOF2 at the top of (c, d).

precipitation trends over the North Island and eastern regions of the South Island (up to a 100% in places; Fig. 6.3f).

6.4.5. Climate modes and the Southern Hemisphere circulation

In order to associate the dominant modes of precipitation variability over New Zealand with the large-scale atmospheric circulation, SLP, winds, and SST anomalies are regressed onto the standardized and detrended SAM, SOI, PC1, and PC2 time-series across the Australasian and surrounding region. Significance levels are estimated following the method of Sciremammano (1979).

The regression of SLP onto the SAM index is characterized by an increased meridional SLP gradient with a positive pressure anomaly at mid-latitudes for 30°–55°S and reduced values over the polar regions south of 55°S (Fig. 6.5a) for a positive SAM phase (e.g., Gillett *et al.*, 2006). The winds adjust to the changed SLP field and show a strengthening of the subpolar westerlies of up to 2 m s^{-1} at the latitude band 50°–65°S and an easterly anomaly over 25°–40°S (Fig. 6.5c). More regionally, around New Zealand, the SAM is associated with increased easterly to northeasterly flow over the country, as shown also by Ummenhofer and England (2007). When using ERA-40 data instead of NNR, the area of significant easterly anomalies in the wind field across New Zealand is slightly reduced. The SST around New Zealand and across the Tasman Sea are negatively correlated with the SAM, as is the equatorial Pacific Ocean (Fig. 6.5e). These characteristic signals associated with the SAM have also been described previously (e.g., Hall and Visbeck, 2002; Sen Gupta and England, 2006).

Regressing SLP onto the SOI shows extensive negative anomalies over the Australasian region and Antarctica, while positive values extend over New Zealand and the southwestern Pacific Ocean (Fig. 6.5b). This regression can be interpreted as a one SD positive anomaly in the SOI; that is, corresponding to moderate La Niña conditions. The wind anomalies in Fig. 6.5d are predominantly easterly across the western equatorial Pacific, as expected, and easterly also over New Zealand (see also Mullan, 1995; Waugh *et al.*, 1997; Kidson and Renwick, 2002; Ummenhofer and England, 2007). As is widely known, a negative phase ENSO is associated with reduced SST along the equatorial central and eastern Pacific, while above-average SST occurs to the south and north in the Pacific, as well as in the western Warm Pool region, as seen in Fig. 6.5f. In addition, positive SST anomalies are observed around New Zealand and in the Southern Ocean south of Australia.

In contrast to the regressions onto the SAM and ENSO time-series, those related to PC1 and PC2 are associated with a more localized reorganization of the atmospheric circulation. PC1 projects strongly onto an anomalously positive area of

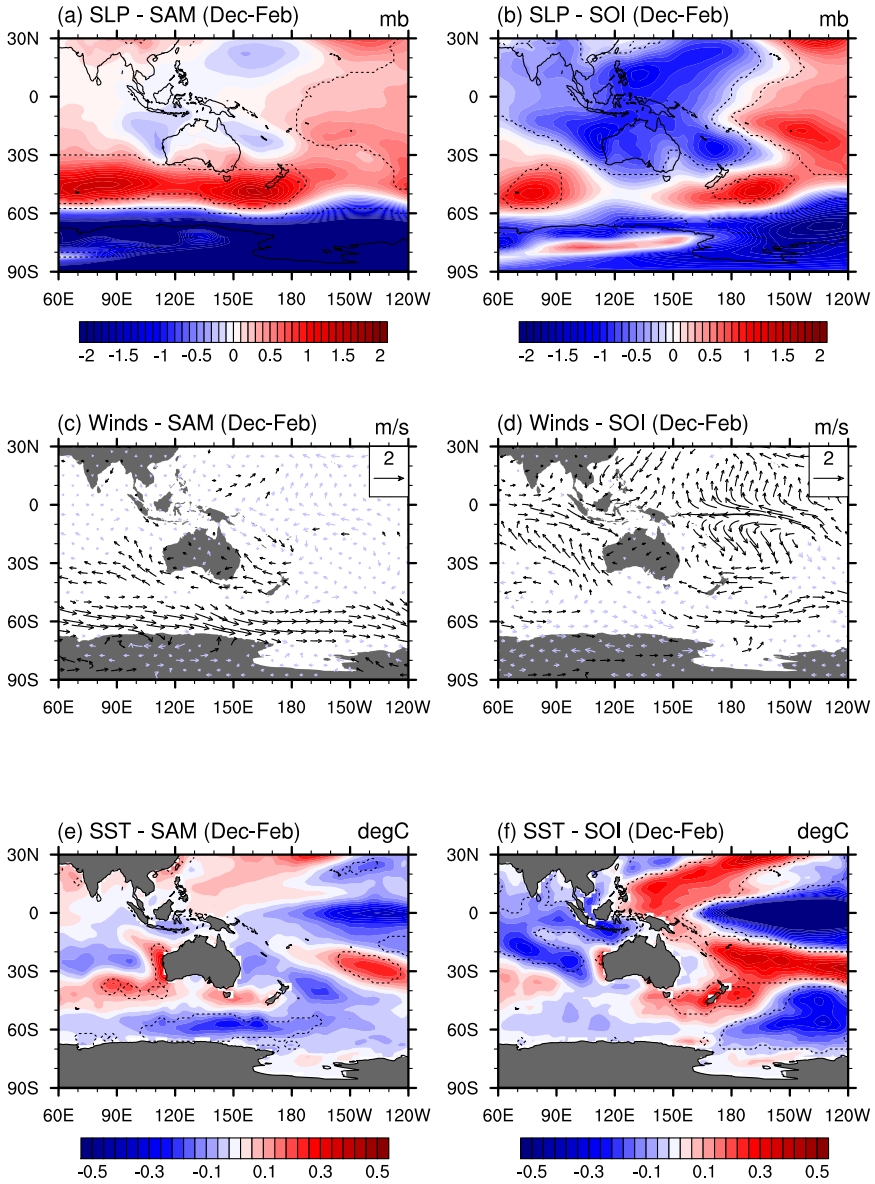

Figure 6.5. Regression of the SAM (left) and SOI (right) time-series for the period 1979–2006 onto (a, b) SLP, (c, d) winds, and (e, f) SST. Dashed lines in (a, b, e, f) and black vectors in (c, d) indicate significant regression coefficients at the 95% confidence level, as estimated after Sciremammano (1979).

SLP across New Zealand, extending west to the Australian Bight and south to 60°S (Fig. 6.6a). Negative correlations between PC1 and SLP occur to the north of New Zealand and over parts of Antarctica. The adjustment of the wind to the region of positive SLP across and south of New Zealand seen for PC1 results in anomalous easterly airflow across the country and a strengthening of the subpolar westerlies for 120°E–160°W (Fig. 6.6c). The area of significantly increased subpolar westerlies is slightly smaller when using ERA-40 (figure not shown) as opposed to NNR data

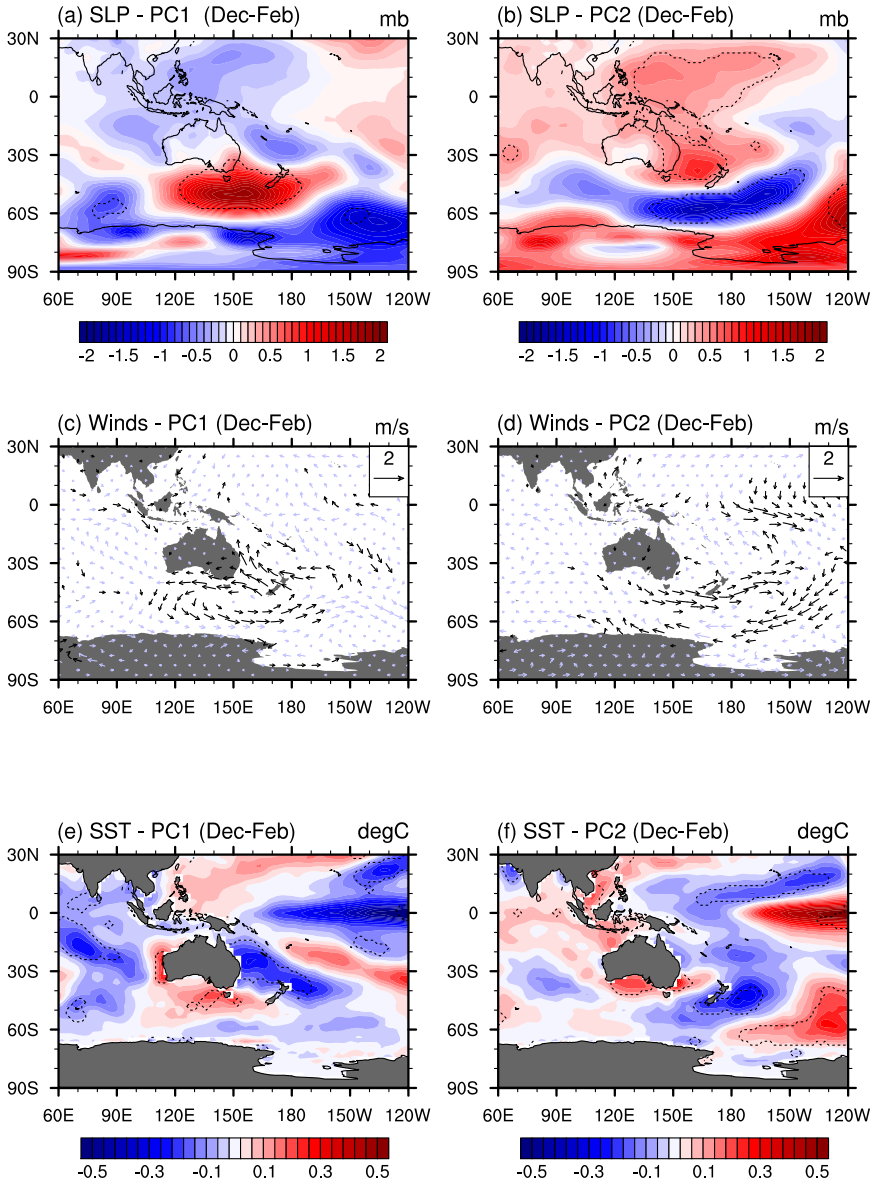

Figure 6.6. Regression of the PC1 (left) and PC2 (right) time-series for the period 1979–2006 onto (a, b) SLP, (c, d) winds, and (e, f) SST. Dashed lines in (a, b, e, f) and black vectors in (c, d) indicate significant regression coefficients at the 95% confidence level, as estimated after Sciremammano (1979).

(shown in Fig. 6.6). This local wind anomaly pattern over New Zealand linked to PC1 is reminiscent of the one associated with a positive SAM phase (Fig. 6.5c). Salinger (1980) describes similar regional pressure and circulation anomalies associated with the leading mode of New Zealand precipitation. PC1 is further associated with anomalously cold SST to the northeast of Australia across the Coral Sea, while above-average SST appears in the latitude band 40°–50°S south of Australia and New Zealand, and across the Tasman Sea; although only parts of this regression are

statistically significant (Fig. 6.6e). In contrast, PC2 shows a positive correlation with SLP for the Australasian region, while negative values are observed over the southwestern Pacific (Fig. 6.6b). This pattern bears close resemblance to the ENSO projection (Fig. 6.5b), though of opposite sign due to the negative nature of the SOI. However, the center of the strongest correlation has intensified and moved directly over New Zealand, while the negative center in the southwest Pacific is situated more to the southwest for PC2 than for ENSO. The predominant wind direction associated with PC2 is westerly (more southwesterly in ERA-40; figure not shown) across New Zealand, as previously suggested to be associated with a positive phase ENSO (cf. Fig. 6.5d; Mullan, 1995; Waugh *et al.*, 1997; Kidson and Renwick, 2002; Ummenhofer and England, 2007). Salinger and Griffiths (2001) ascribe an increased frequency of rain-producing synoptic disturbances and showers to such an enhanced westerly circulation regime, which is consistent with the precipitation pattern (Fig. 6.4d). In addition, the regression of PC2 onto SST (Fig. 6.6f) closely mirrors the ENSO projection (Fig. 6.5f).

The regression of different climate variables onto the four time-series – namely the ENSO, SAM, PC1, and PC2 – further demonstrates that the SAM and PC1 and ENSO and PC2 show many similarities. The SAM, trending towards its positive phase, with an increased meridional SLP gradient and a coinciding strengthening and southerly shift in the westerlies, is thus able to explain some of the negative precipitation trends over much of New Zealand (seen already in Fig. 6.3e). In fact, over New Zealand, the signature in the wind field linked to PC1 (Fig. 6.6c), which explains 64% of the observed precipitation variability including the prominent west coast precipitation trends (Fig. 6.4c, e), closely resembles circulation changes expected under a SAM trend toward a more positive phase.

6.5. Discussion and conclusions

We have investigated how trends in New Zealand precipitation over the period 1979–2006 might be linked to, and explained by, recent changes in the large-scale atmospheric circulation of the Southern Hemisphere. Results of the breakpoint analysis (Fig. 6.1) seem to support a regime shift over New Zealand in the mid-1970s, with a change from predominantly easterly/northeasterly to westerly/southwesterly airflow (Salinger and Mullan, 1999; Salinger and Griffiths, 2001), affecting the country's precipitation. Increasingly drier conditions across much of New Zealand during austral summer since 1979 (Fig. 6.2) are, in large part, consistent with recent trends in ENSO and the SAM (Fig. 6.3). Over the North Island and western regions of the South Island in particular, negative trends in precipitation could potentially

be accounted for by the SAM. The contribution of ENSO to these drying trends is of considerably smaller magnitude, especially when considering the uncertainties associated with recent changes in ENSO behavior.

During the period 1976–1998, westerly and southwesterly airflow anomalies dominated over New Zealand (Salinger and Griffiths, 2001), and were associated with increased frequency of El Niño events (Salinger and Mullan, 1999). Increased westerly airflow over the country is a feature at odds with a trend toward the positive-index phase of the SAM. A positive phase in the SAM would normally be associated with predominantly easterly to northeasterly wind anomalies over New Zealand (Fig. 6.5c) and drier conditions for western regions of both islands (Fig. 6.3c; Ummenhofer and England, 2007). Considering the observed trends in New Zealand precipitation (Fig. 6.2), at least during austral summer and autumn when changes in the SAM are maximal (Thompson and Solomon, 2002; Arblaster and Meehl, 2006), the SAM's effect appears to dominate with widespread drying. The apparent contradiction in zonal flow anomaly found in Salinger and Griffiths (2001) and Salinger and Mullan (1999) with the present work might be due to the different study periods and/or the focus on the DJF season here. Decadal variations in the SAM's influence, both on long-term trends and on seasonal to interannual timescales, can also not be excluded, so that the exact contribution of the SAM to trends might be dependent on the time period being investigated. The sparse data record prior to 1979 in the Southern Hemisphere makes it difficult to extend these analyses further back in time, at least based on observations/reanalysis data. Jones and Widmann (2003) find the SAM index, estimated and reconstructed from tree-rings and station-based data for the past century, to vary in its influence on the general atmospheric circulation over the New Zealand region on decadal to multi-decadal timescales. They suggest that the SAM strongly modulates the circulation during the period 1930–1975, while its impact is weaker for the period 1976–1994.

In addition, considering New Zealand's rich orography and its interaction with the atmospheric flow, local modulation of large-scale circulation changes can be expected. However, when looking at the close match of Figs. 6.5 and 6.6, local variations seem to be aligned fairly well with the large-scale changes. The upward trend in the SAM is not mirrored by increasing frequency of dry years for the two New Zealand islands for the period 1960–2004 (Ummenhofer and England, 2007). This could be due to opposing precipitation trends for the western and eastern regions of the islands. In contrast, for the North Island over the last few decades, both a more positive SAM and an increased frequency of El Niño events (Salinger and Griffiths, 2001) potentially act in concert towards overall drier conditions for the entire island, a feature already apparent in the multi-decadal precipitation decline

of -8.13 mm yr^{-1} averaged over the North Island (Ummenhofer and England, 2007). Furthermore, as Ummenhofer and England (2007) show North Island precipitation to be modulated by local SST on interannual timescales, localized effects of recent SST changes could also contribute to New Zealand precipitation trends, locally enhancing convective precipitation. This is especially apparent when considering the strong warming of ocean temperatures observed around New Zealand and especially across the Tasman Sea (e.g., Cai *et al.*, 2005a; Cai, 2006; AGO, 2007).

Changes in precipitation in other regions of the Southern Hemisphere have recently been linked to trends in the SAM. For the DJF season, trends in the SAM seem to contribute to wetter conditions over southeastern Australia during 1979–2005 (Hendon *et al.*, 2007). For southwest Western Australia (SWWA), up to 70% of the recent observed decline in austral winter rainfall is found to be congruent with trends in the SAM (Cai and Cowan, 2006). In contrast, Meneghini *et al.* (2007) suggest that the long-term trend in SWWA winter rainfall is not related to the SAM, while current short-term decreases in winter rainfall in southern South Australia, Tasmania, and Victoria are. Despite these possible contradictions, implications for water management are considerable, especially as climate model simulations for the 21st Century project continued upward trends in the SAM toward its high-index phase (Fyfe *et al.*, 1999; Kushner *et al.*, 2001). Thus, regions presently experiencing SAM-related precipitation changes are likely to be affected further. For New Zealand, this situation could be further exacerbated if precipitation trends due to the SAM and ENSO act in concert, as shown to be the case over the North Island of New Zealand in this study.

Acknowledgements. We thank the National Institute of Water and Atmospheric Research in New Zealand for providing the precipitation data set used in this study. Use of reanalysis data from the National Center for Atmospheric Research, jointly developed with the National Center for Environmental Prediction and provided through the NOAA Climate Diagnostics Center (http://www.cdc.noaa.gov), and the ERA-40 data by the European Centre for Medium-Range Weather Forecasting is gratefully acknowledged. We are grateful to Andrea Taschetto for help with some of the statistical analyses employed. The comments of three anonymous reviewers helped improve the original manuscript. CCU and ASG were supported by the University of New South Wales under a University International Postgraduate Award and MHE by the Australian Research Council.

Chapter 7

The Autumn Break for Cropping in Southeast Australia: Trends, Synoptic Influences and Impacts on Yield

Michael Pook[1], Shaun Lisson[2], James Risbey[1], Caroline Ummenhofer[3], Peter McIntosh[1], and Melissa Rebbeck[4]

[1] CSIRO Marine and Atmospheric Research, Hobart, Tasmania, and Wealth from Oceans National Research Flagship, CSIRO, North Ryde, New South Wales, Australia
[2] CSIRO Sustainable Ecosystems, University of Tasmania, Private Bag 54, Hobart, Tasmania and Wealth from Oceans National Research Flagship, CSIRO, North Ryde, New South Wales, Australia
[3] Climate and Environmental Dynamics Laboratory, School of Mathematics and Statistics, University of New South Wales, Sydney, Australia
[4] South Australian Research and Development Institute, Climate Applications Unit, Adelaide, South Australia

Manuscript for: International Journal of Climatology
Status: submitted

7.1. Abstract

The autumn break is the first rainfall event of the season which provides sufficient moisture to induce germination of the crop and which is then able to supply the necessary soil moisture to sustain the plants in the first phase of their growth. Two definitions of the autumn break have been developed for northwestern Victoria; a so-called ideal break and a minimum rainfall condition for sowing a crop termed a minimal break. Application of the ideal break definition for an eight station average reveals that autumn breaks have been less reliable and have tended to occur later in the latter half of the record than in the first half of the 20th Century. Ideal autumn breaks occurred in 41 years in the first half (1889 to 1947) and 34 years in the second half (1948 to 2006). In the decade to 2006, there have been only 3 ideal breaks (1999, 2000, and 2005). None of the selected rainfall stations has recorded an 'extreme' wet autumn over the last eleven years, the longest period ever recorded for this criterion. A synoptic analysis for the period 1956 to 2006 has established that breaks are predominantly associated with systems known as cutoff lows but their influence has declined markedly in the past decade. Changes in the characteristics of autumn breaks over the historical record suggest that significant shifts in atmospheric circulation may have occurred but lack of upper air data precludes detailed synoptic analyses prior to 1956.

A farming system model (APSIM) has been employed to simulate a wheat crop in northwestern Victoria under historical conditions for a range of management options. Average yield across all years of the simulation declines with delay in sowing date after late April but there is a marked interannual variability in yield response to sowing date which is related to rainfall distribution in each year. Trends in mean yield and mean sowing date in the simulation indicate that the most recent drought in southeastern Australia is comparable in severity with the two major droughts in the 20th Century.

7.2. Introduction

The autumn break is a keenly anticipated event in the southern Australian agricultural calendar. It sets the time when successful sowing of grain crops can proceed and initiates pasture growth which can then be 'autumn saved' for grazing during the dormant winter period. Failure to have an autumn break can have severe financial repercussions, particularly when available soil moisture is low following a dry summer.

The definition of the autumn break is problematic since farmers and graziers can have differing opinions on the effectiveness of autumn rainfall depending on the predominant enterprise of the farm, soil types, regional climatology, and farming methods. Hence, the definition of the autumn break will vary to some extent from farmer to farmer and district to district. In order to set the parameters of meaningful definitions we have conducted meetings and surveys with groups of grain farmers in southeastern Australia. The definitions adopted for this study and presented in Section 3 of the paper have been developed from these discussions.

The grain-growing season in southeastern parts of mainland Australia extends from about April to the end of October (French and Schultz, 1984; Robertson and Kirkegaard, 2005; Pook *et al.*, 2006). During this period the region receives the majority of its annual rainfall, evaporation is lowest and the number of rain days per month is highest. The mean growing season rainfall over the majority of the region is less than 300 mm and rainfall events tend to be infrequent (less than 35% of days receive at least 0.2 mm of rain). Crop success also depends on soil moisture at the time of planting (French and Schultz, 1984; Carberry *et al.*, 2000).

The portion of northwestern Victoria shown in Fig. 7.1 is an important grain-growing region of Australia and produces the majority of grain grown in the state of Victoria. Based on an average over the five years to 2004–05, Victoria contributes about 11% of the total Australian wheat crop and 13% of Australia's total winter crop production (ABARE, 2007). Wheat is the dominant crop grown in this region often (but not always) in rotation with other grain crops (e.g., barley, oats, canola, lentils, lupins, chickpeas) and a pasture phase. Although lacking organic matter the predominantly solonized brown soils (commonly known as mallee soils) of the region are moderately fertile (McGarity, 1987). In the absence of nutrient deficiencies in the soil, major constraints on wheat growth in this region include the timing and amount of autumn rains for sowing, duration of the winter minima in solar radiation and temperature, timing of the earliest 'safe-ear' emergence in relation to frost occurrence and the rapid increase in temperature and evapotranspiration in late spring (Nix, 1987). The water supply to the growing crop is the most critical

factor affecting wheat yields in this as in many other water-limited environments of Australia (French and Schultz, 1984; Stephens and Lyons, 1998). Water deficiencies act to reduce the grain number per ear as well as the individual grain size (Donald and Puckridge, 1987).

Although cereal crops are normally sown in May and June, varying seasonal conditions and farming methods may dictate that sowing begins as early as April or is postponed until as late as August in an extremely dry season (Stephens and Lyons, 1998). As sowing is typically carried out from April to June we consider the autumn break to occur in any of the months, March to June.

Some farmers wait for an autumn break before sowing but an increasing number sow into a dry seed bed, especially those that employ minimum tillage techniques in order to preserve soil moisture. In these operations crops are planted according to a schedule rather than in response to individual rain events. As crops are almost exclusively rainfed there are considerable risks in committing to a sowing program very early in the season but the potential gains in yield of sowing when soil temperatures are favorable for germination, survival and plant vigor are very attractive to farmers (Stephens and Lyons, 1998). Notwithstanding these potential gains there is nevertheless a risk of severe damage from frost for those plantings which result in flowering prior to early October and consequently, cultivation techniques which minimize this risk have been developed in some regions (Rebbeck *et al.*, 2007).

Improved prediction skill for autumn break events would contribute to improved efficiency by influencing the total area sown, choice of crop and variety, controlling production costs such as those associated with seed, fertilizer and fuel, and minimizing the risk of crop failure. Current predictions of seasonal climate based on the ENSO state are relatively unreliable in the austral autumn as there is a significant reduction in forecast skill around this time of the year (McIntosh *et al.*, 2005).

Pook *et al.* (2006) have argued that seasonal rainfall represents the integrated contribution of a number of discrete synoptic weather systems and it is important to identify those systems responsible for rainfall events and the mechanisms contributing to rainfall generation. In this study we have employed the techniques of synoptic climatology to identify the synoptic systems responsible for the significant autumn rainfall events which contribute to the autumn break in a given year in order to better understand the physical processes and detect trends in frequency of occurrence of particular synoptic types. In order to better represent the effects of the autumn break on crop performance this paper explores trends in selected wheat growth variables simulated in a farming system model under a range of sowing conditions at one location in the study region.

7.3. Data and method

7.3.1. Data sources

Daily rainfall was extracted from the Patched Point Data set supplied by the Queensland Department of Natural Resources and Mines (DNRM; Jeffrey *et al.*, 2001) for eight rainfall stations which were selected to represent northwestern Victoria from a high-quality Australian historical data set (Lavery *et al.*, 1997). The Patched Point Dataset uses original Bureau of Meteorology observations for a particular meteorological station infilled where necessary with interpolated data. The locations are the same as those employed in Pook *et al.* (2006) and are shown in Fig. 7.1.

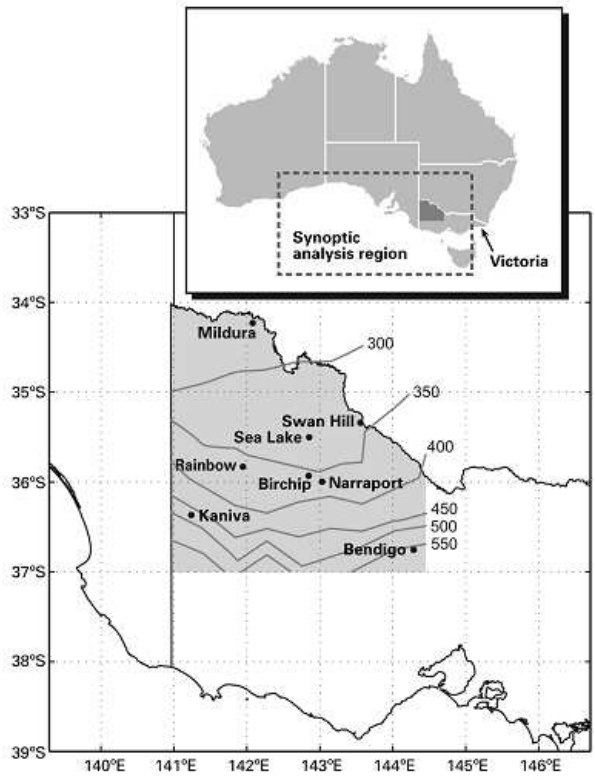

Figure 7.1. Map of northwestern Victoria showing the network of high quality rainfall stations used in the analysis. The large dotted box over the map of Australia defines the region within which the analysis of synoptic systems was confined. The dark shaded area indicates the region of southeastern Australia included in the lower part of the diagram. Annual rainfall (mm) for northwestern Victoria is represented by isohyets (after Pook *et al.*, 2006).

The synoptic analysis was conducted using the National Centers for Environmental Prediction (NCEP) - National Center for Atmospheric Research (NCAR) climate reanalysis data set (Reanalysis 1) that will be referred to as the NCEP data

set (Kalnay *et al.*, 1996; Kistler *et al.*, 2001). NCEP produces 4 analyses per day (at six-hourly intervals from 0000 UTC) at a resolution of 2.5° latitude by 2.5° longitude for the standard atmospheric levels from the surface to the lower stratosphere. For the purposes of this study, fields were extracted for mean sea level pressure (MSLP), the 500 hPa pressure surface and the (computed) 1000–500 hPa atmospheric thickness and the 1000–500 hPa thickness anomaly relative to the long-term climatology.

Daily weather maps at 2300 UTC published in the Australian Bureau of Meteorology's 'Monthly Weather Review' series (Simmonds and Richter, 2000) were used in parallel with NCEP for the period from 1970 to 2006. These charts have been prepared by expert analysts and include frontal analysis which has been performed manually by interpretation of satellite imagery in addition to conventional analysis of synoptic data (Guymer, 1987). The inclusion of the manual analyses was considered to be an essential component of the analysis project as the NCEP numerical reanalyses lack this human input and do not have sufficient horizontal resolution to locate fronts reliably (Pook *et al.*, 2006). The starting point for the original analysis was set at 1970 since techniques for incorporating the subjective interpretation of satellite cloud imagery into an objective analysis scheme became established practice in the World Meteorological Centre, Melbourne, around that time (Guymer, 1987; Seaman and Hart, 2003) and secondly, NCEP analyses for the Southern Hemisphere have been found to have systematic biases prior to 1970, particularly at high latitudes (Hines *et al.*, 2000). Other reported errors in NCEP, such as those related to the absence of satellite temperature soundings prior to 1979 (Kistler *et al.*, 2001), are not regarded as significant because of the proximity of our analysis region to the Australian radiosonde network and since the Australian MSLP analyses were consistently consulted in parallel.

In order to extend this study further back in time a selection of MSLP, 700 hPa and 500 hPa analyses were obtained from the Australian Bureau of Meteorology for 2300 UTC and 1100 UTC each day. This chart series was available from 1956 but the lack of a sufficiently dense upper air data network for the Australian region prior to that year precludes a comprehensive synoptic analysis for an earlier period (Bradshaw, 1997). Additionally, the NCEP data set is considered to be unreliable in the Southern Hemisphere prior to 1958 (Kistler *et al.*, 2001). It should be noted that the Australian analyses (1956–1969) are copies of the actual operational charts and may lack the dynamical consistency of the later period (from 1970). However, when these charts are used in parallel with the NCEP data, we believe that a reliable synoptic classification can be made for the major rainfall events associated with the autumn break over southern Australia.

7.3.2. Method

For each autumn break, according to the definitions adopted, an assessment was made of the nature of the synoptic system responsible for the precipitation event. The analysis region was defined by a fixed box with limits, 30°S, 125°E; 30°S, 147.5°E; 45°S, 147.5°E, and 45°S, 125°E as shown in Fig. 7.1. Synoptic systems were classified according to the classification scheme which is discussed by Pook *et al.* (2006). The four categories are cold frontal systems of all types, cold-cored lows which have become cut-off from the westerly airstream (cutoff lows), troughs in the easterlies and a combined category designated 'others' that includes systems not found in the main categories.

The relationship between crop performance and autumn rainfall was explored within an agricultural systems model. Crop production systems are characterized by complex interactions between climate, soil attributes, management operations and varietal characteristics. Dynamic simulation models that capture this inherent complexity provide an efficient means for analysing systems performance across a wide range of conditions. In this study, the farming system model APSIM (Agricultural Production Systems sIMulator; Keating *et al.*, 2001) has been used to explore seasonal trends in selected wheat growth variables under a range of sowing conditions at Birchip, NW Victoria (for location, see Fig. 7.1). APSIM simulates agricultural production systems by combining modules describing the specific processes within the system under investigation. The soil water module SOILWAT2 (Probert *et al.*, 1997), the soil nitrogen module SOILN2 (Probert *et al.*, 1997), and the surface residue module RESIDUE2 (Probert *et al.*, 1997) were linked with the wheat crop module APSIM-WHEAT (Keating *et al.*, 2001), which simulates wheat growth and development in response to climatic, soil and management inputs. All management details were specified via the MANAGER module. For comprehensive descriptions of each of these modules see the relevant link in the APSIM website: http://www.apsim.info/apsim/.

The wheat variety Yitpi was sown in each year of the historical climate record between 1890 and 2005, according to a range of rainfall related sowing conditions based on a prescribed rainfall total ('rain threshold', mm) accumulated over a prescribed period ('rain window', days). The sowing conditions were applied over a fixed 'sowing window' from March 1 to June 30. Years in which the sowing conditions were not met over this sowing window were sown dry on June 30. Combinations of sowing conditions include a 10 mm threshold accumulated over a 3 day window, 10 mm over 7 days, 15 mm over 3 days, 15 mm over 7 days, 25 mm over 3 days, 25 mm over 7 days, 30 mm over 7 days. The simulation was set up such that nitrogen was

non-limiting. APSIM assumes that all other nutrients are non-limiting and that the crop is free of disease, insect damage, weed competition and other related yield constraint. No irrigation was applied. These conditions enabled a focused analysis of the effect of sowing condition and seasonal rainfall on the performance of the wheat cropping system.

A hypothetical clay soil was used for the simulations, with parameters derived from selected references and expert knowledge of 'average' parameter values for soils of this texture. The profile had a maximum rooting depth of 90 cm divided into four layers with a total plant extractable soil water content of 126 mm. The analysis was based on the long-term (1889–2005) climate record for Birchip (Woodlands). The record consists of daily maximum and minimum temperatures, radiation and rainfall totals.

7.4. Characteristics of autumn rainfall in NW Victoria

The autumn season in southern Australia generally coincides with the period of soil preparation and planting of winter crops which are subsequently harvested in the austral summer. Although autumn is officially defined as the season extending over the three calendar months of March, April, and May (Crowder, 1995), planting often continues well into June, depending on seasonal conditions (Stephens and Lyons, 1998). Therefore, in this study, we consider that the four month period from March to the end of June is a more meaningful period over which to investigate rainfall variability and trends as well as the autumn break itself. This crop establishment period (MAMJ) will be referred to as autumn for the remainder of this paper.

Autumn rainfall and annual rainfall have been averaged over the eight station network and smoothed with an eleven year running mean starting in 1894. Fig. 7.2 demonstrates that autumn rainfall and annual rainfall have been decreasing during the past decade. In particular, autumn rainfall has declined to its lowest value in more than one hundred years. This contrasts with annual rainfall which was lower in 1940 and 1900. The drought that persisted from 1895 to 1903 is known as the 'Federation Drought' and is regarded by most authors as the longest, most severe and widespread in the history of Australia dating from European settlement (Foley, 1957; Whetton, 1997; Wright, 2004). The 1939 to 1945 drought is the second longest period of drought since the Federation Drought and was responsible for devastating stock losses (Foley, 1957; Wright, 2004).

Not only has there been a major decline in autumn mean rainfall since 1991 but there has also been a change in the characteristics of rainfall events. Autumn rainfall anomalies for each of the eight stations in the network have been extracted

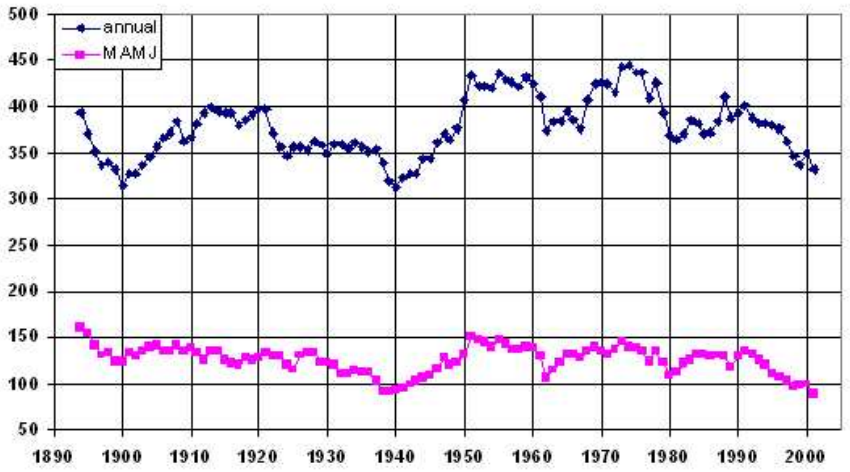

Figure 7.2. Growing season autumn (MAMJ) rainfall and annual rainfall (mm) averaged over the eight stations in northwestern Victoria which have been selected for their 'high-quality' status (Lavery *et al.*, 1997). The data have been smoothed with an eleven year running mean centred on the year shown on the x-axis.

and 'extreme' wet (dry) years defined as years in which the anomaly is at least one standard deviation above (below) the long-term mean for that station. The number of stations indicating an 'extreme' wet season during the period 1889 to 2006 is shown in Fig. 7.3. The length of the most recent period from 1996 to 2006 where no station has recorded an 'extreme' wet autumn, is unprecedented in the record. By way of contrast, the occurrence of 'extreme' dry autumns in this period (not shown) is unremarkable.

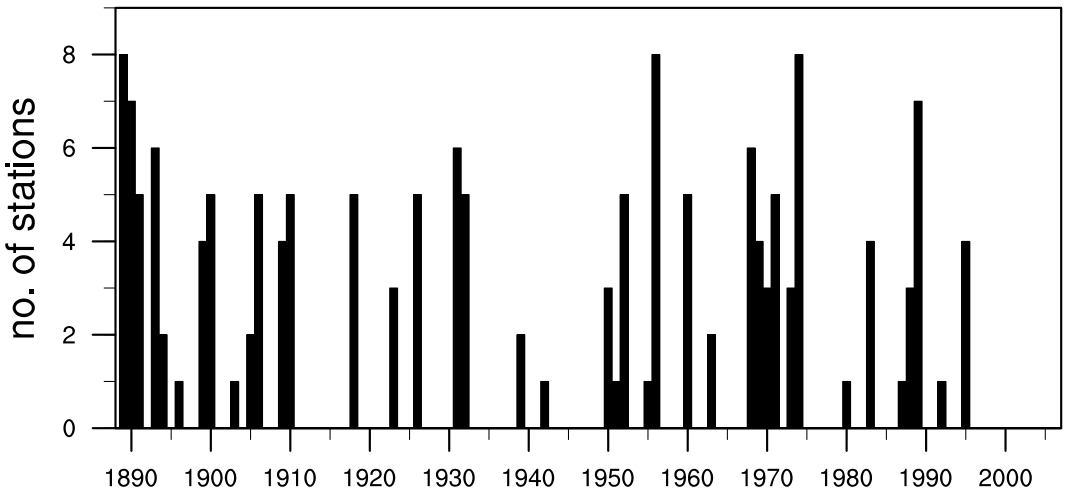

Figure 7.3. The number of stations (from the total of eight) indicating an extreme wet (rainfall exceeds one standard deviation) MAMJ season for the period 1889–2006.

As a preliminary step in the investigation of the autumn break the overall characteristics of daily rainfall in northwestern Victoria were examined for all months. The distribution of daily rainfall in the region is strongly biased towards falls of 5 mm or less (Fig. 7.4). More than 40% of daily rainfall is found in this category with a further 25% in the range from 5 to 10 mm. Over the period from 1889 to 2005, approximately 6% of daily rainfall events are represented by falls of 25 mm or more. For this group of heavy rainfall events, Fig. 7.5 shows the percentage which have occurred in each month. From Fig. 7.5 it is apparent that the highest frequency of occurrence of these heavy rainfall days is in February (20%) with a secondary maximum in October (13%). Approximately 27% of these events have occurred in the March to June period with the highest incidences during autumn occurring in March (10.3%) and May (9%).

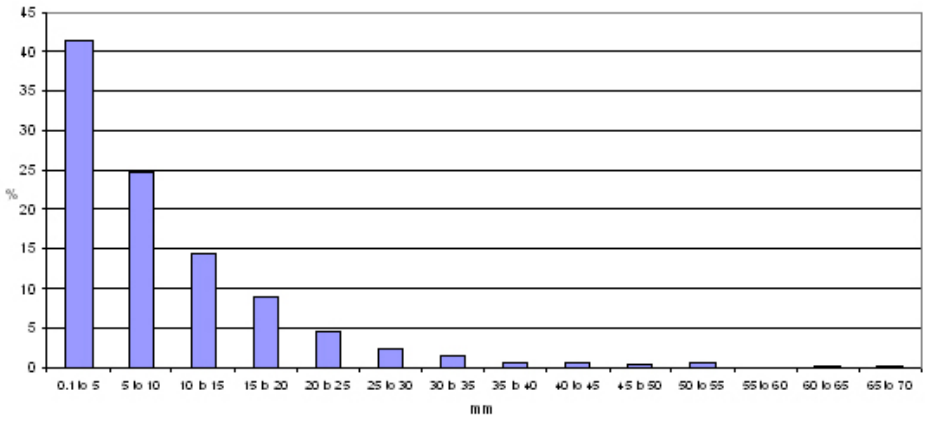

Figure 7.4. Distribution of daily rainfall in 5 mm intervals for the eight station average, expressed as a percentage of the total rainfall for all months over the period 1889 to 2005.

7.5. Defining the autumn break

The autumn break is the first rainfall event of the season which provides sufficient moisture to induce germination of the crop and which is then able to supply the necessary soil moisture to sustain the plants in the first phase of their growth. A common problem for all crops and pasture is the occurrence of a 'false break' where sufficient rain falls to trigger germination but the subsequent soil moisture is insufficient to allow the seedlings to survive (Clark *et al.*, 2003b).

Following a series of workshops with groups of grain growers in southeastern Australia it was found, however, that there was considerable variation of opinion as to what constituted the autumn break for cropping in a region. Considerations of mean rainfall for the area, soil type, crop type, individual farmer preferences and

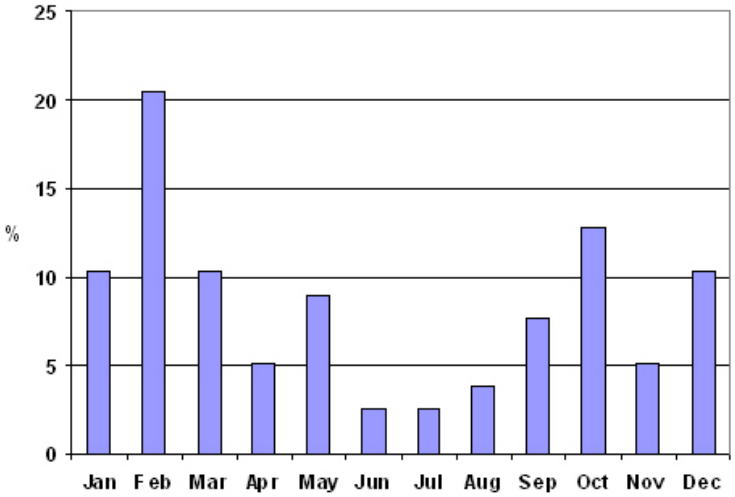

Figure 7.5. Monthly percentage of daily rainfall events resulting in at least 25 mm for the eight station average (period from 1889 to 2005).

available technology were all influences on the amount of rain required to achieve the autumn break for any given farm. In any event, most farmers were prepared to sow a crop in response to a rainfall event that was less than the ideal for their location and cropping plan. There was general agreement though that the autumn break consisted of a significant fall of rain over a period of several days and ideally, this was followed by another fall within the subsequent fortnight. Since the primary purpose of this study was to investigate the synoptic systems responsible for the autumn break and to determine long-term trends, two definitions based on rainfall over selected periods were developed.

The first definition employed was that of an 'ideal' break which was considered to have occurred when a mean fall of 25 mm or more across the 8-station network was received over a period of 3 days or less. Application of this threshold revealed that there were also occasions in the record when, although the strict three-day criterion had not been met, rainfall of the order of the monthly average occurred over a period of a week. Hence, this definition was widened to include a second condition; 'or, 30 mm or more falls over 7 days or less'.

Since some farmers in the drier regions of the study area indicated that they would sow a crop given a lower rainfall than required for an 'ideal' break, alternative definitions setting lower rainfall thresholds were investigated. Thresholds requiring mean falls of 20 mm and 15 mm across the 8-station network over a period of 3 days or less were suggested. However, in order to set a realistic minimum requirement across the study region the lowest threshold for an autumn break was set at 15 mm or more over 7 days or less. This process resulted in an 'ideal' break definition and

a 'minimal' break definition for application in this study.

In summary, an ideal break is defined as occurring if either:

1. A mean fall of 25 mm or more across the 8-station network is received over a period of three days or less, or

2. A mean fall of 30 mm or more across the 8-station network occurs over seven days or less.

The definition adopted for a minimal break is:

1. A mean fall of 15 mm or more across the 8-station network is received over a period of seven days or less.

7.6. Results

7.6.1. Heavy rainfall events

The effectiveness of the definition of the ideal break was initially tested by determining the number of events throughout the historical record which meet the first criterion (1) of the definition. In order to obtain a clearer indication of trend, the data were filtered with an eleven year running mean. Fig. 7.6a demonstrates that the number of events in the crop establishment period that meet this criterion has declined over the record. The lowest values of the running mean (< 0.4 per annum) occurred in 1937, 1938, 1939, 1980 and 2001. Since 1966 there has been a noticeable decline in the mean and the variability in this series. For this period (1966 to 2001), the mean is 0.6 and the coefficient of variation is 21.2% compared to the long-term values of 0.8 and 31.4%, respectively. However, the period from 1977 to 2001 is unprecedented in the record with a further decline of the mean to 0.5 while the coefficient of variation has decreased to 16.1%.

The change in the statistics of wet events in the crop establishment period suggests the possibility of a shift in the seasonal atmospheric circulation over time. In Fig. 7.6b, the time series of the number of wet events in the second half of the growing season (JASO) indicates that there has been a gradual trend to higher numbers of wet events in the record. The lowest value (0.3) occurred in 1900, 1901, 1902 and 1927. Despite the overall upward trend, it is apparent that there has been a rapid decline since 1998.

7.6.2. Timing of the break

Not only has there been a downward trend in the number of autumn wet events over the record but the timing of the autumn break has been getting progressively later. A trend to later breaks is apparent for both the ideal break and the minimal break. Fig. 7.7a demonstrates that the number of days until the first criterion for

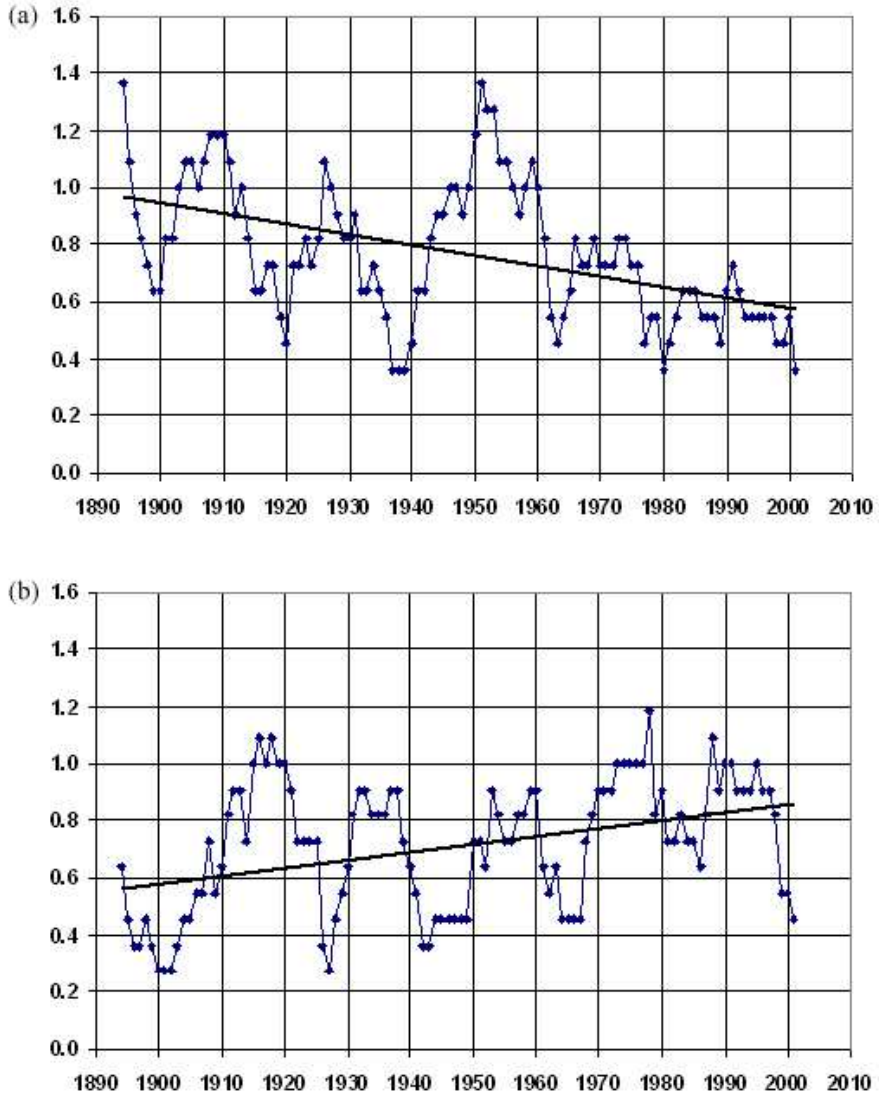

Figure 7.6. Eleven year running mean (centered) of the number of rainfall events per annum resulting in 25 mm or more over 3 days or less in (a) MAMJ, and (b) JASO. Linear trends are significant at 99.9% confidence.

an ideal break is met each year shows an increasing trend. The trend of 6.3 days per decade is significant at the 97% confidence level (Draper and Smith, 1998). In this analysis events prior to March are not considered and the autumn break can only occur from Julian Day 61. For the minimal break rule requiring at least 15 mm in 7 days or less, Fig. 7.7b indicates that the long-term trend is also towards later breaks (3 days per decade later), which is significantly different from zero at the 98% confidence level (Draper and Smith, 1998).

Now we apply the full definition of the ideal break to ascertain whether or not an autumn break occurred in each of the years from 1889 to 2006. Fig. 7.8 shows the month in which an ideal autumn break occurred throughout the entire rainfall

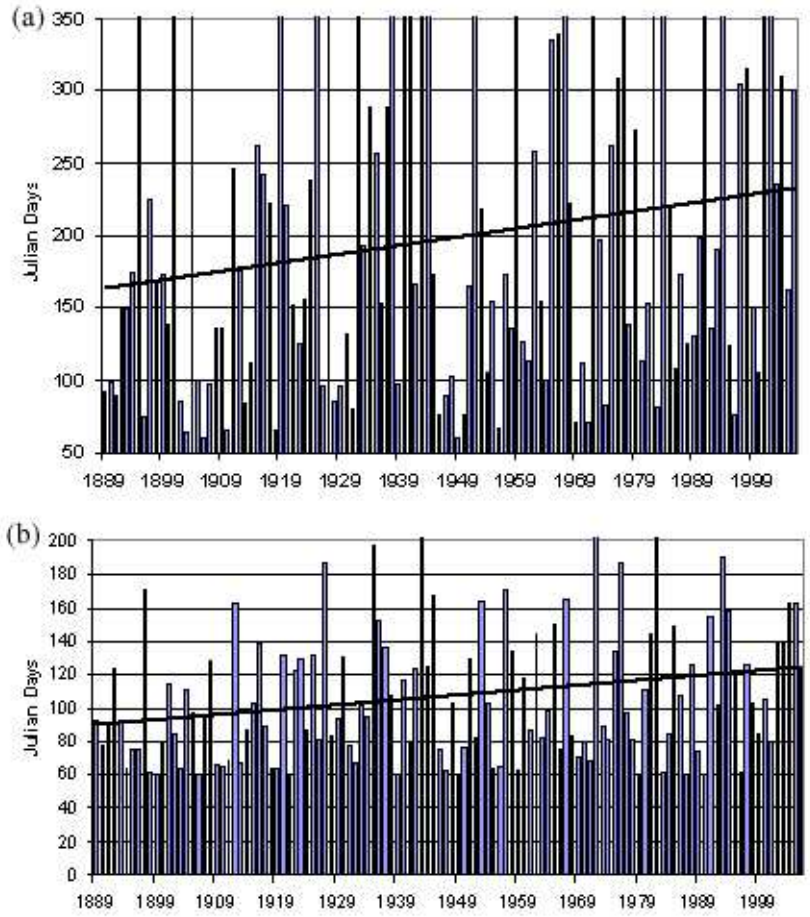

Figure 7.7. Number of days to first event satisfying autumn break criteria for (a) 25 mm in 3 days or less; and (b), 15 mm in 7 days or less (period 1889 to 2006).

record. Years in which an autumn break did not occur are shaded gray. Clearly, there are more breaks in the first half of the record than in the second half of the 20th Century. For the period from 1889 to 1947 there were 41 ideal breaks according to our definition (approximately 70% of years) while from 1948 to 2006, there were only 34 (58% of years). During the period for which we have carried out the synoptic system analysis (1956 to 2006), there were 28 breaks (i.e. 55% of the years had ideal breaks). Furthermore, breaks occur earlier in the first half of the record than in the second half. In particular, 15 breaks identified in the first half of the record occurred in the month of March while only 8 breaks in the second half were in March. The numbers of breaks occurring in the other three months were roughly equal in each half of the record.

In Fig. 7.8, the years from 1956 to the present span the period covered in the synoptic analysis. The period from 1997 to 2006 is particularly noteworthy as it has the lowest number of ideal breaks (3) of any decade in the record. Although it

was demonstrated in Fig. 7.2 that the eleven year running mean of annual rainfall was slightly lower in 1900 and 1940 than the present, the running mean of autumn rainfall (MAMJ) is at its lowest in 1938 and 2001.

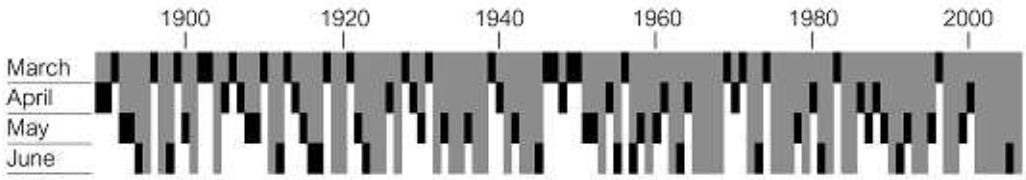

Figure 7.8. Month in which an ideal autumn break occurred (in black) for the period 1889 to 2006. The columns representing years where an autumn break did not occur by the end of June are shaded gray.

7.6.3. Synoptic climatology of autumn breaks

Synoptic systems responsible for ideal autumn breaks were identified for the period from 1956 to 2006. Following the method employed by Pook *et al.* (2006) for daily rainfall, a synoptic system was identified as being predominantly responsible for each event. The dominant synoptic systems responsible for the autumn break were found to be cutoff lows and frontal systems which included simple cold fronts, cold fronts where a wave had formed or complex systems comprising several fronts or front and prefrontal trough combinations. Descriptions of these synoptic types can be found in Pook *et al.* (2006) and the significance of the cutoff low in the Australian context has been demonstrated by numerous authors (see for example, Wright, 1989; Mills and Wu, 1995; Sturman and Tapper, 1996; Griffiths *et al.*, 1998; Reeder and Smith, 1998; Qi *et al.*, 1999). In cases where the second criterion of the ideal break definition applied, it was sometimes necessary to classify two separate systems in combination in order to account for the requisite 30 mm of rain over seven days or less. These cases are included under the classification, 'others' in Table 7.1 which gives the statistics of the synoptic analysis.

Table 7.1. The number of synoptic systems in each month assessed as being responsible for the Autumn Break (1956–2006).

	March	**April**	**May**	**June**
Easterly Trough	2	0	0	0
Cutoff Lows	2	5	7	3
Frontal Systems	2	3	1	1
Others	0	0	1	1

Over the five decades of the synoptic analysis there were 28 years (55%) in which the ideal autumn break definition was satisfied for the eight station mean. Cutoff lows accounted for 61% of the breaks identified while 25% of the breaks were attributed to frontal systems. Tropical dips or easterly troughs were found to have been responsible for only 7% of autumn break occurrences. There is a marked variation in the number of autumn breaks identified in each decade and in the relative contributions of synoptic systems to the autumn break across the five decades under consideration. Fig. 7.9 gives the relative frequency of occurrence of ideal autumn breaks and the associated synoptic systems for five decades beginning in 1956. Half of the breaks identified over the 51 years studied have occurred in only two decades; seven in the first, from 1956 to 1965, and a further seven in the fourth decade from 1986 to 1995. Cutoff lows were directly responsible for eleven of these breaks (approximately 78%) and partly responsible for another two. The decade from 1966 was marked by six autumn breaks. By way of contrast, the decades from 1976 to 1985 and 1996 to 2005 each had breaks in only four years. All the autumn breaks in the former were assessed as being associated with cutoff lows while in the latter decade only one resulted from a cutoff low.

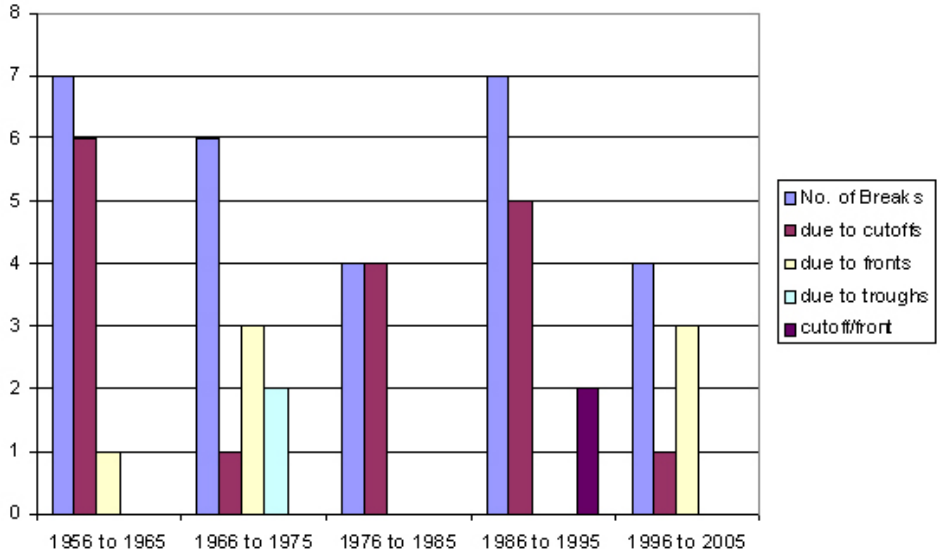

Figure 7.9. Distribution of synoptic systems associated with autumn breaks in the five decades since 1956. The total number of autumn breaks in each decade is also shown.

7.6.4. Impacts of the autumn break on wheat yield

Typically, the more demanding the sowing condition, as exemplified by a shorter rain window and/or larger rain threshold, the later the sowing date (Table 7.2).

The average yield across all years of the simulation declines with delay in sowing date as demonstrated in Fig. 7.10. This can be generally attributed to a shorter vegetative growth phase (i.e. reduced yield potential) and increased water stress as crop maturity is pushed later into the hotter and drier months of the year. Nevertheless, yield response to sowing date varies substantially from year to year (results not shown). In some years, later sowings result in a more favorable alignment of rainfall supply and crop demand, leading to higher yields compared with earlier sowings. Average pre-sow and in-crop rainfall totals were relatively consistent across the sowing treatments.

Table 7.2. Seasonal averages (1889–2005) for wheat yield (kg/ha), day of sowing, pre-sow rainfall total from harvest of previous season crop to sowing of current season crop (mm) and in-crop rainfall total from sowing to harvest (mm) for each sowing treatment.

Rain threshold (mm)	10	10	15	15	25	25	30
Rain window (days)	3	7	3	7	3	7	7
Yield (kg/ha)	2622	2722	2340	2530	1934	2200	2079
Sow day	114	103	131	119	155	141	149
Pre-sow rainfall (mm)	158	160	156	159	170	161	165
In-crop rainfall (mm)	195	193	197	194	183	192	188

Fig. 7.11 shows the 5-year running average for wheat yield, sowing day, and in-crop rainfall for the 15mm over 7 day sowing rule treatment. Trends for the other sowing rule treatments were similar and are not shown. The most recent simulated 5-year running average yield of 1542kg/ha is the lowest since 1944 (Fig. 7.11a). While this yield level is substantially higher than the lows experienced during the droughts of the early 1900s (298kg/ha) and early 1940s (586kg/ha), the trend is downward.

The model run demonstrates that the simulated date of sowing has been getting progressively later over the past 10 years (Fig. 7.11b). In 1996, the 5-day average sowing day was day 105 but this had increased to day 150 in 2005. While somewhat earlier than the simulated peak in the extreme drought in the 1940s (day 175), the current trend is for increasingly later sowings. The current average sowing date is much later than the latest sowing date simulated during the drought during the early 1900s (viz. day 131 in 1901).

The in-crop rainfall plot (Fig. 7.11c) shows that the current running average is at or near the lowest level over the period of simulation and has been declining steadily over the past ten years. There is no evidence from the modeling study to suggest a

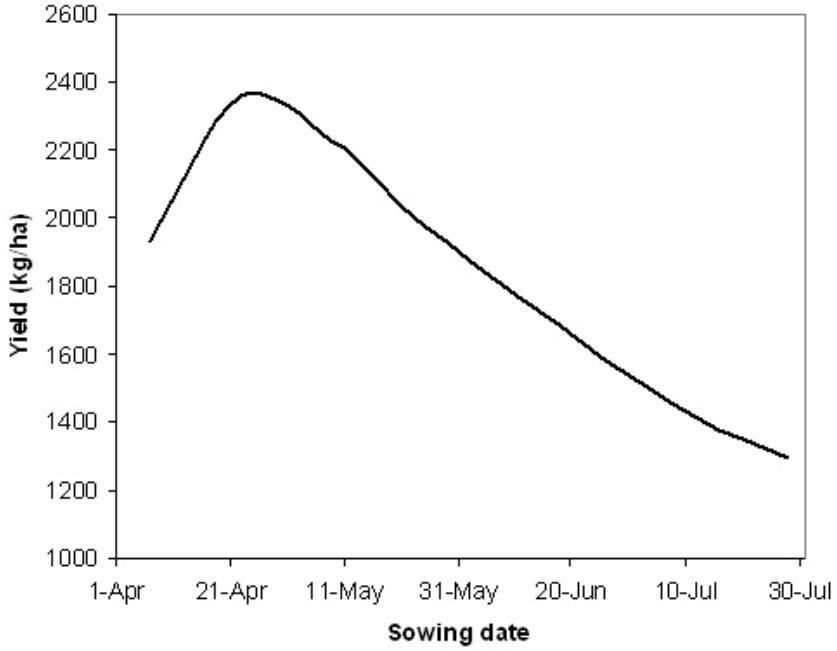

Figure 7.10. Simulated wheat yield response to fixed sowing date at Birchip (see location map in Fig. 7.1) using APSIM and averaged over the period 1890–2005. Simulations are based on a generic soil with plant extractable soil water volume of 126 mm to 90 cm depth. Crops are rainfed, and nutrient unlimited.

decline in pre-sow rainfall in recent times nor a decline in deep drainage below the root zone (not shown).

7.7. Discussion

The synoptic analysis has established that autumn breaks are associated principally with three types of synoptic weather systems: cutoff lows, fronts interacting with subtropical or tropical moisture sources, and deep easterly troughs. Of these, the cutoff low is the dominant type. However, the contribution of cutoff lows has declined markedly in the most recent decade. This is a significant result as it has previously been demonstrated that cutoff lows are responsible for the highest proportion (approximately 55%) of autumn rainfall in the region and that these synoptic systems account for 80% of daily rainfall events exceeding a mean value of 25mm across the eight stations during the entire growing season (Pook *et al.*, 2006). Hence, it is likely that the decline in the occurrence of heavy rainfall events in the crop establishment period and the complete absence of 'extreme' wet autumns from 1996 to 2006 is largely a consequence of the decline in active cutoff lows. Such a decrease could be the result of a decrease in frequency and/or intensity, changes in preferred tracks or in the ability of cutoff lows to access moisture.

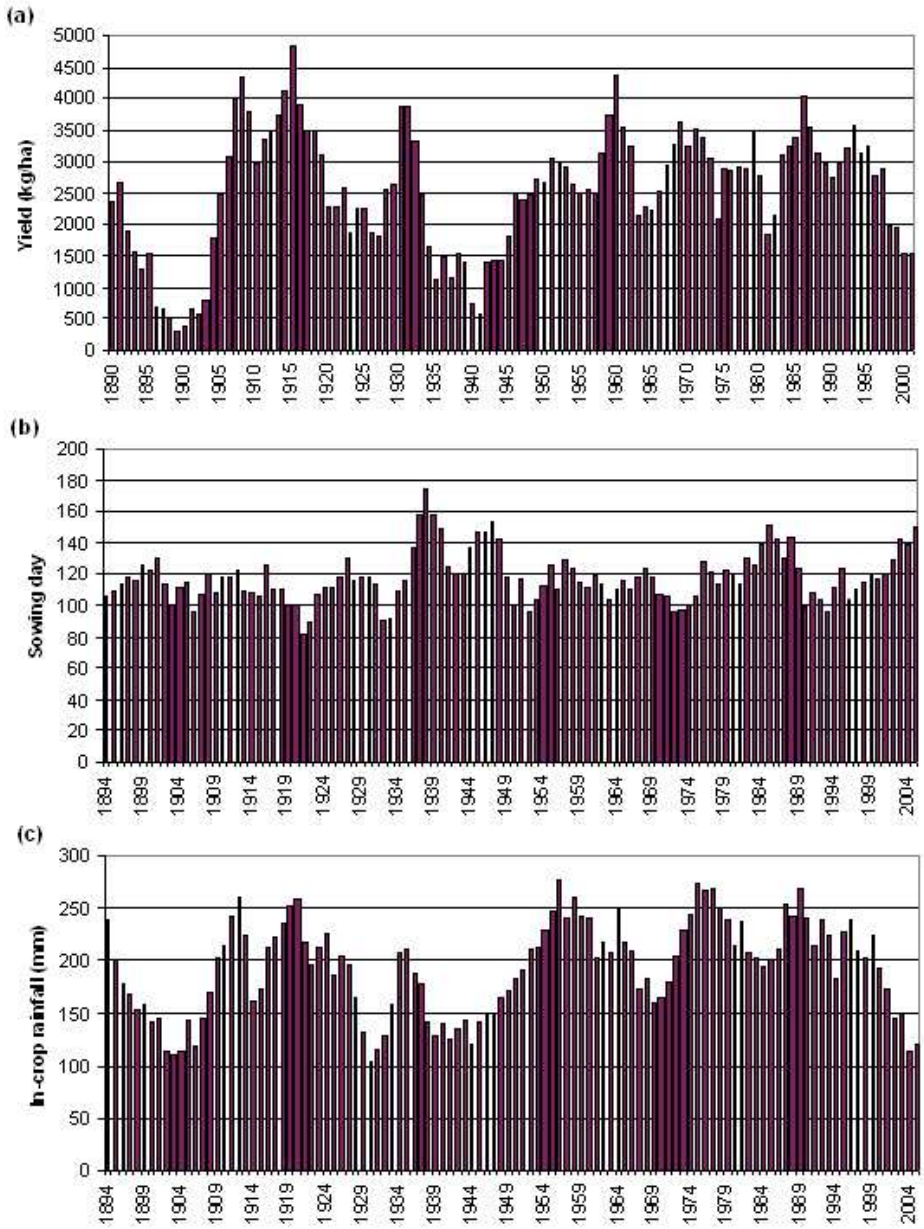

Figure 7.11. Simulated five-year running mean from the APSIM model of (a) wheat yield (kg per Ha), (b) day of sowing, and (c) in-crop rainfall.

A preliminary examination does not indicate any marked decrease in the frequency of occurrence of cutoff lows within our analysis region during the autumns of this period (not shown). It is important to note, however, that the analysis detects all cutoff systems (recorded as cutoff low days) that meet the specified criteria, whether they produce rain or not (Pook *et al.*, 2006). Hence, more research is needed to determine whether there have been significant changes in the intensity of cutoff lows, preferred tracks, and the moisture pathways supplying these cyclones. Mean trajectories indicate that air parcels carry moisture from the tropics down to the

mid-latitudes, particularly for the higher rainfall events. The atmosphere is quite variable and trajectories are observed from oceanic regions to the northeast, north and northwest of Australia, as well as occasionally originating over the Southern Ocean (McIntosh *et al.*, 2007).

However, particular emphasis needs to be placed on the influence of the tropical Indian Ocean, as recent work (Meyers *et al.*, 2007) has demonstrated that June to November rainfall in Australia is well correlated with patterns of tropical sea surface temperature (SST) that represent measures of the combined states of the Indian and Pacific Oceans. Considerable emphasis has been devoted to the interaction of the El Niño-Southern Oscillation (ENSO) phenomenon over the Pacific Ocean with the atmospheric circulation and rainfall in the Australian region (Allan, 1988; Philander, 1990; Allan *et al.*, 1996; Whetton, 1997). Notwithstanding the established strong links between Australian climate variability and the Pacific Ocean, Saji *et al.* (1999) and Webster *et al.* (1999) have demonstrated that the Indian Ocean zonal dipole mode (IODM) is a basin-scale pattern of surface and subsurface ocean temperature that also has detectable impacts on the interannual climate anomalies of Indian Ocean rim countries. Ashok *et al.* (2003a) have presented evidence of a significant impact of the IODM on winter rainfall in western and southern Australia. Nicholls (1989) has previously found a correlation between winter rainfall in central and southeastern Australia with Indian Ocean SST that is largely independent of the Pacific Ocean influence but his spatial pattern of SST does not closely match that of the IODM. It is important to establish whether the state of the Indian Ocean during autumn may be a more important indicator of cool season rainfall probability in southern Australia than conditions in the Pacific Ocean.

A clearer understanding of the role of cutoff lows in the climate system and the factors controlling the interannual variability of cutoff low rainfall has wider implications than the effects on agricultural production in southern Australia. As these systems are responsible for the majority of heavy rainfall events from autumn through the growing season they provide key inputs to stream flows, water storages and the recharge of groundwater in the region. Autumn breaks are important influences on the hydrology of catchments and changes in reliability of these major rainfall events, such as have occurred during the last decade of the time series, can have serious repercussions for water availability in subsequent seasons.

The relationship between crop performance and climatological variables is complex and it is not unusual for the interannual variability of crop yields to run counter to that expected intuitively from the broad climate indicators in a given season, such as total rainfall. In order to deal with this problem we have employed the APSIM farming system model to simulate the effects of interannual variability of autumn

climatological conditions on the performance of a wheat crop. By altering conditions within the model it was possible to carry out a focused century-long analysis of the effect of sowing condition and seasonal rainfall on the performance of the wheat cropping system in a clay soil in northwestern Victoria. Although the autumn break is only one component of the growing season and good crop growth also depends on the overall distribution of rainfall and particularly, on the 'finishing rains' in spring, the sowing date has been identified as a significant influence on yield. Decline in the average yield across all years of the simulation is related to delay in sowing date because of a truncated vegetative growth phase and the tendency for water stress to develop in late-maturing crops. Significantly, the application of sowing rules in the model hindcasts provides a consistent method to demonstrate how severely the drought from 1996 to 2006 has contributed to a progressively later mean sowing date and declines in yield. It also makes possible realistic comparisons of growing conditions and yields in previous droughts.

7.8. Conclusions

Two definitions of the autumn break developed for northwestern Victoria (ideal break and minimal break) have been employed to produce a synoptic climatology of the break phenomenon and identify trends in the climate record. Ideal autumn breaks occurred in approximately 70% of years (41 events) in the first half of the historical record (1889 to 1947) while from 1948 to 2006 only 58% of years (34 events) had ideal breaks according to our definition. In the period for which a synoptic analysis has been completed (1956 to 2006) ideal autumn breaks have occurred across the 8 station network in 55% of years (28 events) but, in the most recent decade (1997–2006) there have been only 3 ideal breaks (1999, 2000, and 2005). The decline in the number of ideal autumn breaks has been accompanied by a trend towards breaks occurring later in the season (by 6.3 days per decade). In the case of the minimal autumn break, the long-term trend over the record is also towards later breaks (by 3 days per decade). During the eleven years from 1996, none of the eight stations recorded an 'extreme' wet autumn (at least 1 standard deviation above the rainfall mean), the longest period that such a sequence has occurred in the record.

The synoptic analysis has established that the cutoff low is the dominant mechanism responsible for ideal autumn breaks. Cutoff lows accounted for 61% of the ideal breaks identified while 25% of the breaks were attributed to frontal systems. Tropical dips or easterly troughs were found to have been responsible for only 7% of autumn break occurrences. However, the influence of the cutoff low appears to

have declined markedly in the past decade. Hence, it is likely that the decline in the occurrence of heavy rainfall events in the crop establishment period and the complete absence of 'extreme' wet autumns after 1995 is largely a consequence of the decline in active cutoff lows.

Simulations carried out in the APSIM crop model have demonstrated that the average crop yield in spring across all years of the simulation tended to decline with delay in sowing date in autumn beyond the end of April. Despite this overall relationship, there is a marked interannual variability in yield response to sowing date which illustrates the significance of matching rainfall with crop demand throughout the entire growth cycle in preference to simple measures of rainfall, such as the growing season total. Nevertheless, rainfall amount from sowing day to harvest day (in-crop rainfall) within the model does provide a useful indication of seasonal conditions. The 5-year running average of the in-crop rainfall has declined steadily in the last decade of the simulation and was only slightly above its lowest value on record at the end of the run. At the same time the mean yield had fallen to its lowest value since 1944. When the minimal break condition was adopted as the sowing rule in the model hindcasts, the mean date of sowing became progressively later during the most recent decade as the yield declined. The mean sowing day according to this rule reached 150 (30 May) in 2005, placing it between the latest sowing date simulated during the major drought in the early 1900s (11 May) and the simulated peak during the drought which began in the late 1930s (24 June).

Acknowledgments. This work was funded by the Managing Climate Variability Program of Land and Water, Australia, and the CSIRO Wealth from Oceans Flagship. C. Ummenhofer was supported by the University of New South Wales under a University International Postgraduate Award and by the Australian Research Council Research Network for Earth System Science (ARCNESS). The support of the Birchip Cropping Group and individual farmers is gratefully acknowledged.

Chapter 8

Variability of Synoptic Features Associated with Cool Season Rainfall in Southeastern Australia

James S. Risbey[1], Michael J. Pook[1], Peter C. McIntosh[1], Caroline C. Ummenhofer[2], and Gary Meyers[3]

[1] CSIRO Marine and Atmospheric Research, Hobart, Tasmania, and Wealth from Oceans National Research Flagship, CSIRO, North Ryde, New South Wales, Australia
[2] Climate and Environmental Dynamics Laboratory, School of Mathematics and Statistics, University of New South Wales, Sydney, Australia
[3] University of Tasmania, Hobart, Australia

Manuscript for: International Journal of Climatology
Status: submitted

8.1. Abstract

Cool season rainfall variability in southeastern Australia is investigated via a classification and characterization of the predominant types of synoptic systems occurring in the region. These types are frontal systems, cutoff low systems, and other systems. Rainfall in the region is dominated by cutoff systems and these systems are the main influence on the interannual variability of rainfall. Both cutoff systems and frontal systems display an enhancement of thermal (thickness) gradient as rainfall increases, but the mechanisms for intensification differ. Cutoff systems intensify in the region in association with local increases in baroclinicity and the subtropical jet, whereas frontal systems tend to intensify via a confluence of subtropical and polar jets. Interannual rainfall variability is examined for groupings of years based on both clustering of continental rainfall patterns and on ENSO/IOD years. Cutoff systems exhibit consistent enhancements of thermal gradients for groupings of years in which they produce more rainfall. For ENSO/IOD groupings, the cutoff thermal gradients are consistent with the underlying SST anomalies. Wet years in southeastern Australia are usually produced by cutoff systems, but can be produced by frontal systems. In those cases the mid-tropospheric flow pattern is reminiscent of the negative Southern Annular Mode (SAM) pattern. The positive SAM pattern is also associated with enhanced rainfall in the southeast via local intensification of blocking and cutoff systems.

8.2. Introduction

Southeastern Australia undergoes significant interannual and decadal rainfall variability and is currently in the midst of an extended period of drought (Gallant *et al.*, 2007; Watkins and Trewin, 2007). The variability of agricultural production in the region is closely related to the variability of rainfall (Nicholls, 1997). Rainfed agriculture in southeastern Australia (grains, sheep, and other livestock) is sensitive to year-to-year fluctuations in rainfall, while irrigated agriculture in the region (fruit, viticulture, dairy) is more sensitive to longer period (decadal) fluctuations in rainfall.

Southeastern Australia is one of the most productive agricultural regions in Australia, though its output varies dramatically in wet and dry seasons in rainfed sectors. The gross domestic product of the rural areas of southeast Australia drops by about 20% in major drought years (Adams *et al.*, 2005). The sources of rainfall variability in the region are thus of interest to agricultural producers. In this paper we document some of the processes associated with rainfall variability in southeastern Australia. In particular, we describe the synoptic features associated with major rainfall events and rainfall variability using a broad set of dynamical diagnostics. We also relate rainfall variability to the major modes of seasonal and interannual variability in the proximate oceans.

The climate of southeastern Australia follows a general Mediterranean pattern, with warm, dry summers, and cooler, wetter winters. The seasonal cycle of rainfall in the region displays a moderate peak in the winter months. Winter rainfall tends to be dominated by mid-latitude storm systems, though interaction with tropical features and moisture sources is often important in the development of these systems over Australia (McIntosh *et al.*, 2007). The amount of rainfall is strongly moderated by location relative to the coast and to the Great Dividing Range (a mountain range skirting the east and southeast edge of the continent; Fig. 8.1). Locations inland of the Great Dividing Range receive much less rainfall than locations on the coastal side of the divide.

One of the major grain growing regions of Australia is located inland of the Dividing Range in southeastern Australia. This region relies in particular on rainfall through the cool season (April–October). Grain yields in the region undergo large fluctuations in association with interannual variations in rainfall. We seek to diagnose and explain some of the sources of that variation. The approach we take is to characterize the different synoptic systems that produce rainfall in this region, and to relate those systems in turn to broader scale features of the circulation.

The analysis of rainfall here is focused on the "Mallee" region, which is part of the inland region described above. The Mallee region is shown in Fig. 8.1. The

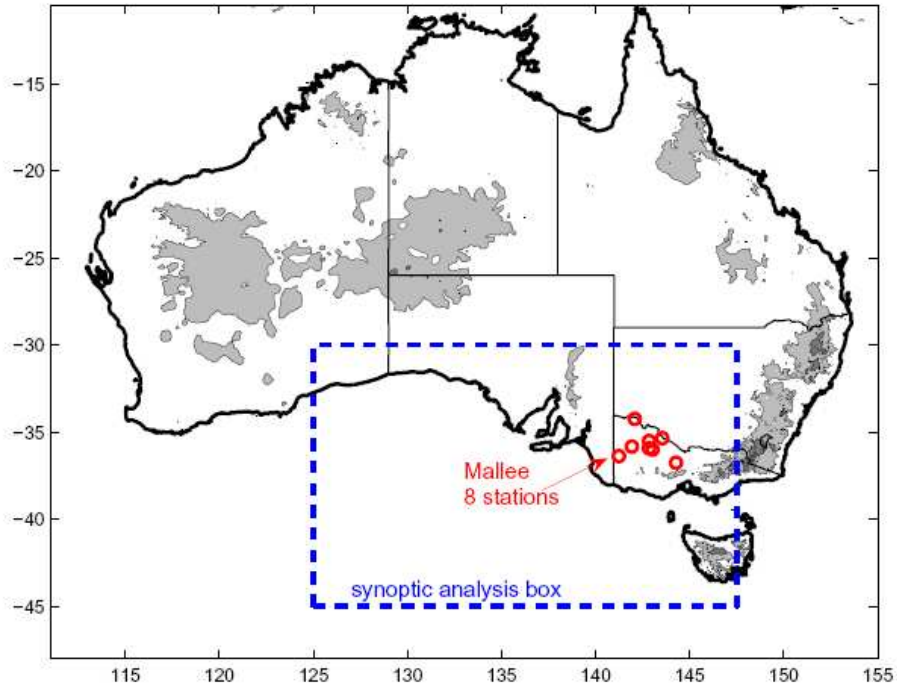

Figure 8.1. Map of Australia showing the locations of the synoptic analysis box and the Mallee rainfall stations. The synoptic box spans latitudes 30°–45°S and longitudes 125°–147.5°E. Areas of topography over 500 m are shaded, highlighting the Great Dividing Range in the southeast of the continent.

selection of this sub-region provides a smaller area that is more homogeneous than the broader southeast from the point of view of any given synoptic storm system. By choosing a smaller region we can be surer that rainfall across the region is the result of the same storm at roughly the same point in the storm's lifecycle. Though there can be large variations in rainfall across the region for any given storm, rainfall is still fairly highly correlated on this scale and it is reasonable to average stations in the region to produce a Mallee rainfall average.

The paper is organized as follows. In the next section we describe the features of rainfall in the Mallee region. Then we describe the major cool season synoptic types and a scheme for classifying them. We then analyze how rainfall is associated with each synoptic type and how the synoptic types vary in wet and dry years in the region. Since much of the interannual variability in rainfall in the region is governed by variations in ocean and atmosphere states in the Pacific and Indian Oceans, we also analyze the modulation of rainfall and synoptic types by the El Niño-Southern Oscillation (ENSO; Philander, 1985) and Indian Ocean Dipole (IOD; Saji *et al.*, 1999) states in the penultimate sections.

8.3. Mallee rain

Rainfall in the Mallee region is represented here by the average of rain over eight stations across the Mallee region. The eight stations are Bendigo, Birchip, Kaniva, Mildura, Narraport, Rainbow, Sea Lake, and Swan Hill. The station locations are indicated by circles in Fig. 8.1. These stations are all part of the Bureau of Meteorology high quality Australian historical data set (Lavery *et al.*, 1997). Any gaps in the Bureau of Meteorology records have been filled with interpolated data from the Queensland Department of Natural Resources and Mines patch point data set (Jeffrey *et al.*, 2001). A full description of the eight station data is provided in (Pook *et al.*, 2006).

For the data set spanning the period 1889–2006, the mean annual rainfall for the eight station average is 380 mm, with a standard deviation of 100 mm. A time-series of the annual rainfall is shown in Fig. 8.2. At least three extended drought periods are apparent in the record, centered around 1900, 1940, and the present period. There is little or no apparent trend in rainfall over the full period of record.

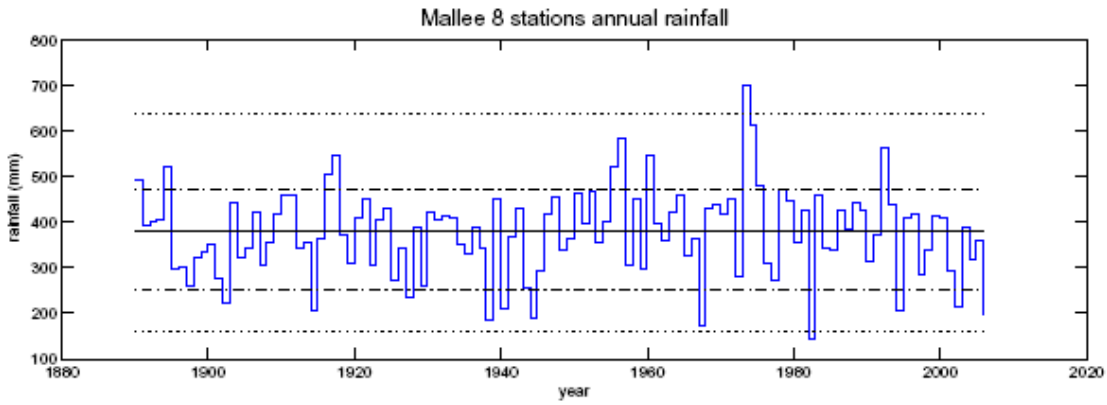

Figure 8.2. Time-series of Mallee eight station annual rainfall (stepped line). The solid line indicates the median rainfall, the dash-dot lines show the 10th and 90th percentile rainfall values, and the dotted lines show the 1st and 99th percentiles.

Annual rainfall amounts for the Mallee are dominated by contributions from daily rainfall in the range from 2–5 mm day^{-1}. The time series of annual rainfall as a function of daily rainfall amount is shown in Fig. 8.3. During wetter years the annual rainfall has larger than normal contributions from daily totals in the range to about 15 mm day^{-1}, while drier periods and years are marked by an absence of contributions from daily totals in this range. The higher rainfall events are important because they underpin variability in the record, and because they tend to provide more useful contributions to crop growth. Rainfall events in the low end of the range

(1–5mm day^{-1}) are less useful because the moisture is more readily evaporated and does not penetrate the soil (McIntosh *et al.*, 2007). Because interannual variability of rainfall and the utility of rainfall is linked to rainfall intensities, it is important to diagnose which synoptic systems produce higher rainfall events. This issue is taken up in Section 8.4.

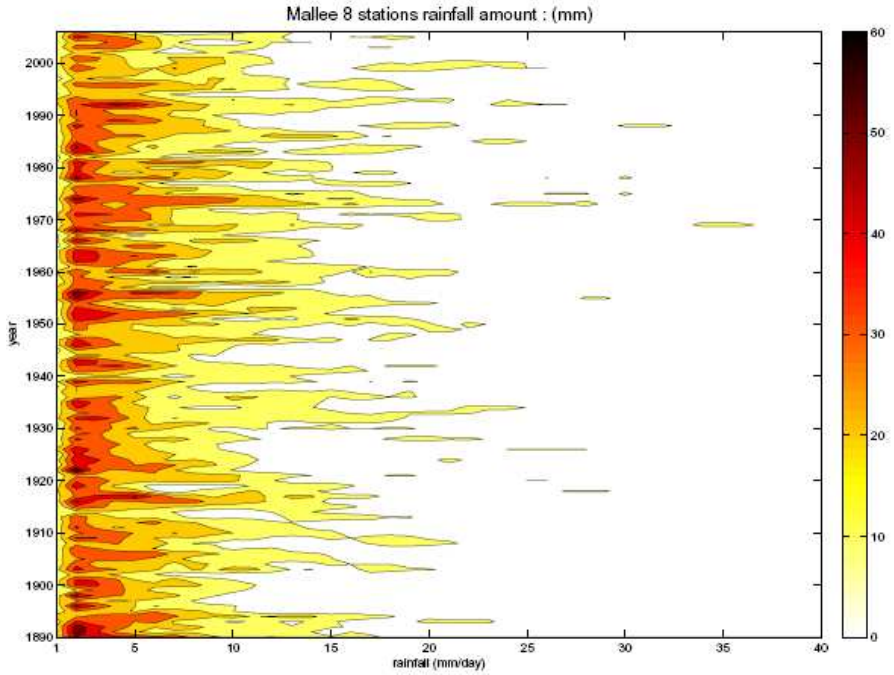

Figure 8.3. Hovmoller time series of Mallee eight station annual rainfall (in mm) as a function of the amount of rainfall per rainfall intensity category. The rainfall intensity categories are calculated from daily rainfall for bins of width 1 mm. The results have been smoothed across bins to facilitate interpretation in the Hovmoller plot. The contoured values show the amount of rain that fell each year in each rain intensity category. These amounts are calculated from the number of events in each category times the amount of rain in the category.

The seasonal cycle of rainfall in the Mallee is dominated by rainfall in the cool season period of April to October, which is nearly twice that which falls in the warm season months. Rainfed grain agriculture in the region follows the cool season maximum, with planting dates around the beginning of this period and harvest dates toward the end of the period. In order to match our analysis with the cool season cropping cycle, we focus on rainfall in the period April through October in the analysis which follows.

8.4. Synoptic classification and data

Cool season rainfall in the Mallee region of southeastern Australia is produced by synoptic systems which generally traverse the westerly belt of the southern oceans and the Australian continent. In order to classify the rain-bearing systems in this region (Pook *et al.*, 2006) defined an analysis box centered on and west of the Mallee region. The location of the box is shown in Fig. 8.1.

We used the synoptic classification of Pook *et al.* (2006) to classify synoptic events. This scheme classifies each day on which rain occurs in the Mallee according to three basic synoptic types. These types are cold-frontal systems of all types, cold-cored lows that have become cut off from the westerly airstream (cutoff lows), and a combined category designated others, which includes particular airstream types, waves in the easterlies, and open troughs aloft (Pook *et al.*, 2006, p.1162). Cutoff low systems are defined by Pook *et al.* (2006) as those where either

- a closed low is present at 500 hPa with an associated cold trough evident in the 1000–500 hPa thickness field (marked by a negative thickness anomaly of at least 20 gpm); or
- a closed low is present in the MSLP field (<1008 hPa) with an associated cold trough aloft with a negative thickness anomaly of at least 20 gpm.

The definitions of frontal systems and cutoff systems employed follow conventional understanding in the literature. A detailed description of each synoptic type is provided in Pook *et al.* (2006).

For the cool season (April–October), cutoff lows account for about half the total rainfall in the Mallee region, frontal systems account for about a third of the total, and other systems account for the remainder (Pook *et al.*, 2006). The interannual variability of cool season Mallee rainfall is dominated by variability in contributions from cutoffs, both because they are the dominant source, and because their rainfall is more variable from year to year than that due to frontal systems (Pook *et al.*, 2006). Further, cutoffs contribute more of the heavier rainfall events, which are generally more useful for crop growth (McIntosh *et al.*, 2007). If we are to gain a better understanding of rainfall variability, then we need to understand which systems generate the rainfall and what drives variability in these systems. A first step in this process is to diagnose and describe these systems. In Section 8.5 we analyze the structure of each synoptic type in the Australian region.

In order to characterize each synoptic type, we have utilized data from the NCEP/NCAR reanalysis over the period 1970–2005 (Kalnay *et al.*, 1996). The reanalysis provides six hourly analyses at the standard atmospheric levels on a 2.5°

$\times$ 2.5°grid. The period since 1970 is generally well characterized in the reanalysis over the Australian region because the upper air network is well developed by then and satellite coverage has commenced (Bromwich and Fogt, 2004).

For each synoptic type, we analyze its thermal signature, measures of its development, and steering of the flow pattern using diagnostics derived from the reanalysis data. For a measure of the thermal signature, we use the 1000–500 hPa thickness anomaly, Z_A. The anomalies are calculated relative to the climatological mean for each location, (x, y), at the relevant time, t:

$$Z_{Ax,y,t} = Z_{500x,y,t} - Z_{1000x,y,t} - \overline{Z_{500x,y} - Z_{1000x,y}} \tag{8.1}$$

where the overbar indicates a climatological mean ($\frac{1}{n}\Sigma_{t=1}^{n} Z_{x,y,t}$).

One measure of development of the systems is provided by the Eady growth rate. This index assesses baroclinic instability through the vertical gradient in horizontal wind in the middle troposphere (Hoskins and Valdez, 1990). The Eady growth rate, σ_{BI}, at a grid point is calculated from:

$$\sigma_{BI} = 0.31 \frac{f}{N} \left| \frac{\partial v}{\partial z} \right| \tag{8.2}$$

where f is the Coriolis parameter, N is the Brunt-Väisällä frequency, z is vertical distance, and v is the horizontal wind vector at 400 and 600 hPa (Paciorek *et al.*, 2002). The seasonal mean Eady growth rate is shown for the Australian region in Fig. 8.4. The Eady growth rate displays a maximum over the east coast of Australia in winter and a secondary maximum at high latitudes. These maxima follow the regions of subtropical and polar jet maxima. In summer, the maximum in Eady growth rate moves south of the continent as the summer jet moves south.

In order to assess system development, we also calculate the relative vorticity, ζ, for each system:

$$\zeta = \frac{\partial v}{\partial x} - \frac{\partial u}{\partial y} \tag{8.3}$$

where u and v are zonal and meridional wind components and x and y are zonal and meridional distance. For the Southern Hemisphere, regions of large negative relative vorticity are indicative of cyclonic storms. The advection of vorticity into an unstable region of the atmosphere is thought to be important for the development of storm systems (Petterssen, 1955). We calculate relative vorticity at 500 hPa to provide an indication of vorticity in the middle troposphere. The seasonal mean relative vorticity for winter and summer over the Australian region is shown in Fig.

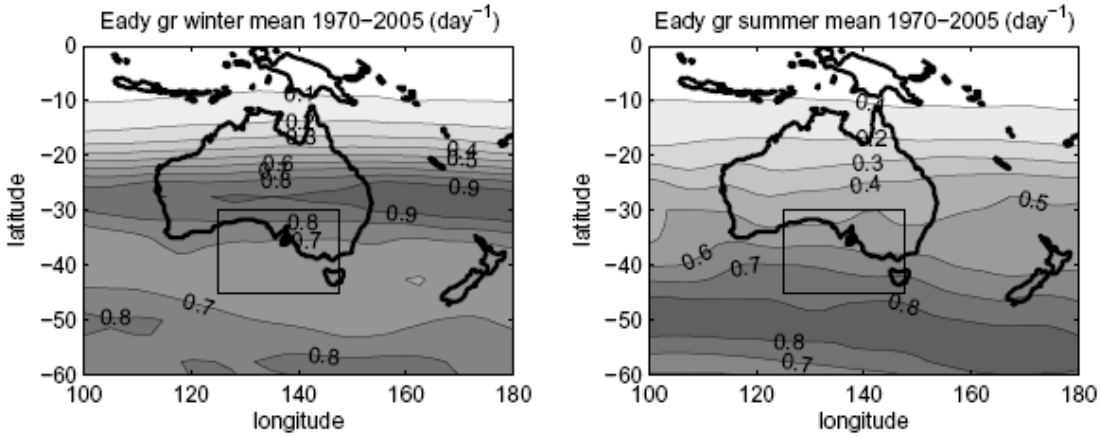

Figure 8.4. Seasonal mean Eady growth rate. Units are day^{-1}. The left panel is for winter (JJA) and the right panel is for summer (DJF). The rectangular box shown here and on subsequent figures is the synoptic analysis box defined in Fig. 8.1

8.5. In winter there is a broad band of cyclonic vorticity across the southern part of the continent, with a maximum off the east coast in the Pacific Ocean. There is a local maximum of anticyclonic vorticity in the Tasman Sea south of Tasmania and New Zealand, which is indicative of a tendency for blocking there (Trenberth and Mo, 1985).

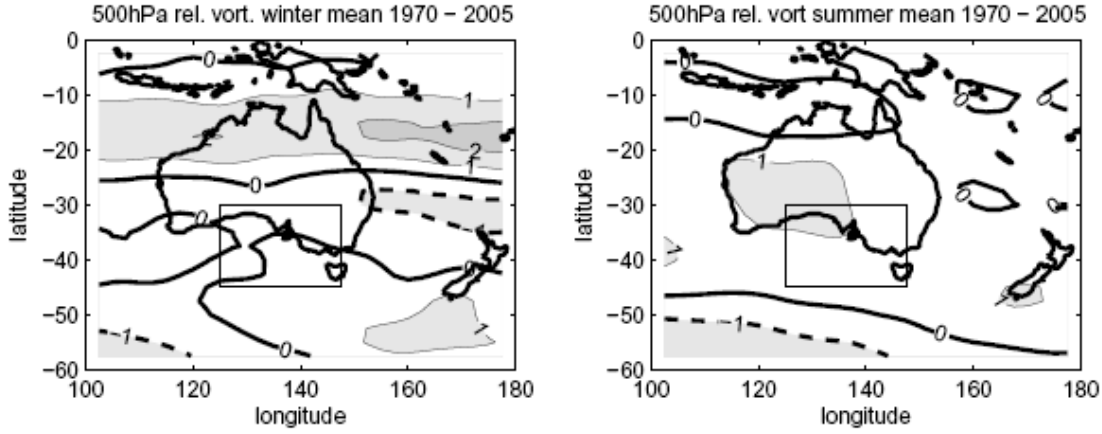

Figure 8.5. Seasonal mean 500 hPa relative vorticity. Units are $10^{-5}s^{-1}$. The left panel is for winter (JJA) and the right panel is for summer (DJF). Negative values indicate cyclonic vorticity.

Another measure of development is provided by consideration of the location of the system relative to the proximate jet stream. The jet stream also provides an indication of the steering of the flow and system. We represent the jet stream here

by the magnitude of the wind vector at 250 hPa, which is a typical level for the jet core. The seasonal mean jet stream for winter and summer over the Australian region is shown in Fig. 8.6. In the winter mean pattern there is a jet spanning the Australian continent with a core centered off the east coast in the Pacific, and split flow in the Tasman Sea. In summer the mean jet core has retreated well south of the Australian continent in Australian longitudes. The jet patterns help explain the seasonal mean relative vorticity patterns shown in Fig. 8.5. For example, the shear and curvature vorticity implied from the jet pattern in winter would predict the winter relative vorticity pattern with a band of anticyclonic vorticity north of the jet stream, a band of cyclonic vorticity south of the jet stream, and a region of anticyclonic vorticity in the Tasman Sea marking the region of split flow in the jet.

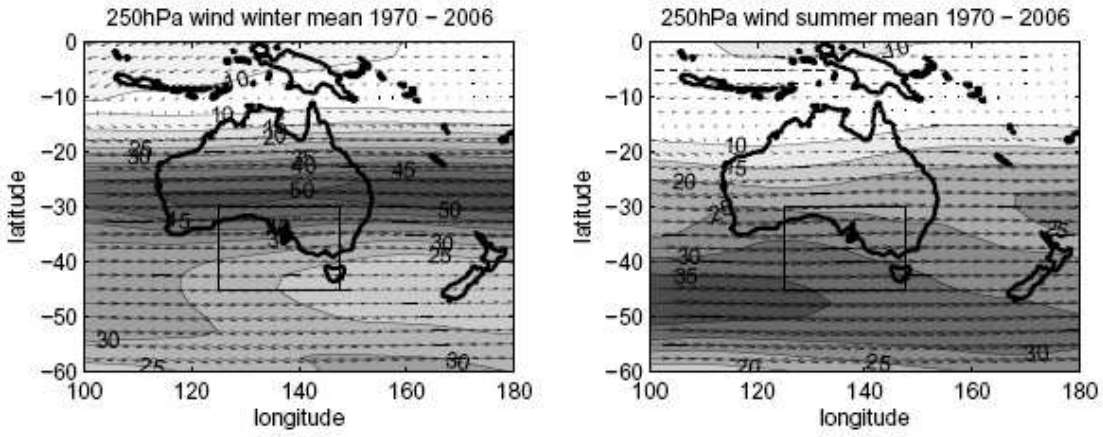

Figure 8.6. Seasonal mean 250 hPa wind. Units are m s^{-1}. The left panel is for winter (JJA) and the right panel is for summer (DJF).

The final index used here to characterize a feature of the synoptic systems is vertical velocity, ω. Vertical velocity provides a further gross measure of instability. Upward vertical velocities are a virtual prerequisite for rainfall. The rain layer in typical synoptic systems may extend over a wide range from the surface to the middle and upper troposphere for convective systems. We have selected 700 hPa to display the vertical velocity as this level is close to the middle of the rain layer for typical systems and will be within the rain layer in most systems. The seasonal mean vertical velocities over Australia are shown in Fig. 8.7. These plots indicate Australias location under regions of mean descent (negative vertical velocities) in the subtropical ridge. In summer, a monsoonal heat low is established in the northern part of the continent, giving rise to mean ascent there. Regions of mean ascent in mid-latitudes are more salient near Australia in winter than summer.

Taken together, the winter mean indicators for Eady growth rate, relative vor-

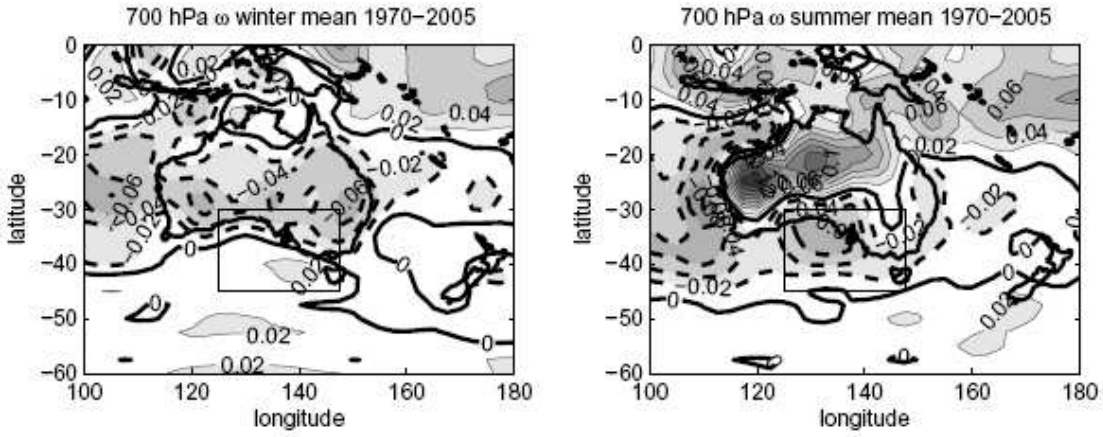

Figure 8.7. Seasonal mean vertical velocity at 700 hPa. Units are Pa s^{-1}. Negative values (dashed contours) indicate descent. Positive values (solid contours) indicate ascent. The zero contour is bold.

ticity, and vertical velocity shown in Figs. 8.4, 8.5, and 8.7 are not particularly propitious for winter rainfall in the Mallee region. In the winter mean fields the Eady growth rate (Fig. 8.4) and relative vorticity (Fig. 8.5) both show maxima well downstream of the Mallee region, off the east coast of Australia. Thus, the main baroclinic zone and cyclonic vorticity regions, which are two critical ingredients for development, are more favorable for storminess in the Pacific than over southeastern Australia. Indeed, the winter mean vertical velocity field (Fig. 8.7) shows downward motion over southeastern Australia, with upward motion off the east coast. Rainfall in the Mallee region is thus dependent on reorganizations and perturbations to the mean field provided by variation in broadscale circulation and the passage of synoptic systems. In the following section we turn to analysis of the synoptic systems that provide these favorable perturbations.

8.5. Daily rainfall and synoptic types

In this section we analyze the signature of each synoptic type according to the diagnostics described above. For each rainfall day in the Mallee region between April 1 and October 31 over the period 1970–2005, the synoptic type has been identified according to the criteria in Section 8.4. We have composited each of the fields above (thickness anomaly, Eady growth rate, relative vorticity, jet stream, vertical velocity) over days with the same synoptic type (cutoffs, fronts, other). We performed this compositing for the extended April–October cool season, and for overlapping three month seasons (AMJ, JJA, ASO). The overlap in seasons was used because the synoptic classification does not include months outside April–October.

The results for the winter season (JJA) are generally typical of the various periods and are shown here.

In each case we are interested in how the gross atmospheric structure varies according to the type of synoptic system. Further, we are also interested in how the structure varies according to the amount of rainfall that the system produces. Thus, we have also further stratified the composites according to the intensity of rainfall. Rainfall days have been classified as weak (0.1–5 mm), moderate (5–15 mm), and heavy (>15 mm).

8.5.1. Thickness anomaly

Composites of thickness anomaly for cutoffs and fronts are shown in Figs. 8.8 and 8.9 respectively. In each case there are marked warm (positive anomaly) and cold (negative anomaly) pools associated with the synoptic systems. The difference is that the cold pools for cutoff systems are cut off from the westerlies by a warm anomaly to the south which wraps around the cold anomaly, whereas for fronts the cold pool is contiguous with the westerly belt in the southern oceans.

As the amount of rain increases, the main change in Figs. 8.8 and 8.9 is that the gradient of thickness anomaly across the synoptic system increases. This gradient increases primarily due to an increase in magnitude of the warm anomaly. The cold anomaly increases in magnitude too, but not to the same degree. The increase in warm anomaly reflects stronger warm air advection ahead of the system, which is characteristic of developing systems (Hirschberg and Fritsch, 1991). The large warm anomaly produces an enhanced thickness gradient across the system, which is a feature of more highly developed systems (Sutcliffe and Forsdyke, 1950) and is thus consistent with the higher rainfall rates. The orientation of thickness anomaly gradients, with enhanced thickness to the northeast of the system center and decreased thickness southwest, would lead to increases in thermal wind directed toward the southeast along the thickness gradient. The enhancement of thermal wind here would produce an acceleration of the jet stream in the vicinity of the system, promoting further development.

8.5.2. Eady growth rate

The Eady growth rate marks areas of favorable baroclinic development for storm systems. The composites of Eady growth rate for cutoffs are shown in Fig. 8.10. The composites of Eady growth rate are compiled for the day prior to the rain event because the storm tends to develop in response to high values of Eady growth rate with a lag of a day or so. For cutoff systems associated with weak rainfall events the

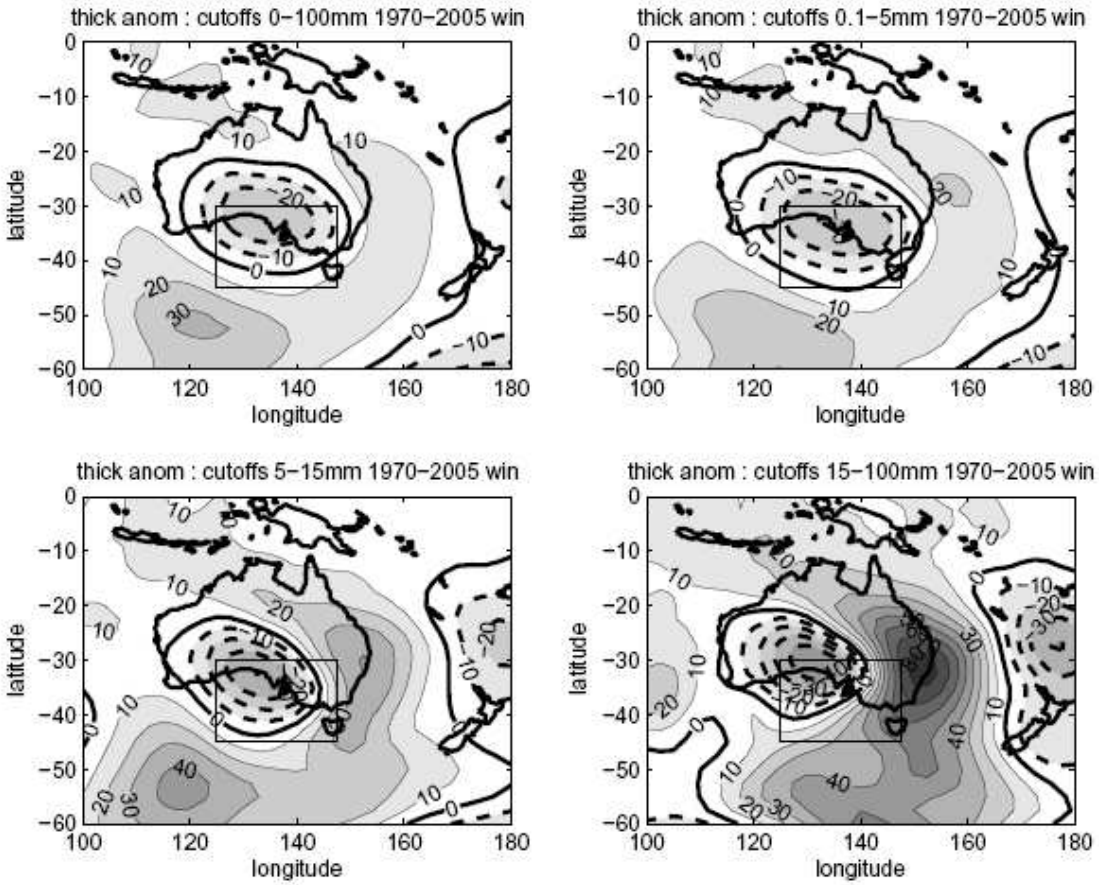

Figure 8.8. Composite of thickness anomaly for cutoff systems that accompany rain days in winters 1970-2005. The top left panel is a composite over all such rain days. The top right panel is a composite over just the subset of rain days that total less than 5 mm. The bottom left is for rain days between 5 and 15 mm, and the bottom right is for rain days greater than 15 mm. Units are m. The box indicates the synoptic analysis region, as in Fig. 8.1. Dash contours indicate negative anomalies and solid contours indicate positive anomalies.

pattern of Eady growth rate resembles the climatological mean pattern, following the major jets. For the heavy rainfall events the area of instability is increasingly concentrated over the analysis region. The pattern for frontal systems (not shown) is similar to that for cutoff systems, but the areal concentration of Eady growth rate is less pronounced for heavier rainfall events. Cutoff systems in the region are associated with, or promote, more concentrated gradients of baroclinic instability than frontal systems, which would be one factor behind their higher rainfall rates. Another factor promoting growth of the systems is the relative vorticity, which is discussed in the next section.

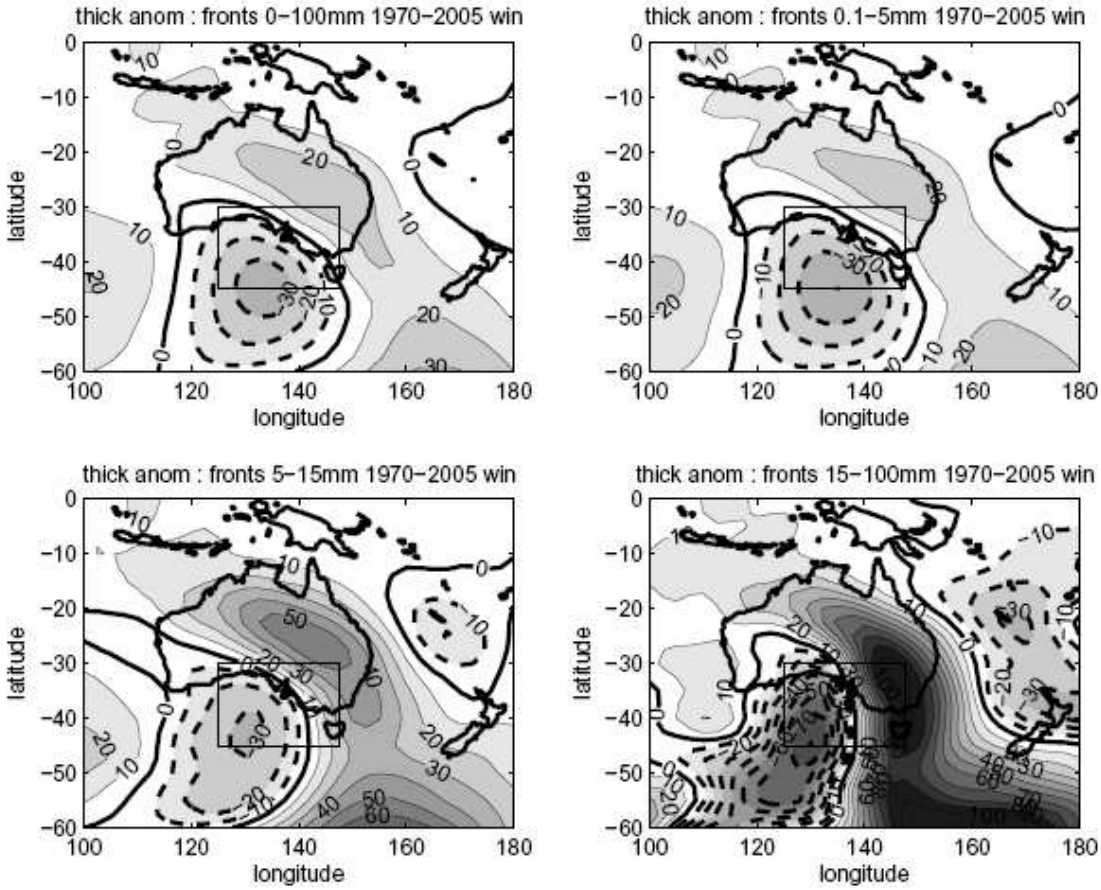

Figure 8.9. As in Fig. 8.8, but for composites of thickness anomaly for frontal systems. Units are m.

8.5.3. Relative vorticity

The relative vorticity for cutoff and frontal systems is shown in Figs. 8.11 and 8.12, respectively. For cutoff systems (Fig. 8.11) the maximum in cyclonic vorticity at the center of the system intensifies as rainfall from the system increases. The cyclonic vorticity maximum is cradled to the south and southeast by a region of enhanced anticyclonic vorticity, which marks the blocking high associated with the cutoff low. This blocking high also intensifies as rainfall from the cutoff low increases. For frontal systems (Fig. 8.12) the relative vorticity maximum also increases as rainfall from the system increases, but the maximum in cyclonic vorticity is weaker and located further south. The cyclonic vorticity maximum extends into the southern ocean in association with the influence of the polar front jet, which extends through this region in the more intense frontal systems (as shown in the next section).

The regions of cyclonic vorticity for cutoff (and front) composites are broadly coincident with the maxima in Eady growth rate indicated in Fig. 8.10. However, the cyclonic vorticity maxima are more strongly localized about the synoptic system

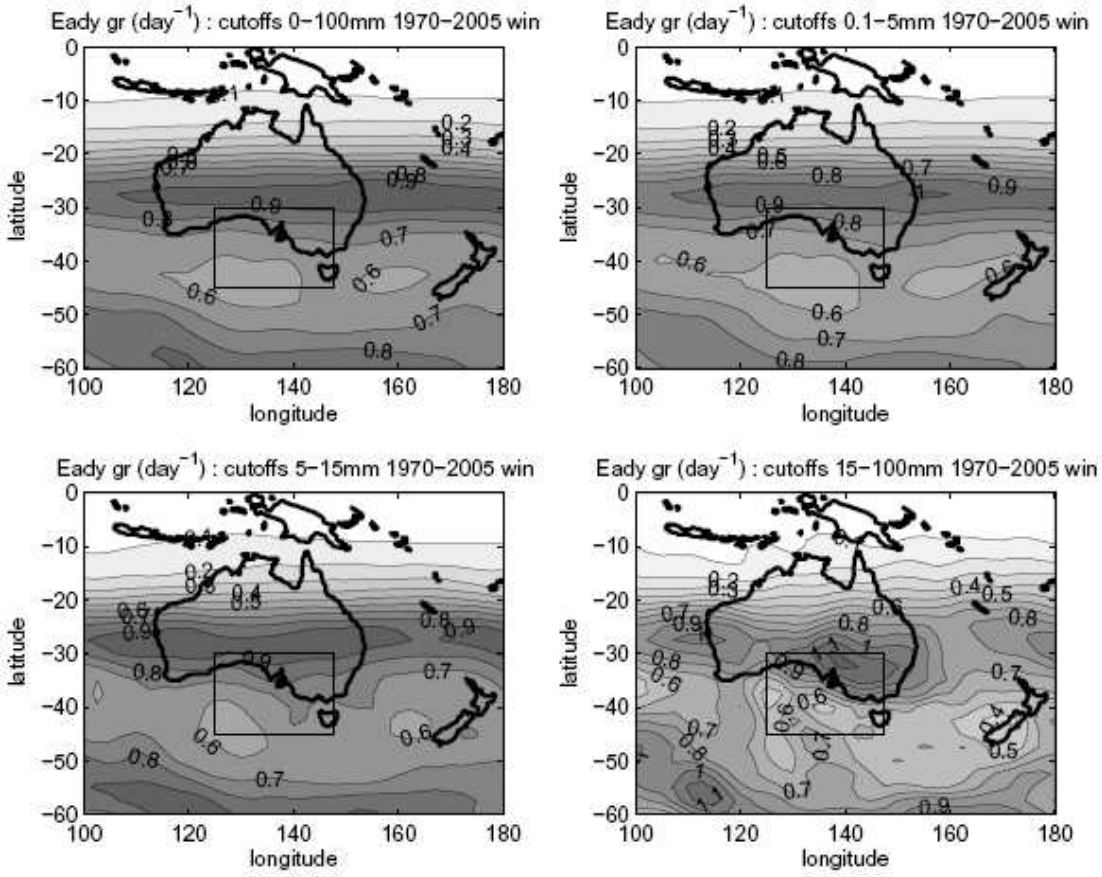

Figure 8.10. As in Fig. 8.8, but for composites of Eady growth rate for cutoff systems. Units are day^{-1}.

than the Eady growth rate maxima. Both Eady growth rate and relative vorticity fields display concentrated maxima in the synoptic box region for the most intense systems. The superposition of baroclinic zone and upper level vorticity displayed here is characteristic of the form of cyclonic development described by Petterssen (1955). The systems intensify as an upper level trough moves over a region of high baroclinic growth rate.

8.5.4. Jet streams

The signatures of the jetstream composites for cutoffs and fronts are quite different and are shown in Figs. 8.13 and 8.14 respectively. For cutoff events (Fig. 8.13) the subtropical jet is pronounced over the Australian continent and distinct from any branches of the polar jet. Cutoff systems are associated with the subtropical jet. As rainfall increases the subtropical jet is increasingly localized over the synoptic analysis region, with rainfall in the favorable right exit region of the jet. This region of the jet is characterized by upper level divergence and generates upward motion

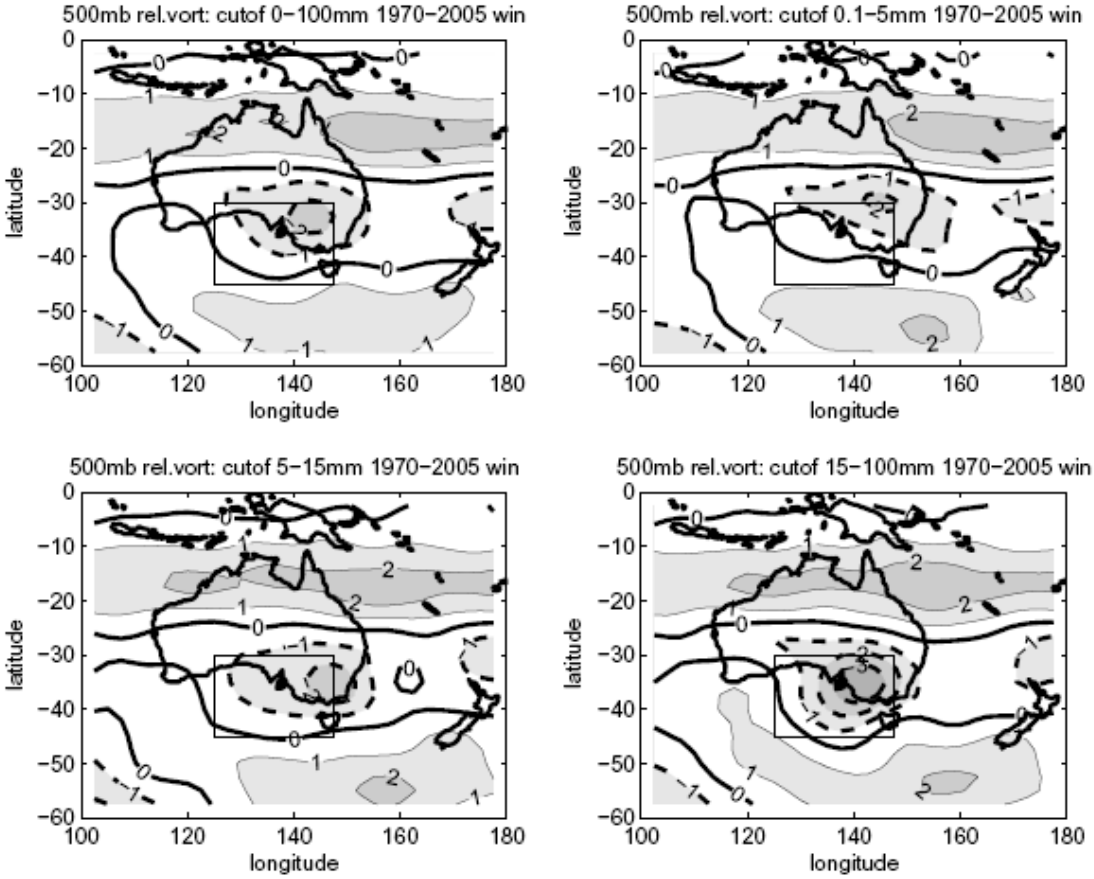

Figure 8.11. As in Fig. 8.8, but for composites of relative vorticity for cutoff systems. Units are $10^{-5}s^{-1}$. Dash contours indicate cyclonic vorticity.

(Barry and Carleton, 2001), as is evident from the vertical velocity field in Fig. 8.15. In addition, the baroclinic growth rates are highest in this region (Fig. 8.10) and thickness anomaly gradients indicate an acceleration of the thermal wind (Fig. 8.8). The acceleration of the thermal wind reinforces the jet, while the jet promotes upward motion and growth of the system. This illustrates the manner in which the jet is both a consequence and cause in its dynamical coupling to the baroclinic zone in intense systems.

In frontal systems (Fig. 8.14) the polar jet merges with the frontal jet in the vicinity of the frontal system. As the intensity of the rainfall event increases, the branch of the polar jet becomes more distinct, linking up directly with the subtropical jet to provide energy and momentum for the frontal system. Intense frontal systems in the region thus tend to gain energy via meridional excursions of the polar jet, while intense cutoff systems gain energy from a localization and concentration of the subtropical jet. Like cutoff systems, intense frontal systems also show strong upward vertical velocities (Fig. 8.16) in the right exit region of the jet (Fig. 8.14). The

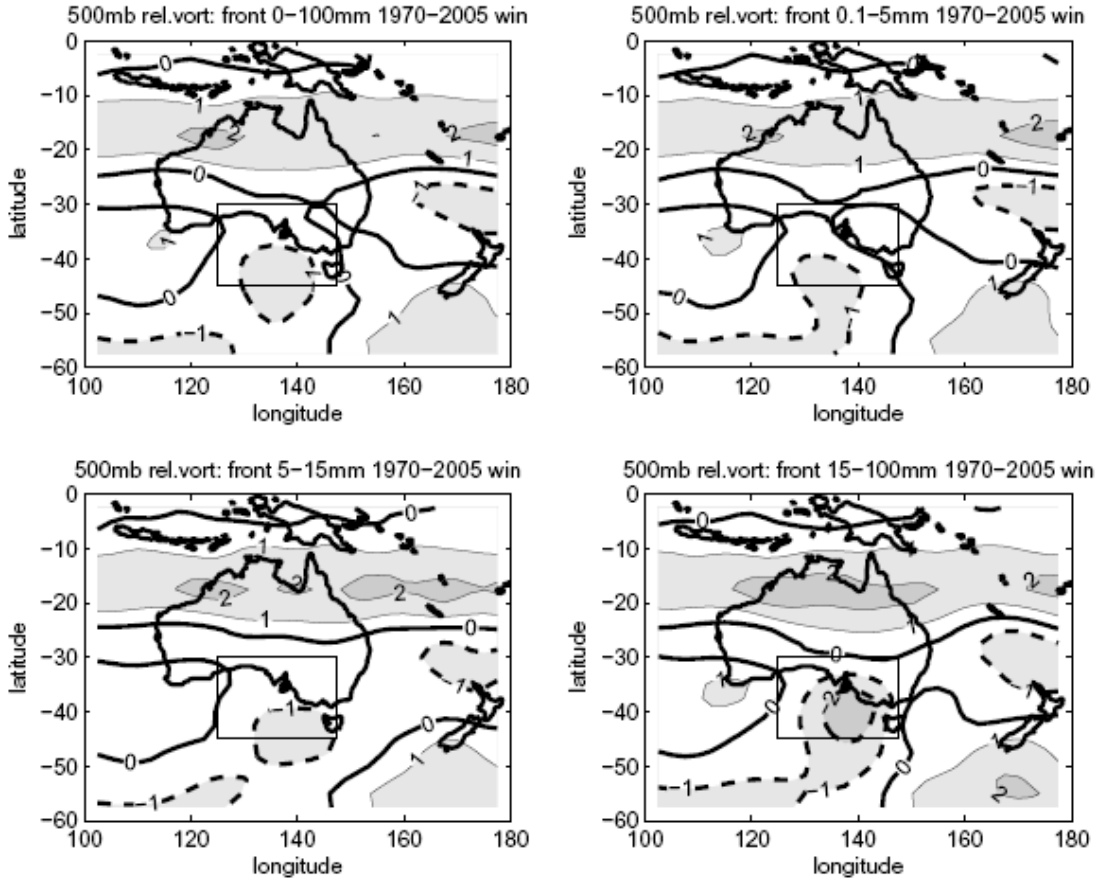

Figure 8.12. As in Fig. 8.8, but for composites of relative vorticity for frontal systems. Units are $10^{-5}s^{-1}$. Dash contours indicate cyclonic vorticity.

increase in upward velocity also occurs in conjunction with strong warm advection. The features of the broader vertical velocity field and the factors which set it are discussed in the next section.

8.5.5. Vertical velocity

Patterns of vertical velocity across storm systems help complete a view of the three dimensional flow structure. Figs. 8.15 and 8.16 show composites of the vertical velocity field for cutoffs and fronts respectively. For both cutoffs and fronts there is a region of pronounced descent behind the system and a region of pronounced ascent ahead of the system. The areas of ascent occur in the regions where warm advection is strongest (indicated by large positive thickness anomalies in Figs. 8.8 and 8.9) and areas of descent occur in the regions where cold advection is strongest (indicated by large negative thickness anomalies in Figs. 8.8 and 8.9) following expectations from quasi-geostrophic theory. The regions of ascent and descent increase in magnitude with increases in rainfall intensity of the systems. For cutoff

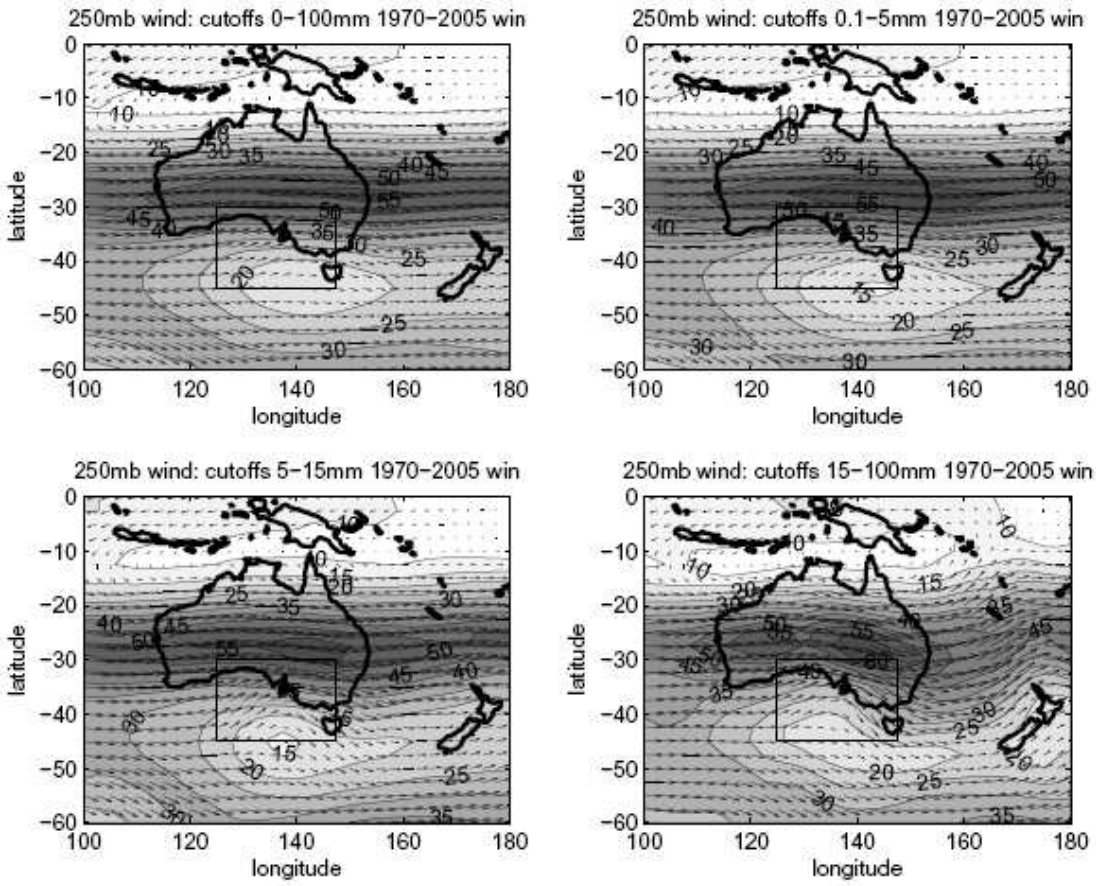

Figure 8.13. As in Fig. 8.8, but for composites of 250 hPa wind for cutoff systems. Units are m s^{-1}.

systems the regions of descent and ascent tend to wrap around one another in classical comma form, indicative of warm moist ascent ahead of the system and cold descent behind the system (e.g., Thorncroft *et al.*, 1993; Griffiths *et al.*, 1998). This feature is also enhanced as rainfall increases. For frontal systems, the region of ascent is more broadly aligned along a meridional band, consistent with the influence and orientation of the polar front jet (Fig. 8.14).

8.6. Interannual rainfall

In the previous section we investigated the variation in synoptic system structure as a function of rainfall intensity using daily rainfall data. In this section we move to the interannual timescale. We start with large scale rainfall patterns on the seasonal scale and investigate whether there are coherent variations in synoptic structure that accompany these patterns. To construct seasonal rainfall patterns we have used gridded rainfall data for Australia spanning the period 1960–2004 (Jeffrey *et al.*,

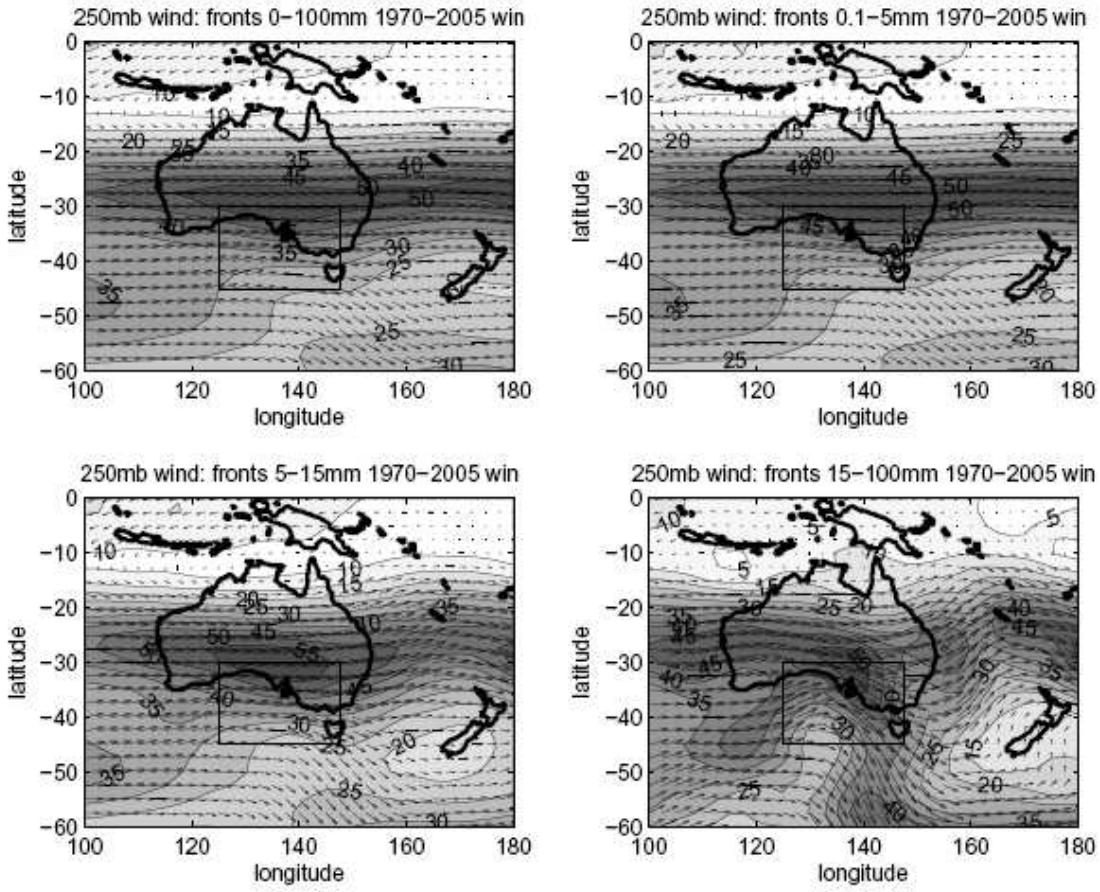

Figure 8.14. As in Fig. 8.8, but for composites of 250 hPa wind for frontal systems. Units are m s^{-1}.

2001). A clustering algorithm (Ward, 1963; Cheng and Wallace, 1993) was employed to identify five dominant patterns of rainfall across the Australian continent. These patterns for the winter season are shown in Fig. 8.17. The patterns correspond to wetter than average conditions across the Great Dividing Range (wet Divide), wet across the southern part of the continent (wet south), wet along the east and west coasts (wet east/west coasts), dry over much of the continent (dry Australia), and wet over much of the continent (wet Australia) respectively. In the Mallee region, the high rainfall years correspond to the 'wet south' and 'wet Australia' patterns. The break up of rainfall by synoptic type for each of these rainfall patterns is shown in Fig. 8.18. Winter rainfall in the Mallee region in the 'wet south' pattern is unusual in that it is dominated by fronts, whereas cutoffs dominate for most other patterns. In particular, the 'wet Australia' pattern is heavily dominated by rainfall from cutoff events.

The thickness anomalies that accompany each of these patterns are shown for cutoff systems in Fig. 8.19 and frontal systems in Fig. 8.20. For rainfall patterns

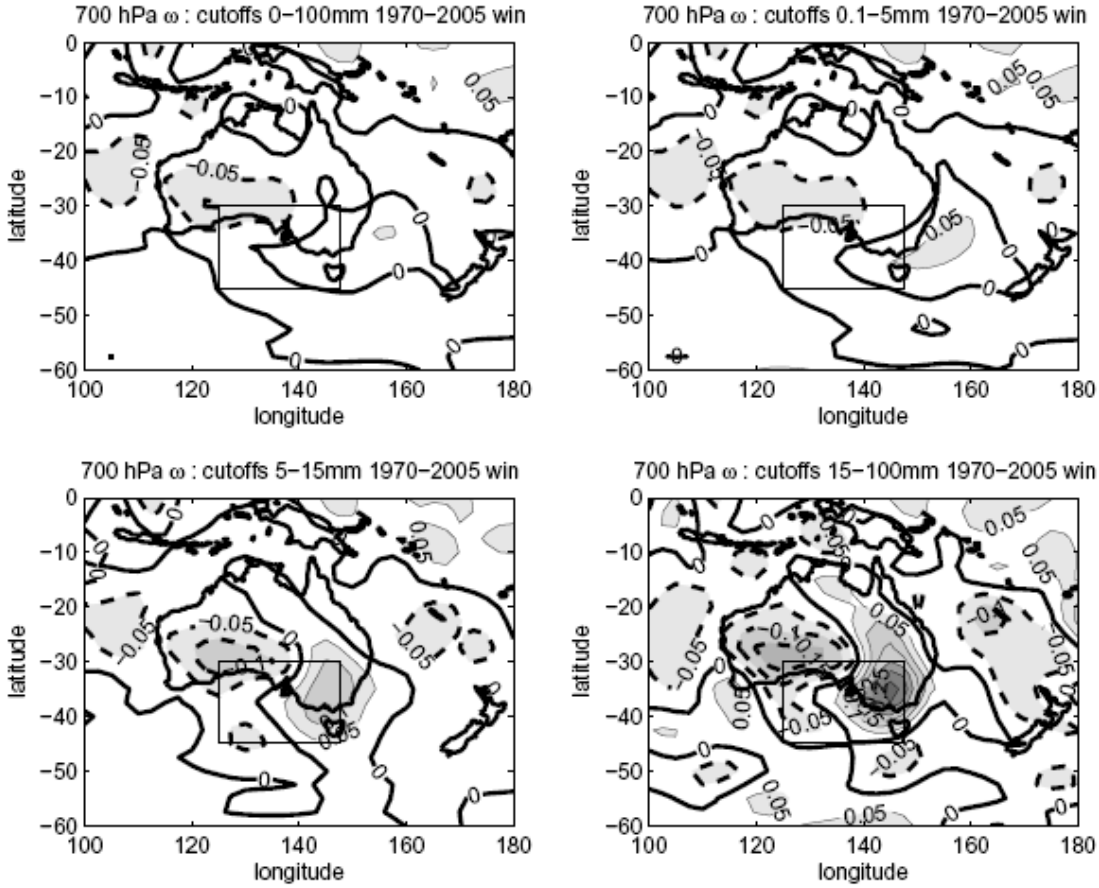

Figure 8.15. As in Fig. 8.8, but for composites of vertical velocity for cutoff systems. Units are Pa s^{-1}. Dash contours indicate descent and solid contours indicate ascent.

with higher than normal cutoff rainfall ('wet Divide' and 'wet Australia'), the cold thickness anomaly is particularly pronounced. For the much wetter 'wet Australia' pattern, the positive thickness anomaly off the east coast is also very pronounced, resulting in a strong thickness gradient. For patterns where frontal rainfall is enhanced ('wet south' and 'wet Australia'), the gradient of thickness anomaly is also strongly enhanced, with a large positive anomaly over northeastern continental Australia.

The mid-tropospheric flow pattern associated with each rainfall cluster grouping is quite distinct. We represent this flow by geopotential height anomalies at 500 hPa in Fig. 8.21. For the rainfall patterns that are wettest in the Mallee ('wet south' and 'wet Australia'), the tropospheric flow is highly zonal with an annulus about the pole. This flow pattern is characteristic of the Southern Annular Mode (SAM) (Thompson and Solomon, 2002). Curiously, these two wet patterns are associated with SAM patterns of opposite sign in Fig. 8.21. The 'wet south' pattern has lower than normal geopotential in the westerly belt and the 'wet Australia' pattern has

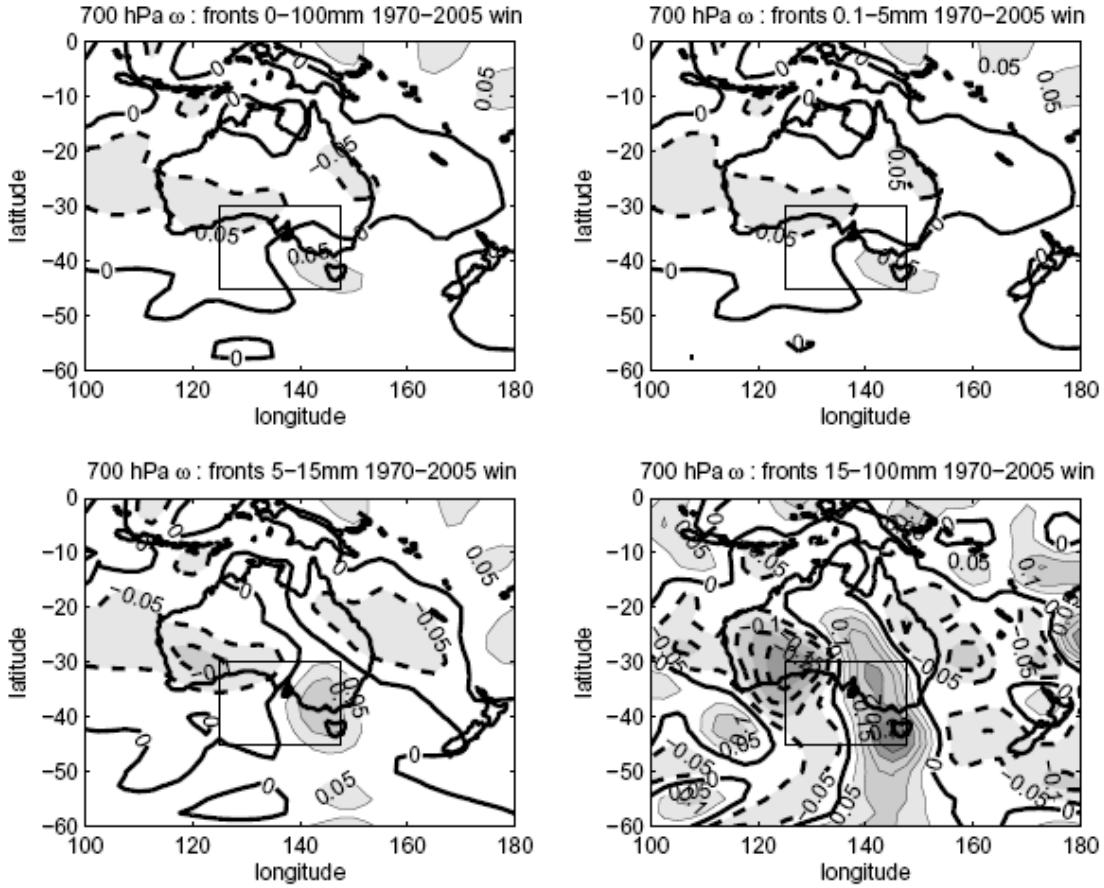

Figure 8.16. As in Fig. 8.8, but for composites of vertical velocity for frontal systems. Units are Pa s^{-1}. Dash contours indicate descent and solid contours indicate ascent.

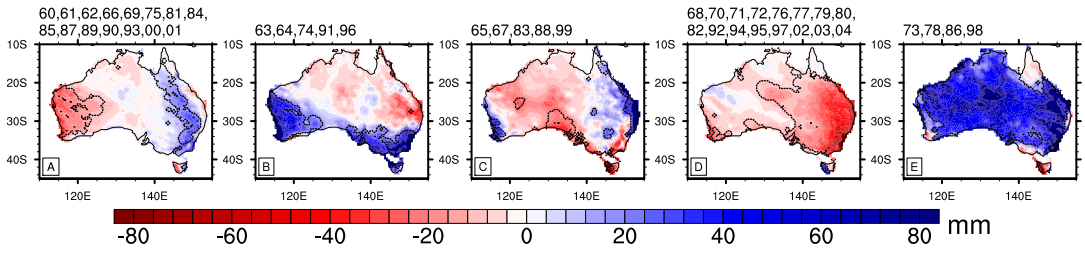

Figure 8.17. Winter rainfall anomaly patterns derived from a pattern cluster algorithm. The patterns are based on winter rainfall from the years 1960–2004. The years comprising each pattern are listed above the pattern. The shorthand descriptor for each pattern given in the text is 'wet Divide', 'wet south', 'wet east/west coasts', 'dry Australia', and 'wet Australia' respectively. The solid lines enclosing shaded areas indicate statistically significant anomalies at the 80% level.

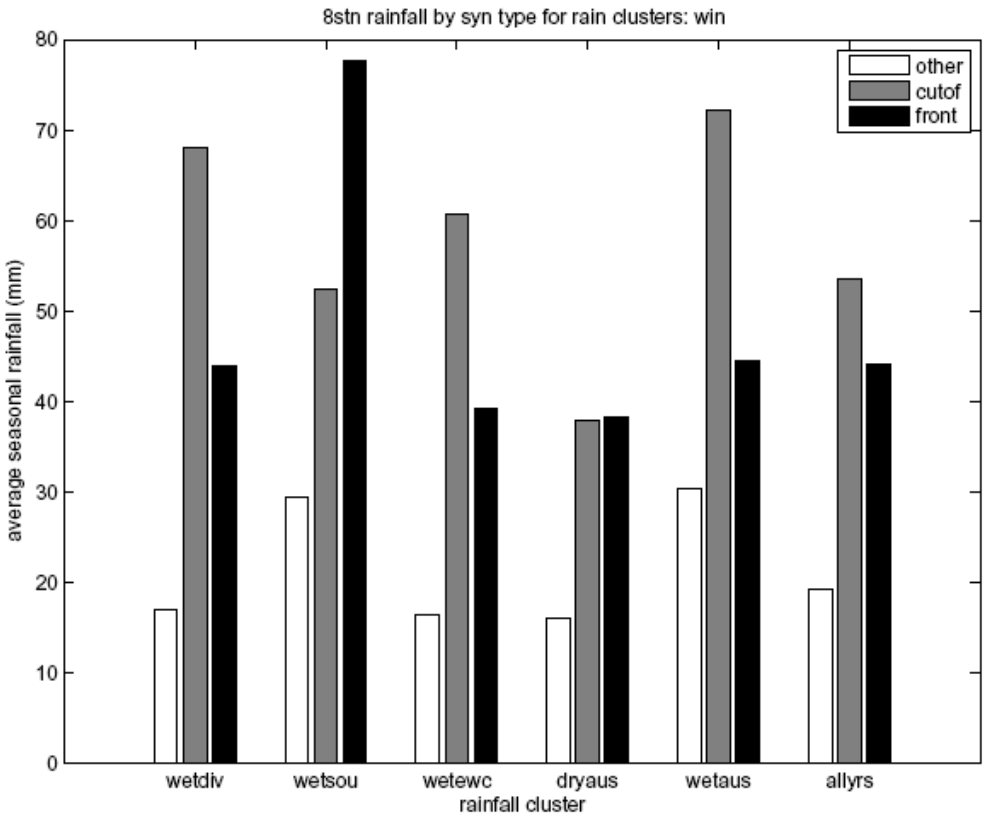

Figure 8.18. Mallee eight station rainfall by synoptic type for the rainfall cluster categories identified in Fig. 8.17. The rainfall amounts plotted are the average winter rainfalls over the years in each rainfall cluster. The shorthand labels given correspond to the 'wet Divide', 'wet south', 'wet east/west coasts', 'dry Australia', and 'wet Australia' patterns respectively, and to all years.

higher than normal geopotential in this belt. The 'wet Australia' pattern is wet because the positive geopotential east of Australia is indicative of blocking there, which is more favorable to the development of cutoff low systems over Australia (Pook *et al.*, 2006). In Fig. 8.18 we note that the 'wet Australia' pattern is dominated by cutoff rainfall in the Mallee. The years associated with this pattern have about twice the cutoff rainfall of other patterns. Conversely, the 'wet south' pattern is dominated by frontal rainfall, which is enhanced across the southern edge of the continent by the equatorward shift of the zonal westerlies indicated in Fig. 8.21.

The jet stream fields associated with each rainfall pattern are not shown here for brevity. They show a strong influence of the subtropical jet. The location of the jet maximum of the subtropical jet shifts from pattern to pattern, with the maximum located proximate to the region which is wet, or east of the continent for the 'dry Australia' pattern. The 'dry Australia' pattern is associated with unusually low blocking activity in the Tasman Sea as indicated by the negative geopotential

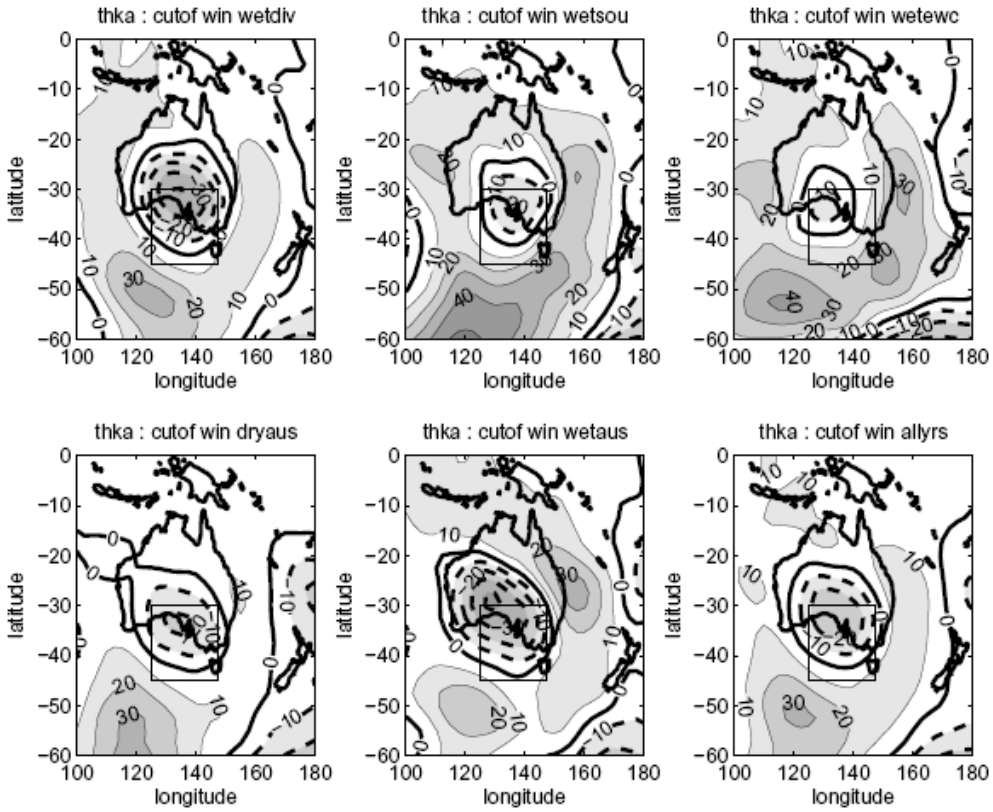

Figure 8.19. Thickness anomaly for the five rainfall cluster patterns shown in Fig. 8.17 for winter days in the set of cluster years for which cutoff low events occur. The six panels correspond to the five patterns ('Wet Divide', 'Wet South', 'Wet East/West Coast', 'Dry Australia', 'Wet Australia') and to all years (1960–2004). Units are m. Dash contours indicate negative anomalies and solid contours indicate positive anomalies.

anomaly in this region in Fig. 8.21 and a much weaker than normal region of anticyclonic vorticity (not shown). The reduction in blocking here reduces the incidence of cutoff lows in the analysis region (Section 8.5.3; Pook *et al.*, 2006), and thus the amount of rainfall from cutoffs (Fig. 8.18).

8.7. ENSO/IOD classification

In the previous section we looked at variation in synoptic structure as a function of variation in interannual rainfall patterns. In this section, we keep the interannual focus, but instead of conditioning results by continental rainfall, we condition by the leading modes of variability of the Indian and Pacific Oceans. Rainfall in the Australian region is strongly influenced by both the El Niño-Southern Oscillation (ENSO; Allan, 1988; Nicholls *et al.*, 1997; Wang and Hendon, 2007) in the Pacific Ocean and the Indian Ocean Dipole (IOD; Ashok *et al.*, 2003a).

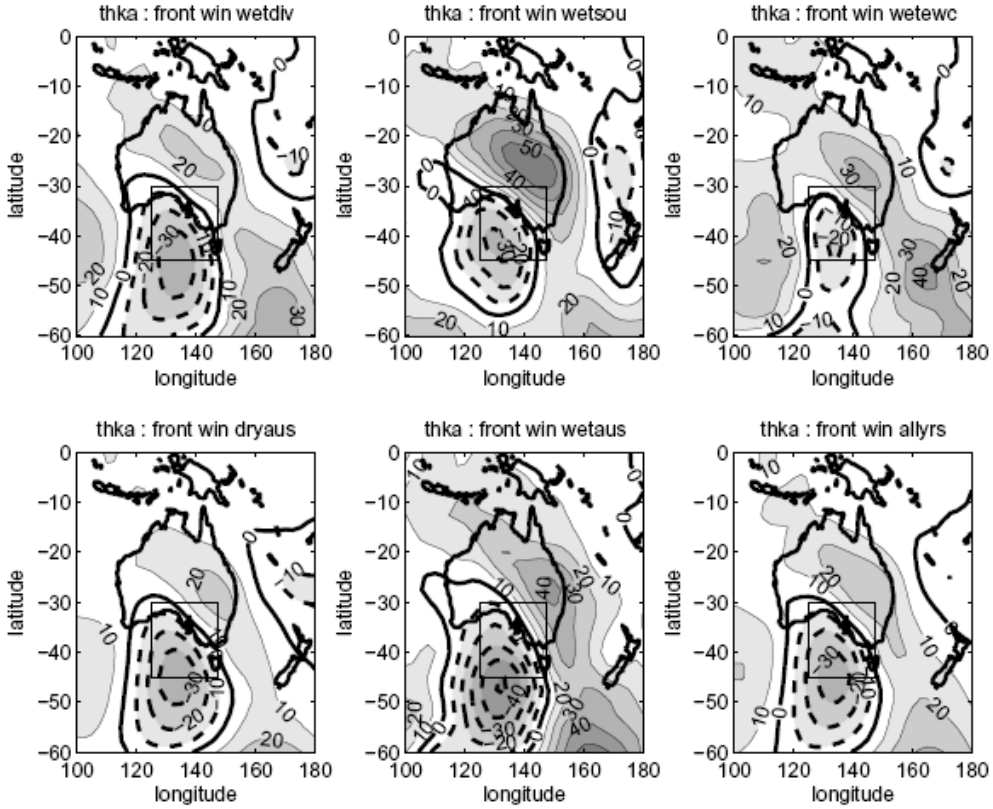

Figure 8.20. As in Fig. 8.19, but for days on which frontal events occur.

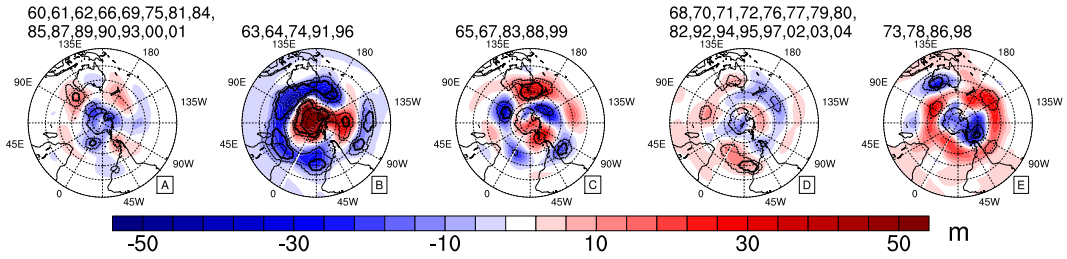

Figure 8.21. 500 hPa geopotential height anomaly patterns corresponding to the rainfall cluster years identified in Fig. 8.17. The five cluster patterns from left to right are 'wet Divide', 'wet south', 'wet east/west coasts', 'dry Australia', and 'wet Australia'.

Meyers *et al.* (2007) have recently classified all years between 1885 and 1999 according to ENSO state (El Niño, neutral, La Niña) and IOD state (IOD+, neutral, IOD-). This classification defines a 3 × 3 matrix with years allocated to the appropriate cells of the matrix. In practice, the El Niño/IOD- and La Niña/IOD+ combinations seldom occur and so there are effectively only seven categories. For the southeast Australia region, wet years in this classification generally correspond

to combinations in which IOD is -ve, and/or there is a La Niña. Dry years generally correspond to combinations in which IOD is +ve and/or there is an El Niño (Meyers *et al.*, 2007).

Thickness anomaly composites for the ENSO/IOD year groupings are shown in Fig. 8.22 for the winter season. Both the El Niño and IOD+ composites (top row and right column in Fig. 8.22) are marked by negative (cool) thickness anomalies over the Pacific Ocean east of Australia and in northeastern Australia. This is consistent with the cool SST anomalies associated with this region for these categories (Meyers *et al.*, 2007). By contrast, the IOD- and La Niña categories (left column and bottom row in Fig. 8.22) show warmer thickness anomalies in this region and warm anomalies northwest of Australia. These warm thickness anomalies are also consistent with the warm SST anomalies in these regions for IOD- and La Niña categories. Thickness anomalies do not mirror SST anomalies at any given point in time, as atmospheric thickness anomalies change more rapidly than oceanic SST anomalies. However, the atmosphere is thermally coupled to the ocean surface, and there does appear to be a relationship between SST and lower tropospheric temperature (thickness) over monthly and seasonal timescales, as exhibited by the corresponding anomaly patterns shown here. This suggests a pathway via which SST anomalies may influence the development of synoptic systems: SST anomalies influence thickness anomalies, which in turn alters thickness gradients, thermal wind, and the potential for systems to develop. Similar relationships based on SST and their gradients have been articulated in observational (Kushnir *et al.*, 2002) and modeling studies (Frederiksen and Balgovind, 1994; Kushnir *et al.*, 2002; Ummenhofer *et al.*, 2007c).

The thickness field is partly set by thermal coupling and other time-mean processes, and partly via the passage of transient systems. When the thickness field in each ENSO/IOD category has the contribution from days in which each synoptic type occurs removed, the resulting patterns are similar to those in Fig. 8.22. This suggests that these fields are reflective of a response to the background SST state. If the thickness anomaly fields in Fig. 8.22 are viewed as background states for synoptic systems in these years, then the El Niño and IOD+ (see top row and right column in Fig. 8.22) cold Pacific region thickness anomalies with warm anomalies to the south and west would tend to generate a thermal wind component that weakens the jet stream. Further, the cool SST/thickness background would weaken the positive (warm) thickness anomaly along the east coast that is characteristic of stronger cutoff systems in this region (see Fig. 8.8). The resulting reduction in thickness gradient is associated with a reduction in rainfall. This is consistent with the reduction of rainfall in El Niño and IOD+ years. Conversely, for La Niña years

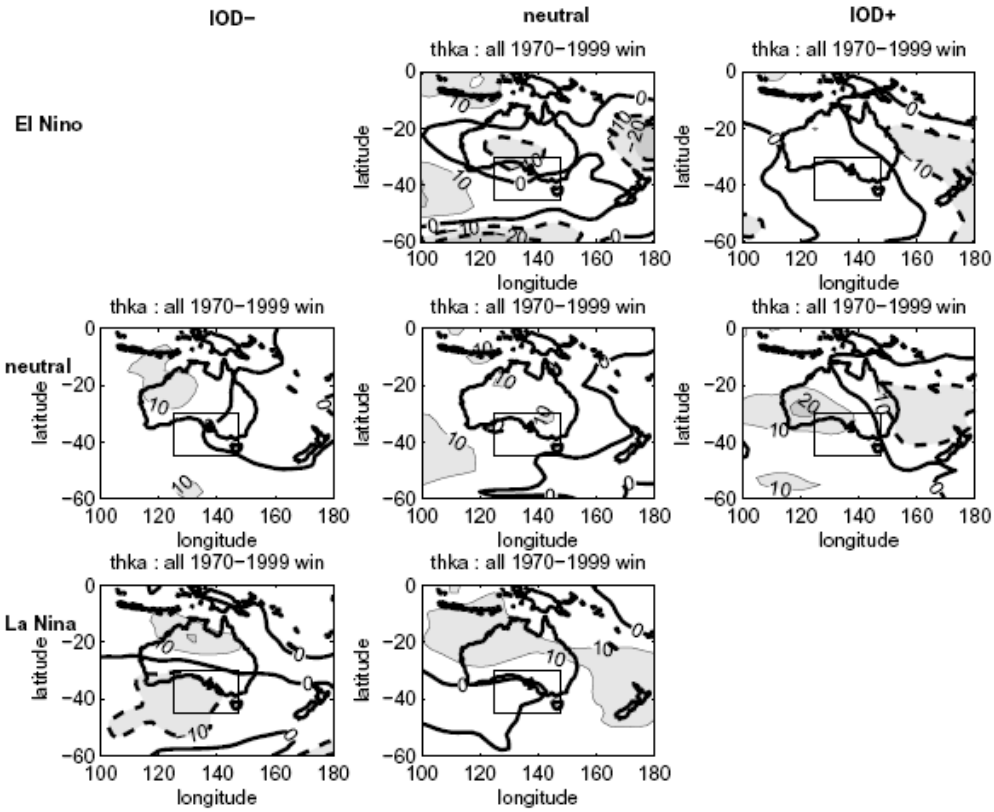

Figure 8.22. Thickness composite anomaly for ENSO/IOD categories for winter. The anomaly is calculated from the set of years 1970–1999. Only those years that fall into each ENSO/IOD category are used to calculate the composite anomaly. Units are m. Dash contours indicate negative anomalies and solid contours indicate positive anomalies.

(bottom row in Fig. 8.22), the positive thickness anomaly over northern Australia and the Pacific Ocean, together with the negative thickness anomaly over southern Australia would result in an enhancement in thermal wind along the jet axis and a strengthening of the jet stream over southeastern Australia, along with an enhancement of thickness gradient for systems in this region. These features are consistent with the increase of rainfall in southeastern Australia in La Niña years.

Within each of the ENSO/IOD categories we can also group the results according to the different synoptic categories. The thickness anomaly composites for cutoff systems in each of the ENSO/IOD categories are shown in Fig. 8.23. Cutoffs have different signatures in the thickness pattern for different ENSO/IOD year groups, with the differences following the background thickness anomalies shown in Fig. 8.22. Where the warm/cold anomalies are pronounced in Fig. 8.22 the warm/cold anomaly is larger in Fig. 8.23. Focusing on the region along the east coast of Australia, the ENSO/IOD category with a positive thickness anomaly in this region in

Fig. 8.22 (La Niña) exhibits an enhanced positive anomaly along the east coast and enhanced thickness gradient across the cutoff system in Fig. 8.23. The ENSO/IOD categories with a negative thickness anomaly along the east coast in Fig. 8.22 (El Niño, El Niño/IOD+, IOD+) have a only a weak positive thickness anomaly associated with the cutoff system in Fig. 8.23. This weak positive anomaly is associated with a weak thickness gradient in the cutoff system and lower rainfall. The consistency of these relationships supports the notion that SST anomalies affect the strength of synoptic systems in the region.

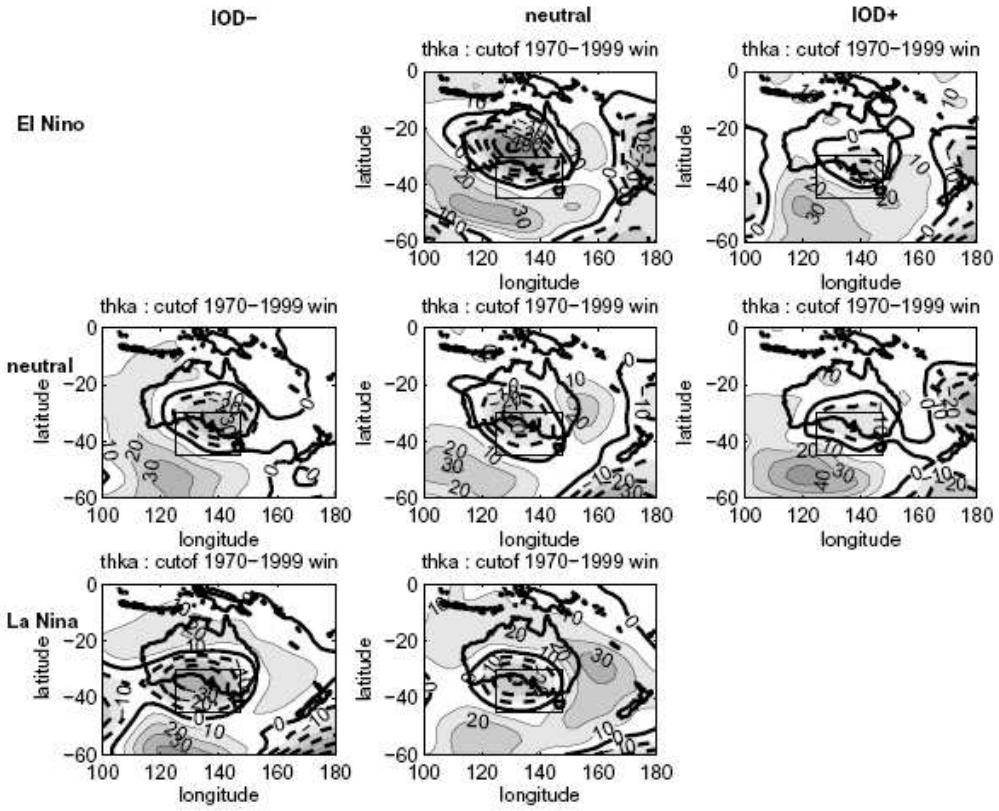

Figure 8.23. As in Fig. 8.22, but the composite is only calculated on days for which cutoff low events occur. Units are m.

The thickness anomaly pattern for cutoffs in La Niña categories shows a strong gradient across southeastern Australia, consistent with cutoff lows producing high rainfall. Composites of 250 hPa wind (jet stream) for cutoff days in each of the ENSO/IOD categories (not shown) show that the subtropical jet has a local maximum over southeastern Australia in the La Niña categories, whereas the maximum is located further east in the Pacific Ocean for El Niño and IOD+ categories, which is too far downstream to promote development of systems over southeastern Australia.

The thickness gradient for cutoffs between the continent and Pacific Ocean is not pronounced for the IOD-/ENSO-neutral category in Fig. 8.23, yet that category

is also favorable to cutoff rainfall. In this category the Eady growth rate (not shown) shows a pronounced local maximum over the central southern portion of the Australian continent, consistent with an enhancement of the jet stream and thermal wind in this region. Those enhancements appear to be associated with the positive thickness anomaly northwest of Australia, which is proximate to the strong warm SST anomaly there in IOD- years.

For composites of frontal systems in the ENSO/IOD category years (not shown), the differences in thickness structure from category to category are not very pronounced. This is consistent with the fact that rainfall from frontal systems in the southeast tends to be fairly constant from year to year. The interannual variability of rainfall in the region is driven by variability in rainfall from cutoff systems (Pook *et al.*, 2006).

8.8. Conclusions

Rainfall in the Mallee region of southeastern Australia is highly variable on interannual time scales. One way to decompose that variability is to analyze the synoptic systems that produce the rainfall. Using a synoptic classification of frontal systems, cutoff lows, and other systems, much of the variability in cool season rainfall (April–October) is dominated by cutoff systems. Wet years in the southeast tend to be wet because there is enhanced rainfall from cutoff systems in those years.

The organization and structure of cutoff systems was shown to be distinct from frontal systems. Cutoff systems display a thermal cold pool cradled to the south by a warm thickness anomaly, which is indicative that the system has been 'cutoff' from the westerly stream. Both cutoff and frontal systems exhibit a strong increase in thickness gradient across the cold and warm pools as the rainfall associated with the system increases. The mechanisms via which these systems intensify appears to be quite different though. Cutoff systems in the region grow in intensity in association with local increases in baroclinicity, vorticity, and a local increase in strength of the subtropical jet. Frontal systems increase in intensity through an enhancement and confluence of both subtropical and polar jets. The baroclinic fields associated with intense fronts are less well localized than for cutoff systems and reflect the differing orientation of the jet systems. The vertical motion in cutoff systems is also more localized (relative to fronts) and displays the more classic comma wraparound of rising warm moist air and descending cold dry air.

In order to test variation of the synoptic types as a function of interannual rainfall variability, we analyzed the dominant spatial patterns of rainfall across the Australian continent using a clustering algorithm. This yielded five robust pattern

types. For the years associated with each pattern we generated composites based on the days within each year that each synoptic type occurred. For the one pattern type ('wet south') in which frontal rainfall predominates in the Mallee, the thickness gradient is enhanced in the frontal composite. Similarly, the thickness gradient is enhanced for composites of cutoffs where cutoff rainfall is enhanced, and the thickness gradient is diminished in dry years.

For the rainfall cluster patterns that are wettest in the Mallee region ('wet south' and 'wet Australia'), the hemispheric mid-tropospheric flow is highly zonal with an annulus about the pole indicative of the SAM. The 'wet south' pattern is indicative of the SAM- phase, while the 'wet Australia' pattern corresponds to the SAM+ phase. This suggests that different phases of the SAM can both be associated with enhanced rainfall in the Mallee region. The mechanisms are different in each case though. The 'wet south' pattern is largely the result of enhanced frontal rainfall, which is associated with the decreased pressure and enhanced equatorward westerly storm track in the SAM- phase. The 'wet Australia' pattern features a region of positive pressure anomalies and enhanced blocking southeast of Australia, which is favorable for the development of cutoff systems over southeastern Australia. This result illustrates that a flow pattern with a decreased or southward shift of the zonal mean storm tracks south of Australia is not necessarily detrimental to rainfall in Australia (cf. Karoly, 2003; Frederiksen and Frederiksen, 2007). In this case the tendency for enhanced blocking promotes cutoff systems in the region that are very efficient at delivering rainfall to the Australian region. Thus, in projecting rainfall changes in the region one needs to consider how any projected circulation changes will affect different synoptic types.

Interannual variability of rainfall and synoptic systems was also assessed for the modes of oceanic variability most important for Australia; ENSO and IOD. When years are stratified according to ENSO and IOD states, the thickness anomaly patterns in the region reflect the underlying SST anomalies characteristic of each state. These thickness anomalies in turn are consistent with the enhancement of thickness gradients for cutoff systems in La Niña and IOD- years and the reduction of thickness gradients for cutoff systems in El Niño and IOD+ years. Frontal systems display less differentiation as a function of ENSO and IOD state, but this is consistent with reduced interannual variability for frontal systems. Ocean SST anomalies along the Pacific coast and north of Australia are consistent with, and appear to influence, the intensity of thermal gradients of cutoff systems in southeast Australia, and thus also their rainfall.

In summary, rainfall variability in southeastern Australia can be described according to the kinds of synoptic classification used here. The predominant synoptic

types have distinct signatures in the thermal field, in vertical motion, in concentration of baroclinic gradients, in vorticity, and in association with the major jet systems. Further, these indicators show consistent changes for the synoptic types as rainfall increases and in wet versus dry years. The changes in these features documented here do not explain the variability, but they help us to understand what it looks like. In order to explain the variability we need to consider how these changes are related to broader circulation changes, and what the factors in turn are that govern these changes.

Acknowledgments. This work was funded by the Wealth from Oceans Flagship and the Managing Climate Variability Program. CCU was supported by UNSW under a University International Postgraduate Award and by ARCNESS.

Chapter 9

Concluding Remarks and Future Work

9.1. Precipitation around the Indian Ocean region

Observed characteristic patterns in Indian Ocean SST (associated with extreme precipitation years in SWWA) were linked to large-scale reorganizations in the basin-wide atmospheric general circulation (England *et al.*, 2006). In ensembles of AGCM simulations forced with these observed SST patterns, Ummenhofer *et al.* (2007b,c) further explored the mechanisms by which the reorganization of the local and regional atmospheric circulation patterns impact precipitation for two specific areas, namely western regions of Australia and East Africa, respectively. In further work, the influence and mechanism of this SST pattern on the modulation of precipitation across the Indian Ocean will be investigated. There are indications that rainfall in Indonesia varies in phase (out of phase) with western Australian (East African) precipitation in observations (e.g. England *et al.*, 2006). Fig. 9.1 supports a similar conclusion from the conducted AGCM experiments, especially prominent for the P_{DRY} case. This most likely relates to the reduction (enhancement) of upward vertical velocity over the Indonesian Archipelago associated with the cold (warm) SST anomalies in the tropical eastern Indian Ocean off the northwest shelf of Australia in P_{DRY} (cf. Fig. 4.9).

9.2. Contribution of local SST to climate anomalies around the Indian Ocean region

The relative importance of local regions of anomalous SST in the Indian Ocean for enhanced East African precipitation was described in Ummenhofer *et al.* (2007b). In addition, Ummenhofer *et al.* (2007c) suggested that the meridional gradient in SST

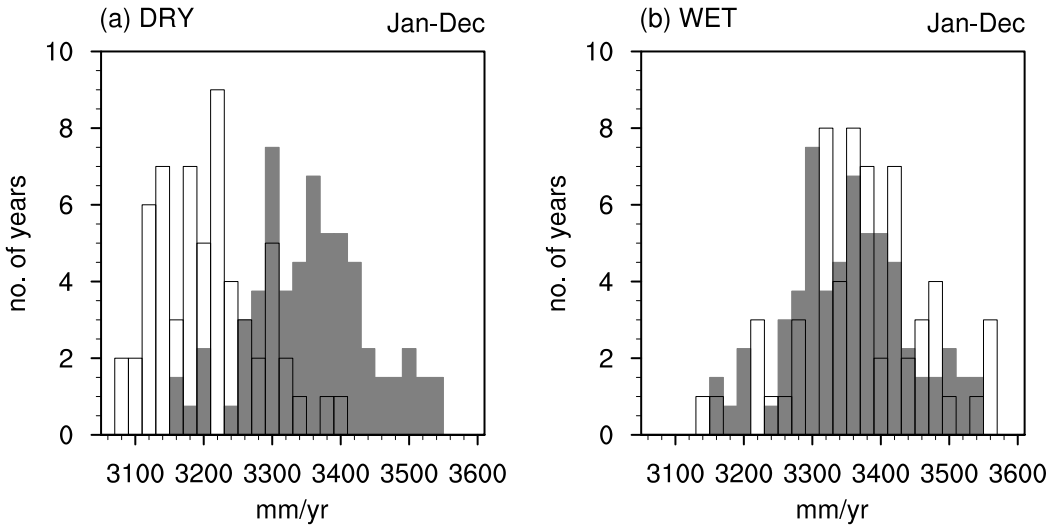

Figure 9.1. Frequency distribution of total rainfall spatially averaged across Indonesia (7°S–1.5°N, 101°–121°E): cumulative rainfall amount (in mm yr^{-1}) summed for the months Jan.–Dec. for the (a) P_{DRY} and (b) P_{WET} case. The shaded gray rainfall distribution represents the CNTRL (normalized to the number of ensemble members in P_{DRY}/P_{WET}), while P_{DRY} and P_{WET} are indicated with black outlines. The following significance level holds, as determined by a Mann-Whitney test (if nothing indicated, below 80%): (a) 99%

anomalies between the eastern tropical and subtropical Indian Ocean is essential for modulations of large-scale rainfall anomalies across western regions of Australia. AGCM experiments with individual and combined poles of SST anomalies across the Indian Ocean will be further investigated for their contributing role in driving precipitation anomalies across Australia. Fig. 9.2 demonstrates the importance of an enhanced (reduced) meridional SST gradient in the eastern Indian Ocean for a shift in the annual rainfall distribution towards its high (low) end for WA. The biggest response in the WA rainfall distribution is seen in the experiments with both the tropical and subtropical pole included, especially for the wet case (Fig. 9.2a, d). The contribution of the tropical pole on its own is far greater than the subtropical pole, which is not surprising considering the close ocean-atmosphere coupling in the tropics relative to the extratropics (Kushnir *et al.*, 2002). This also relates to the magnitude of the SST anomaly in the tropical pole, and the coincident magnitude of the change in the meridional SST gradient, relative to the subtropical pole (see Section 9.3).

9.3. Improved predictions from Indian Ocean variability

Future work is planned to gain a better understanding of the development and seasonal evolution of the characteristic SST patterns in Indian Ocean. As shown by

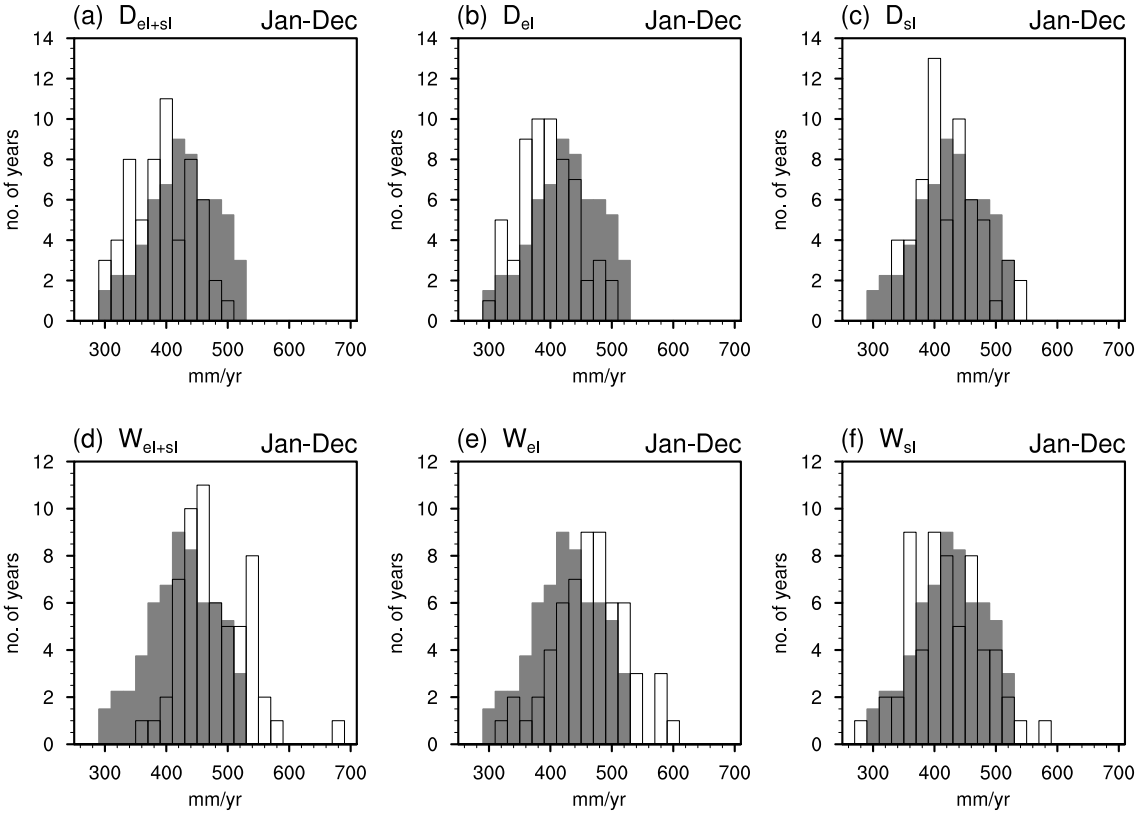

Figure 9.2. Frequency distribution of total rainfall spatially averaged across Western Australia (21°–35°S, 115°–129°E): cumulative rainfall amount (in mm yr^{-1}) summed for the months Jan.–Dec. for the P_{DRY} cases for the poles (a) D_{eI+sI}, (b) D_{eI}, and (c) D_{sI} and for the P_{WET} cases (d) W_{eI+sI}, (e) W_{eI}, and (f) W_{sI}. The shaded gray rainfall distribution represents the CNTRL (normalized to the number of ensemble members in P_{DRY}/P_{WET}), while P_{DRY} and P_{WET} for the different poles are indicated with black outlines. The following significance levels hold, as determined by a Mann-Whitney test (if nothing indicated, below 80%): (a) 99%, (b) 99%, (d) 99%, (e) 99%.

England *et al.* (2006) and Ummenhofer *et al.* (2007b,c), these distinct SST patterns can induce considerable local and regional changes in the general atmospheric circulation across the Indian Ocean, with impacts on precipitation over the adjacent land masses. Therefore, improved knowledge of the seasonal evolution of the described Indian Ocean SST anomalies could help in seasonal forecasting. Oceanic precursors for variability of the regional atmospheric circulation over the Indian Ocean basin are more likely to prove promising for increased lead times than indices based on atmospheric fields. To investigate the predictive potential of the characteristic SST patterns, simulations are planned with an ocean model, the NCAR CCSM3 run in the standard ocean-ice configuration with forcing from the Common Ocean-ice Reference Experiments (CORE). A set of ensemble simulations is envisaged, in which the ocean is forced with observed atmospheric boundary conditions encountered

during extreme dry and wet rainfall years in SWWA. These changed atmospheric fields include surface wind anomalies across the Indian Ocean basin during extreme rainfall years in SWWA, such as those described by England *et al.* (2006). In addition, simulations with anomalous surface heat fluxes during those extreme rainfall years will be conducted. Similar to the experimental setup for the atmospheric model described in Ummenhofer *et al.* (2007b), experiments with the ocean model will include the entire pattern across the Indian Ocean, as well as individual and combined poles, to assess the contribution of regional and local ocean-atmosphere interactions for the large-scale circulation.

Particular emphasis will be put on the initial oceanic and atmospheric conditions necessary for the formation of the individual poles. These include the depth of the thermocline in the east (Meyers *et al.*, 2007), the barrier layer, timing and strength of the surface wind anomalies (Feng and Meyers, 2003; Wijffels and Meyers, 2004), and their influence on coastal upwelling off Sumatra/Java. In this context, the influence of ENSO variability on the tropical Indian Ocean, particularly during the formation phase of the tropical IOD, as previously suggested (e.g., Goddard and Graham, 1999; Latif *et al.*, 1999; Black *et al.*, 2003; Feng and Meyers, 2003; Wijffels and Meyers, 2004; Meyers *et al.*, 2007), will be analyzed as well. The processes responsible for the continued formation of the poles with anomalous SST will be investigated. A heat budget analysis of individual poles will be used to quantify the contribution of competing influences/processes/mechanisms to the formation of the poles. The propagation of a subsurface oceanic signal, possibly as a Rossby wave from the eastern to western Indian Ocean, will be explored to distinguish between atmospheric influences and internal ocean dynamics for the formation of the western Indian Ocean warm SST anomalies during a positive IOD event (Gary Meyers 2007, personal communication).

A first indication of possible predictive potential can be gained from Fig. 9.3. Fig. 9.3a–c depicts the evolution of observed area-averaged Indian Ocean SST anomalies in the regions of the individual poles marked in Fig. 4.1 for each year during the period 1970–2006. In addition, the seasonal evolution of the difference in SST anomalies between poles, i.e. P_{wI} - P_{eI} and P_{sI} - P_{eI}, are indicated (Fig. 9.3d–e). Years that England *et al.* (2006) defined as extreme dry (wet) in SWWA are highlighted in red (blue), respectively. For the eastern pole P_{eI} (= P1; Fig. 9.3a), there is a general tendency for SST anomalies during dry (wet) SWWA years to be negative (positive) for the better part of the year. Anomalies over the western pole P_{wI} are less distinguishable between dry and wet years (Fig. 9.3b). The same is true for the southern pole P_{sI} (= P2; Fig. 9.3c), though very cold SST anomalies are not seen during dry SWWA years, but frequently for wet years. When focusing on

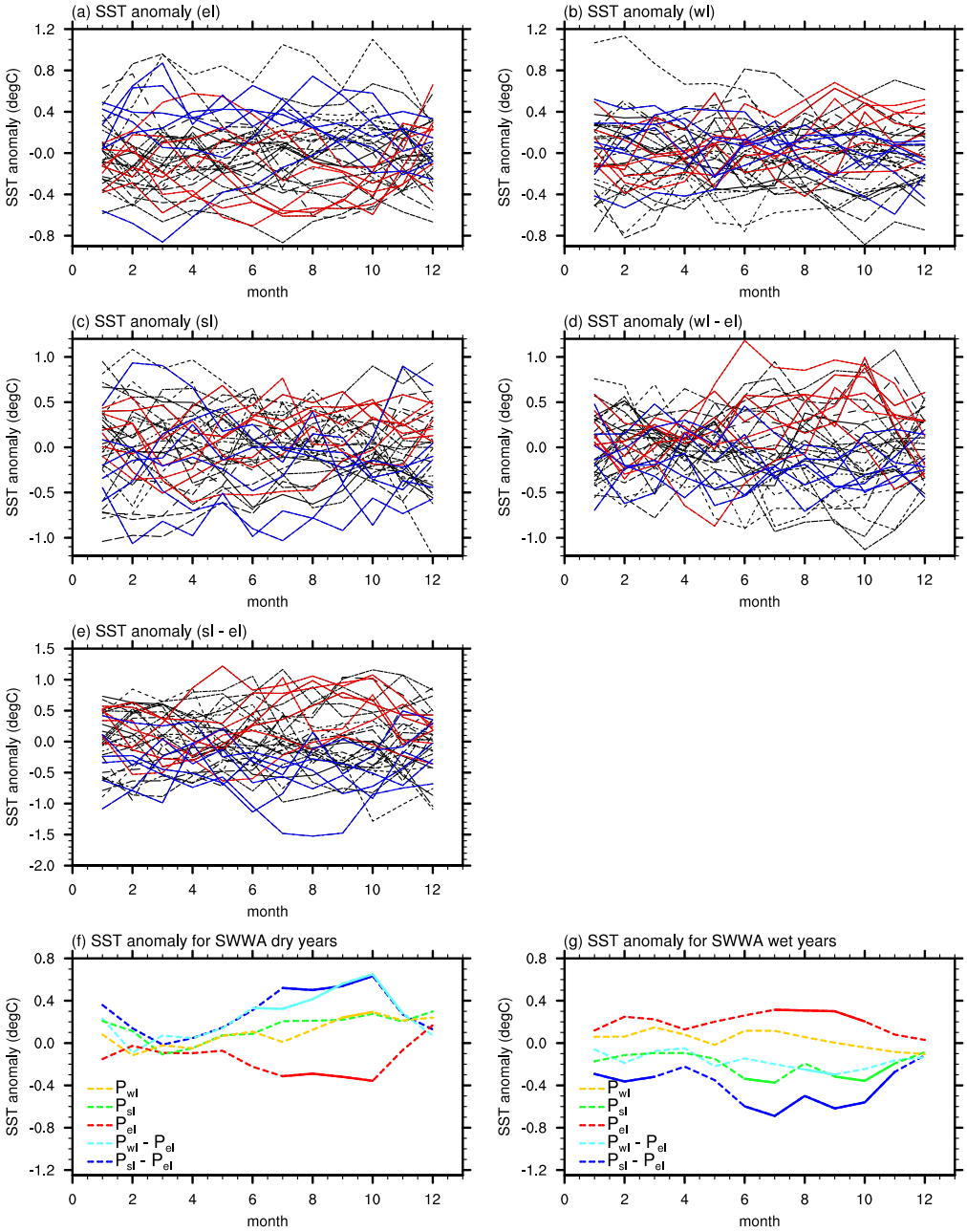

Figure 9.3. (a–e) Seasonal cycle of SST anomalies for different poles, with dry (red) / wet (blue) years in SWWA highlighted, for individual years during the period 1970–2006. (f, g) Average seasonal cycle of SST anomalies for dry/wet years in SWWA for different poles, with solid lines indicating significant anomalies (at 90% confidence level).

the difference between the western and eastern pole P_{wI} - P_{eI}, the SST anomalies between the dry and wet SWWA years diverge over the second half of the year (Fig. 9.3d), which is consistent with the phase-locking of the IOD with its peak in October/November (e.g., Saji *et al.*, 1999; Webster *et al.*, 1999; Li *et al.*, 2003; Zhang and Yang, 2007). Similarly, the meridional gradient between the southern and

eastern pole P_{sI} - P_{eI} reaches highest values during the second half of the year, as described by Ummenhofer *et al.* (2007c), and diverging SST anomalies are observed after May (Fig. 9.3e). The seasonal development of SST anomalies for the different poles and difference between them is averaged across dry and wet SWWA years (as defined by England *et al.*, 2006), respectively (Fig. 9.3f, g). From June/July onwards, the SST anomalies in P_{eI} and the differences between the poles P_{sI} - P_{eI} and P_{wI} - P_{eI} during dry SWWA years differ significantly (at the 90% confidence level) from the anomalies during wet years (Fig. 9.3f). The zonal SST difference in the tropical Indian Ocean (P_{wI} - P_{eI}) is less distinct during wet years, while the SST anomalies in P_{eI} and P_{sI} - P_{eI} are significantly different from the dry years (Fig. 9.3g). In fact, the meridional gradient of P_{sI} - P_{eI} during wet years is already significantly different for a period very early on in the year for January to March.

The divergent tendencies in the seasonal evolution of SST anomalies for the various poles for extreme dry and wet SWWA years indicates that upper ocean dynamics/processes over the Indian Ocean are fundamentally different. It is of interest to further pursue if these differences are due to internal dynamics of the ocean, or result from anomalous ocean-atmosphere interactions. The results presented in previous chapters indicate that anomalous SST patterns are indeed capable of driving the observed atmospheric general circulation changes, and ultimately the shifts in precipitation. Longer persistence of oceanic anomalies and their gradual build-up (cf. Fig. 9.3f–g) provides hope for improved seasonal rainfall forecasts based on a better understanding of the seasonal evolution/development of the ocean anomalies with longer lead-times.

The above hypothesis will be tested by forcing the ocean model with the characteristic dry/wet SWWA anomalous atmospheric fields (heat fluxes/winds) only for the first few months of the year. If there is any predictive potential in the system, the characteristic SST patterns in the various poles should persist for several months even when reverting back to climatological atmospheric forcing due to the "inertia" of the ocean. Ideally, model simulations will be repeated in a coupled model to assess the ocean-atmosphere feedbacks of the induced anomalies in the coupled system. These experiments would follow the approach used successfully by Sen Gupta and England (2007).

9.4. SWWA climate variability on historic/paleo-timescales

Future work is planned to assess recent trends and interannual to seasonal variability in SWWA precipitation and its links to Indian Ocean climate over centennial timescales in the historic/geologic record. This will involve use of proxies for Indian

Ocean SST in the regions defined by the individual poles from coral records. Kuhnert *et al.* (1999, 2000) describe SST records inferred from skeletal $\delta^{18}O_2$ in corals which roughly coincide with the positions of P_{sI} (= P2) and P_{eI} (= P1), respectively. These proxy SST records cover the period 1795–1995 and 1879–1995, respectively, providing sufficient overlap with historic observation-based measurements to assess their quality/accuracy. It would thus be possible to assess variability and trends of SST in these poles, as well as the gradient between them (P_{sI} - P_{eI}) over an extended period. This could then be related to long-term SWWA precipitation proxy data available at seasonal resolution from speleothem records for the past century (Treble *et al.*, 2003, 2005a,b). The sudden decrease in SWWA winter rainfall in the 1970s (e.g., Allan and Haylock, 1993) could thus be assessed on longer centennial timescales and possibly related to changes in Indian Ocean climate inferred from SST proxies.

9.5. Extratropical influences on Australian precipitation

Impacts of extratropical influences on Australian rainfall will be explored following methodology already successfully applied to New Zealand precipitation. The relative contribution of tropical (as associated with ENSO) and extratropical (as associated with SAM) influences to New Zealand precipitation variability and long-term trends were assessed by Ummenhofer and England (2007) and Ummenhofer *et al.* (2007a), respectively. The SAM plays an important role in modulating New Zealand precipitation on seasonal to interannual timescales via changes to the atmospheric circulation and moisture fluxes over the country (Ummenhofer and England, 2007). Similarly, on longer timescales, the SAM contributes significantly to recent drying trends over wide parts of New Zealand during austral summer (Ummenhofer *et al.*, 2007a). For Australia, the positive-trending SAM is suggested to account for recent positive trends in DJF rainfall for southeastern Australia (Hendon *et al.*, 2007) and decreases in JJA SWWA rainfall trends (Cai and Cowan, 2006). In contrast, Meneghini *et al.* (2007) only find short-term declines in winter rainfall in Victoria and Tasmania linked to the SAM, while not for SWWA. Future work is planned to better understand extratropical influences associated with the SAM on winter precipitation across southern regions of Australia. Recent work by van Ommen *et al.* (2007) shows a tentative out-of-phase relationship between SWWA and Antarctic precipitation from paleo-climate proxy records. It is intended to pursue such extratropical teleconnections further, combining output from climate model simulations with reanalyses and observations, as well as proxy records. This research could overlap with the investigation of present SWWA precipitation trends

and variability in the long-term historic context (see Section 9.4).

Bibliography

ABARE, 2007: Australian crop report. Technical report, No. 141 (February 2007), Australian Bureau of Agricultural and Resource Economics, pp. 19.

Adams, P., M. Horridge, J. Madden and G. Wittwer, 2005: Drought, regions and the Australian economy between 2001-2 and 2004-5. Technical report, Monash University, Centre of Policy Studies, Melbourne.

AGO, 2007: Detecting, understanding and attributing climate change. Technical report, Australian Greenhouse Office, Commonwealth of Australia, Canberra, pp. 26.

Allan, R., J. Lindesay and D. Parker, 1996: *El Niño Southern Oscillation and climate variability*. CSIRO Publishing, Melbourne, pp. 405.

Allan, R. J., 1988: El Niño Southern Oscillation influences in the Australasian region. *Progress in Physical Oceanography*, **12**, 313–348.

Allan, R. J. and M. R. Haylock, 1993: Circulation features associated with the winter rainfall decrease in Southwestern Australia. *Journal of Climate*, **6**, 1356–1367.

Allan, R. J., C. J. C. Reason, J. A. Lindesay and T. J. Ansell, 2003: Protracted ENSO episodes and their impacts in the Indian Ocean region. *Deep-Sea Research II*, **50**, 2331–2347.

Alory, G., S. Wijffels and G. Meyers, 2007: Observed temperature trends in the Indian Ocean over 1960–1999 and associated mechanisms. *Geophysical Research Letters*, **34**, L02606, doi:10.1029/2006GL028 044.

Ansell, T. J., C. J. C. Reason and G. Meyers, 2000a: Variability in the tropical southeast Indian Ocean and links with southeast Australian winter rainfall. *Geophysical Research Letters*, **27**, 3977–3980.

Ansell, T. J., C. J. C. Reason, I. N. Smith and K. Keay, 2000b: Evidence for decadal variability in southern Australian rainfall and relationships with regional pressure and sea surface temperature. *International Journal of Climatology*, **20**, 10, 1113–1129.

Arblaster, J. M. and G. A. Meehl, 2006: Contributions of external forcings to Southern Annular Mode trends. *Journal of Climate*, **19**, 2896–2905.

Arblaster, J. M., G. A. Meehl and A. M. Moore, 2002: Interdecadal modulation of Australian rainfall. *Climate Dynamics*, **18**, 519–531.

Ashok, K., W.-L. Chun, T. Motoi and T. Yamagata, 2004a: Decadal variability of the Indian Ocean dipole. *Geophysical Research Letters*, **31**, L24207, doi:10.1029/2004GL021 345.

Ashok, K., Z. Guan, N. H. Saji and T. Yamagata, 2004b: Individual and combined influences of the ENSO and Indian Ocean Dipole on the Indian summer monsoon. *Journal of Climate*, **17**, 3141–3155.

Ashok, K., Z. Guan and T. Yamagata, 2001: Impact of the Indian Ocean dipole on the relationship between the Indian monsoon rainfall and ENSO. *Geophysical Research Letters*, **28**, 23, 4499–4502.

Ashok, K., Z. Guan and T. Yamagata, 2003a: Influence of the Indian Ocean Dipole on the Australian winter rainfall. *Geophysical Research Letters*, **30**, 15, doi:10.1029/2003GL017 926.

Ashok, K., Z. Guan and T. Yamagata, 2003b: A look at the relationship between the ENSO and the Indian Ocean dipole. *Journal of the Meteorological Society of Japan*, **81**, 41–56.

Barry, R. and A. Carleton, 2001: *Synoptic and dynamic climatology*. Routledge, London, pp. 644.

Basher, R. E. and C. S. Thompson, 1996: Relationship of air temperature in New Zealand to regional anomalies in sea-surface temperature and atmospheric circulation. *International Journal of Climatology*, **16**, 405–425.

Behera, S. K., R. Krishnan and T. Yamagata, 1999: Unusual ocean-atmosphere conditions in the tropical Indian Ocean during 1994. *Geophysical Research Letters*, **26**, 3001–3004.

Behera, S. K., P. S. Salvekar and T. Yamagata, 2000: Simulation of interannual SST variability in the tropical Indian Ocean. *Journal of Climate*, **13**, 3487–3499.

Behera, S. K. and T. Yamagata, 2001: Subtropical SST dipole events in the southern Indian Ocean. *Geophysical Research Letters*, **28**, 2, 327–330.

Birkett, C., R. Murtugudde and R. Allan, 1999: Indian Ocean climate event brings floods to East Africa's lakes and the Sudd Marsh. *Geophysical Research Letters*, **26**, 8, 1031–1034.

Bjerknes, J., 1969: Atmospheric teleconnections from the equatorial Pacific. *Monthly Weather Review*, **97**, 163–172.

Black, E., 2003: The impact of Indian and Pacific Ocean processes on the East African short rains. *CLIVAR-Exchanges*, **8**, 2/3.

Black, E., J. Slingo and K. R. Sperber, 2003: An observational study of the relationship between excessively strong short rains in coastal East Africa and Indian Ocean SST. *Monthly Weather Review*, **131**, 74–94.

Boville, B. A. and P. R. Gent, 1998: The NCAR Climate System Model, version one. *Journal of Climate*, **11**, 1115–1130.

Bowden, J. H. and F. H. M. Semazzi, 2007: Empirical analysis of intraseasonal climate variability over the Greater Horn of Africa. *Journal of Climate*, **20**, 5715–5731.

Bradshaw, B., 1997: Instrumental and observing networks. In E. K. Webb, ed., *Windows on meteorology: Australian perspective*, 127–141. CSIRO Publishing, Melbourne.

Broad, K. and S. Agrawala, 2000: The Ethiopia food crisis - uses and limits of climate forecasts. *Science*, **289**, 1693–1694.

Bromwich, D. H. and R. L. Fogt, 2004: Strong trends in the skill of the ERA-40 and NCEP-NCAR reanalyses in the high and midlatitudes of the Southern Hemisphere, 1958–2001. *Journal of Climate*, **17**, 4603–4619.

Brown, E. T., T. C. Johnson, C. A. Scholz, A. S. Cohen and J. W. King, 2007: Abrupt change in tropical African climate linked to the bipolar seesaw over the past 55,00o years. *Geophysical Research Letters*, **34**, L20702, doi:10.1029/2007GL031 240.

Cai, W., 2006: Antarctic ozone depletion causes an intensification of the Southern Ocean super-gyre circulation. *Geophysical Research Letters*, **33**, L03712, doi:10.1029/2005GL024 911.

Cai, W., D. Bi, J. Church, T. Cowan, M. Dix and L. Rotstayn, 2006: Pan-oceanic response to increasing anthropogenic aerosols: Impacts on the Southern Hemisphere oceanic circulation. *Geophysical Research Letters*, **33**, L21707, doi:10.1029/2006GL027 513.

Cai, W., M. Collier, P. Durack, H. Gordon, A. C. Hirst, S. P. O'Farrell and P. H. Whetton, 2003a: The response of climate variability and mean state to climate change: preliminary results from the CSIRO MK3 coupled model. *CLIVAR-Exchanges*, **8**, 8–11.

Cai, W. and T. Cowan, 2006: SAM and regional rainfall in IPCC AR4 models: Can anthropogenic forcing account for southwest Western Australian winter rainfall reduction? *Geophysical Research Letters*, **33**, L24708, doi:10.1029/2006GL028 037.

Cai, W., G. Shi, T. Cowan, D. Bi and J. Ribbe, 2005a: The response of the Southern Annular Mode, the East Australian Current, and the southern mid-latitude ocean circulation to global warming. *Geophysical Research Letters*, **32**, L23706, doi:10.1029/2005GL024 701.

Cai, W., G. Shi and Y. Li, 2005b: Multidecadal fluctuations of winter rainfall over southwest Western Australia simulated in the CSIRO Mark 3 coupled model. *Geophysical Research Letters*, **32**, L12701, doi:10.1029/2005GL022 712.

Cai, W., P. H. Whetton and D. J. Karoly, 2003b: The response of the Antarctic Oscillation to increasing and stabilized atmospheric CO2. *Journal of Climate*, **16**, 1525–1538.

Cai, W., P. H. Whetton and A. B. Pittock, 2001: Fluctuations of the relationship between ENSO and northeast Australian rainfall. *Climate Dynamics*, **17**, 421–432.

Carberry, P. S., G. L. Hammer, H. Meinke and M. Bange, 2000: The potential value of seasonal climate forecasting in managing cropping systems. In G. Hammer, N. Nicholls and C. Mitchell, eds., *Application of seasonal climate forecasting in agricultural and natural ecosystems – The Australian experience*, 167–181. Kluwer Academic Publishing, Dordrecht.

Carleton, A. M., 2003: Atmospheric teleconnections involving the Southern Ocean. *Journal of Geophysical Research*, **108**, C4, doi:10.1029/2000JC000 379.

Chase, T. N., J. A. Knaff, R. A. Pielke Sr. and E. Kalnay, 2003: Changes in global monsoon circulations since 1950. *Natural Hazards*, **29**, 229–254.

Cheng, X. and J. M. Wallace, 1993: Cluster analysis of the Northern Hemisphere wintertime 500-hPa height field: spatial patterns. *Journal of the Atmospheric Sciences*, **50**, 16, 2674–2696.

Chiew, F. H. S., T. C. Piechota, J. A. Dracup and T. A. McMahon, 1998: El Niñno/Southern Oscillation and Australian rainfall, streamflow and drought: Links and potential for forecasting. *Journal of Hydrology*, **204**, 138–149.

Chou, C., J.-Y. Tu and P.-H. Tan, 2007: Asymmetry of tropical precipitation change under global warming. *Geophysical Research Letters*, **34**, L17708, doi:10.1029/2007GL030 327.

Clare, G. R., B. B. Fitzharris, T. J. H. Chinn and M. J. Salinger, 2002: Interannual variation in end-of-summer snowlines of the Southern Alps of New Zealand, and relationships with Southern Hemisphere atmospheric circulation and sea surface temperature patterns. *International Journal of Climatology*, **22**, 107–120.

Clark, C. O., P. J. Webster and J. E. Cole, 2003a: Interdecadal variability of the relationship between the Indian Ocean zonal mode and East African coastal rainfall anomalies. *Journal of Climate*, **16**, 548–554.

Clark, S. G., E. A. Austen, T. Prance and P. D. Ball, 2003b: Climate variability effects on simulated pasture and animal production in the perennial pasture zone of south-eastern Australia. 1. Between year variability in pasture and animal production. *Australian Journal of Experimental Agriculture*, **43**, 1211–1219.

Colberg, F., C. J. C. Reason and K. Rodgers, 2004: South Atlantic response to ENSO induced climate variability in an OGCM. *Journal of Geophysical Research*, **109**, doi:10.1029/2004JC002 301.

Collins, W. D., C. M. Bitz, M. L. Blackmon, G. B. Bonan, C. S. Bretherton, J. A. Carton, P. Chang, S. C. Doney, J. J. Hack, T. B. Henderson, J. T. Kiehl, W. G. Large, D. S. McKenna, B. D. Santer and R. D. Smith, 2006: The Community Climate System Model Version 3 (CCSM3). *Journal of Climate*, **19**, 2122–2143.

Crowder, R. B., 1995: *The wonders of the weather*. Australian Government Publishing Service, Canberra, pp. 270.

Czaja, A. and C. Frankignoul, 1999: Influence of the North Atlantic SST on the atmospheric circulation. *Geophysical Research Letters*, **26**, 2969–2972.

DAFWA, 2006: Seasonal update, November 2006. Technical report, Department of Agriculture and Food, Government of Western Australia, pp. 10.

de Wit, M. and J. Stankiewicz, 2006: Changes in surface water supply across Africa with predicted climate change. *Science*, **311**, 1917–1921.

Deser, C., A. Capotondi, R. Saravanan and A. S. Phillips, 2006: Tropical Pacific and Atlantic climate variability in CCSM3. *Journal of Climate*, **19**, 2451–2481.

Diaz, H. F., M. P. Hoerling and J. K. Eischeid, 2001: ENSO variability, teleconnections and climate change. *International Journal of Climatology*, **21**, 1845–1862.

Donald, C. M. and D. W. Puckridge, 1987: The ecology of the wheat crop. In A. Lazenby and E. M. Matheson, eds., *Australian field crops. Vol. 1: Wheat and other temperate cereals*, 570. Angus and Robertson.

Draper, N. R. and H. Smith, 1998: *Applied regression analysis*. Wiley-Interscience, USA, pp. 706.

Drosdowsky, W., 1993a: An analysis of Australian seasonal rainfall anomalies: 1950–1987. I: Spatial patterns. *International Journal of Climatology*, **13**, 1–30.

Drosdowsky, W., 1993b: Potential predictability of winter rainfall over southern and eastern Australia using Indian Ocean sea-surface temperature anomalies. *Australian Meteorological Magazine*, **42**, 1–6.

England, M. H. and F. Huang, 2005: On the interannual variability of the Indonesian throughflow and its linkage with ENSO. *Journal of Climate*, **18**, 1435–1444.

England, M. H., C. C. Ummenhofer and A. Santoso, 2006: Interannual rainfall extremes over Southwest Western Australia linked to Indian Ocean climate variability. *Journal of Climate*, **19**, 1948–1969.

Epstein, P. R., 1999: Climate and health. *Science*, **285**, 347–348.

Fedorov, A. V. and G. S. Philander, 2000: Is El Niño changing? *Science*, **288**, 1997–2002.

Feng, M. and G. Meyers, 2003: Interannual variability in the tropical Indian Ocean: a two-year time-scale of Indian Ocean Dipole. *Deep-Sea Research II*, **50**, 2263–2284.

Fitzharris, B. B., T. J. Chinn and G. N. Lamont, 1997: Glacier balance fluctuations and atmospheric circulation patterns over the Southern Alps, New Zealand. *International Journal of Climatology*, **17**.

Foley, J. C., 1957: Droughts in Australia: Review of records from earliest years of settlement to 1955. Technical report, Australian Bureau of Meteorology, Bulletin no. 43, pp. 281.

Folland, C. K. and M. J. Salinger, 1995: Surface temperature trends and variations in New Zealand and the surrounding ocean, 1871–1993. *Journal of Climate*, **15**, 1195–1218.

Frederiksen, C. S. and R. C. Balgovind, 1994: The influence of the Indian Ocean / Indonesian SST gradient on the Australian winter rainfall and circulation in an atmospheric GCM. *Quarterly Journal of the Royal Meteorological Society*, **120**, 923–952.

Frederiksen, C. S. and J. S. Frederiksen, 1996: A theoretical model of Australian Northwest cloudband disturbances and Southern Hemisphere storm tracks: The role of SST anomalies. *Journal of Atmospheric Sciences*, **53**, 10, 1410–1432.

Frederiksen, C. S. and J. S. Frederiksen, 2005a: Mid-1970s changes in the Southern Hemisphere winter circulation. Technical report, Indian Ocean Climate Initiative stage 2: report of phase I activity.

Frederiksen, C. S., D. P. Rowell, R. C. Balgovind and C. K. Folland, 1999: Multidecadal simulations of Australian rainfall variability: the role of SSTs. *Journal of Climate*, **12**, 357–379.

Frederiksen, J. S. and C. S. Frederiksen, 2005b: Decadal changes in Southern Hemisphere winter cyclogenesis. Technical report, CSIRO Marine and Atmospheric Research Paper, No. 002, Australia, pp. 35.

Frederiksen, J. S. and C. S. Frederiksen, 2007: Interdecadal changes in Southern Hemisphere winter storm track modes. *Tellus*, **59A**, 599–617.

French, R. J. and J. E. Schultz, 1984: Water use efficiency of wheat in a Mediterranean-type environment. I. The relation between yield, water use and climate. *Australian Journal of Agricultural Research*, **35**, 743–764.

Fuchs, T., S. U. and B. Rudolf, 2007: Global Precipitation Analysis Products of the GPCC. Technical report, Global Precipitation Climatology Centre (GPCC), Deutscher Wetterdienst, Offenbach a. M., Germany, pp. 10.

Funk, C., G. Senay, A. Asfaw, J. Verdin, J. Rowland, D. Korecha, G. Eilerts, J. Michaelsen, S. Amer and R. Choularton, 2005: Recent drought tendencies in Ethiopia and equatorial-subtropical eastern Africa. Technical report, Famine

Early Warning System Network at UCBS Climate Hazard Group, USGS National Center for EROS, and Chemonics International, pp. 12.

Fyfe, J. C., 2003: Extratropical Southern Hemisphere cyclones: harbingers of climate change? *Journal of Climate*, **16**, 2802–2805.

Fyfe, J. C., 2006: Southern Ocean warming due to human influence. *Geophysical Research Letters*, **33**, L19701, doi:10.1029/2006GL027 247.

Fyfe, J. C., G. J. Boer and G. M. Flato, 1999: The Arctic and Antarctic Oscillations and their projected changes under global warming. *Geophysical Research Letters*, **26**, 11, 1601–1604.

Gallant, A., K. Hennessy and J. Risbey, 2007: Trends in rainfall indices for six Australian regions: 1910-2005. *Australian Meteorological Magazine*, in press.

Garnier, B. J., 1958: Climatic characteristics. In B. J. Garnier, ed., *The climate of New Zealand*, 14–33. Edward Arnold Publishers Ltd., London.

Gentilli, J., 1972: *Australian climate patterns*. Thomas Nelson, Adelaide.

Gentilli, J., 1991: Homologous peri-oceanic west coast climates in the Southern Hemisphere. *Journal of the Royal Society of Western Australia*, **74**, 15–33.

Giannini, A., R. Saravanan and P. Chang, 2003: Oceanic forcing of Sahel rainfall on interannual to interdecadal time scales. *Science*, **302**, 1027–1030.

Gille, S. T., 2002: Warming of the Southern Ocean since the 1950s. *Science*, **295**, 5558, 1275–1277.

Gillett, N. P., R. J. Allan and T. J. Ansell, 2005: Detection of external influence on sea level pressure with a multi-model ensemble. *Geophysical Research Letters*, **32**, L19714, doi:10.1029/2005GL023 640.

Gillett, N. P., T. D. Kell and P. D. Jones, 2006: Regional climate impacts of the Southern Annular Mode. *Geophysical Research Letters*, **33**, L23704, doi:10.1029/2006GL027 721.

Gillett, N. P. and D. W. J. Thompson, 2003: Simulation of recent Southern Hemisphere climate change. *Science*, **302**, 273–275.

Gillett, N. P., F. W. Zwiers, A. J. Weaver and P. A. Stott, 2003: Detection of human influence on sea-level pressure. *Nature*, **422**, 292–294.

Goddard, L. and N. E. Graham, 1999: Importance of the Indian Ocean for simulating rainfall anomalies over eastern and southern Africa. *Journal of Geophysical Research*, **104**, D16, 19 099–19 116.

Gong, D. and S. Wang, 1999: Definition of Antarctic Oscillation index. *Geophysical Research Letters*, **26**, 4, 459–462.

Gordon, H. B. and S. P. O'Farrell, 2004: Transient climate change in the CSIRO coupled model with dynamical sea-ice. *Monthly Weather Review*, **125**, 875–907.

Griffiths, M., M. J. Reeder, D. J. Low and R. A. Vincent, 1998: Observations of a cut-off low over southern Australia. *Quarterly Journal of the Royal Meteorological Society*, **124**, 1109–1132.

Guilyardi, E., 2006: El Niño-mean state-seasonal cycle interactions in a multi-model ensemble. *Climate Dynamics*, **26**, 329–348.

Guymer, L. B., 1987: Operational application of satellite imagery to synoptic analysis in the Southern Hemisphere. Technical report, No. 29, Bureau of Meteorology, pp. 87.

Hack, J. J., J. M. Caron, S. M. Yeager, K. W. Oleson, M. M. Holland, J. E. Truesdale and P. J. Rasch, 2006: Simulation of the global hydrological cycle in the CCSM Community Atmosphere Model Version 3 (CAM3): Mean features. *Journal of Climate*, **19**, 2199–2221.

Hall, A. and M. Visbeck, 2002: Synchronous variability in the Southern Hemisphere atmosphere, sea ice, and ocean resulting from the annular mode. *Journal of Climate*, **15**, 3043–3057.

Hartmann, D. L., J. M. Wallace, V. Limpasuvan, D. W. J. Thompson and J. R. Holton, 2000: Can ozone depletion and global warming interact to produce rapid climate change? *Proceedings of the National Academy of Science*, **97**, 4, 1412–1417.

Harzallah, A. and R. Sadourny, 1995: Internal versus SST-forced atmospheric variability as simulated by an atmospheric general circulation model. *Journal of Climate*, **8**, 474–495.

Hastenrath, S., 2007: Circulation mechanisms of climate anomalies in East Africa and the equatorial Indian Ocean. *Dynamics of Atmospheres and Oceans*, **43**, 25–35.

Hastenrath, S., A. Nicklis and L. Greischar, 1993: Atmospheric-hydrospheric mechanisms of climate anomalies in the western equatorial Indian Ocean. *Journal of Geophysical Research: Oceans*, **98**, 20 219–20 235.

Hastenrath, S., D. Polzin and P. Camberlin, 2004: Exploring the predictability of the 'Short rains' at the coast of East Africa. *International Journal of Climatology*, **24**, 1333–1343.

Hastenrath, S., D. Polzin and C. Mutain, 2007: Diagnosing the 2005 drought in equatorial East Africa. *Journal of Climate*, **20**, 4628–4637.

Held, I. M. and B. J. Soden, 2006: Robust responses of the hydrological cycle to global warming. *Journal of Climate*, **19**, 5686–5699.

Hendon, H. H., D. W. J. Thompson and M. C. Wheeler, 2007: Australian rainfall and surface temperature variations associated with the Southern Hemisphere Annular Mode. *Journal of Climate*, **20**, 2452–2467.

Hines, K. M., D. H. Bromwich and G. J. Marshall, 2000: Artificial surface pressure trends in the NCEP-NCAR reanalysis over the Southern Ocean and Antarctica. *Journal of Climate*, **13**, 3940–3952.

Hirschberg, P. and J. Fritsch, 1991: Tropopause undulations and the development of extratropical cyclones. Part I: Overview and observations from a cyclone event. *Monthly Weather Review*, **119**, 496–517.

Hirst, A. C., P. O. O'Farrell and H. B. Gordon, 2000: Comparison of a coupled ocean-atmosphere model with and without oceanic eddy-induced advection. Part I: ocean spinup and control integrations. *Journal of Climate*, **13**, 139–163.

Hope, P. and N. Nicholls, 2004: Shifts in systems associated with Perth winter rainfall since the mid-1970s. In *Conference Proceedings of 11th National Conference of the Australian Meteorological and Oceanographic Society*. Brisbane, Australia.

Hope, P. K., 2006: Projected future changes in synoptic systems influencing southwest Western Australia. *Climate Dynamics*, **26**, 765–780.

Hope, P. K., W. Drosdowsky and N. Nicholls, 2006: Shifts in the synoptic systems influencing southwest Western Australia. *Climate Dynamics*, **26**, 751–764.

Hoskins, B. J. and P. J. Valdez, 1990: On the existence of storm tracks. *Journal of Atmospheric Sciences*, **47**, 1845–1864.

Hulme, M., R. Doherty, T. Ngara, N. M. and D. Lister, 2001: African climate change: 1900–2100. *Climate Research*, **17**, 145–168.

Hunt, B. G., 2001: A description of persistent climatic anomalies in a 1000-year climatic model simulation. *Climate Dynamics*, **17**, 717–733.

Hurrell, J. W., 1995: Decadal trends in the North Atlantic Oscillation and relationships to regional temperature and precipitation. *Science*, **269**, 676–679.

Hurrell, J. W., J. J. Hack, A. S. Phillips, J. Caron and J. Yin, 2006: The dynamical simulation of the Community Atmosphere Model version 3 (CAM3). *Journal of Climate*, **19**, 2162–2183.

Iizuka, S., T. Matsuura and T. Yamagata, 2000: The Indian Ocean SST dipole simulated in a coupled general circulation model. *Geophysical Research Letters*, **27**, 3369–3372.

IOCI, 2001: Second research report - Towards understanding climate variability in south western Australia. Technical report, Second Research Phase of the Indian Ocean Climate Initiative, Perth, Australia, pp. 204.

IOCI, 2002: Climate variability and change in south west Western Australia. Technical report, Indian Ocean Climate Initiative Panel, Perth, Australia, pp. 43.

IPCC, 2007: Summary for policy makers. In S. Solomon, D. Qin, M. Manning, Z. Chen, M. Marquis, K. B. Averyt, M. Tignor and H. L. Miller, eds., *Climate Change 2007: The Physical Science Basis. Contribution of Working Group I to the Fourth Assessment Report of the Intergovernmental Panel on Climate Change*, 1–18. Cambridge University Press, Cambridge, United Kingdom, and New York, NY, USA.

Janowiak, J. E., 1988: An investigation of interannual rainfall variability in Africa. *Journal of Climate*, **1**, 240–255.

Janowiak, J. E., C. R. Gruber, R. E. Kondragunta, R. E. Livezey and G. F. Huffman, 1998: A comparison of the NCEP-NCAR reanalysis precipitation and the GPCP rain gauge-satellite combined dataset with observational error considerations. *Journal of Climate*, **11**, 2960–2979.

Janowiak, J. E. and P. Xie, 1999: CAMS_OPI: A global satellite-rain gauge merged product for real-time precipitation monitoring applications. *Journal of Climate*, **12**, 3335–3342.

Jeffrey, S. J., J. O. Carter, K. B. Moodie and A. R. Beswick, 2001: Using spatial interpolation to construct a comprehensive archive of Australian climate data. *Environmental Modelling and Software*, **16**, 309–330.

Johnson, T. C., E. T. Brown, J. McManus, S. Barry, P. Barker and F. Gasse, 2002: A high-resolution paleoclimate record spanning the past 25,000 years in southern East Africa. *Science*, **296**, 113–116.

Jones, J. M. and M. Widmann, 2003: Instrument- and tree-ring-based estimates of the Antarctic Oscillation. *Journal of Climate*, **16**, 3511–3524.

Jones, J. M. and M. Widmann, 2004: Early peak in Antarctic Oscillation index. *Nature*, **432**, 290–291.

Juillet-Leclerc, A., S. Thiria, P. Naveau, T. Delcroix, N. Le Bec, D. Blamart and T. Correge, 2006: SPCZ migration and ENSO events during the 20th century as revealed by climate proxies from a Fiji coral. *Geophysical Research Letters*, **33**, L17710, doi:10.1029/2006GL025 950.

Kalnay, E., M. Kanamitsu, R. Kistler, W. Collins, D. Deaven, L. Gandin, M. Iredell, S. Saha, G. White, J. Woollen, Y. Zhu, M. Chelliah, W. Ebisuzaki, W. Higgins, J. Janowiak, K. Mo, C. Ropelewski, J. Wang, A. Leetmaa, R. R., J. R. and D. Joseph, 1996: The NCEP/NCAR 40-year reanalysis project. *Bulletin of the American Meteorological Society*, **77**, 437–471.

Karoly, D. J., 2003: Ozone and climate change. *Science*, **302**, 236–237.

Karoly, D. J., D. G. Vincent and J. M. Schrage, 1998: General circulation. In D. J. Karoly and D. G. Vincent, eds., *Meteorology of the Southern Hemisphere*, 47–85. American Meteorological Society, Boston, MD.

Keable, M., I. Simmonds and K. Keay, 2002: Distribution and temporal variability of 500 hPa cyclone characteristics in the Southern Hemisphere. *International Journal of Climatology*, **22**, 131–150.

Keating, B. A., H. Meinke, M. E. Probert, N. I. Huth and I. G. Hills, 2001: Nwheat: Documentation and performance of a wheat module for APSIM. Technical report, Tropical Agronomy Memorandum, CSIRO Division of Tropical Agriculture, St Lucia, Queensland, Australia.

Kidson, J. W. and J. A. Renwick, 2002: Patterns of convection in the tropical Pacific and their influence on New Zealand weather. *International Journal of Climatology*, **22**, 151–174.

Kiehl, J. T. and P. R. Gent, 2004: The Community Climate System Model, version 2. *Journal of Climate*, **17**, 3666–3682.

Kijazi, A. L. and C. J. C. Reason, 2005: Relationships between intraseasonal rainfall variability of coastal Tanzania and ENSO. *Theoretical and Applied Climatology*, **82**, 153–176.

Kistler, R., E. Kalnay, W. Collins, S. Saha, G. White, J. Woollen, M. Chelliah, W. Ebisuzaki, M. Kanamitsu, V. Kousky, H. van den Dool, R. Jenne and M. Fiorino, 2001: The NCEP-NCAR 50-year reanalysis: Monthly means CD-rom and documentation. *Bulletin of the American Meteorological Society*, **82**, 247–267.

Kobayashi, C. and S. Maeda, 2006: Phase shift of the seasonal cycle in the Hadley Circulation in recent decades. *Geophysical Research Letters*, **33**, L22703, doi:10.1029/2006GL027 682.

Kuhnert, H., J. Ptzold, B. Hatcher, K.-H. Wyrwoll, A. Eisenhauer, L. B. Collins, Z. R. Zhu and G. Wefer, 1999: A 200-year coral stable oxygen isotope record from a high-latitude reef off Western Australia. *Coral Reefs*, **18**, 1–12.

Kuhnert, H., J. Ptzold, K.-H. Wyrwoll and G. Wefer, 2000: Monitoring climate variability over the past 116 years in coral oxygen isotopes from Ningaloo Reef, Western Australia. *International Journal of Earth Sciences*, **88**, 725–732.

Kushner, P. J., I. M. Held and T. L. Delworth, 2001: Southern Hemisphere atmospheric circulation response to global warming. *Journal of Climate*, **14**, 2238–2249.

Kushnir, Y., W. A. Robinson, I. Blad, N. M. J. Hall, S. Peng and R. Sutton, 2002: Atmospheric GCM response to extratropical SST anomalies: Synthesis and evaluation. *Journal of Climate*, **15**, 2233–2256.

Landman, W. A. and S. J. Mason, 1999: Changes in the association between Indian Ocean sea-surface temperatures and summer rainfall over South Africa and Namibia. *International Journal of Climatology*, **19**, 1477–1492.

Latif, M., D. Dommenget, M. Dima and A. Grötzner, 1999: The role of Indian Ocean sea surface temperature in forcing East African rainfall anomalies during December-January 1997/98. *Journal of Climate*, **12**, 3497–3504.

Lavery, B., G. Joung and N. Nicholls, 1997: An extended high-quality historical rainfall dataset for Australia. *Australian Meteorological Magazine*, **46**, 27–38.

Lee, T., I. Fukumori and D. Menemenlis, 2002: Effects of the Indonesian throughflow on the Pacific and Indian Oceans. *Journal of Physical Oceanography*, **32**, 1404–1429.

Levitus, S., J. I. Antonov, T. P. Boyer and C. Stephens, 2000: Warming of the world ocean. *Science*, **287**, 5461, 2225–2229.

Li, C. Y. and M. Q. Mu, 2001: The influence of the Indian Ocean dipole on atmospheric circulation and climate. *Advances in Atmospheric Science*, **18**, 831–843.

Li, F., L. E. Chambers and N. Nicholls, 2005a: Relationships between rainfall in the southwest of Western Australia and near-global patterns of sea surface temperature and mean sea level pressure variability. *Australian Meteorological Magazine*, **54**, 23–33.

Li, T., B. Wang, C.-P. Chang and Y. Zhang, 2003: A theory for the Indian Ocean dipole-zonal mode. *Journal of the Atmospheric Sciences*, **60**, 2119–2135.

Li, Y., 2007: Changes of winter extreme rainfall over Southwest Western Australia and the linkage to the Southern Annular Mode. In *Proceedings of 10th International Meeting on Statistical Climatology*. Beijing, China.

Li, Y., W. Cai and E. P. Campbell, 2005b: Statistical modeling of extreme rainfall in southwest Western Australia. *Journal of Climate*, **18**, 852–863.

Linthicum, K. J., A. Anyamba, C. J. Tucker, P. W. Kelley, M. F. Myers and C. J. Peters, 1999: Climate and satellite indicators to forecast Rift Valley fever epidemics in Kenya. *Science*, **285**, 397–400.

Loschnigg, J., G. A. Meehl, P. J. Webster, J. M. Arblaster and G. P. Compo, 2003: The Asian monsoon, the tropospheric biennial oscillation, and the Indian Ocean zonal mode in the NCAR CSM. *Journal of Climate*, **16**, 1617–1642.

Lu, J., G. A. Vecchi and T. Reichler, 2007: Expansion of the Hadley cell under global warming. *Geophysical Research Letters*, **34**, L06805, doi:10.1029/2006GL028 443.

Lyon, B. and S. J. Mason, 2007: The 1997–1998 summer rainfall season in Southern Africa. Part I: Observations. *Journal of Climate*, **20**, 5134–5148.

Madden, R. A., D. J. Shea, R. W. Katz and J. W. Kidson, 1999: The potential long-range predictability of precipitation over New Zealand. *International Journal of Climatology*, **19**, 405–421.

Mann, M. E. and J. M. Lees, 1996: Robust estimation of background noise and signal detection in climate time series. *Climatic Change*, **33**, 409–445.

Mapande, A. T. and C. J. C. Reason, 2005a: Interannual rainfall variability over western Tanzania. *International Journal of Climatology*, **25**, 1355–1368.

Mapande, A. T. and C. J. C. Reason, 2005b: Links between rainfall variability on intraseasonal and interannual scales over western Tanzania and regional circulation and SST patterns. *Meteorology and Atmospheric Physics*, **89**, 215–234.

Marshall, G. J., 2002: Trends in Antarctic geopotential height and temperature: A comparison between radiosonde and NCEP-NCAR reanalysis data. *Journal of Climate*, **15**, 659–674.

Marshall, G. J., 2003: Trends in the Southern Annular Mode from observations and reanalyses. *Journal of Climate*, **16**, 4134–4143.

Marshall, G. J. and S. A. Harangozo, 2000: An appraisal of NCEP/NCAR reanalysis MSLP data variability for climate studies in the South Pacific. *Geophysical Research Letters*, **27**, 3057–3060.

Marshall, G. J., P. A. Stott, J. Turner, W. M. Connolley, J. C. King and T. Lachlan-Cope, 2004: Causes of exceptional atmospheric circulation changes in the Southern Hemisphere. *Geophysical Research Letters*, **31**, doi:10.1029/2004GL019 952.

McAlpine, C. A., J. Syktus, R. C. Deo, P. J. Lawrence, H. A. McGowan, I. G. Watterson and S. R. Phinn, 2007: Modeling the impact of historical land cover change on Australia's regional climate. *Geophysical Research Letters*, **34**, L22711, doi:10.1029/2007GL031 524.

McBride, J. L., 1987: The Australian summer monsoon. In C. P. Chang and T. N. Krishnamurti, eds., *Monsoon meteorology*, 203–231. Oxford University Press.

McBride, J. L. and N. Nicholls, 1983: Seasonal relationships between Australian rainfall and the Southern Oscillation. *Monthly Weather Review*, **111**, 1998–2004.

McGarity, J. W., 1987: Soils of the Australian wheat-growing areas. In A. Lazenby and E. M. Matheson, eds., *Australian field crops. Vol. 1: Wheat and other temperate cereals*, 570. Angus and Robertson.

McIntosh, P. C., A. J. Ash and M. S. Smith, 2005: From oceans to farms: The value of a novel statistical climate forecast for agricultural management. *Journal of Climate*, **18**, 4287–4302.

McIntosh, P. C., M. J. Pook, J. S. Risbey, S. N. Lisson and M. Rebbeck, 2007: Seasonal climate forecasts for agriculture: Towards better understanding and value. *Field Crops Research*, doi:10.1016/j.fcr.2007.03.019.

McPhaden, M. J., S. E. Zebiak and M. H. Glantz, 2006: ENSO as an integrating concept in Earth Science. *Science*, **314**, 1740–1745.

Meehl, G. A. and J. M. Arblaster, 1998: The Asian-Australian monsoon and El Niño-Southern Oscillation in the NCAR Climate System Model. *Journal of Climate*, **11**, 1356–1385.

Meehl, G. A., J. M. Arblaster, D. M. Lawrence, A. Seth, E. K. Schneider, B. P. Kirtman and D. Min, 2006: Monsoon regimes in the CCSM3. *Journal of Climate*, **19**, 2482–2495.

Meehl, G. A., J. M. Arblaster and J. Loschnigg, 2003: Coupled ocean-atmosphere dynamical processes in the tropical Indian and Pacific Oceans and the TBO. *Journal of Climate*, **16**, 2138–2158.

Meehl, G. A., J. M. Arblaster and C. Tebaldi, 2005: Understanding future patterns of increased precipitation intensity in climate model simulations. *Geophysical Research Letters*, **32**, L18719, doi:10.1029/2005GL023 680.

Meehl, G. A., P. R. Gent, J. M. Arblaster, B. L. Otto-Bliesner, E. C. Brady and A. Craig, 2001: Factors that affect the amplitude of El Niño in global coupled climate models. *Climate Dynamics*, **17**, 515–526.

Meehl, G. A., T. F. Stocker, W. D. Collins, P. Friedlingstein, A. T. Gaye, J. M. Gregory, A. Kito, R. Knutti, J. M. Murphy, A. Noda, S. C. B. Raper, I. G. Watterson, A. J. Weaver and Z.-C. Zhao, 2007: Global climate projections. In S. Solomon, D. Qin, M. Manning, Z. Chen, M. Marquis, K. B. Averyt, M. Tignor and H. L. Miller, eds., *Climate Change 2007: The physical science basis. Contribution of Working Group I to the Fourth Assessment Report of the Intergovernmental Panel on Climate Change*, 747–845. Cambridge University Press, Cambridge, United Kingdom, and New York, NY, USA.

Meneghini, B., I. Simmonds and I. N. Smith, 2006: Association between seasonal Australian rainfall and the Southern Annular Mode. In *Proceedings of 8th International Conference on Southern Hemisphere Meteorology and Oceanography*, 311–313. INPE, Foz do Iguacu, Brazil.

Meneghini, B., I. Simmonds and I. N. Smith, 2007: Association between Australian rainfall and the Southern Annular Mode. *International Journal of Climatology*, **27**, 109–121.

Meyers, G., 1996: Variation of Indonesian throughflow and the El-Niño-Southern Oscillation. *Journal of Geophysical Research*, **101**, 12 255–12 263.

Meyers, G., P. McIntosh, L. Pigot and M. Pook, 2007: The years of El Niño, La Niña and interactions with the tropical Indian Ocean. *Journal of Climate*, **20**, 2872–2880.

Mills, G. A. and B.-J. Wu, 1995: The 'Cudlee Creek' flash flood – an example of synoptic-scale forcing of a mesoscale event. *Australian Meteorological Magazine*, **44**, 201–218.

Mosley, P. and C. Pearson, 1997: Introduction: hydrological extremes and climate in New Zealand. In M. P. Mosley and C. P. Pearson, eds., *Floods and droughts: the New Zealand experience*, 1–14. New Zealand Hydrological Society Inc., Wellington.

Mullan, A. B., 1995: On the linearity and stability of Southern Oscillation-climate relationships for New Zealand. *International Journal of Climatology*, **15**, 1365–1386.

Mullan, A. B., 1998: Southern Hemisphere sea-surface temperatures and their contemporary and lag association with New Zealand temperature and precipitation. *International Journal of Climatology*, **18**, 817–840.

Murphy, B. F. and J. Ribbe, 2004: Variability of southeastern Queensland rainfall and climate indices. *International Journal of Climatology*, **24**, 703–721.

Murphy, B. F. and B. Timbal, 2008: A review of recent climate variability and climate change in southeastern Australia. *International Journal of Climatology*, **28**, 859–879.

Mutai, C. C., M. N. Ward and W. Colman, 1998: Towards the prediction of East Africa short rains based on sea surface temperature-atmosphere coupling. *International Journal of Climatology*, **18**, 975–997.

Nagarajan, B. and A. R. Aiyyer, 2004: Performance of the ECMWF Operational Analyses over the tropical Indian Ocean. *Monthly Weather Review*, **132**, 2275–2282.

Nagura, M. and M. Konda, 2007: The seasonal development of an SST anomaly in the Indian Ocean and its relationship to ENSO. *Journal of Climate*, **20**, 38–52.

Neelin, J. D., M. Münnich, H. Su, J. E. Meyerson and C. E. Holloway, 2006: Tropical drying trends in global warming models and observations. *Proceedings of the Academy of Sciences*, **103**, 6110–6115.

Nicholls, N., 1989: Sea surface temperatures and Australian winter rainfall. *Journal of Climate*, **2**, 965–973.

Nicholls, N., 1997: Increased Australian wheat yield due to recent climate trends. *Nature*, **387**, 484–4853.

Nicholls, N., 2006: Detecting and attributing Australian climate change: a review. *Australian Meteorological Magazine*, **55**, 199–211.

Nicholls, N., 2007: Detecting, understanding and attributing climate change. Technical report, Australian Greenhouse Office, Commonwealth of Australia, Canberra, pp. 26.

Nicholls, N., W. Drosdowsky and B. Lavery, 1997: Australian rainfall variability and change. *Weather*, **52**, 66–71.

Nicholls, N., B. Lavery, C. Frederiksen and W. Drosdowsky, 1996: Recent apparent changes in relationships between the El Niño-Southern Oscillation and Australian rainfall and temperature. *Geophysical Research Letters*, **23**, 23, 3357–3360.

Nicholson, S. E., 2001: Climatic and environmental change in Africa during the last two centuries. *Climate Research*, **17**, 123–144.

Nix, H. A., 1987: The Australian climate and its effects on grain yield and quality. In A. Lazenby and E. M. Matheson, eds., *Australian field crops. Vol. 1: Wheat and other temperate cereals*, 570. Angus and Robertson.

Ogallo, L. J., 1988: Relationships between seasonal rainfall in East Africa and the Southern Oscillation. *Journal of Climatology*, **8**, 1, 31–43.

Oki, T. and S. Kanae, 2006: Global hydrological cycles and world water resources. *Science*, **313**, 1068–1072.

Paciorek, C. S., J. S. Risbey, V. Ventura and R. D. Rosen, 2002: Multiple indices of Northern Hemisphere cyclone activity, winters 1949–99. *Journal of Climate*, **15**, 1573–1590.

Petterssen, S., 1955: A general survey of factors influencing development at sea level. *Journal of Meteorology*, **12**, 36–42.

Philander, S. G., 1985: El Niño and La Niña. *Journal of Atmospheric Sciences*, **42**, 23, 2652–2662.

Philander, S. G., 1990: *El Niño, La Niña and the Southern Oscillation*. Academic Press, San Diego, pp. 293.

Pitman, A. J., G. T. Narisma, S. Pielke, R. A. and N. J. Holbrook, 2004: Impact of land cover change on the climate of southwest Western Australia. *Journal of Geophysical Research*, **109**, D18109, doi:10.1029/2003JD004 347.

Pook, M., P. C. McIntosh and G. A. Meyers, 2006: The synoptic decomposition of cool season rainfall in the southeastern Australian cropping region. *Journal of Applied Meteorology and Climatology*, **45**, 1156–1170.

Power, S., F. Tseitkin, V. Mehta, B. Lavery, S. Torok and N. Holbrook, 1999: Decadal climate variability in Australia during the twentieth century. *International Journal of Climatology*, **19**, 169–184.

Power, S., F. Tseitkin, S. Torok, B. Lavery, R. Dahni and B. McAvaney, 1998: Australian temperature, Australian rainfall and the Southern Oscillation, 1910–1992: Coherent variability and recent changes. *Australian Meteorological Magazine*, **47**, 85–101.

Power, S. B. and I. N. Smith, 2007: Weakening of the Walker Circulation and apparent dominance of El Niño both reach record levels, but has ENSO really changed? *Geophysical Research Letters*, **34**, L18702, doi:10.1029/2007GL030 854.

Priestley, C. H. B. and A. J. Troup, 1966: Droughts and wet periods and their association with SST. *Australian Journal of Science*, **29**, 56–57.

Probert, M. E., J. P. Dimes, B. A. Keating, R. Dalal and W. M. Strong, 1997: APSIM's water and nitrogen modules and simulation of the dynamics of water and nitrogen in fallow systems. *Agricultural Systems*, **56**, 1–28.

Qi, L., L. M. Leslie and S. X. Zhao, 1999: Cut-off low pressure systems over southern Australia: climatology and case study. *International Journal of Climatology*, **19**, 1633–1649.

Qian, W. H., H. R. Hu, Y. Deng and J. W. Tian, 2002: Signals of interannual and interdecadal variability of air-sea interaction in the basin-wide Indian Ocean. *Atmosphere–Ocean*, **40**, 293–311.

Rao, V. B., A. M. C. do Carmo and S. H. Franchito, 2002: Seasonal variations in the Southern Hemisphere storm tracks and associated wave propagation. *Journal of the Atmospheric Sciences*, **59**, 6, 1029–1040.

Rao, V. B., A. M. C. do Carmo and S. H. Franchito, 2003: Interannual variations of storm tracks in the Southern Hemisphere and their connections with the Antarctic Oscillation. *International Journal of Climatology*, **23**, 1537–1545.

Rayner, N. A., D. E. Parker, E. B. Horton, C. K. Folland, L. V. Alexander and D. P. Rowell, 2003: Global analyses of SST, sea ice and night marine air temperature since the late nineteenth century. *Journal of Geophysical Research*, **108**, 4407, doi:10.1029/2002JD002 670.

Reason, C. J. C., 1999: Interannual warm and cool events in the subtropical/mid-latitude south Indian Ocean region. *Geophysical Research Letters*, **26**, 2, 215–218.

Reason, C. J. C., 2002: Sensitivity of the southern African circulation to dipole sea-surface temperature patterns in the South Indian Ocean. *International Journal of Climatology*, **22**, 377–393.

Reason, C. J. C., R. J. Allan, J. A. Lindesay and T. J. Ansell, 2000: ENSO and climatic signals across the Indian Ocean basin in the global context: Part I, Interannual composite patterns. *International Journal of Climatology*, **20**, 1285–1327.

Reason, C. J. C., C. R. Godfred-Spenning, R. J. Allan and J. A. Lindesay, 1998: Air-sea interaction mechanisms and low-frequency climate variability in the south Indian Ocean region. *International Journal of Climatology*, **18**, 391–405.

Reason, C. J. C. and D. Jagadheesha, 2005: A model investigation of recent ENSO impacts over southern Africa. *Meteorology and Atmospheric Physics*, **89**, 181–205.

Reason, C. J. C. and M. Roualt, 2005: Links between the Antarctic Oscillation and winter rainfall over western South Africa. *Geophysical Research Letters*, **32**, L07705, doi:10.1029/2005GL022 419.

Rebbeck, M., C. Lynch, P. T. Hayman and V. O. Sadras, 2007: Delving of sandy surfaced soils reduces frost damage in wheat crops. *Australian Journal of Agricultural Research*, **58**, 1–8.

Reeder, M. J. and R. K. Smith, 1998: Mesoscale meteorology. In D. J. Karoly and D. G. Vincent, eds., *Meteorology of the Southern Hemisphere*, 201–314. American Meteorological Society, No. 49.

Renwick, J. and D. Thompson, 2006: The Southern Annular Mode and New Zealand climate. *Water & Atmosphere*, **14**, 2, 24–25.

Renwick, J. A., 2004: Trends in the Southern Hemisphere polar vortex in NCEP and ECMWF reanalyses. *Geophysical Research Letters*, **31**, doi:10.1029/2003GL019 302.

Renwick, J. A., J. J. Katzfey, K. C. Nguyen and J. L. McGregor, 1998: Regional model simulations of New Zealand climate. *Journal of Geophysical Research*, **103**, 5973–5982.

Risbey, J. S., M. J. Pook, P. C. McIntosh, C. C. Ummenhofer, G. Meyers and M. J. Reeder, 2007: Variability of synoptic features associated with cool season rainfall in southeastern Australia. *International Journal of Climatology*, submitted.

Robertson, M. J. and J. A. Kirkegaard, 2005: Water-use efficiency of dryland canola in an equi-seasonal rainfall environment. *Australian Journal of Agricultural Research*, **56**, 1373–1386.

Rocha, A. and I. Simmonds, 1997a: Interannual variability of south-eastern African summer rainfall. Part I: Relationships with air-sea interaction processes. *International Journal of Climatology*, **17**, 235–265.

Rocha, A. and I. Simmonds, 1997b: Interannual variability of south-eastern African summer rainfall. Part II: Modelling the impact of sea-surface temperatures on rainfall and circulation. *International Journal of Climatology*, **17**, 267–290.

Rodwell, M. J., D. P. Rowell and C. K. Folland, 1999: Oceanic forcing of the wintertime North Atlantic Oscillation and European climate. *Nature*, **398**, 320–323.

Rotstayn, L. D., W. Cai, M. R. Dix, G. D. Farquhar, Y. Feng, P. Ginoux, M. Herzog, A. Ito, J. E. Penner, M. L. Roderick and M. Wang, 2007: Have Australian rainfall and cloudiness increased due to the remote effects of Asian anthropogenic aerosols? *Journal of Geophysical Research*, **112**, doi:10.1029/2006JD007 712.

Rowell, D. P., 1998: Assessing potential seasonal predictability with an ensemble of multidecadal GCM simulations. *Journal of Climate*, **11**, 109–120.

Saji, N., T. Ambrizzi and S. E. T. Ferraz, 2005: Indian Ocean Dipole Mode events and austral surface temperature anomalies. *Dynamics of Atmospheres and Oceans*, **39**, 87–101.

Saji, N. H., B. N. Goswami, P. N. Vinayachandran and T. Yamagata, 1999: A dipole mode in the tropical Indian Ocean. *Nature*, **401**, 360–363.

Saji, N. H. and T. Yamagata, 2003a: Possible impacts of Indian Ocean dipole mode events on global climate. *Climate Research*, **25**, 151–169.

Saji, N. H. and T. Yamagata, 2003b: Structure of SST and surface wind variability during Indian Ocean dipole mode events: COADS observations. *Journal of Climate*, **16**, 2735–2751.

Salinger, M. J., 1980: New Zealand climate: I. Precipitation patterns. *Monthly Weather Review*, **108**, 1892–1904.

Salinger, M. J., R. E. Basher, B. B. Fitzharris, J. E. Hay, P. D. Jones, J. P. Macveigh and I. Schmidely-Leleu, 1995: Climate trends in the southwest Pacific. *International Journal of Climatology*, **15**, 285–302.

Salinger, M. J. and G. M. Griffiths, 2001: Trends in New Zealand daily temperature and rainfall extremes. *International Journal of Climatology*, **21**, 1437–1452.

Salinger, M. J. and A. B. Mullan, 1999: New Zealand climate: temperature and precipitation variations and their links with atmospheric circulation 1930-1994. *International Journal of Climatology*, **19**, 1049–1071.

Salinger, M. J., J. A. Renwick and A. B. Mullan, 2001: Interdecadal Pacific Oscillation and South Pacific climate. *International Journal of Climatology*, **21**, 1705–1721.

Santoso, A., 2005: *Evolution of climate anomalies and variability of Southern Ocean water masses on interannual to centennial timescales*. Phd thesis, University of New South Wales, Sydney, Australia, pp. 326.

Sciremammano, F., 1979: A suggestion for the presentation of correlations and their significance levels. *Journal of Physical Oceanography*, **9**, 1237–1276.

Seaman, R. and T. Hart, 2003: The history of PAOBS in the Australian Bureau of Meteorology. *Australian Meteorological Magazine*, **52**, 241–250.

Sen Gupta, A. and M. H. England, 2006: Coupled ocean-atmosphere-ice response to variations in the Southern Annular Mode. *Journal of Climate*, **19**, 4457–4486.

Sen Gupta, A. and M. H. England, 2007: Coupled ocean-atmosphere feedback in the Southern Annular Mode. *Journal of Climate*, **20**, 3677–3692.

Silvestri, G. E. and C. S. Vera, 2003: Antarctic Oscillation signal on precipitation anomalies over southeastern South America. *Geophysical Research Letters*, **30**, 21, doi:10.1029/2003GL018 277.

Simmonds, I., 1990: A modelling study of winter circulation and precipitation anomalies associated with Australian region ocean temperatures. *Australian Meteorological Magazine*, **38**, 151–161.

Simmonds, I. and K. Keay, 2000: Mean Southern Hemisphere extratropical cyclone behavior in the 40-year NCEP-NCAR reanalysis. *Journal of Climate*, **13**, 873–885.

Simmonds, I. and T. Richter, 2000: Synoptic comparison of cold events in summer and winter in Melbourne and Perth. *Theoretical and Applied Climatology*, **67**, 19–32.

Simmonds, I. and A. Rocha, 1991: The association of Australian winter climate with ocean temperatures to the west. *Journal of Climate*, **4**, 1147–1161.

Simmonds, I., A. Rocha and D. Walland, 1992: Consequences of winter tropical pressure anomalies in the Australian region. *International Journal of Climatology*, **12**, 419–434.

Smith, I. N., P. McIntosh, T. J. Ansell, C. J. C. Reason and K. McInnes, 2000: Southwest western Australian winter rainfall and its association with Indian Ocean climate variability. *International Journal of Climatology*, **20**, 15, 1913–1930.

Smith, T. M. and R. W. Reynolds, 2003: Extended reconstruction of global sea surface temperatures based on COADS data (1854–1997). *Journal of Climate*, **16**, 1495–1510.

Smith, T. M. and R. W. Reynolds, 2004: Improved extended reconstruction of SST (1854–1997). *Journal of Climate*, **17**, 2466–2477.

Sohn, E., 2007: The Big Dry. *Science News*, **172**, 17.

Stephens, D. J. and T. J. Lyons, 1998: Variability and trends in sowing dates across the Australian wheatbelt. *Australian Journal of Agricultural Research*, **49**, 1111–1118.

Sterl, A. and W. Hazeleger, 2005: The relative roles of tropical and extratropical forcing on atmospheric variability. *Geophysical Research Letters*, **32**, L18716, doi:10.1029/2005GL023 757.

Streten, N. A., 1981: Southern Hemisphere sea surface temperature variability and apparent associations with Australian rainfall. *Journal of Geophysical Research*, **86**, C1, 485–497.

Streten, N. A., 1983: Extreme distributions of Australian annual rainfall in relation to sea surface temperature. *Journal of Climatology*, **3**, 143–153.

Sturman, A. and N. Tapper, 1996: *The weather and climate of Australia and New Zealand*. Oxford University Press, Australia, pp. 476.

Suppiah, R., 1992: The Australian summer monsoon. *Progress in Physical Geography*, **16**, 283–318.

Suppiah, R., 2004: Trends in the Southern Oscillation phenomenon and Australian rainfall and changes in their relationship. *International Journal of Climatology*, **24**, 269–290.

Sutcliffe, R. and A. Forsdyke, 1950: Use of upper air thickness patterns in forecasting. *Quarterly Journal of the Royal Meteorological Society*, **76**, 189–217.

Suzuki, R., S. K. Behera, S. Iizuka and T. Yamagata, 2004: Indian Ocean subtropical dipole simulated using a coupled general circulation model. *Journal of Geophysical Research*, **109**, C09001, doi:10.1029/2003JC001 974.

Thompson, D. W. J. and S. Solomon, 2002: Interpretation of recent Southern Hemisphere climate change. *Science*, **296**, 895–899.

Thompson, D. W. J. and J. M. Wallace, 2000: Annular modes in the extratropical circulation. Part I: Month-to-month variability. *Journal of Climate*, **13**, 1000–1016.

Thompson, D. W. J., J. M. Wallace and G. C. Hegerl, 2000: Annular modes in the extratropical circulation. Part II: Trends. *Journal of Climate*, **13**, 1018–1036.

Thorncroft, C., B. Hoskins and M. McIntyre, 1993: Two paradigms of baroclinic-wave life-cycle behaviour. *Quarterly Journal of the Royal Meteorological Society*, **119**, 17–55.

Tierney, J. E. and J. M. Russell, 2007: Abrupt climate change in southeast tropical Africa influenced by Indian monsoon variability and ITCZ migration. *Geophysical Research Letters*, **34**, L15709, doi:10.1029/2007GL029 508.

Timbal, B., 2004: Southwest Australia past and future rainfall trends. *Climate Research*, **26**, 3, 233–249.

Timbal, B. and J. M. Arblaster, 2006: Land cover change as an additional forcing to explain the rainfall decline in the south west of Australia. *Geophysical Research Letters*, **33**, L07717, doi:10.1029/2005GL025 361.

Timbal, B., J. M. Arblaster and S. Power, 2006: Attribution of the late-twentieth-century rainfall decline in southwest Australia. *Journal of Climate*, **19**, 2046–2062.

Timmermann, A., J. Oberhuber, A. Bacher, M. Esch, M. Latif and E. Roeckner, 1999: Increased El Niño frequency in a climate model forced by future greenhouse warming. *Nature*, **398**, 694–697.

Treble, P., J. M. G. Shelley and J. Chappell, 2003: Comparison of high resolution sub-annual records of trace elements in a modern (1911–1992) speleothem with instrumental climate data from southwest Australia. *Earth and Planetary Science Letters*, **216**, 141–153.

Treble, P. C., W. F. Budd, P. K. Hope and P. K. Rustomji, 2005a: Synoptic-scale climate patterns associated with rainfall $\delta^{18}O_2$ in southern Australia. *Journal of Hydrology*, **302**, 270–282.

Treble, P. C., J. Chappell, M. K. Gagan, K. D. McKeegan and T. M. Harrison, 2005b: In situ measurement of seasonal $\delta^{18}O_2$ variations and analysis of isotopic trends in a modern speleothem from southwest Australia. *Earth and Planetary Science Letters*, **233**, 17–32.

Trenberth, K. E. and K. Mo, 1985: Blocking in the Southern Hemisphere. *Monthly Weather Review*, **113**, 3–21.

Trenberth, K. E. and D. J. Shea, 1987: On the evolution of the Southern Oscillation. *Monthly Weather Review*, **115**, 3078–3096.

Ummenhofer, C. C. and M. H. England, 2007: Interannual extremes in New Zealand precipitation linked to modes of Southern Hemisphere climate variability. *Journal of Climate*, **20**, 5418–5440.

Ummenhofer, C. C., A. Sen Gupta and M. H. England, 2007a: Causes of late twentieth Century trends in New Zealand precipitation. *Journal of Climate*, revised.

Ummenhofer, C. C., A. Sen Gupta, M. H. England and C. J. C. Reason, 2007b: Contributions of Indian Ocean sea surface temperatures to Enhanced East African rainfall. *Journal of Climate*, to be submitted.

Ummenhofer, C. C., A. Sen Gupta, M. J. Pook and M. H. England, 2007c: Anomalous rainfall over southwest Western Australia forced by Indian Ocean sea surface temperatures. *Journal of Climate*, revised.

Uppala, S. M., P. W. Kallberg, A. J. Simmons, U. Andrae, V. da Costa Bechtold, M. Fiorino, J. K. Gibson, J. Haseler, A. Hernandez, G. A. Kelly, X. Li, K. Onogi, S. Saarinen, N. Sokka, R. P. Allan, E. Andersson, K. Arpe, M. A. Balmaseda, A. C. M. Beljaars, L. van de Berg, J. Bidlot, N. Bormann, S. Caires, F. Chevallier, A. Dethof, M. Dragosavac, M. Fisher, M. Fuentes, S. Hagemann, E. Holm, B. J. Hoskins, L. Isaksen, P. A. E. M. Janssen, R. Jenne, A. P. McNally, J.-F. Mahfouf, J.-J. Morcrette, N. A. Rayner, R. W. Saunders, P. Simon, A. Sterl, K. E. Trenberth, A. Untch, D. Vasiljevic, P. Viterbo and J. Woollen, 2005: The ERA-40 re-analysis. *Quart. J. Roy. Meteor. Soc.*, **131**, 2961–3012.

van Ommen, T., V. Morgan and M. Curran, 2007: Probing past climate variability in the Australian region using Antarctic ice cores. In *Greenhouse2007*. Sydney, Australia.

Vecchi, G. A. and B. J. Soden, 2007: Global warming and the weakening of the tropical circulation. *Journal of Climate*, **20**, 4316–4340.

Vecchi, G. A., B. J. Soden, A. T. Wittenberg, I. M. Held, A. Leetmaa and M. J. Harrison, 2006: Weakening of tropical Pacific atmospheric circulation due to anthropogenic forcing. *Nature*, **441**, 73–76.

Verdin, J., C. Funk, G. Senay and R. Choularton, 2005: Climate science and famine early warning. *Philosophical Transactions of the Royal Society B*, **360**, 2155–2168.

Verdon, D. C. and S. W. Franks, 2006: Long-term behaviour of ENSO: interactions with the PDO over the past 400 years inferred from paleoclimate records. *Geophysical Research Letters*, **33**, L06712, doi:10.1029/2005GL025 052.

Verschuren, D., K. R. Laird and B. F. Cumming, 2000: Rainfall and drought in equatorial east Africa during the past 1,100 years. *Nature*, **403**, 410–414.

Voice, M. E. and B. G. Hunt, 1984: A study of the dynamics of drought initiation using a global general circulation model. *Journal of Geophysical Research*, **89**, 9504–9520.

von Storch, H. and F. W. Zwiers, 1999: *Statistical analysis in climate research*. Cambridge University Press, Cambridge, pp. 484.

Walland, D. J., S. B. Power and A. C. Hirst, 2000: Decadal climate variability simulated in a coupled general circulation model. *Climate Dynamics*, **16**, 201–211.

Wang, C. and J. Picaut, 2004: Understanding ENSO physics - a review. In C. Wang, S.-P. Xie and J. A. Carton, eds., *Earth's climate: The ocean-atmosphere interaction*, volume 147, 21–48. American Geophysical Union, Washington, DC.

Wang, G. and H. Hendon, 2007: Sensitivity of Australian rainfall to inter-El Niño variations. *Journal of Climate*, **20**, 4211–4226.

Ward, J., 1963: Hierarchical grouping to optimize an objective function. *Journal of the American Statistical Association*, **58**, 236–244.

Watkins, A. and B. Trewin, 2007: Australian climate summary: 2006. *Bullettin of the Australian Meteorological and Oceanographic Society*, **20**, 10–17.

Watterson, I. G., 2001: Wind-induced rainfall and surface temperature anomalies in the Australian region. *Journal of Climate*, **14**, 9, 1901–1922.

Waugh, J., H. Freestone and D. Lew, 1997: Historic floods and droughts in New Zealand. In M. P. Mosley and C. P. Pearson, eds., *Floods and droughts: the New Zealand experience*, 29–50. New Zealand Hydrological Society Inc., Wellington.

Webster, P. J., A. M. Moore, J. P. Loschnigg and R. R. Leben, 1999: Coupled ocean-atmosphere dynamics in the Indian Ocean during 1997–98. *Nature*, **401**, 356–360.

Wentz, F. J., L. Ricciardulli, K. Hilburn and C. Mears, 2007: How much more rain will global warming bring? *SciencExpress*, 10.1126/science.1140746.

Whetton, P., 1997: Floods, droughts and the Southern Oscillation connection. In E. K. Webb, ed., *Windows on meteorology: Australian perspective*, 180–199. CSIRO Publishing, Melbourne.

White, W. B., 2000: Influence of the Antarctic circumpolar wave on Australian precipitation from 1958 to 1997. *Journal of Climate*, **13**, 2125–2141.

White, W. B. and N. J. Cherry, 1999: Influence of the Antarctic Circumpolar Wave upon New Zealand temperature and precipitation during autumn-winter. *Journal of Climate*, **12**, 960–976.

Wijffels, S. and G. Meyers, 2004: An intersection of oceanic waveguides - variability in the Indonesian Throughflow region. *Journal of Physical Oceanography*, **34**, 1232–1253.

Wright, P. B., 1974: Seasonal rainfall in southwestern Australia and the general circulation. *Monthly Weather Review*, **102**, 219–232.

Wright, W. J., 1989: A synoptic climatological classification of winter precipitation in Victoria. *Australian Meteorological Magazine*, **37**, 217–229.

Wright, W. J., 2004: *Drought, dust and deluge: A century of climate extremes in Australia*. Australian Government, Bureau of Meteorology, Australia, pp. 78.

Xie, P. and P. A. Arkin, 1996: Analyses of global monthly precipitation using gauge observations, satellite estimates, and numerical model predictions. *Journal of Climate*, **9**, 840–858.

Xie, S.-P., H. Annamalai, F. A. Schott and J. McCreary, J. P., 2002: Structure and mechanisms of South Indian Ocean climate variability. *Journal of Climate*, **15**, 864–878.

Yamagata, T., S. A. Behera, S. A. Rao, Z. Guan, K. Ashok and N. H. Saji, 2003: Comments on "Dipoles, temperature gradients, and tropical climate anomalies". *Bulletin of the American Meteorological Society*, **84**, 1418–1422.

Yamagata, T., S. K. Behera, J. Luo, S. Masson and M. R. Jury, 2004: Coupled ocean-atmosphere variability in the tropical Indian Ocean. In C. Wang, S.-P. Xie and J. A. Carton, eds., *Earth's climate: The ocean-atmosphere interaction*, volume 147, 189–211. American Geophysical Union, Washington, DC.

Yin, J. H., 2005: A consistent poleward shift of the storm tracks in simulations of 21st century climate. *Geophysical Research Letters*, **32**, doi:10.1029/2005GL023 684.

Zelle, H., G. J. van Oldenborgh, G. Burgers and H. Dijkstra, 2005: El Niño and greenhouse warming: Results from ensemble simulations with the NCAR CCSM. *Journal of Climate*, **18**, 4669–4683.

Zhang, G. and H. Wang, 2006: Toward mitigating the double ITCZ problem in NCAR CCSM3. *Geophysical Research Letters*, **33**, L06709, doi:10.1029/2005GL025 229.

Zhang, Q. and S. Yang, 2007: Seasonal phase-locking of peak events in the eastern Indian Ocean. *Advances in Atmospheric Sciences*, **24**, 781–798.

Zhang, X., F. W. Zwiers, G. C. Hegerl, F. H. Lambert, N. P. Gillett, S. Solomon, P. A. Stott and T. Nozawa, 2007: Detection of human influence on twentieth-century precipitation trends. *Nature*, **448**, 461–466.

Zheng, X. and C. S. Frederiksen, 2006: A study of predictable patterns for seasonal forecasting of New Zealand rainfall. *Journal of Climate*, **19**, 3320–3333.

Acronyms

ACW	Antarctic Circumpolar Wave
AGCM	Atmospheric general circulation model
APSIM	Agricultural Production Systems sIMulator
AR4	Assessment Report Four
BoM	Australian Bureau of Meteorology
CAM	Community Atmosphere Model
CAMSOPI	Climate Anomaly Monitoring System-OLR Precipitation Index
CCSM	Community Climate System Model
CDC	Climate Diagnostics Center
CMAP	CPC Merged Analysis of Precipitation
COADS	Comprehensive Ocean-Atmosphere Data Set
CORE	Common Ocean-ice Reference Experiments
CPC	Climate Prediction Center
CSIRO	Commonwealth Scientific and Industrial Research Organisation
DJF	December-January-February
DMI	Dipole Mode Index
DNRM	Queensland Department of Natural Resources and Mines
ECMWF	European Centre for Mid-Range Weather Forecasting
ENSO	El Niño-Southern Oscillation
EOF	Empirical orthogonal function
ERA-40	ECMWF 40-year Re-analysis
GCM	General circulation model
GPCC	Global Precipitation Climatology Center
GPCP	Global Precipitation Climatology Project
IOCI	Indian Ocean Climate Initiative
IOD	Indian Ocean Dipole
IODM	Indian Ocean zonal dipole mode
IPCC	Intergovernmental Panel on Climate Change
IPO	Interdecadal Pacific Oscillation
ITCZ	Intertropical Convergence Zone
ITF	Indonesian Throughflow
JASO	July-August-September-October
JJA	June-July-August

MAM	March-April-May
MAMJ	March-April-May-June
MSLP	Mean sea level pressure
NCAR	National Center for Atmospheric Research
NCEP	National Center for Environmental Prediction
NIWA	National Institute of Water and Atmospheric Research
NNR	NCEP-NCAR reanalysis
NOAA	National Oceanic and Atmospheric Association
NWWA	Northwest Western Australia
OLR	Outgoing longwave radiation
OND	October-November-December
PC	Principal component
PDO	Pacific Decadal Oscillation
POP	Parallel Ocean Program
PSD	Power spectral density
SAM	Southern Annular Mode
SAT	Surface air temperature
SD	Standard deviation
SDI	Subtropical Dipole Index
SEA	Southeastern Australia
SIOD	Subtropical Indian Ocean Dipole
SLP	Sea level pressure
SOI	Southern Oscillation Index
SON	September-October-November
SPCZ	South Pacific Convergence Zone
SST	Sea surface temperature
SWWA	Southwest Western Australia
TBO	tropospheric biennial oscillation
UTC	Coordinated Universal Time
WA	Western Australia